PhD Thesis in Sciences

Hololab
Faculty of Sciences
University of Liège, Belgium

Achromatization of nonimaging Fresnel lenses for photovoltaic solar concentration using refractive and diffractive patterns

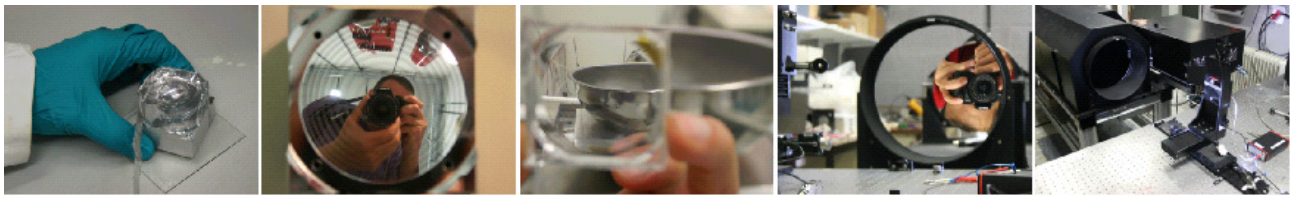

- Fabian LANGUY -

December 2012

Achromatization of nonimaging Fresnel lenses for photovoltaic solar concentration using refractive and diffractive patterns

Composition of the Jury

Prof. Philippe ANDRÉ	University of Liège (Be)
Dr. Giovanni FLAMAND	Imec, Leuven (Be)
Prof. Serge HABRAKEN	University of Liège (Be)
Dr. Ralf LEUTZ	Concentrator Optics GmbH (De)
Dr. Jérôme LOICQ (Secretary)	University of Liège (Be)
Prof. Ngoc Duy NGUYEN (President)	University of Liège (Be)

Supervisor

Prof. Serge HABRAKEN
shabraken@ulg.ac.be
Hololab
Université de Liège – Bat. B5a
Allée du 6 août, 17
4000 Liège, Belgium

Council Members

Dr. Cédric LENAERTS, Centre Spatial of Liège
Dr. Jérôme LOICQ, Centre Spatial of Liège

Main collaborators

Amos S.A. - Liège, Belgium
Centre Spatial of Liège – Liège, Belgium
Optim Test Center – Liège, Belgium

A thesis presented by
Fabian LANGUY
for the degree of Doctor of Philosophy
at the Faculty of Sciences

flanguy@ulg.ac.be

Remerciements

Il est de coutume de remercier en premier lieu le promoteur de thèse, il faut savoir que c'est bien au-delà de la tradition que je tiens à commencer par remercier le Professeur Serge Habraken pour l'accueil qu'il m'a réservé durant ces 5 années de recherches au sein du laboratoire Hololab. J'ai particulièrement apprécié le fin dosage entre sa porte toujours ouverte dans les moments où j'en avais besoin et la grande liberté que j'ai pu prendre dans le cadre de mes recherches. Je ne pense pas qu'il se soit écoulé la moindre réunion en sa présence où nous n'ayons pas ri ! C'est à la fois dans un contexte très professionnel et très humain que cette thèse a vu le jour et ce fut un réel plaisir pour moi.

Mais le plaisir quotidien que j'ai pris à me rendre au laboratoire, je le dois surtout aux collègues de bureau : Caroline, Céline (merci pour la relecture !), Christian, Cédric, Donat, Eddy, Fabrice, Georges, Grégory, Marc, Monsieur Renotte, Pascal, Pierre, Serge, Stéphane et Vanessa ainsi qu'aux secrétaires Angela, Christine, Claire, Florence et Sylvia et autres personnes croisées au détour d'un couloir : Arthur, Marie, Nico, Jacqueline et Marie-Claire. Un merci particulier aux membres du midi gâteau inauguré par Louise : Caroline, Christian, Coline, Dounia, Grégory, Marjorie, Pierre, Stef & Denis à qui je pense bien fort et auxquels je remets tous mes vœux de bonheur en compagnie leur petit Basile. Et puis il eût les ô combien sympathiques heures supp' qu'on doit à Pascal avec ses célèbres apéro bières ainsi que quelques variantes (en particulier le porto, merci Marc mais surtout l'inoubliable apéro vodka, merci Christian).

Les collègues du CSL ont aussi joué une part importante dans mes recherches : Cédric, Jérôme, Karl, Laurence, Paola et Tanguy. L'expérience du CSL fut indispensable à l'aboutissement de cette thèse. Je tiens à remercier Tanguy pour le temps qu'il m'a consacré pour le simulateur solaire et pour tous ses éclairages lors des conférences à Valence et Hambourg, que de bons moments passés ensemble à faire du tourisme scientifico-gastronomique... Je tiens également à remercier en particulier Cédric et Jérôme, membres de mon comité de thèse, pour leur accompagnement, les discussions scientifiques, les nombreuses remarques constructives sur mes écrits et leur soutien depuis mes débuts en 2008. Je n'oublie pas là non plus les deux sympathiques petits restaurants avec toi Jérôme, merci.

Merci aussi aux partenaires de projets. Romain et Jean-François pour Amos S.A. ainsi que Olivier et Jérôme pour Optim Test Center.

Thank you very much Ralf Leutz for all the interesting and friendly discussions we had at various international congress.

Il y a aussi tous ces gens qui m'ont soutenu d'une manière ou d'une autre.

Je pense à mes amis Tournaisiens Julien, Simon et Thomas. Et puis les liégeois des premiers jeudis du mois, ainsi que Domi, Épa, Caro et la famille Jacquinet. Si j'ai eu ma place à l'Université de Liège, c'est en grande partie grâce à eux. Salutations également aux collègues des FUNDP.

Mais dans cette thèse, quatre noms s'élèvent parmi tous...

Il y eu en premier lieu mon collègue du bureau, Christian, avec qui j'ai partagé quatre ans au R/54, une sacrée note de téléphone aussi. Il est venu plusieurs fois dormir à la maison et réciproquement, avec qui j'ai refais le monde, avec qui j'ai cueilli des champignons et quelques sous-plats... Nous nous sommes soutenus dans les moments difficiles mais avons surtout passé plein de bons moments. Merci l'ami !

Deuxièmement, je tiens à saluer bien bas ce cher Nico. Chimiste, presque physicien, menuisier, alter et médecin de famille devenu ami ! J'attends toujours de monter le Sart-Tilman à vélo avec toi !

En troisièmement, mon second collègue de bureau, Pascal d'une attention constante et apaisant, jamais de mauvaise humeur malgré la tonne de boulot qui lui tombait dessus... Il m'en a fait des éloges (notamment suite à toutes les questions d'optique qu'il m'a posées), sans doute lui en ai-je fait nettement moins. Et pourtant... dans son humilité et son calme relatif regorge une quantité de qualités, une énergie et un goût de la vie et des choses simples qui font naître en vous une affection particulière. Comment, dès lors, refuser la demande que Lauriane et Pascal m'ont faite, cet immense honneur qu'ils m'ont fait en me proposant de devenir parrain de leur premier enfant !?! J'en profite donc pour faire un petit coucou à ma filleule Zoélie.

Et quatrièmement il y a Louise ! Ma très chère Louise... Pendant neuf ans, tu es parvenue à mettre de la couleur, de l'élégance et du charme à la physique. Tu as égaillé les nombreuses heures de cours passées ensemble, tu m'as fait connaître tes talents de cuisinière, ton hospitalité. Quel bonheur ce fut pour moi quand j'ai appris que tu viendrais me rejoindre à Liège ! Mais malheureusement, tu as aussi cette satanée tendance à faire en sorte que quand j'écris des remerciements tu te trouves à quelques heures d'avion de moi. Mais saches que tu ne te débarrasseras pas aussi facilement de moi !

Je tiens aussi à remercier ma famille.

Papa et maman qui m'ont toujours soutenu et encouragé. Dans une confiance mutuelle, ils m'ont permis de grandir, de m'épanouir, de choisir librement mes études et de les mener à bien. Ils se sont toujours réjouis pour moi, même si c'était pour leur annoncer que j'allais signer pour un travail à Liège. Maman, toujours souriante et accueillante, et papa toujours d'accord pour rendre service à son fiston, quitte à devoir relire et corriger 250 pages de thèse en anglais ! Merci beaucoup !

Mes grands-parents paternels, toujours présents, m'ont toujours accompagné dans l'accomplissement de mes projets. Ils m'ont toujours accueilli à bras ouverts et ont été d'une grande aide pour la famille dans les moments plus difficiles. Il m'a même été donné de pouvoir parler du contenu de ma thèse avec eux, ce que j'ai fait avec vraiment peu de monde ! Lors des mes années d'études universitaires, j'ai passé quelques blocus chez eux est j'ai eu droit à quelques cours de maths particuliers ! Qu'ils viennent encore dire qu'ils n'ont pas toute leur tête mes extraordinaires grands-parents.

Merci aussi à mamounette ! Elle aussi a toujours pris des nouvelles de ma thèse, c'est sans doute la personne la plus impatiente que je passe ma défense. Il faut savoir qu'à son âge, ma grand-mère lit des romans plein de physique !

Je profite également de l'occasion pour saluer la famille VdK, et les remercier pour le chaleureux accueil qu'ils me réservent à chaque fois.

Pour terminer, il y a une et unique personne qui mérite bien à elle seule une place d'honneur parmi ces remerciements...

Bien que peu présente sur mon lieu de travail (je n'oublierai cependant certainement pas ta génialissime visite surprise pendant un de mes cours !) et dans la participation à mes recherches proprement dites, tu as joué un rôle principal pour le bon déroulement de cette thèse, avec des petites pensées quotidiennes, tu as égaillé mes réveils matinaux nécessaires pour partir au boulot de bonne humeur... Et malgré tous ces bons côtés, tout ce que tu as fait pour moi, tu es l'unique personne qui a dû subir les revers de cette thèse lorsque je dus me coucher à des heures tardives, lorsque nous passions les trajets de train toi face à moi, mais moi face à mon ordinateur. Pendant ces moments qui n'avaient rien d'agréable, tu as gardé le sourire, tu restais fière de moi, d'une compréhension hors du commun et faisait en sorte que tout se passa au mieux dans une douceur et dans l'envie de bien faire les choses qui te sont propres. Merci pour tout l'amour que tu m'as accordé, la confiance en moi que tu as ancrée et ta joie de vivre que tu m'as partagée. Je t'aime Coline.

Table of Contents

Résumé

Dans le domaine de la concentration solaire photovoltaïque, l'inconvénient majeur des lentilles par rapport aux miroirs se situe au niveau du chromatisme : la loi de la réfraction impliquant directement l'indice de réfraction qui est lui-même dépendant de la longueur d'onde. D'un point de vue théorique, les miroirs peuvent concentrer la lumière solaire jusqu'à 46 000×, ce qui correspond la limite thermodynamique par rapport au diamètre angulaire du Soleil, d'environ 0,5°. Par contre, du fait de leur chromaticité, les lentilles en PMMA sont limitées à une concentration d'environ 1000×, sans même tenir compte de la taille angulaire de la source. De plus, l'inhomogénéité spectrale réduit l'efficacité des cellules solaires.

Cette thèse a comme objectif de développer des lentilles achromatiques adaptées à la concentration solaire. C'est-à-dire alliant haute concentration, faible coût de production et tolérance quant aux erreurs de fabrication.

Dans un premier temps, des recherches ont été menées sur une lentille hybride en plastique combinant une lentille de Fresnel réfractive avec une lentille diffractive. Ces recherches ont montré que facteur de concentration peut être multiplié par 4. Le design de la lentille diffractive nécessite la maîtrise théorique des réseaux de diffraction blazés afin de pouvoir les optimiser. La lentille diffractive pouvant être considérée comme un réseau à période variable. Cependant, pour parvenir à une haute efficacité de diffraction, nous montrerons que la lentille diffractive doit être composée de deux couches de matériaux différents, ce qui a comme conséquence de rendre le système très peu tolérant aux erreurs de fabrication.

En second lieu, nous nous sommes tournés vers des doublets de Fresnel achromatiques. Ceux-ci permettent d'atteindre des facteurs de concentration extrêmement élevés ($> 100\,000\times$) pour des rayons collimatés sous incidence normale. Tout comme les miroirs, le facteur de concentration n'est alors plus limité par l'aberration chromatique mais par le *f*-number.

Un singulet, une lentille hybride et un doublet achromatique ont été fabriqués par injection plastique à partir de moules réalisés par tournage diamant. A l'aide d'un simulateur solaire continu leurs performances ont été évaluées. Il s'avère que les résultats expérimentaux obtenus sont en très bonne adéquation avec les calculs théoriques et les simulations réalisées par lancer de rayons.

Il ressort de cette thèse que les doublets achromatiques représentent une solution tolérante à faibles coûts de production pour parvenir à un flux blanc fortement concentré. Alors que les lentilles hybrides composées d'une lentille diffractive bicouche sont trop peu tolérantes aux erreurs de fabrications, de nombreuses applications développées ou en cours de développement sont issues du travail de recherche lié à cette thèse de doctorat.

1 Introduction

1.1. Why concentrated photovoltaics?

The only goal of concentrated photovoltaics (CPV) is to reduce the cost of photovoltaic power generation: the lower the price of photovoltaic energy, the better the consumer's wallet. To achieve this reduction, an optical system (mirrors or lenses) is used to concentrate light onto a small photovoltaic cell. Since solar cells are far more expensive than the optical part for an equivalent surface, reducing the solar cell area translates into saving money. But looking only at the economic aspect would mean neglecting the ecological part of CPV. Detractors of photovoltaics claim that solar cells are polluting to produce. For the moment, the energy payback time (EPBT, i.e. the period of time over which the energy produced by a solar panel equals the energy needed to produce this panel) is about five years for silicon technologies [Sto08] while the lifetime of solar panels is about 30 years. It is funny to point out that some are proud to claim that their own product has the lowest EPBT with e.g. 0.9 year for thin films but for a lifetime of only 4 years... Greenwashing occurs as much in renewable energies as in fossil fuels. But in addition to economical advantages, CPV allows to use fewer PV cells for the same amount of energy produced. So, if the concentrating system has a lower ecological footprint, the energy produced is greener. Fthenakis and Kim [Fth11] deduced from their investigations that the EPBT is reduced to about two years thanks to CPV. On the other hand, we will be soon facing a lack of raw materials like indium and gallium [Bih10] used for CPV. Anyway, high solar concentration is part of the solution for cheaper and greener energy. Finally,

compared to silicon technologies with a module efficiency of about 14%, the electrical power produced per square meter is higher (since the efficiency of a HCPV module lies around 30%).

1.2. Aim of the thesis and research method

Two technologies are competing on the CPV market: lenses and mirrors, each technology having its own pros and cons. Lenses suffer from a wavelength dependence: short wavelengths being more refracted than long wavelengths. This causes an important spread of the focal spot, which implies that one cannot concentrate the solar irradiance as much as reflecting technologies do. Moreover, the non-uniformity of the flux reaching the solar PV cell reduces the efficiency of the cell [Dom12]. On the other hand, lenses are more tolerant to manufacturing errors than mirrors. To combine advantages of tolerant designs with low chromaticity, we decided to investigate ways of turning lenses more independent to the wavelength, by using either refractive or diffractive solutions. The choice of materials and means of production is governed by the need of cost-effective optics. This requires thin, light and cheap lenses. Hence the use of plastic Fresnel lenses provided by mass production process, like injection moulding or embossing.

After some theoretical considerations, we will show that only two optical plastics are suitable for CPV: the poly(methyl methacrylate) and the polycarbonate (PMMA and PC). We will then discuss some parameters affecting the optical performances of solar concentrators using lenses. Among them, we will particularly focus on the chromatic effects. Since the change of refractive index with wavelength is intrinsic to the lens material, we will prove that the maximum concentration with lenses is limited by the longitudinal chromatic aberration (LCA) whatever the design parameters. On the other hand, we will also show that the angular size of the source limits the concentration ratio as a function of the *f*-number. Finally, we will show that the LCA is the main limiting factor for typical Fresnel singlets, hence the need to investigate ways to reduce the chromatic aberration of Fresnel lenses.

One solution consists in combining a refractive Fresnel lens with a diffractive lens. Indeed, contrary to refractive lenses, diffractive lenses make long wavelengths converge faster than short wavelengths. By combining them together in an appropriate way, an achromatic system can be achieved in a single piece. In order to optimize the design of the diffractive lens, several tools will be developed. Indeed, theories allowing to rigorously calculate the diffraction are critically time consuming and hard to implement. We will therefore look at a simplified theory, namely the scalar theory, and determine its validity domain. Then this theory will

be used to optimize the diffraction efficiency of the first order. Unfortunately, even optimized, monolayer diffractive lenses critically suffer from a lack of diffraction efficiency to compete with other primary optics for CPV. A second diffractive layer is necessary to achieve high diffraction efficiency from 380 to 1600 nm.

The other solution presented in this thesis combines a converging refractive Fresnel lens with a diverging refractive Fresnel lens to form an achromatic Fresnel doublet. This solution allows to drastically reduce the LCA, therefore the maximum concentration is no longer driven by the LCA but is governed by the *f*-number and the angular aperture of the Sun, as for reflecting technologies.

We will present a method for designing nonimaging optical systems. Our method is inspired by Ralf Leutz but is slightly modified to enhance the concentration ratio for flat optical systems. We will explain how to optimize the flat Fresnel singlet, the flat hybrid (refractive/diffractive) lens and the refractive doublet based on a new achromatization equation. These three kinds of lenses will be manufactured by injection moulding, from a mould made by diamond turning. Tolerances of each design will be investigated and compared. This will be done with paraxial calculations, ray-tracing simulations and experimentally, using the continuous solar simulator from the Centre Spatial of Liège. Before the experimental part, this solar simulator will be characterized in order to check if its parameters match that of the Sun.

To put it in a nutshell, the aim of this thesis consists in the development and characterization of cost-effective nonimaging achromatic Fresnel lenses.

.

2 | Theoretical background for photovoltaic solar concentration

In order to properly design a solar concentrator for photovoltaics, numerous notions are needed.

Firstly, since a solar concentrator aims to concentrate sunlight at a photovoltaic cell, it is of importance to characterise both the solar spectrum reaching the optical component and the behaviour of the solar cell under a concentrated flux with spectral inhomogeneities due to the chromatic aspect of lenses.

Secondly, an optical background for CPV will be provided. Since cost-efficient lenses are made of plastic, optical properties of dielectric will be discussed. Then nonimaging optics will be introduced. Indeed, aiming a high concentration is different from aiming image-forming optical systems. Higher concentration ratios can be achieved with nonimaging designs than with imaging designs. However, we will deduce that one cannot concentrate the Sun as much as desired. The concentration factor is limited by the angular size of the source and obeys the law of étendue conservation.

2.1. Brief history of photovoltaic solar concentration

"*When you don't know where you are going look at where you come from*". In the light of this Berber maxim, let's take a look at the three origins of concentrated photovoltaics.

Firstly, CPV is related with the solar concentration as the ancient populations knew it tens of centuries ago. The ability of concave reflective surfaces to set fire was as useful as scheming. The legend claims that, in 214 BC, Archimedes would have delayed the siege of Syracuse by the Roman Republic using concave mirrors in order to set fire to enemy ships. More than mirrors, burning glasses were commonly used in the Antiquity [Sin87]. The oldest unearthed lens artifact, the Nimrud lens exposed at the British museum, is 3000 years old. Modern optics, meanwhile, was born only in the very beginning of the second millennium with the discovery of the refraction law by Alhazen[1] [Wol95].

Secondly, CPV is related with the photovoltaic effect discovered in 1839 by Alexandre-Edmond Becquerel, father of Henri Becquerel. It took many years before obtaining satisfactory solar cell efficiencies. In the 1950s, the advent of spatial programs boosted the investigations dedicated to solar cells. Indeed, spacecrafts and on-board scientific equipment found in photovoltaics the solution to obtain an abundant energy source in space. During these years, efficiency of solar cells was improved by up to 10%.

Finally, the energy crisis of the 1970s illuminated minds on the need to diversify energy sources and to reduce production costs, which gave rise to photovoltaic solar concentration among others.

1 Also known as Ibn Sahl or Ibn al Haytham

2.2. Sun's spectra

For a work dealing with solar energy, some information about the Sun is probably not superfluous.

Every single second, our star emits some 383 10^{24} joules, 170 10^{15} watts reach the Earth's atmosphere while humanity consumes on average a ten thousandth part of this power (~16 10^{12} watts). In other words, every hour, the Sun provides our planet with as much energy as mankind uses every year [Mor06]. To optimize their solar concentrators, optical designers have to know how the energy emitted by the Sun reaches the surface of the Earth.

2.2.1. Sun's radiant exitance

The Sun's emission may be approximated by a black-body of 5780 K for which the spectral radiant exitance is given by Planck's formula[2]:

$$M_{e\lambda}=\frac{2\pi h c^2 \lambda^{-5}}{e^{\frac{hc}{\lambda k_B T}}-1}\left[W\cdot m^{-2}\cdot m^{-1}\right] . \tag{2.1}$$

This spectral radiant exitance may be integrated over the full spectrum in order to find the radiant exitance of the black-body, which corresponds to Stefan's law:

$$M_e=\sigma T^4\left[W\cdot m^{-2}\right]. \tag{2.2}$$

Applying this formula to the effective temperature of the Sun, we find

$$M_{e\odot}=\sigma T_{\odot}^4=63\,MW\cdot m^{-2} \tag{2.3}$$

where the subscript $\odot$ refers to the Sun. The total flux emitted by the Sun is given by the integration over its surface:

$$\Phi_{e\odot}=4\pi r_{\odot}^2 M_{e\odot}=3.850\,10^{26}\,W . \tag{2.4}$$

Assuming that the energy remains constant along every sphere centred on the Sun, we are able to estimate the irradiance on Earth's orbit:

2 Values and meaning of very well-known physical quantities are not mentioned in this section. See Appendix II "List of acronyms and symbols" if needed.

$$E_e(Earth)=\frac{\Phi_{e\odot}}{4\pi d_{SE}^2}=1367\ W\cdot m^{-2} \tag{2.5}$$

where d_{SE} is the distance between the Sun and the Earth, about 1.496×10^8 km. This value is in good agreement with satellite observations indicating an average value of 1367 ± 4 W/m² [Men05]. This value is known as the solar constant.

2.2.2. Irradiance on Earth and air mass

The solar constant deduced in the previous section does not correspond to the energy received on the ground. The flux reaching the Earth depends on the zenith angle of the Sun ($z_\odot$) and on the attenuation due to the Earth's atmosphere. The zenith angle of the Sun is defined as the angular distance from the Sun to the rising vertical at the observation place. It depends on the latitude of the observation point (Φ) and the declination of the Sun ($\delta_\odot$) which is its angular distance from the equatorial plane as shown in Fig. 2.1. This last value is independent from the observation point but varies during the year. It is counted positively from the equatorial plan towards the North and negatively towards the South.

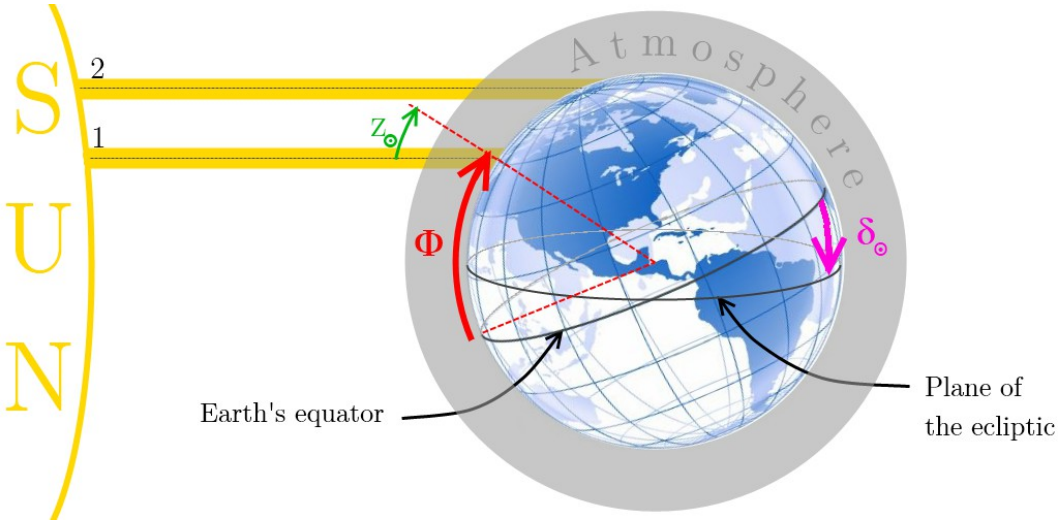

Fig. 2.1: Two schematic beams from the Sun reaching the Earth through the atmosphere. Representation of the zenith angle, the latitude and Sun's declination.

As can be deduced from Fig. 2.1, the zenith angle of the Sun at solar noon corresponds to the difference between the latitude and the declination angle:

$$z_\odot=\Phi-\delta_\odot. \tag{2.6}$$

The declination angle is given approximately by

$$\delta_{\odot}=\text{asin}\left[\sin(-23.44\,^{\circ})\cdot\cos(\zeta)\right] \tag{2.7a}$$

with

$$\zeta=360\,^{\circ}\frac{D+10}{365.24}+\frac{360\,^{\circ}}{\pi}\cdot 0.0167\sin\left(\frac{360\,^{\circ}}{365.24}(D-2)\right) \tag{2.7b}$$

where D is the day of civil calendar. Equations (2.7a) and (2.7b) lead to an error $<\pm 0.2°$ [Wil09]. In these equations, 365.24 is the tropical year, 0.0167 corresponds to Earth's eccentricity, 10 (in N+10) is the offset between the winter solstice and January 1, while 2 (in N-2) is related to the number of days between January 1 and Earth's perihelion.

It may be deduced from Fig. 2.1 that the irradiance on Earth, considered as a perfect sphere, is given by

$$E_e(Earth)=1367\cdot\cos(z_{\odot})\cdot\tau_{atm} \tag{2.8}$$

where τ_{atm} corresponds to the global transmission of the Earth's atmosphere. The greater the zenith angle of the Sun, the longer the path of the Sun beams through the atmosphere, the lower τ_{atm}. The atmosphere reduces the intensity of the flux reaching the Earth but also affects the whole spectral distribution. The transmission depends on a huge amount of parameters (e.g. humidity, ozone and CO_2 concentration). Standards had thus to be determined so that scientists may compare their results. This has led to the definition of the air mass coefficient (AM) [NREL]:

$$AM=\frac{L(z_{\odot})}{L(z_{\odot}=0)} \tag{2.9}$$

on the ground level it can be approximated by

$$AM\simeq\frac{1}{\cos(z_{\odot})} \tag{2.10}$$

with L the path of Sun's beams in Earth's atmosphere. The higher the zenithal angle, the thicker the path of the sun beams in the atmosphere (see beams 1 and 2 in Fig. 2.1). Following Eq. (2.9), the AM0 spectrum corresponds to the standard spectrum outside the atmosphere, AM1 is the shortest air mass at sea level, when $z_{\odot}$=0. But the most common air mass is AM1.5 (i.e. $z_{\odot}$=48.19°) since regions like the United States of America, Europe and Japan lie at this mid-latitude.

The distinction between the direct and global flux must be done, especially for solar concentration. The flux coming directly from the Sun within an angular diameter of ~0.5° on a surface pointing to the Sun is called the direct normal irradiance (usually simply referred to as direct radiation) while global radiation includes direct, diffuse and reflected radiations. The only two reference spectra, namely AM1.5d and AM1.5g (d for direct, g for global), are both incorporated in a single standard document "ASTM G-173-03". They were determined under specific conditions, as the 1976 U.S. Standard Atmosphere and an air mass of 1.5 ($z_{\odot}$=48.19°). It has to be pointed out that the AM.1.5g was deduced on a 37° tilted surface towards the South. So, with a 11.19° off-axis angle between the normal to the tiled plane and the Sun. More information may be found about standard spectra in reference [Mye02].

Several spectra from SMARTS 2.9.5 are shown in Fig. 2.2. SMARTS is the acronym for "Simple Model of the Atmospheric Radiative Transfer of Sunshine". This model predicts clear-sky spectral irradiances taking into account the absorption due to the atmosphere of the Earth [Gue04].

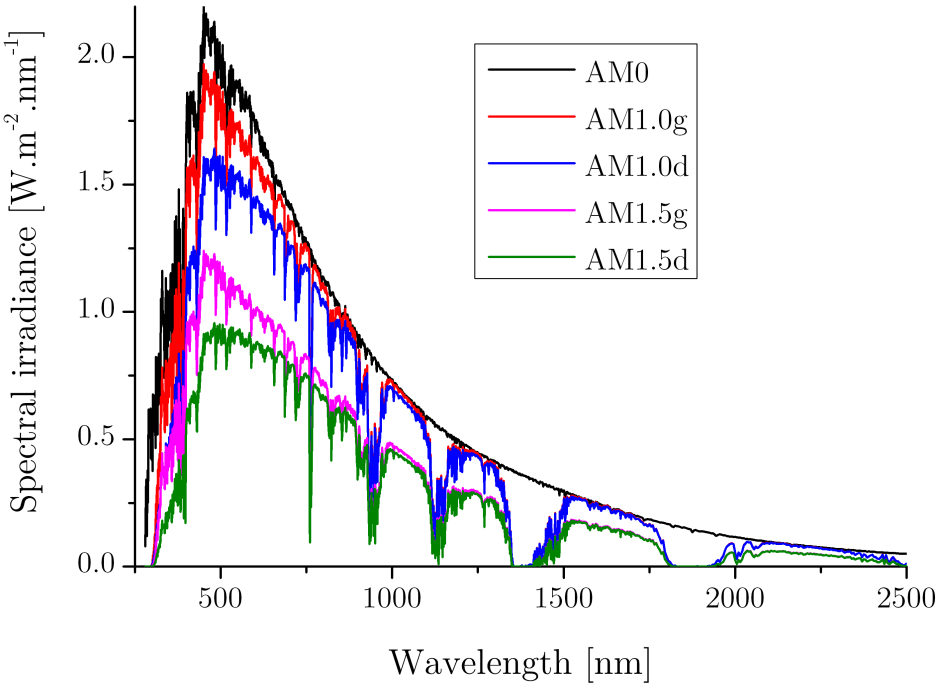

Fig. 2.2: Spectra AM0, AM1.0g, AM1.0d, AM1.5g and AM1.5d obtained with SMARTS 2.9.5. Only AM1.5g and AM1.5d are official reference spectra

2.3. Solar cells for CPV

To convert sunlight into electricity by the photovoltaic effect, an electrical device is needed: the solar cell. Its efficiency is calculated from the AM1.5g spectrum in standard test conditions: a temperature of 25 °C and an irradiance of 1sun. Under concentrated light, the efficiency is calculated at 25°C with the AM1.5d spectrum. This section aims at the behaviour description of solar cells used in CPV on the base of well-known solar cell equations. The theory of *pn*-junctions will not be tackled here.

2.3.1. Basic principles

Assuming that only radiative recombinations take place in the *pn*-junction, single junction solar cells may be represented by the equivalent circuit presented in Fig. 2.3.

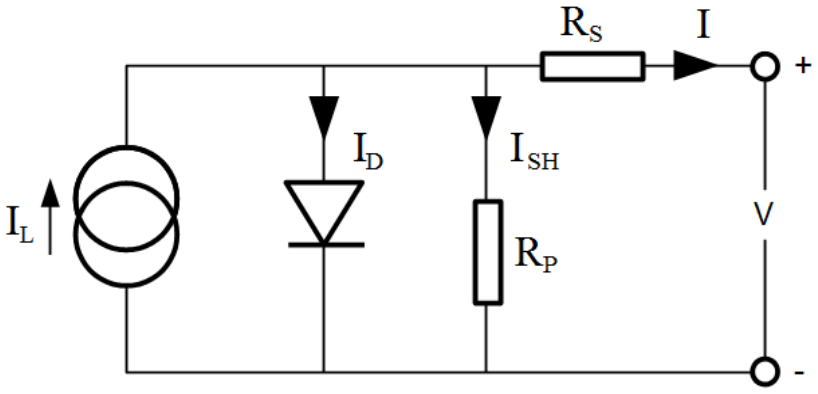

Fig. 2.3: Equivalent circuit of an ideal single junction solar cell

The current, I, collected at the output of the cell depends on the generated current I_L, the current diverted to the diode I_D, and the shunt current, I_{SH}:

$$I = I_L - I_D - I_{SH} \tag{2.11}$$

I_D and I_{SH} depend on the output tension V and on R_P. The current-voltage equation takes the form

$$I = I_L - I_0 \left[\exp\left(\frac{q(V + IR_S)}{k_B T} \right) - 1 \right] - \frac{V + IR_S}{R_P} \tag{2.12}$$

where I_0 is the reverse saturation current of the diode. The series resistance R_S represents the bulk resistance (due to the fact that solar cell materials are not

perfect conductors), and the parallel resistance R_P is caused by leakage of current from one terminal to the other due to poor insulation. So, the ideal solar cell would have R_S=0 and R_P =∞.

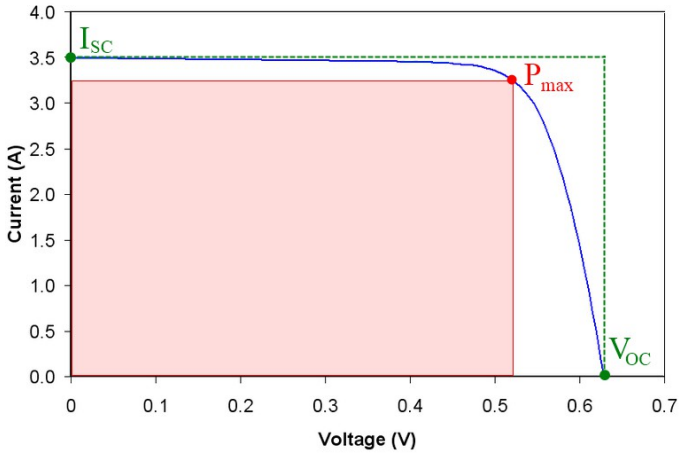

Fig. 2.4: Example of I-V characteristic of a solar cell (blue)

A typical arbitrary I-V curve characteristic is presented in Fig. 2.4. Three parameters are important to characterize the efficiency of the cell:

- the **short circuit current** I_{SC}, obtained when the solar cell is short circuited, the output voltage is thus zero. In practice, I_{SC} is usually almost equal to I_L and are thus often interchangeable.
- the **open circuit voltage** V_{OC} corresponding to the voltage measured when the terminals of the solar cells are not connected. In this condition, the total recombination rate in the cell is equal to the total generation rate,
- the **fill factor** FF corresponding to the ratio of the actual maximum achievable power, P_{max} (in red in Fig. 2.4), to the product of the short circuit current and the open circuit voltage:

$$FF = \frac{P_{max}}{I_{SC} V_{OC}} \tag{2.13}$$

The external quantum efficiency of a solar cell η_{cell} is finally given by the ratio of the produced electrical energy to the incoming radiant energy emitted by the Sun (Q_{in}), and the maximal efficiency has the form of

$$\eta_{cell}^{max} = \frac{P_{max}}{Q_{in}} = \frac{I_{SC} \cdot V_{OC} \cdot FF}{Q_{in}}. \tag{2.14}$$

In first approximation, I_{SC}, V_{OC} and FF are given in absolute by the following equations [Wur05 p.157]

$$I_{SC} = e \int_{E_g}^{\infty} P(h\nu)\, dI_{\gamma}(h\nu) \tag{2.15}$$

where I_{γ} is the photon current, P is the probability that an incident photon generates an electron-hole pair and e the elementary charge. Both depends on the photon energy, $h\nu$. For V_{OC}, we have two equivalent equations:

$$V_{OC} = \frac{k_B T}{e} \ln\left(\frac{n_e n_h}{n_i^2}\right) \tag{2.16}$$

and

$$V_{OC} = \frac{k_B T}{e} \ln\left(1 + \frac{I_{SC}}{I_0}\right) \tag{2.17}$$

with n_e, n_h and n_i the electrons, the holes and the intrinsic carriers concentrations.

And finally for the FF, we have the equation that follows:

$$FF < 1 - \frac{k_B T}{V_{OC}} \tag{2.18}$$

Effects of some parameters are discussed in following sub-chapters.

Note that the simplified model presented in Fig. 2.3 and Eq. (2.12) can be completed to take into account more physical effects as the non-ideality of the diode or recombinations due to impurities e.g. but this is not of high importance for this thesis.

2.3.2. Multijunction solar cell

If a photon excites an electron of a semiconductor of bandgap energy, E_g, with an energy lower than E_g, then the hole-electron pair creation will not occurs. Consequently, the photon will be transmitted or reflected by the semiconductor. But, if the photon has an energy $h\nu$ higher than E_g, it can make the electron passing from the valence band to the conduction band, leaving a hole in the

valence band. The electron-hole pair will release thermal energy and will relax to the band edges, thus the energy equivalent to $h\nu$-E_g is lost. This phenomenon is called thermalization and is represented in Fig. 2.5. With an energy bandgap of 1.1 eV, under AM1.5 spectrum, the maximum efficiency of silicon is limited by thermalization losses to 33% [Wur05].

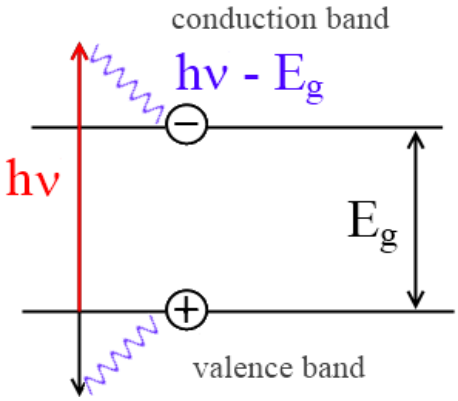

Fig. 2.5: Thermalization losses when $h\nu > E_g$

Solar cell efficiency can be increased by both decreasing thermalization losses and enlarging the absorption spectrum, with the use of multijunction (MJ) solar cells. An example of triple junction cell and its spectral efficiency is presented in Fig. 2.6. With a negative energy bandgap gradient (the greater energy bandgap facing the Sun), the i^{th} subcell sees only photons with an energy lower than the previous energy bandgap ($E_{g,i-1}$). With an infinite number of junctions, the difference between adjacent energy bandgaps (E_i-E_{i-1}) tends to 0, and the thermalization losses may be prevented. However a 100% efficiency MJ solar cell is impossible to achieve: the flux that can be converted is the difference between the absorbed radiative flux and emitted radiative flux so that at a temperature of 300 K, the maximum efficiency of a cell composed of an infinite number of junctions is 68.2% and 86.8% under not concentrated light and maximum concentration respectively [DeV80, Hon02] (the reason of higher efficiencies with concentrated light is explained in section 2.3.4.). Nowadays, the maximum efficiency achieved with a triple junction under concentrated light is scarcely the half of the maximum value: 43.5% (see Fig. 2.10, page 33 at the end of this section).

Typically, for a triple junction solar cell under 1 sun radiation, the short circuit density is about 15mA/cm², the V_{OC} is about 3A and the FF about 85%. The efficiency of triple junction solar cells is usually around 30%.

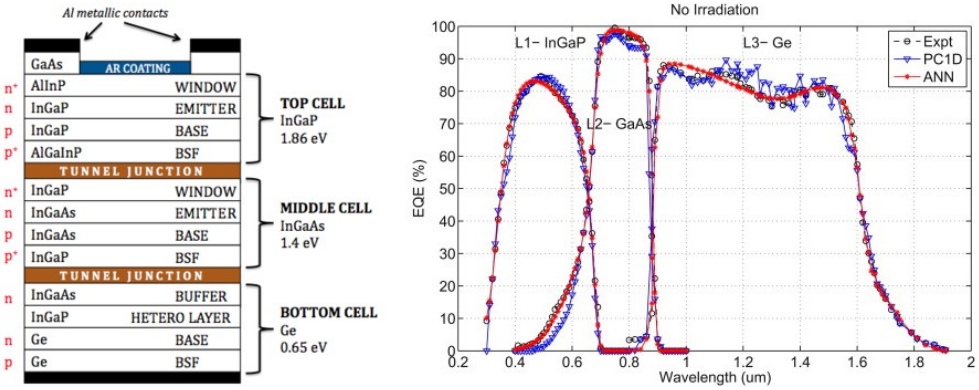

Fig. 2.6: (Left) Example of triple junction solar cell (BSF means back surface field) and (right) part of Sun's spectrum converted by each subcell [Pat12].

It can be deduced from Fig. 2.6 that short wavelengths (< 350 nm), and wavelengths longer than 1600 nm are of small interest in CPV since the irradiance is low (see AM1.5d spectrum) and the external quantum efficiency of a typical triple junction solar cell is smaller than 40%.

The main obstacle in the improvement of the efficiency of MJ solar cells lies mainly in the requirement of lattice matching and current matching between subcells since junctions are monolithically stacked. Lattice matching is required to avoid interface defects that would lead to undesirable recombinations decreasing the efficiency of the cell [Sas09]. Current matching is imposed by the subcells stacked in series (see Fig. 2.7).

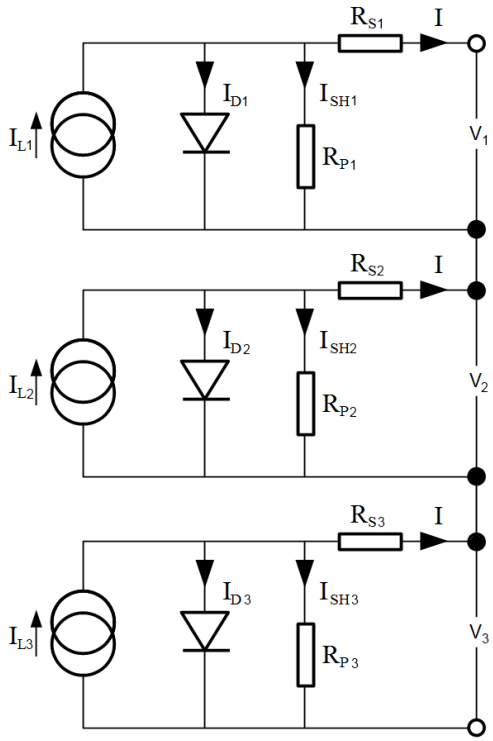

Fig. 2.7: Triple junction solar cell with junction stacked in series

Mechanically stacked multijunction solar cells, i.e. connected in parallel, not in series, are under development at the Catholic University of Leuven (Be) in collaboration with Imec. This technology avoids both problems of current and lattice matching but encounters problems of reflection losses and series resistance losses for now [Zha11].

2.3.3. Temperature effects

The energy bandgap varies with temperature: one may observe experimentally a decrease of this energy while increasing the temperature. This is due to two phenomena: the thermal dilatation modifying interatomic distances and, to a greater extent, the electron-phonon interaction [Var69]. Since the bandgap decreases, a higher number of photons may be collected and participate to the photoelectric effect i.e. I_{SC} increases as may be deduced from Eq. (2.15). The intrinsic carriers concentration also increases with temperature ($n_i \propto T^3 \exp(-E_g/k_BT)$ [Pri12]), this parameter has the most influence making dV_{OC}/dT negative following Eq. (2.16). It has to be pointed out that V_{OC} decreases more rapidly than I_{SC} increases leading to lower product $I_{SC}V_{OC}$. Moreover the fill factor also decreases since, in Eq. (2.18), it is a function of $-T/V_{OC}$, thus the global effect of the temperature is a reduction of the efficiency. Literature [Pri12, Nis06] claims e.g. an absolute variation of about -0.07%/K for Si and a triple junction solar cell under 1 sun, and -0.04%/K under 200 suns[3].

2.3.4. Effects of concentrated light

Concentrated light also affect the efficiency of solar cells. With a higher photon current, I_{SC} increases, affecting the open circuit voltage, which in its turn affects the fill factor.

Following Eq. (2.15), the short circuit current will increase proportionally to the irradiance. Thus, accordingly to Eq. (2.17), the open circuit voltage increases logarithmically with the intensity since we may consider that $I_{SC} \gg I_0$. Thirdly, based on Eq. (2.18), the fill factor also increases with light intensity but only slightly given that V_{OC} is much larger than k_BT. Finally, when the denominator of the cell's efficiency increases, it is exactly compensated at the numerator by the increasing of I_{SC} but the increasing of V_{OC} (and FF) remains. Therefore, the efficiency of the cell increases with light intensity and therefore with sun concentration. Another way to understand the higher efficiency of cell under concentrated light lies in Carnot's principle expresses the maximum efficiency

3 Drop of efficiency given by $d\eta/dT$ (and not $1/\eta \cdot d\eta/dT$). 1 sun=1000W/m²

achievable at cell's temperature under a source of temperature T_{source}:

$$\eta_{cell}^{max} = 1 - \frac{T_{cell}}{T_{source}} \tag{2.19}$$

Under concentrated light, the cell sees a hotter source than under non-concentrated light. Thus the efficiency increases with concentration.

However, due to resistive losses (Joule's law), the higher the current produced the higher the temperature of the cell which reduces cell's efficiency as discussed in the above sub-chapter and confirmed by Carnot's principle.

2.3.5. Non-uniform illumination effects

Non-uniform illumination of the solar cell is a common effect of solar concentration affecting the efficiency of a solar cell in two ways.

Firstly, a non-uniform total irradiance – due to the optical design or due to soiling – over the full cell induces internal current flows resulting in a voltage reduction [Cov05]. A simple example helps understanding this drop of voltage. Consider a solar cell with a fraction *f* illuminated and the other part (1-*f*) in the dark. The cell is approximately equivalent to two cells as depicted in fig [Dha81].

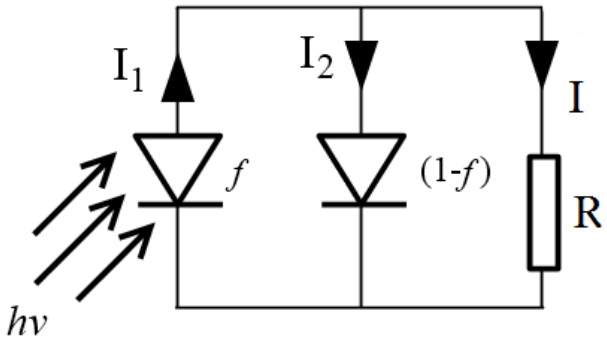

Fig. 2.8: Equivalent circuit of a non-uniformly illuminated solar cell

The cell in the dark will act as a resistance in parallel, hence reducing the parallel resistance and finally the output voltage. In addition, temperature increases higher where illumination is higher decreasing again the efficiency. This issue is called “hot spot” problem. An example comparing I-V curves for uniform and non-uniform illumination is shown in Fig. 2.9

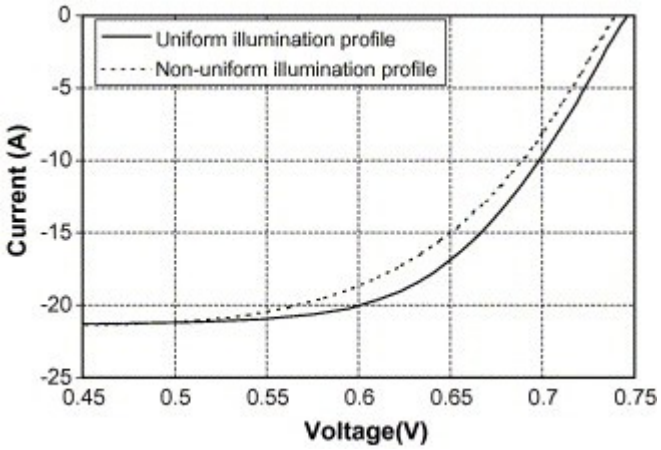

Fig. 2.9: Example of I–V curves for uniform and non-uniform illumination [Cov05]

Secondly, spectral distribution also plays a role in monolithically stacked MJ solar cells since current matching is necessary for junctions stacked in series. Moreover, unicolor hot spots worsens the problem: even if the total irradiance is uniform, a certain spectrum of wavelengths may be particularly well focused creating a hot spot problem on a specific subcell.

The first problem arises for both mirrors and lenses while the second is specific to lenses since the focal distance changes with the wavelength.

To put it in a nutshell, MJ cells present higher performances while illuminated with a spectrally and spatially homogeneous flux. These two assumptions have been experimentally shown [Sch12, Ant01, Dom12] even if they are hard to model quantitatively [Seg12]. We refer the interested reader to a recent paper from Baig *et al.* reviewing the causes and consequences of non-uniform illumination [Bai12].

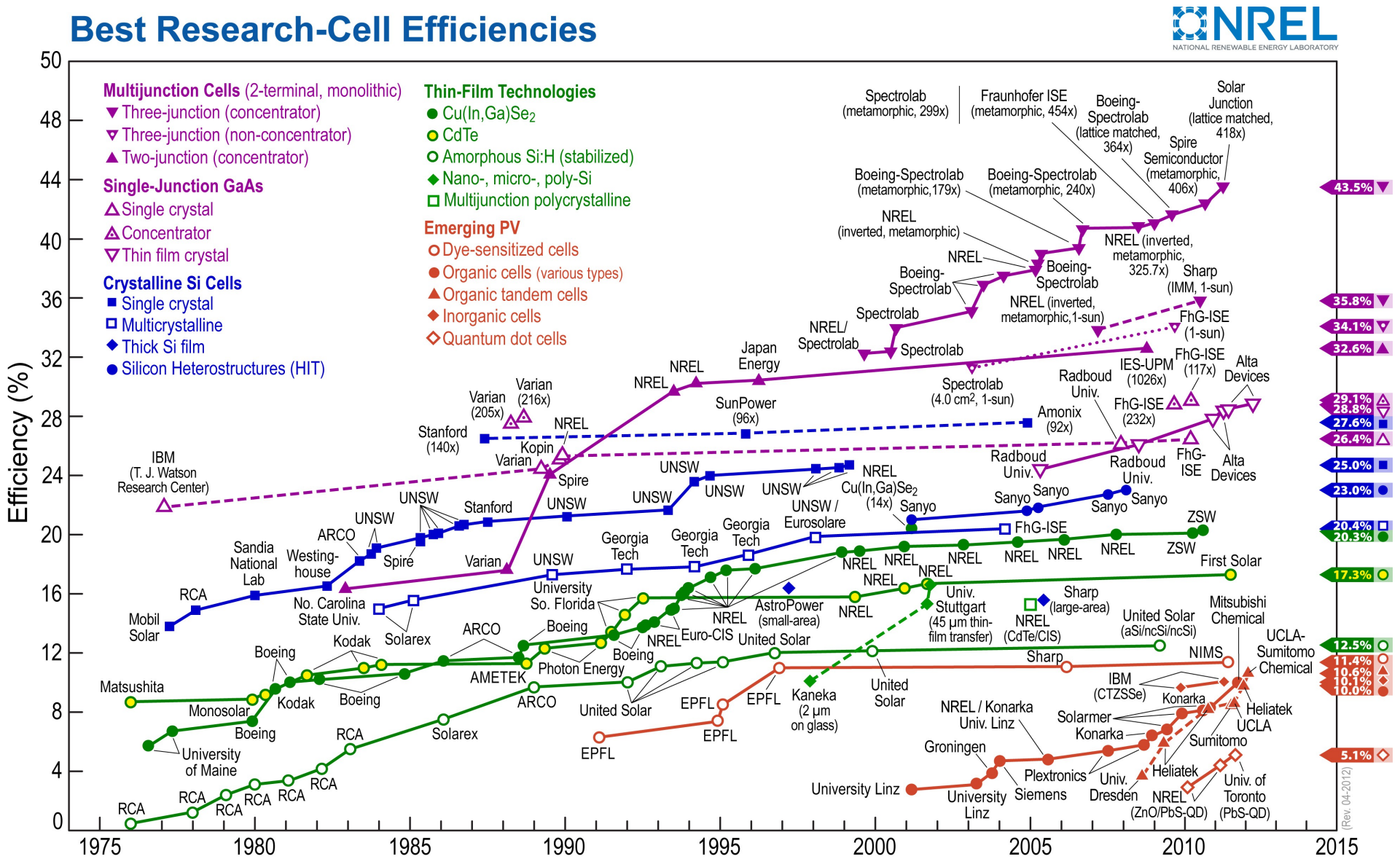

Fig. 2.10: Conversion efficiencies of best research solar cells worldwide from 1976 through 2012 for various photovoltaic technologies. Efficiencies determined by certified agencies/laboratories. Source: National Renewable Energy Laboratory (NREL), Golden, CO

2.4. Optical background

2.4.1. Optical properties of dielectrics

A dielectric can be defined as an electrical insulator material, as for example plastic lenses used in solar concentration. In the absence of electrical field, electrical charges within the dielectric are not moving from a macroscopic point of view. At a microscopic level, charges are moving around the average position of equilibrium. Instead of being set in motion by an electrical field $\vec{E}$ as for conductors, the electrical charges are only shifted from their average position of equilibrium (positive charges in the same direction as the electrical field and negative charges in the opposite direction). This results in the polarization of the material described by the polarization density $\vec{P}$ defined as follows[4]

$$\vec{P} = \varepsilon_0 \chi_e \vec{E} \tag{2.20}$$

where ε_0 is the vacuum permittivity and χ_e the electric susceptibility. It can be shown the phase velocity of a wave varies with the real part χ_e:

$$v_\phi = \frac{c}{\sqrt{1+\Re\{\chi_e\}}} \tag{2.21}$$

and is thus related to the refractive index.

$$n = \frac{c}{v_\phi} = \sqrt{1+\Re\{\chi_e\}}. \tag{2.22}$$

A perfect dielectric would have a refractive index purely real [Cha05]. The imaginary part being related to the absorption of light, an ideal dielectric does not absorb light. In practice, the imaginary part is several orders of magnitude smaller than the real part.

2.4.1.1. Refraction and reflection

When arriving at flat interface between an incident medium of refractive index n_i and a second medium of refractive index n_t, an incoming light beam is affected by two phenomena: reflection and refraction. The three beams of interest (the incident beams, the refracted beams and the reflected beams) lie in the same plane. The very well-known formula of reflection is

4 Here, we ignore non-linear effects.

$$\theta_i = \theta_r \tag{2.23}$$

and the refraction angle is governed Snell's law (also called Snell-Descartes law)

$$n_i \sin\theta_i = n_t \sin\theta_t. \tag{2.24}$$

where angles (of incidence θ_i, of reflection θ_r, and of refraction θ_t) are measured from the normal to the plane. Reflections obeying Eq. (2.23) are called specular reflections (contrary to diffuse reflection). Note that, light rays with an incidence angle greater than the critical angle θ_c, there is no refracted beams, only reflected beam. This limit angle is known as the critical angle, which equation is $\theta_c = \text{asin}(n_2/n_1)$ and this reflection phenomenon is called total internal reflection (TIR). Reflection, refraction and TIR are depicted in Fig. 2.11.

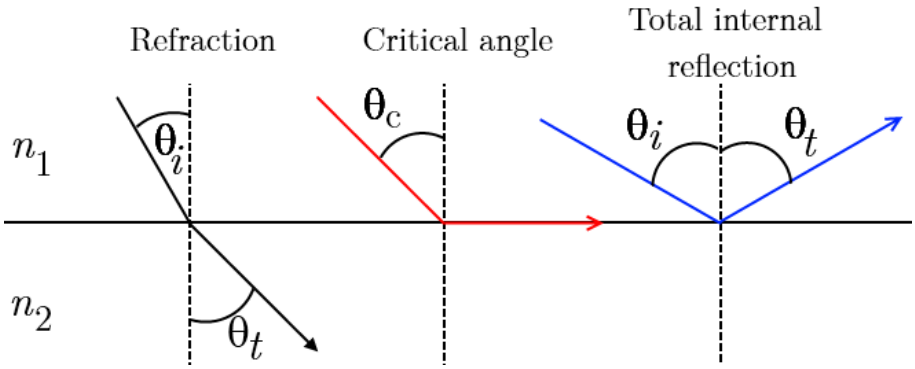

Fig. 2.11: Refraction, critical angle and TIR a the interface between two media of different refractive indices ($n_2 > n_1$)

These formulae are valid for flat interfaces without gradient of phase discontinuity, $d\phi/dx$, introduced by the interface. Otherwise the generalize laws of reflection, Eq. (2.25), and refraction, Eq. (2.26), are needed as shown by Yu *et al.* in an article published in Nature in 2011 [Yu11].

$$\sin(\theta_r) - \sin(\theta_i) = \frac{\lambda}{2\pi n_i}\frac{d\phi}{dx} \tag{2.25}$$

$$n_t \sin(\theta_r) - n_i \sin(\theta_i) = \frac{\lambda}{2\pi}\frac{d\phi}{dx} \tag{2.26}$$

2.4.1.2. Fresnel coefficients

The proportion of light reflected and transmitted depends the incidence angle and on the polarization state of the beam. A beam is in a transverse magnetic (TM) state if the electric field vibrates in the plane of incidence (which is determined by

the incidence beam and the normal to the interface). When the electric field vibrates perpendicularly to the plane of incidence, then this is the transverse electric (TE) case. Any polarization state may be constructed as the vectorial sum of a TE component and a TM component.

Fresnel reflection coefficient (r) refers the ratio of the reflected field amplitude to the incoming field amplitude. However, the energy is proportional to the square of the amplitude. The reflectance coefficient R in the TE case is

$$R_{TE} = r_{TE}^2 = \left.\frac{E_r^2}{E_0^2}\right|_{TE} = \left| \frac{n_1 \cos\theta_i - n_2 \sqrt{1 - \left(\frac{n_1}{n_2}\sin\theta_i\right)^2}}{n_1 \cos\theta_i + n_2 \sqrt{1 - \left(\frac{n_1}{n_2}\sin\theta_i\right)^2}} \right|^2 \tag{2.27}$$

and for the transverse magnetic waves we have

$$R_{TM} = \left| \frac{n_1 \sqrt{1 - \left(\frac{n_1}{n_2}\sin\theta_i\right)^2} - n_2 \cos\theta_i}{n_1 \sqrt{1 - \left(\frac{n_1}{n_2}\sin\theta_i\right)^2} + n_2 \cos\theta_i} \right|^2 . \tag{2.28}$$

Consequently to the principle of energy conservation, the transmittance coefficients are simply given by (1-R). Looking at Eq. (2.28) we can deduce that there is a particular angle of incidence,

$$\theta_B = \operatorname{atan}\left(\frac{n_2}{n_1}\right) \tag{2.29}$$

for which the reflectance in TM is zero, this angle is known as Brewster's angle.

The reflectance coefficients have been depicted in Fig. 2.12 for the case where light travels from a lower refractive index to an upper refractive index and inversely. If the light is not polarised (NP), the reflection coefficient is given by the arithmetic mean of R_{TM} and R_{TE}: R_{NP}=0.5 (R_{TM} + R_{TE})

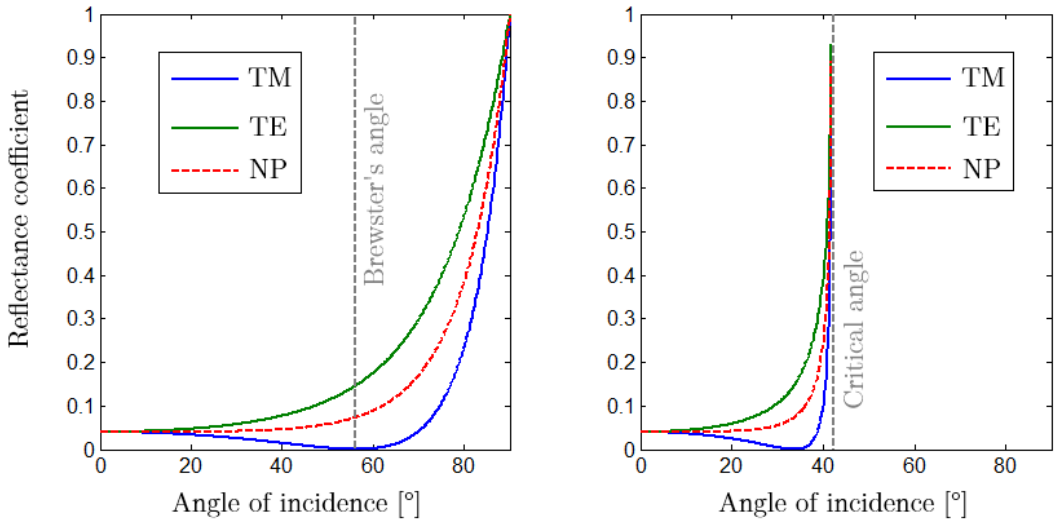

Fig. 2.12: Reflectance coefficients for TM, TE and NP cases.
Left: for n_1=1, n_2=1.5. Right: n_1=1.5, n_2=1

We clearly observe in Fig. 2.12 that, for NP beams, the higher the incidence angle the higher the reflectance coefficient. Also, up to 10° before Brewster's angle, the reflectance coefficient is almost constant.

2.4.1.3. Roughness and scattering

Roughness can be defined as the micro deviation of a real surface from its ideal form. It can be quantified in several ways.

- The peak to valley distance is a measure of the distance separating the lowest and the highest point of the considered surface.
- Considering an ideal surface $z_0(x)$, the average error value of a profile $z(x)$, $\overline{\Delta z}$ is given by the mathematical formula in Eq. (2.30)

$$\overline{\Delta z}=\frac{1}{L}\int_0^L \Delta z(x)\,dx=\frac{1}{L}\int_0^L \Big(z(x)-z_0(x)\Big)\,dx \tag{2.30}$$

  a surface with $\overline{\Delta z}(x)=0$ would be perfectly smooth.
- The arithmetic average of absolute values roughness, R_{avg} is defined as

$$R_{avg}=\frac{1}{L}\int_0^L \Big(\Delta z(x)-\Delta z\Big)\,dx. \tag{2.31}$$

- The root mean square roughness, R_{q} is expressed as

$$R_q = \sqrt{\frac{1}{L}\int_0^L \left(\Delta z(x) - \Delta z\right)^2 dx}. \tag{2.32}$$

This last parameter is in straight relation with the scattered light (see Fig. 2.13). For light passing from a medium of refractive index n_0 to another medium of refractive index n_1, the total reflectance R_{tot} remains unchanged but the specular reflectance R_0 decreases as the scattered reflectance R_S increases, following

$$R_{tot} \simeq R_0 + R_S = R_0 + R_{tot}\left(4\pi n_0 \frac{R_q}{\lambda}\right)^2 \tag{2.33}$$

The same phenomenon occurs for the transmittance. The total transmittance T_{tot} remains unchanged but is divided into a specular transmittance (T_0) and scattered transmittance in accordance with Eq. (2.34)

$$T_{tot} \simeq T_0 + T_S = T_0 + T_{tot}\left(2\pi(n_0 - n_1)\frac{R_q}{\lambda}\right)^2 \tag{2.34}$$

Eqs. (2.33) and (2.34) are valid only for surfaces with $R_q \ll \lambda$ [Car02].

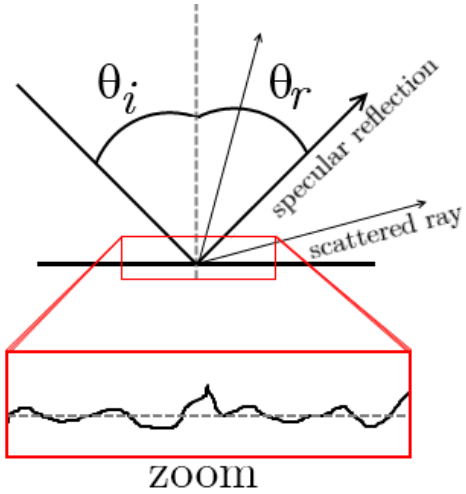

Fig. 2.13: Roughness and scattering

2.4.1.4. Absorption and light diffusion

In an ideal homogeneous dielectric medium, a collimated light beam travels in straight line without energy loss. In reality, a part of the light will be diffused and another part will absorbed by the medium.

When travelling through a medium, a fraction of the incident light will be randomly scattered several times, this effect is known as diffusion (or multiple scattering). To some negligible effects, scattering (and therefore diffusion) is an elastic effect. Also, the incident beam undergoes a diminution of its radiant flux due to absorption by the medium. For both the absorption and the diffusion, the longer the path travelled (x), the higher the losses which can be described by Beer-Lambert law:

$$Q_e = Q_{e0}\exp\left(-\mu x\right). \tag{2.35}$$

Usually, the two processes cannot be experimentally distinguished and μ is known as the attenuation coefficient, corresponding to the sum of the absorption coefficient μ_a and the diffusion coefficient μ_d.

The absorption can be deduced from the extinction coefficient k (the imaginary part of the refractive index) with Eq. (2.36):

$$\mu_a(\lambda) = \frac{4\pi k(\lambda)}{\lambda}. \tag{2.36}$$

2.4.1.5. Chromatic dispersion

We recall the effect of en electric field that causes the polarization of the material which is proportional to its susceptibility, which, in is turn, affects the refractive index

$$n = \frac{c}{v_\phi} = \sqrt{1+\Re\{\chi_e\}}. \tag{2.37}$$

In fact, the polarization density $\vec{P} = \epsilon_0 \chi \vec{E}$ [C/m²] depends on the frequency of the electrical field. A dipole can be seen as a mechanical oscillator with a pulsation of resonance (eigenfrequency) ω_0. Since the electrical field imposes a frequency ω to an electron of charge q_e and mass m_e, the system can be approximated by a forced oscillator without damping coefficient [Cha05] described by

$$q_e E\cos\omega t - m_e\omega_0^2 x = m_e\frac{d^2x}{dt^2} \tag{2.38}$$

which has a solution of the form

$$x(t)=\frac{q_e}{m_e\left(\omega_0^2-\omega^2\right)}E(t). \tag{2.39}$$

For N electrons by unit of volume with k eigenfrequencies, the amplitude of the polarization density becomes

$$\left|\vec{P}\right|=\varepsilon_0\chi_e E=N\,q_e\,x=\sum_k\frac{f_k N q_e^2}{m_e\left(\omega_{0,k}^2-\omega^2\right)}E \tag{2.40}$$

where f_k are the oscillator strengths ($\sum_k f_k=1; f_k>0$). Thus,

$$\chi_e=\sum_k\frac{f_k N q_e^2}{\varepsilon_0 m_e\left(\omega_{0,k}^2-\omega^2\right)}. \tag{2.41}$$

Hence,

$$n(\omega)=\sqrt{1+\sum_k\frac{f_k N q_e^2}{\varepsilon_0 m_e\left(\omega_{0,k}^2-\omega^2\right)}} \tag{2.42}$$

and finally we can express the refractive index as a function of the wavelength

$$n(\lambda)=\sqrt{1+\sum_k\frac{A_k\lambda}{\lambda^2-\lambda_{0,k}^2}}. \tag{2.43}$$

where coefficients A_k must be expressed in the same unit as the wavelength.

The variation of refractive index with the wavelength is known as dispersion. It is responsible of the chromatic aberration which is a central point of this thesis. At least ten different dispersion formulae exist. For examples Buchadahl's equation, Geffcken's equation, Hartmann's equation, Herzberger's equation, Helmholtz-Ketteler-Drude equation, Schott's equation (also known as Laurent's equation) and Sellmeier's equation. Only Cauchy, Laurent and Sellmeier's equations are commonly used nowadays. The first successful algebraic expression of the dispersion curve is owed to Cauchy. His equation is expressed as

$$n(\lambda)=A+\frac{B}{\lambda^2}+\frac{C}{\lambda^4} \tag{2.44}$$

the precision is typically in the order of 10^{-4} in the visible region (between 10^{-3} to

10^{-2} without the term in λ^{-4}). Laurent's equations is given by

$$n(\lambda)=\sqrt{A_0+A_1\lambda^2+\frac{A_2}{\lambda^2}+\frac{A_3}{\lambda^4}+\frac{A_4}{\lambda^6}+\ldots} \tag{2.45}$$

some additional terms are sometimes used to improve the precision in the UV or NIR region. Typically, the error on the refractive index is under 3×10^{-6}. Finally, the Sellmeier equation is defined as

$$n(\lambda)=\sqrt{1+\sum_k \frac{A_k\lambda}{\lambda^2-\lambda_{0,k}^2}} \tag{2.46}$$

which is exactly the same expression as Eq. (2.43) deduced here above. Three resonance wavelengths (one in the IR and two in the UV region round 8 µm, 50 nm and 150 nm respectively) are sufficient for the main majority of dielectrics to obtain a inaccuracy smaller than 10^{-6} [Bac95].

The dispersive behaviour of a material is usually referred to the Abbe number, defined as

$$v_d=\frac{n_d-1}{n_F-n_C} \tag{2.47}$$

where *d*, *F* and *C* refer three Fraunhofer lines, at 587.5618, 486.134 and 656.281 nm, respectively. The higher the Abbe number, the lower the variation of refractive index with wavelength.

2.4.2. Concentrator optics

2.4.2.1. Nonimaging optics

In solar concentration, the way beams reach the absorber has no importance: the Sun has not to be imaged by the optical system providing beams reach the target. This field of optics is called nonimaging optics. While in imaging optics, beams coming from a point A of the object are directed towards A' in the image plane, nonimaging optics collects beams to concentrate them onto the absorber (sometimes referred to as 'receiver'), as illustrated in Fig. 2.14.

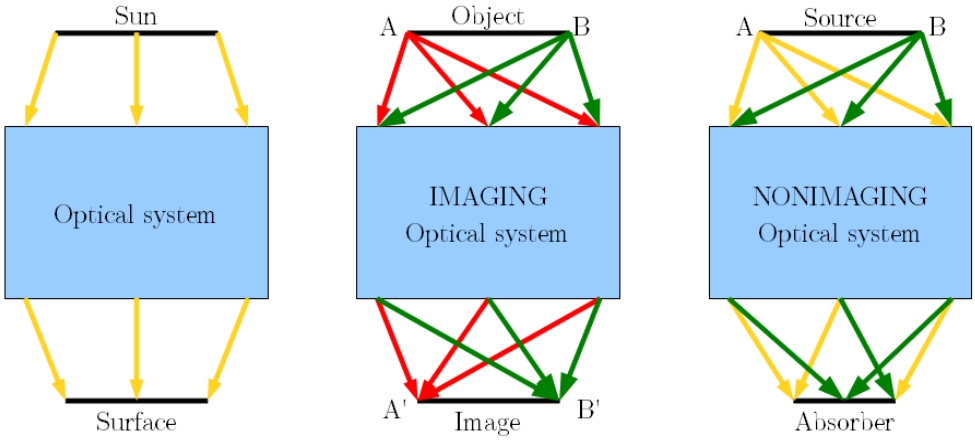

Fig. 2.14: Comparison between imaging optics and nonimaging optics

The geometrical concentration (C_{geo}) ratio is defined as the aperture of the collecting surface, S_C, divided by the absorber aperture, S_A.

$$C_{geo} = S_C / S_A \tag{2.48}$$

However, all the beams collected do not reach the absorber, so we define the optical efficiency η_{opt} as the ratio of the radiant fluxes

$$\eta_{opt} = \Phi_{e,C} / \Phi_{e,A} \tag{2.49}$$

So the effective concentration, namely the optical concentration (C_{opt}), factor is given by

$$C_{opt} = C_{geo} \cdot \eta_{opt} \tag{2.50}$$

C_{geo} can be as high as desired (although not useful) but C_{opt} is limited by physical laws, as will be shown in the next sub-chapter

2.4.2.2. Étendue conservation and maximum concentration

The maximum concentration is related to the conservation of the étendue, G, defined in Eq. (2.51) with parameters represented in Fig. 2.15*.

$$G = \iint d^2 G = \iint n^2 \, dS \cos\theta \, d\Omega \tag{2.51}$$

The étendue corresponds to the geometrical extent, in other words it characterises how the light is dispersed angularly and spatially (corresponding respectively to surface S and solid angle Ω in Eq. (2.51) with an angle θ between dS and $d\Omega$ and beams emitted in a material with a refractive index n).

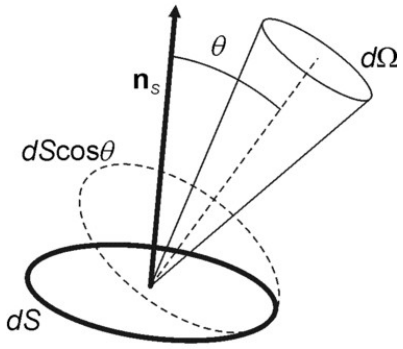

Fig. 2.15: Étendue for a differential surface element*

It may be defined in two different ways looking at the source side or the absorber side. From the source point of view, it is the product of the source area times the solid angle subtended by the entrance pupil of the absorber as seen from the source. From the absorber point of view, the étendue is the area of the entrance pupil times the solid angle the source subtends as seen from the pupil. It may be shown that étendue is conserved [Cha08], i.e. an optical system does not modify the étendue. One consequence of the étendue conservation is the limitation of the maximal concentration. For a planar aperture surface S receiving light from a cone with a half angle θ_S, the integration of Eq. (2.51) leads to

$$G = n^2 S \int \cos\theta \, d\Omega = n^2 S \iint \cos\theta \;\; \sin\theta \;\; d\theta \, d\varphi \tag{2.52}$$

following the definition of the solid angle. Then,

$$G = n^2 S \int_{\varphi=0}^{2\pi} \int_{\theta=0}^{\theta_S} \frac{\sin 2\theta}{2} \, d\theta \, d\varphi \tag{2.53}$$

* Image source: http://en.wikipedia.org/wiki/File:Etendue-Definition.png (CC BY-SA 3.0)

Finally,

$$G = n^2 S \pi \sin^2 \theta_S \tag{2.54}$$

For a surface S_2 collecting the beams emitted by a surface S_1, the étendue conservation, may thus be simply written as follows

$$n_1^2 S_1 \sin^2 \theta_1 = n_2^2 S_2 \sin^2 \theta_2, \tag{2.55}$$

which is known as the "sine condition". The geometrical concentration factor may be expressed as

$$C_{geo} = \frac{S_1}{S_2} = \frac{n_2^2 \sin^2 \theta_2}{n_1^2 \sin^2 \theta_1}. \tag{2.56}$$

The maximum concentration ratio is achieved with n_1=1 and θ_2=90°:

$$C_{geo}^{max} = \frac{n_2^2}{\sin^2 \theta_1}. \tag{2.57}$$

This last equation is known as the sine law of concentration [Win05] and may also be drawn from the principles of the thermodynamic.

To calculate the maximum thermodynamic concentration, we will refer to Fig. 2.16

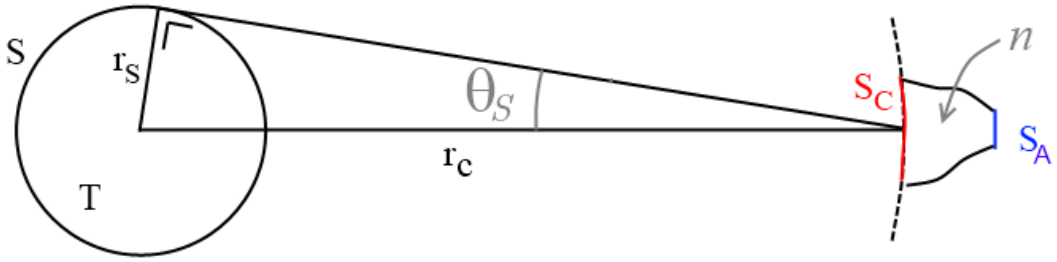

Fig. 2.16: Schematic representation of a source/collector/absorber system

A black-body source emits a radiant flux following Stefan-Boltzmann law

$$\Phi_S = 4\pi r_S^2 \sigma T^4 \tag{2.58}$$

where r_S is the radius of the source, σ the Stefan constant and T the temperature of the source. The radiant flux reaching the collecting aperture, S_C, situated on a sphere with radius r_C centred on the source is

$$\Phi_C = \frac{4\pi r_S^2 \sigma T^4}{4\pi r_C^2} S_C \tag{2.59}$$

The maximum flux captured by the absorber is identical to the one collected S_C. Assuming that the absorber is a black-body too, the second law of thermodynamics states that its maximum temperature is T. Therefore the flux emitted by the absorber is

$$\Phi_A = n^2 S_A \sigma T^4 \tag{2.60}$$

A thermal equilibrium is necessary to maintain a stable temperature of the absorber: the flux emitted by the absorber must compensate for the absorbed flux. In other words, the flux emitted and absorbed must be the same. Thus,

$$\Phi_A = S_A \sigma T^4 = \Phi_C = \frac{4\pi n^2 r_S^2 \sigma T^4}{4\pi r_C^2} S_C \tag{2.61}$$

and finally,

$$\frac{S_C}{S_A} = \frac{r_C^2}{r_C^2} = \frac{n^2}{\sin^2 \theta_S} \tag{2.62}$$

which is equivalent to Eq. (2.57). Surpassing this maximum limit would induce a warming of the source by the absorber which is physically impossible from an optical and thermodynamic point of view.

2.4.2.3. Edge-ray principle, acceptance angle and CPC

The edge-ray principle is one of the nonimaging design method [Rie94]. The underlying principle of this theory is quite basic: if every rays coming from the edge of a source reach the absorber, then any inner ray from the source will reach the receiver. Therefore the design is established by considering only rays from the edge of the source. In a two-dimensional design, the usual method is to send either edge-ray to either end of the absorber.

This principle found its most famous application in the design of Compound Parabolic Concentrators (CPC). A CPC, shown in Fig. 2.17, is a nonimaging reflector able to achieve, theoretically, a concentration equivalent to the maximum limit predicted by the law of étendue conservation. As can be seen in Fig. 2.17, the slope of the reflecting surface is calculated to make beams with an incoming angle θ reach one end of the absorber (beams with an incoming angle $-\theta$ reach the

other end of the absorber). Therefore the reflecting surface has a parabolic shape. Beams with a smaller incoming angle will reach the absorber while beams with an incoming angle greater than the design angle will be retroreflected as shown in Fig. 2.17.

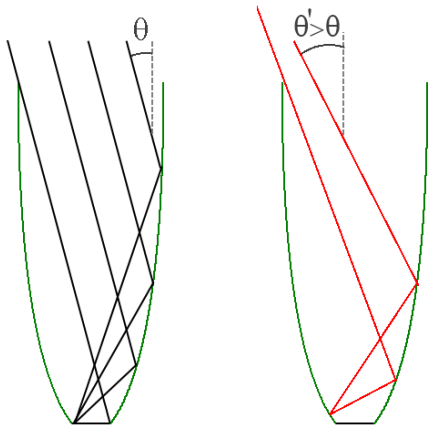

Fig. 2.17: Compound parabolic concentrator.
Left: design angle. Right: retroreflection of a beam with incoming angle greater than the design angle.

Unfortunately CPCs suffer from two important drawbacks. Firstly, the flux distribution on the absorber is highly non-uniform [Cha05]. Secondly, the aspect ratio of the CPC is critically high for small angular aperture: for Sun's angular aperture, the height is about 50×10^3 the radius of the absorber! This is the reason why CPC are never used as primary optics for HCPV.

Usually, nonimaging solar concentrators are designed for an acceptance angle higher than the angular size of the source (because of tracking errors, manufacturing errors etc.). Mainly two definitions of the acceptance angle are encountered in CPV. It may be defined as the maximum angle that a light ray can have, relative to the axis of the concentrator, so that it may be concentrated onto the absorber. In other words, beams with a higher incidence angle than the acceptance angle will necessary miss the solar cell. Otherwise, the acceptance may be defined as the incidence angle at which the concentrator collects 90% of the on-axis power. In this thesis we will refer to the first definition.

2.5. A note on concentrator performance criteria

A glimpse at the literature shows the diversity of designs in CPV. Some are reflective, some are refractive and some combine both. The concentrator may have secondary optics or not. The *f*-number varies from a design to another. The materials, the thickness are different, the acceptance angle, the uniformity of the flux reaching the cell, the diameter change from a concentrator to another, the

optical elements may be flat or curved...

Several criteria are relevant such as the geometrical concentration ratio combined with the optical efficiency and the acceptance angle. However, these criteria are not absolute: at equivalent optical efficiency, between a concentrator of 300× with an acceptance angle of 1.5° and a concentrator of 600× with an acceptance angle of 0.4°, which is best? This depends on other parameters such as the tracker used, the efficiency of the cell, the need for frequent cleaning, the life-time etc. Finally, investors will prefer a concentrator that is cheaper per kWh produced. The evolution of energy prices and raw materials (mainly silicon and petrol) is therefore of primary importance. If silicon and III-V materials become expensive, high concentration will be preferred. But if the price of silicone drops considerably, there will be no economic need for solar concentration. So, the "ideal" concentrator varies from time to time and establishing relevant criteria is not that simple.

One useful merit function dedicated to concentrator optics is the Concentration Acceptance (angle) Product (CAP)

$$CAP = \sqrt{C_{geo}} \sin \theta_a \tag{2.63}$$

where θ_a is usually defined as the incidence angle at which the concentrator collects 90% of the on-axis power. It measures how much the concentrator approach the ideal acceptance angle. This equation follows from Eq (2.57), the sine law of concentration. The CAP is therefore always smaller than the refractive index of the medium surrounding the absorber, n. The closer the CAP from n, the better the concentrator, i.e. the concentrator has the higher acceptance angle for the concentration ratio or inversely. Typical CAPs are in the range of 0.1 to 0.7 [Ben10] and are mainly used to compared concentrator with secondary optics.

2.6. Chapter conclusions

In order to design an efficient solar concentrator, we characterized Sun's spectra. At our latitudes, AM1.5d spectrum is taken as a reference for CPV. If we take into account the external quantum efficiency of a typical triple junction solar cell and the AM1.5d, we can deduce a typical wavelength range of interest of ~350 nm to 1600 nm. The study of the multijunction solar cell showed that, in order to enhance the efficiency of a solar concentrator module, the flux seen by the MJ cell should be as white as possible (i.e. spectrally homogeneous), highly concentrated (the higher, the better for an ideal cell) and spatially homogeneous. However, it is difficult to meet these three conditions simultaneously. Spectral homogeneity is

undermined by the dispersive behaviour of dielectrics. Very high concentration reflective designs, like CPC, require large overall dimensions (hardly compatible with low-cost technologies) producing a non-uniform irradiance on the solar cell.

3 Realistic design parameters of a nonimaging refractive Fresnel lens

How to design a Fresnel lens? With which *f*-number? How many teeth? In which material? Should the lens be large or small? How does the chromatic aberration affect the concentration? Which are the critical aspects? Which parameters deteriorate the performance of a Fresnel lens?

In this chapter general answers and orders of magnitude will be provided in accordance with CPV requirements.

3.1. Important Fresnel lenses parameters

3.1.1. Shape error of lenses and mirror

The first question that probably arises when an optical designer wishes to create its first solar concentrator is "Should I design a lens or a mirror?". A glimpse at the literature [Leu01] informs that usually lenses sound like CPV and mirrors like concentrated solar thermal, but exceptions exist [Sol09, Leu99]. Mirrors are said to be prone to manufacturing errors (see Fig. 3.1). An error ε (in °) on the slope of the mirror leads to twice this error on the reflected beam. So, the relation between the deviation angle of the reflected beam, D_{mirror}, and the slope error is

$$D_{mirror} = 2\varepsilon, \tag{3.1}$$

whatever the incoming angle.

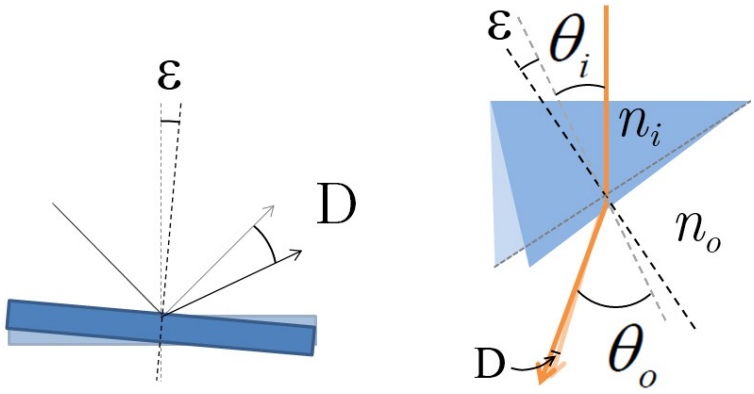

Fig. 3.1: Sketch of the effect of slope error on the deviation angle for a mirror (left) and a dielectric (right)

Lenses are said to be more tolerant to manufacturing errors. We prove in Appendix III.2 that the deviation error coefficient can be approximated by tan θ_o/tan θ_i, i.e. the deviation angle for a lens, D_{lens}, is

$$D_{lens} \simeq \frac{\tan\theta_0}{\tan\theta_i}\varepsilon \tag{3.2}$$

where parameters are in accordance with Fig. 3.1. Therefore, the usual assumption is proved to be true for beams passing from a higher refractive index to a lower refractive index and for small incoming angles otherwise, as shown on the left and right part of Fig. 3.2 respectively.

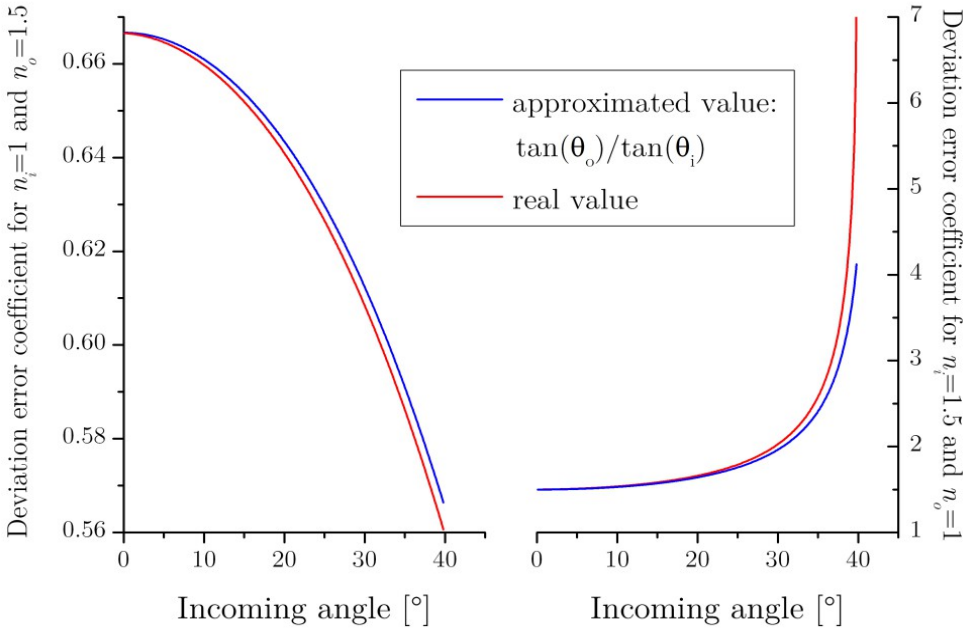

Fig. 3.2: Deviation error coefficient for n_i=1 and n_o=1.5 (left) and n_i=1.5 and n_o=1 (right) with a 2° slope error ε. Comparison between the approximated coefficients (blue curves) and the real error coefficients (red curves)

It can be shown that the front and back interfaces of a lens are partially self-correcting [Leu01 p. 103] and lenses offer more flexibility in the design. On the other hand, contrary to mirrors, lenses suffer from chromatic aberrations. The aim of this thesis consisting in the achromatization of lenses, mirrors will no longer be discussed.

3.1.2. Fresnel grooves

In CPV, Fresnel lenses are used instead of non-Fresnel lenses only in order to decrease the cost of the solar concentrator. The non-active part of the lens is removed in order to obtain a thin, light and cheap lens. Instead of a continuous profile, the surface of the Fresnel lens (sketched in Fig. 3.3) is textured, having several so-called "teeth" or "grooves". To reduce the production costs, Fresnel lenses for CPV are manufactured by injection moulding or hot embossing.

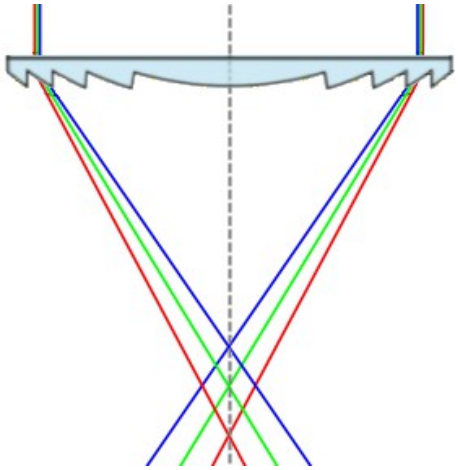

Fig. 3.3: Sketch of a converging refractive Fresnel lens

The thinner the lens, the cheaper the mould to manufacture, the less the material to be used for each lens and the lower the cooling time. Thus the fresnelization of lenses is of high importance to reduce production costs. This despite the degradation of the optical quality of the lenses. Indeed, the fresnelization of lenses induces optical losses that are not offset by the gain in transmittance. For instance, to remove the lens from its mould, a mould release angle is necessary, called "draft angle", represented in red on Fig. 3.4b. Usually δ=2° is sufficient for the draft angle. This angle is obviously responsible for optical losses.

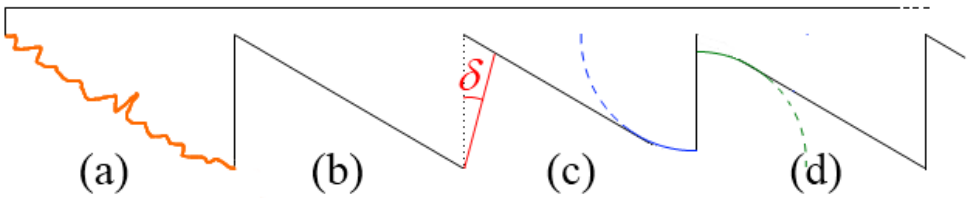

Fig. 3.4: Optical losses due the fresnelization of a lens. (a) Roughness of the prism facet, (b) draft angle, (c) tip radius, (d) valley radius

Added to this draft angle are the roughness errors to be attributed mainly to the rounded machining tool, to vibrations and poor sharpening of the tool (see Fig. 3.4a). Also the finite size of the machining tools (see Chap 7.2.) produces rounded facets at the peaks (Fig. 3.4c) and valleys (Fig. 3.4d). The error at the tip may be further increased by a poor plastic injection causing an incomplete filling of the mould.

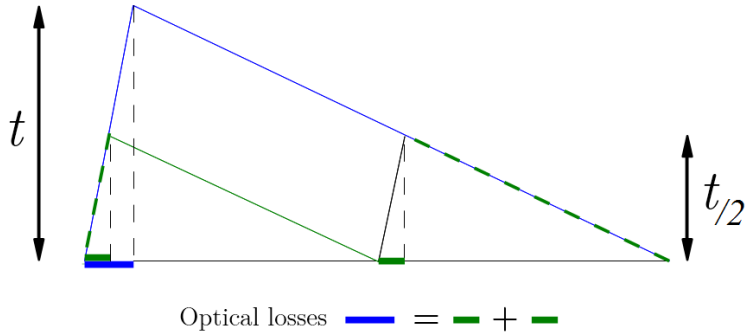

Fig. 3.5: Fresnelization of a lens: no change in the optical losses while considering a linear lens with only draft angle

For a linear (cylindrical) Fresnel lens, the number of teeth forming the lens is not driven by the draft angle since dividing by a factor A the number of teeth would increase the thickness of the teeth of the same factor A, as depicted in Fig. 3.5 for a halved value of the thickness t. The number of dead zones would be thus divided by A but these dead zones will be A times bigger. This reasoning is no longer valid for concentrators of rotational symmetry for which it is best to minimize losses on the edge of the lens since optical losses increase with the square of the radius. Anyway, the higher the number of teeth, the higher the optical losses due to tips and valleys, but the cheaper the manufacturing costs...

Fresnel lenses may be designed “grooves-in” (teeth facing the inside of the module) or “grooves-out” (teeth facing the Sun) as shown in Fig. 3.6. The grooves-out design offers advantages in terms of optical efficiency [Kuh07] and tolerances [Leu01]. Nevertheless, since CPV is particularly sensitive to soiling problems [Viv10], grooves-in designs are highly recommended. In both cases, the lens designer can freely choose the relation between the teeth: constant width, constant thickness or no constant at all.

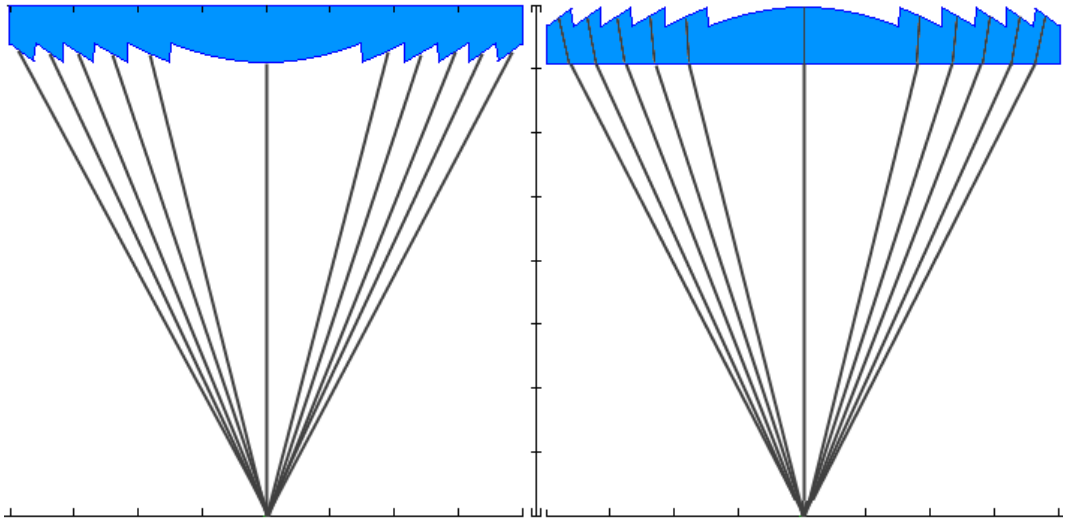

Fig. 3.6: Simple Fresnel lenses. Left: grooves-in design. Right: grooves-out design.

3.1.3. Optical plastics for cost-effective lenses

In CPV, the optical elements are the keys that allow for the cost reduction of the power produced, they need to present good optical performance and processability at low cost. Glasses do not fulfil this last condition and are also too heavy to be used as primary optics. Optical plastics (OPs) however are good candidates as lens materials: they are cheap (<10 €/kg) [Nalux], about three times lighter than glasses and offer a good transmittance between 400 and 1600 nm. The poly(methyl methacrylate) (PMMA) highly predominant in CPV [Mil11]. Polycarbonate (PC) is also described as a good candidate [Mak07, Mil11] for CPV applications. Compared to PMMA, PC has a higher toughness, needs a lower cooling time but presents a lower optical transmittance (~3% lower) and is more sensitive to UV-induced degradation, leading to a faster yellowing of the material. Important researches have been purposefully conducted to enhance the durability of PC up to 20 years [Bit08]. Its high refractive index (~1.6 at 500 nm) and high dispersion curve are not favourable for high concentration but may be of great interest if combined with another PMMA e.g. (see Chap. 5). We compare some properties of PC and PMMA in Table 3.1. Dispersion, transmission, and yellowing index curves of PC and PMMA are compared in Fig. 3.7, Fig. 3.8 and Fig. 3.9 respectively.

Table 3.1 Properties of PMMA and PC

	PMMA	PC
Density	1200 kg/m^3	1200 kg/m^3
Refractive index (λ_d=587.56nm)	1.492	1.584-1.586
Abbe number v_d	57	30
Glass transition temperature (T_g)	~100°C	~150°C
Melting temperature (T_m)	135°C	155°C
Shrinkage	0.2-0.8%	0.5-0.7%
Transmittance (visible) (*)	91-93%	87-89%
Turbidity[5] (*)	>1%	>1%
Thermal expansion coefficient (α_L)	3.6-6.5 $\times$ 10^{-5}/K	6-7 $\times$ 10^{-5}/K
Thermal variation of refractive index (dn/dT)	-1.05 $\times$ 10^{-4}/K	–1.2 $\times$ 10^{-4}/K
Price	2-4€/kg	2.5-4€/kg

* For a 2 mm thick sample

Ref: [Omn12] and [Web03]

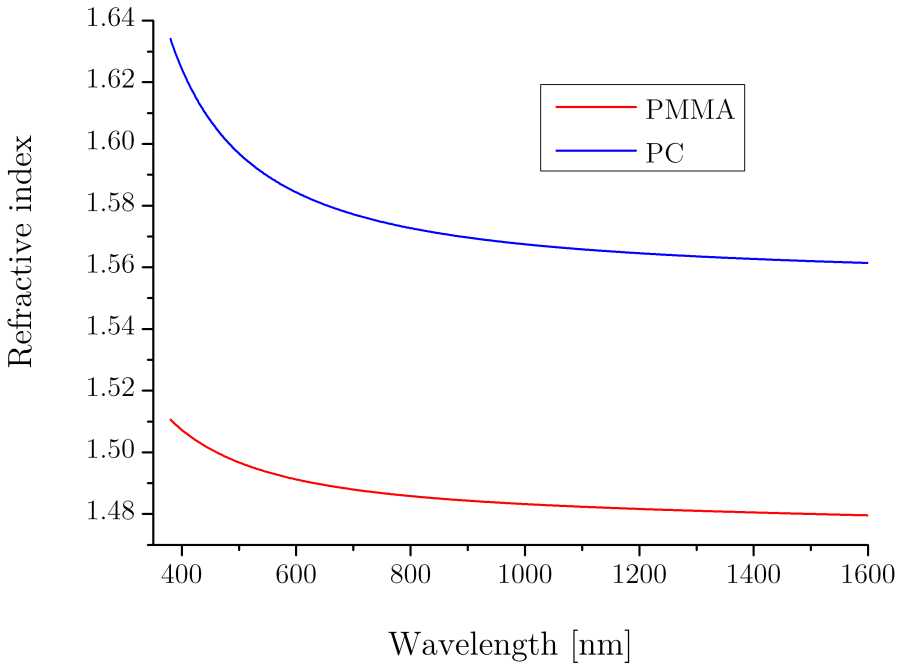

Fig. 3.7: Dispersion curves of PC and PMMA [Lyt09]

5 Turbidity (or haze). In plastic production, haze is defined as the percentage of light that is deflected more than 2.5° from the incoming light direction

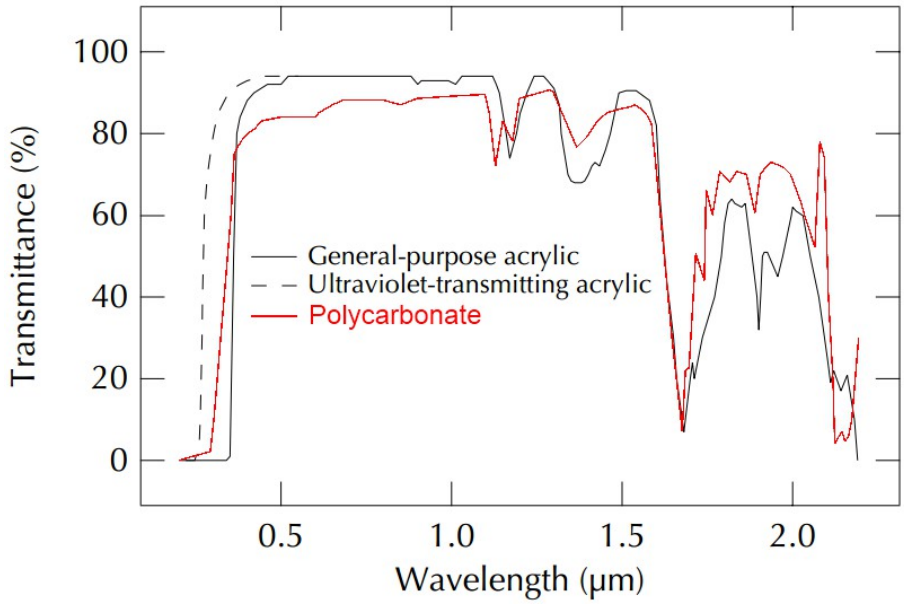

Fig. 3.8: Transmittance (including Fresnel reflections) of two kinds of PMMA (acrylic) and PC [Fre11]. Samples thickness = 3.2 mm,

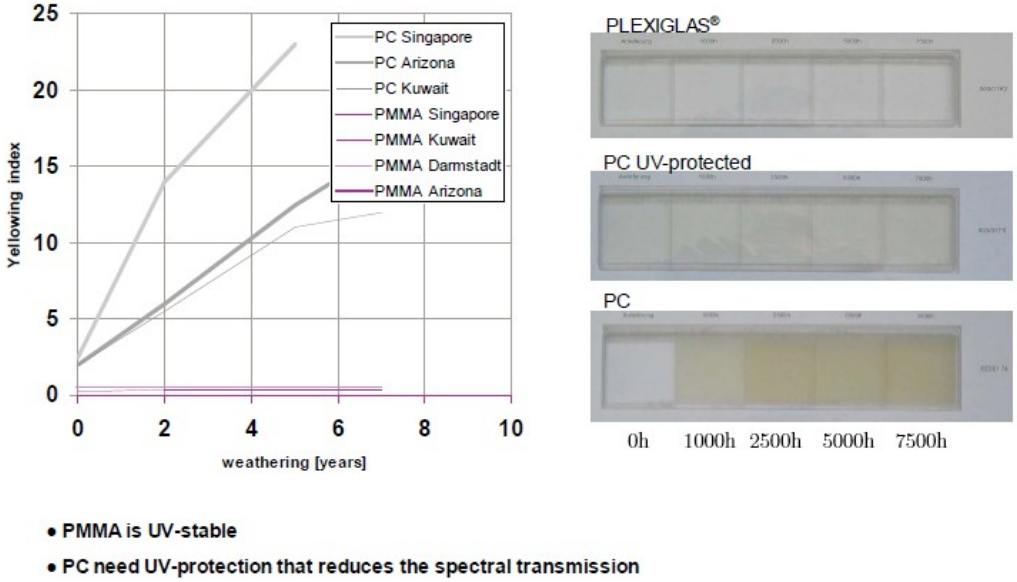

Fig. 3.9: Yellowing curve and aged sample of PMMA, PC UV-protected and PC from Evonik [Roc09]

Note that silicone-on-glass (SOG), an alternative to bulk PMMA, is gaining increasing attention mainly thanks to its higher transmittance, higher mechanical stability and larger bandwidth [Mil11, Tho12]. However it is still at a research level and exhibits some drawbacks like higher chromatic dispersion, higher production costs and higher weight.

3.1.4. F-number and acceptance angle

The *f*-number (F#) is defined as the ratio of the focal length, to the diameter of the lens. It refers to the "speed" of the optical system: the greater the *f*-number, the slower the convergence. What is the ideal *f*-number for solar concentration? The answer is not straightforward. E.g. fast systems (small *f*-numbers) favour coma aberration but tracking tolerances demand fast systems [Leu09]. Without aberration, for a given radius of the lens (R_l) and semi-angular aperture of the source (θ_S) the minimum radius of the absorber (R_a) is determined by the chief ray passing through the centre of the lens without being deviated (Fig. 3.10).

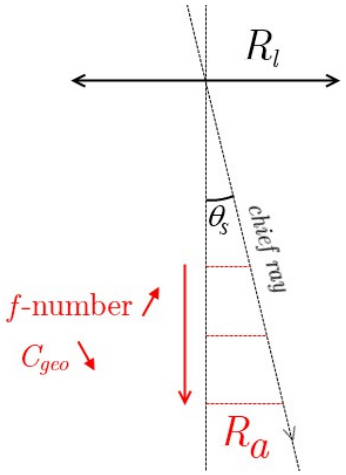

Fig. 3.10: Relation between *f*-number, angular size of the source and maximum concentration

The maximum concentration ratio is thus simply given by

$$C_{geo}^{2D} = \left(\frac{R_l}{R_a}\right)^2 = \left(\frac{1}{2\mathrm{F}\#\tan\theta_S}\right)^2 \tag{3.3}$$

The following figure, Fig. 3.11, represents Eq. (3.3) for Sun's angular aperture.

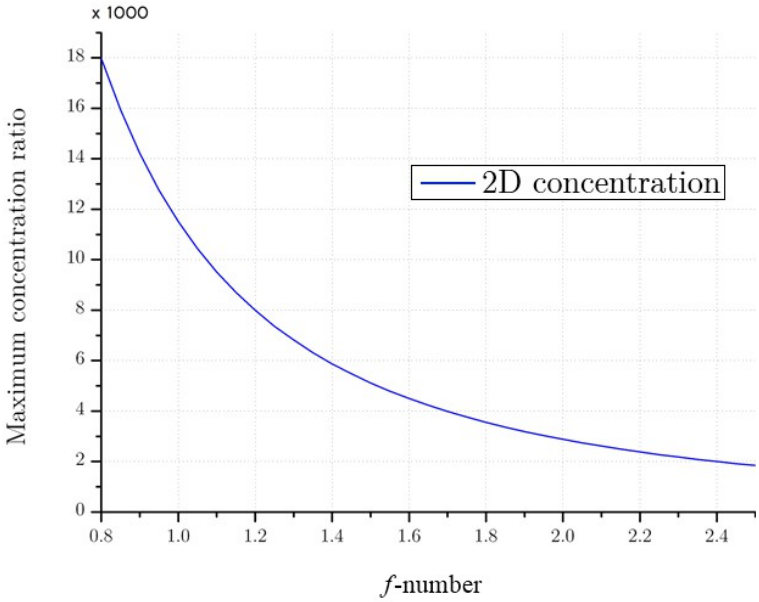

Fig. 3.11: Maximum concentration for *f*-number between 0.8 and 2.5 using the angular aperture of the Sun

It should be noted that the *f*-number cannot be as small as desired: it is limited by the critical angle. Fig. 3.12 represents the relation between the prism angle β (corresponding also to the incoming angle on the second interface) and the deviation angle ψ for the last prism of a plano-convex Fresnel lens of index n immersed into air.

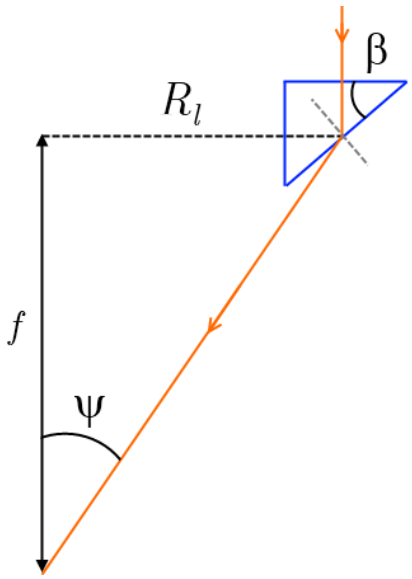

Fig. 3.12: Relation between prism angle and deviation angle for a plano-convex Fresnel lens

Relation between ψ and β may be easily shown using trigonometry [see Appendix III.3]

$$\beta = \operatorname{atan}\left(\frac{\sin\psi}{n-\cos\psi}\right) \tag{3.4}$$

$$\psi = \operatorname{asin}\left(n\sin\beta\right) - \beta \tag{3.5}$$

Since β is limited by the critical angle given by $\operatorname{asin}(1/n)$, the maximum deviation angle is given by

$$\psi_{max} = \operatorname{asin}\left(1\right) - \operatorname{asin}\left(\frac{1}{n}\right). \tag{3.6}$$

Therefore the expression of the minimal *f*-number is expressed as

$$F\#_{min} = \frac{1}{2\tan\left(\psi_{max}\right)}. \tag{3.7}$$

For a refractive index of 1.5, the critical angle is 41.81°. In this case the maximum deviation angle equals 48.19° and the minimum F# is 0.45. However, for angles higher than Brewster's angle, the reflectance coefficient increases drastically (see Fig. 2.12 in Chap. 2.4.). Consequently, F# smaller than 0.75 are very rare exceptions in optics. In CPV, lenses with low *f*-number (lower than 1.2 according to Kühnlenz *et al.* [Kuh07]) are not recommended from the optical efficiency point of view.

When the half-angular size of the Sun (~0.265°) is taken into account, ray-tracing simulations show that, for a typical Fresnel lens, an *f*-number close to 2 maximizes the effective concentration [Reg10, Vic09]. This value depends on the material used and on the design of the lens. An *f*-number close to 2 is optimal for flat Fresnel lenses manufactured out of PMMA without secondary optics.

In case of misalignment between the source and the optical axis of the concentrator, beams are no longer refracted towards the solar cell. Misalignment may be due to several causes like tracking error, manufacturing error, module bending. To prevent electrical production falling back to zero, the design acceptance angle is usually greater than the angular size of the Sun. Typical tracking errors are smaller than 0.1° [Luq07]. There are two main ways to enhance the acceptance angle: designing curved lenses or using a secondary optics. However, this thesis treats on the achromatization of the primary optics manufactured by injection moulding from diamond-turned moulds which is hardly compatible with curved surfaces. Nevertheless, we will design nonimaging flat Fresnel lenses to manage to angular aperture of the Sun.

3.1.5. Size of the lens

Once the *f*-number chosen, the lens radius and the thickness of the lens have to be fixed. Duerr *et al.* explain that, to some extent, the smaller the lens the lower the production costs [Due10]. Indeed, for a given *f*-number, sizing down the lens makes the full module thinner. There is thus less material to use (to buy) and to manufacture and the whole module will be lighter with a lower lateral wind resistance. Moreover, the thinner the lens, the lower the absorption. Also, scaling down the size of the PV cell makes the passive cooling easier.

On the other hand, if Fresnel lens prisms approach a thickness close to the wavelength, the lens may act as a diffractive lens and geometrical optics becomes no longer available (see Chap. 4). Still in the same paper from Duerr *et al.*, it is shown that geometrical optics and wave optics are in good agreement until ~25 prisms of equal widths forming a plano-convex lens with a diameter of 10 mm. If the thickness of the lens is decreased down to an optical thickness of an half-wavelength, then interferences will act as an "anti-transmission" coating but, above all, the lens would be more subject to bending and failure.

From a manufacturing point of view, small lenses suffer more than large lenses from tip radius and valley radius. Moreover, a trade-off between the cooling time per lens and the number of pieces needed for a given area has to be carried out. With very small lenses, the cooling time is low (it increases exponentially with the thickness) but a huge amount of pieces are needed, leading to an important machining time and an increased risk of master failure.

According to Mäkinen and de Schipper [Mak07], cheaper primary optics is reached with a lens diameter of 158 mm and a thickness of 1.6 mm for an amount of ~17 €/m². This cost-optimized size is similar that of a compact disk. Depending on the surface to be covered, the price could be decreased down to under 10 €/m².

3.2. Design of grooves-in flat Fresnel lenses

3.2.1. Newton's method

Designing a flat Fresnel lens made with one material in order to make a given incidence converge into a single focal point may be achieved with a simple analytical solution. When the design gets more complicated, analytical solutions are harder or even impossible to determine. Therefore, the use of Newton's method can be appropriate. It will be used in the next paragraph to design nonimaging Fresnel lenses. The method of Newton is not a design tool; this is a

quick iterative method for finding the root of a function *f(x)*, that we will use in our programs to design Fresnel lenses.

The method of Newton is based on a Taylor series expansion to the first order:

$$f(x) \simeq f(x_0)+f'(x_0)\left(x-x_0\right) + \left[\frac{f''(x_0)}{2!}\left(x-x_0\right)^2+\ldots+\frac{f^{(n)}(a)}{n!}\left(x-a\right)^n\right] \tag{3.8}$$

where x_0 has to be guessed. To determine the first approximated root x_1 we use

$$0=f(x)\simeq f(x_0)+f'(x_0)\left(x-x_0\right), \tag{3.9}$$

hence

$$x_1=x_0-\frac{f(x_0)}{f'(x_0)}. \tag{3.10}$$

From x_1 and new better approximated root can be found in the same way and the process

$$x_{k+1}=x_k-\frac{f(x_k)}{f'(x_k)} \tag{3.11}$$

is repeated till the absolute value of the last approximated root becomes negligible

$$\left|f(x_{k+1})\right|<\varepsilon_1. \tag{3.12}$$

Without analytical expression of the derivative, Eq. (3.11) has to be modified using an approximation of the derivative

$$f'(x_k)\simeq\frac{f(x_k)-f(x_k+\varepsilon_2)}{\varepsilon_2} \tag{3.13}$$

with ε_2 close to zero.

was used by R. Leutz to design dome-shaped Fresnel lenses [Leu00] and in Hololab for freeform Fresnel lenses [Reg10].

3.2.2. Simple imaging flat Fresnel lenses

To create an imaging flat Fresnel lens, optical designers have to determine the prism angle (β) that makes an on-axis monochromatic beam converge to the focal point F. Using the geometry presented in Fig. 3.13, the prism angle equation is simply [Leu01]

$$\beta(r)=\operatorname{atan}\left(\frac{r}{n\sqrt{r^2+\left(bfl+s(r)\right)^2}-\left(bfl+s(r)\right)}\right) \tag{3.14}$$

where *bfl* is the back focal length and $s(r)$ is the sag equation of the surface (in other words the deepness of the profile related to the vertex). In addition to the very fast calculation, the advantage of designing such a lens is that it is not limited by the discretization step.

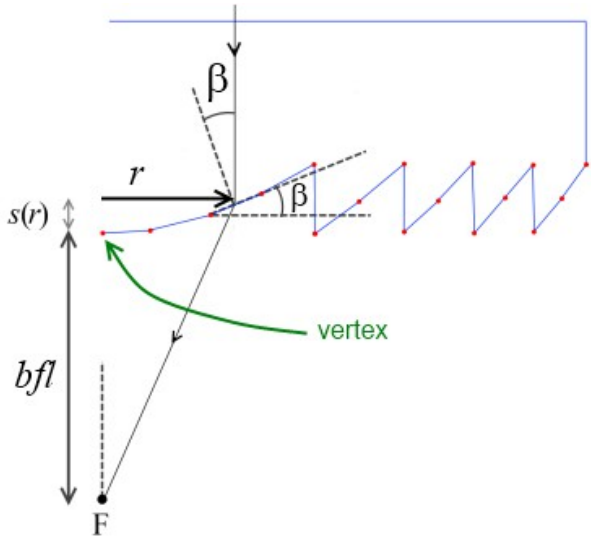

Fig. 3.13: Simple imaging Fresnel lens

3.2.3. Nonimaging Fresnel lenses

Nonimaging design methods consider the angular aperture of the source, to which a tracking error angle could be added up. In imaging designs, beams forming the cone of incidence will not be refracted symmetrically around the absorber which negatively impacts the concentration factor.

To avoid the problem of superimposed segments, a minimum discretization step is required. It can be obtained via a simple geometrical criterion:

$$step \geq 2(h+t)\tan\left[\operatorname{asin}\left(\frac{\sin\theta}{n}\right)\right] \tag{3.15}$$

with h and t the bulk and the teeth thickness as shown in the figure below.

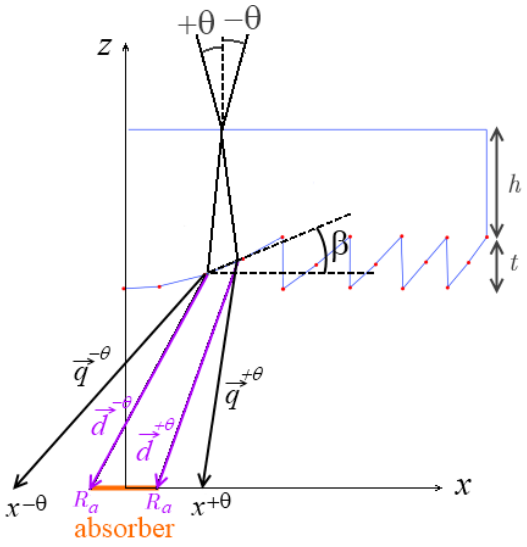

Fig. 3.14: Nonimaging Fresnel lens. Edge-rays (represented by vectors $\vec{q}$ in black) reach the plane of the absorber at a distance $x^{-\theta}$ and $x^{+\theta}$ while the vectors $\vec{d}$ from the lens to the corresponding end of the absorber are plotted in purple.

3.2.3.1. Edge-rays and prism to absorber end parallelism

In its Master thesis, Donat Regaert followed the optimization proposed by Ralf Leutz [Leu00] but for *flat* Fresnel lenses (which is different from *dome-shaped* Fresnel lenses designed by Ralph Leutz). He used Newton's method to find the ideal value of the prism angle. The criterion D. Regaert used consists in the parallelism between the refracted edge-rays (vectors $\vec{q}^{-\theta}$ and $\vec{q}^{+\theta}$ in Fig. 3.14) and the vector from the prism to either end of the absorber (vectors $\vec{d}^{-\theta}$ and $\vec{d}^{+\theta}$ in Fig. 3.14). The break condition in Newton's algorithm loop is

$$\left|\frac{q_x^{\pm\theta}}{q_z^{\pm\theta}}-\frac{d_x^{\pm\theta}}{d_z^{\pm\theta}}\right|\leqslant\varepsilon \tag{3.16}$$

where the subscript refer to the component x or z of the vector. For each incidence angle, a prism angle is obtained: $\beta^{+\theta}$ with the incidence angle $+\theta$ and $\beta^{-\theta}$ for the incidence angle $-\theta$. In its algorithm, contrary to R. Leutz, D. Regaert imposed the prism angle β to be the average value of $\beta^{-\theta}$ and $\beta^{+\theta}$:

$$\beta=0.5\left(\beta^{+\theta}+\beta^{-\theta}\right). \tag{3.17}$$

This nonimaging design method is dependent on the size of the absorber (related to the vectors $\vec{d}^{\mp\theta}$) and therefore on the geometrical concentration factor. Unfortunately, the maximum concentration factor is, in principle, not known

before the finalization of the lens design. To illustrate the problematic encountered with this optimization technique, two $f/1$ nonimaging lenses "optimized" for an acceptance angle of 5° were designed. The design 2D-geometrical concentration factors selected are 3× for the first design and 15× for the second one. The ray-tracing of the edge-rays at the border of the lenses has been depicted in Fig. 3.15. This clearly shows that edge-rays impact the plane of the absorber asymmetrically around the centre of the absorber with both too high and too law design concentration factors. The effective concentration ratio, which does not corresponds to the design concentration ratio, is given by

$$C_{geo}^{eff} = \left(\frac{R_l}{\max\{x^{+\theta}, x^{-\theta}\}} \right)^2 \tag{3.18}$$

where $x^{-\theta}$ and $x^{+\theta}$ are the radial coordinate of the edge-rays the in the plane of the absorber (see Fig. 3.15).

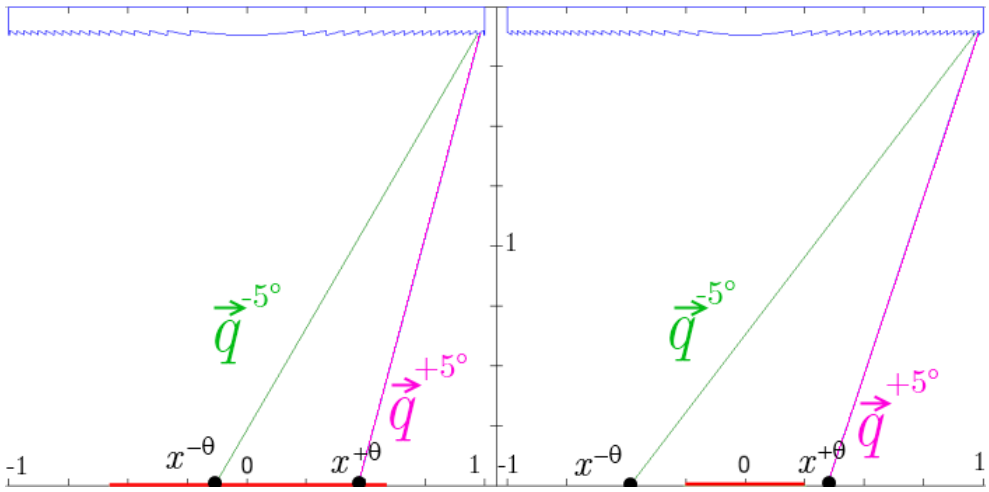

Fig. 3.15: Axis to scale with arbitrary units. Nonimaging lenses designed using the parallelism between edge-ray vectors and prism to either absorber end vectors ($\vec{q}$). Left: design C_{geo}= 3×, effective C_{geo}= 4.4×. Right: design C_{geo}=15×, effective C_{geo}=3.6×. The design absorbers are depicted in red. Lenses characteristics: $f/1$, incoming angles = design angles = ± 5°.

The issue encountered with the parallelism criterion lies in the impossibility to fulfil both Eq. (3.16) and a close value of the prism angles required by both edge-rays of the flat lens:

$$\left|\beta^{+\theta} - \beta^{-\theta}\right| \leqslant \varepsilon_2 \tag{3.19}$$

Even if this optimisation technique is not convenient for flat Fresnel lenses, Ralf Leutz showed in its PhD thesis that it is particularly useful for dome-shaped Fresnel lenses.

3.2.3.2. Edge-rays symmetry

To enhance even more the concentration factor, we suggest using another criterion to break Newton's algorithm loop: we impose that the edge-rays impact symmetrically the plane of the absorber, as shown in Fig. 3.15. This automatically ensures the highest concentration ratio for the design acceptance angle. Mathematically this corresponds to the following inequality condition

$$\frac{\left|x^{-\theta}+x^{+\theta}\right|}{2\,bfl\,\tan\theta}\leqslant\varepsilon \tag{3.20}$$

The unnecessary denominator comes from Eq. (3.3) in order to obtain a dimensionless condition. Condition (3.20) is independent on the geometrical concentration. To compare with the previous design method, a $f/1$ concentrator designed with the edge-rays symmetry method achieves a concentration factor of 6.7× for an acceptance angle of 5° as shown in Fig. 3.16 (instead of 4.4× and 3.6× for the designs presented in Fig. 3.15).

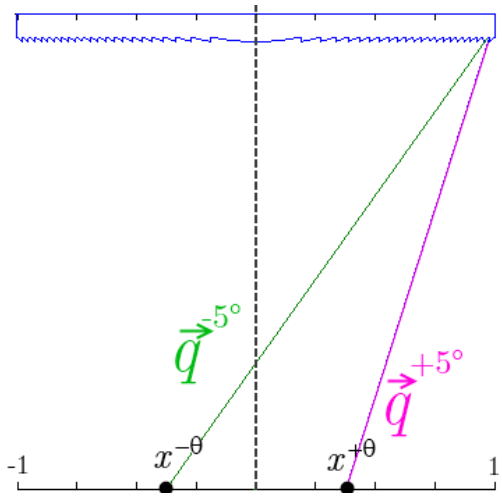

Fig. 3.16: Nonimaging lens designed to obtain edge-rays impacting symmetrically the plane of the absorber.

3.2.4. Concentration ratio comparison between imaging and nonimaging method

Because of the ease of use (no need of the geometrical concentration) and the concentration gain obtained with the edge-rays symmetry design, the parallelism-based nonimaging method will no longer be used.

To investigate the benefit of edge-rays nonimaging Fresnel lenses, a comparison with imaging Fresnel lenses was performed for several *f*-numbers (1, 2 and 5)

designed for several acceptance angles (0°, 0.265°, 0.365°, 1° and 5°). Results are presented in Tables 3.2. for various incoming angles (as well 0°, 0.265°, 0.365°, 1° and 5°).

To perform these simulations we used the following parameters (which are in accordance with Chap. 3.1.)

- a design step of 0.01 mm,
- a lens radius (R_l) of 20 mm,
- a thickness of teeth, t, of 0.385 mm,
- a refractive index of 1.4896 (PMMA at 650 nm)
- a lens thickness, h, (teeth excluded) of 2 mm.

Winston explains [Win05 p.191] that for a small acceptance angle and an f-number greater than 2 (approximately), the imaging and the nonimaging designs achieve equivalent performances. The same conclusion can be reached from Tables 3.2.

Fig. 3.17 is particularly relevant to emphasize the difference between an imaging lens and a nonimaging lens: while the on-axis rays of the imaging lens impact the centre of the absorber and the edge-rays impact asymmetrically the absorber, the edge-rays beams exiting the nonimaging lens reach the absorber symmetrically to its centre.

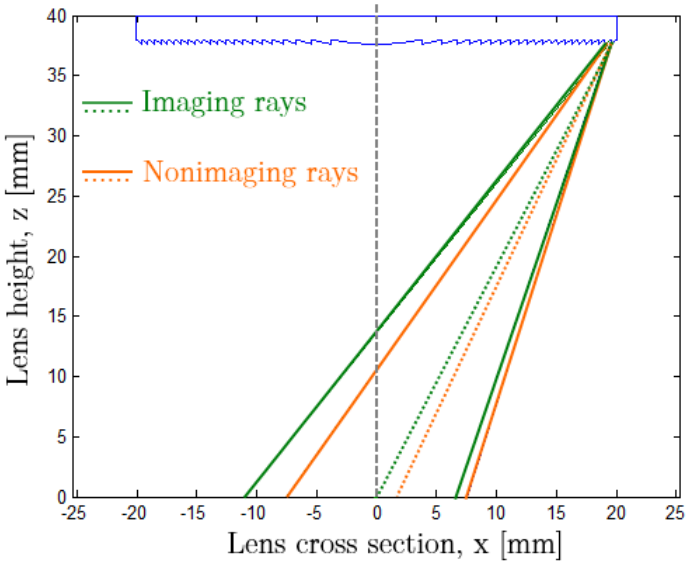

Fig. 3.17: Comparison between imaging and nonimaging $f/1$ lens design for an acceptance angle of ±5°. Edge-rays are in full lines and on-axis incoming rays in dotted lines.

Tables 3.2 Maximum concentration for imaging and edge-rays symmetry nonimaging Fresnel lenses. Three *f*-number (1, 2 and 5) and five angles are investigated (0°, 0.265°, 0.365°, 1° and 5°)

***f*/1 lens** (**θ** design)	Angular radius of the source				
	0.0°	0.265°	0.365°	1.0°	5.0°
Imaging lens	-	2080 ×	1085 ×	135 ×	2.7 ×
Nonimaging lens (0.265°)	1.3e7 ×	2136 ×	1107 ×	136 ×	2.7 ×
Nonimaging lens (0.365°)	3.4e6 ×	2089 ×	1126 ×	137 ×	2.8 ×
Nonimaging lens (1.0°)	6.3e4 ×	1573 ×	913 ×	151 ×	2.9 ×
Nonimaging lens (5.0°)	153 ×	101 ×	88 ×	44 ×	6.7 ×

***f*/2 lens** (**θ** design)	Angular radius of the source				
	0.0°	0.265°	0.365°	1.0°	5.0°
Imaging lens	-	1899 ×	999 ×	131 ×	4.7 ×
Nonimaging lens (0.265°)	2.3e8 ×	1910 ×	1003 ×	131 ×	4.7 ×
Nonimaging lens (0.365°)	6.4e7 ×	1901 ×	1007 ×	132 ×	4.7 ×
Nonimaging lens (1.0°)	1.1e6 ×	1774 ×	958 ×	134 ×	4.8 ×
Nonimaging lens (5.0°)	1918 ×	485 ×	344 ×	87 ×	5.4 ×

***f*/5** (**θ** design)	Angular radius of the source				
	0.0°	0.265°	0.365°	1.0°	5.0°
Imaging lens	1.7e18 ×	438 ×	231 ×	31 ×	1.2 ×
Nonimaging lens (0.265°)	5.5e8 ×	439 ×	231 ×	31 ×	1.2 ×
Nonimaging lens (0.365°)	1.5e8 ×	438 ×	231 ×	31 ×	1.2 ×
Nonimaging lens (1.0°)	2.7e6 ×	428 ×	228 ×	31 ×	1.2 ×
Nonimaging lens (5.0°)	4409 ×	254 ×	154 ×	26 ×	1.2 ×

3.3. Performance deterioration factors

3.3.1. Maximum concentration for lenses: *f*-number and LCA

In section 3.1.4., we discussed the effect of the *f*-number on the concentration factor: the higher the *f*-number, the lower the maximum concentration, following

$$C_{geo}^{2D}=\left(\frac{1}{2\,\mathrm{F}\#\tan\theta_S}\right)^2 \tag{3.21}$$

with θ_S the angular radius of the Sun. However, up to now, only achromatic concentrators have been considered. We know that mirrors can theoretically achieve the thermodynamic limit of concentration. But what about lenses? We will prove that the longitudinal chromatic aberration (LCA) also limits the maximum concentration ratio.

It should already be noted that the *f*-number limits the concentration because of the angular size of the source, while the LCA is an intrinsic properties of the lens material and is independent on the angular size of the source, as will be shown in the next section.

3.3.1.1. Longitudinal chromatic aberration

In paraxial conditions, the focal distances of a simple thin lens (that is a lens with a thickness much smaller than its focal length) depends on its refractive index n_l as well on the refractive index of the surrounding medium n_m and on its front and back radii of curvature: RoC_1 and RoC_2 (see Fig. 3.18).

$$f=\left(\frac{1}{RoC_1}-\frac{1}{RoC_2}\right)^{-1}\frac{1}{n_l-n_m} \tag{3.22}$$

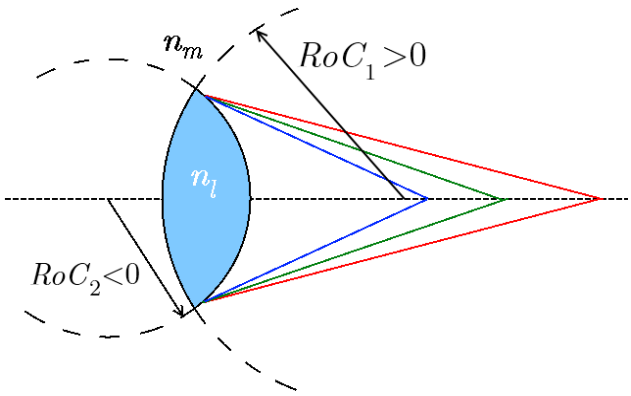

Fig. 3.18: Lens diagram

The sign convention used for the two radii of curvature in the above equation is depicted in Fig. 3.18, and is the same as the convention used in most of the books treating on optics, like ref. [Hec02].

For easier reading, the parenthesis containing the radii of curvature may be replaced by an equivalent radius of curvature, RoC_{eq}. If air is the surrounding medium (i.e. $n_m \simeq 1$) the last equation takes the form of

$$f(\lambda)=\frac{RoC_{eq}}{n_l(\lambda)-1} \tag{3.23}$$

where we highlighted the wavelength dependence of f and n. Knowing this wavelength dependence, if we place a lens in a concentrator design we can observe the chromatic effect.

Let's suppose that the absorber is situated at a distance F from the lens, which is assumed to correspond to the focal length of λ_0, $f(\lambda_0)$. The longitudinal chromatic aberration is defined as the difference between the focal distance and the position of the absorber

$$LCA=f(\lambda)-F=f(\lambda)-f(\lambda_0). \tag{3.24}$$

In order to compare optical systems, a normalization with λ_0 is needed and is annotated with an asterisk:

$$LCA^*=\frac{f(\lambda)-f(\lambda_0)}{f(\lambda_0)}. \tag{3.25}$$

Using Eq. (3.23), the $LCA*$ proves to be independent of the distance of the absorber, it only on depends on the refractive indices of the lens material:

$$LCA^*=\frac{n(\lambda_0)-n(\lambda)}{n(\lambda)-1}. \tag{3.26}$$

This last equation is quite similar to the definition of the inverse of the Abbe number (see Chap 2.4.1.5.).

3.3.1.2. LCA and maximum concentration

To maximize the concentration ratio, let's have a look at Fig. 3.19 where the LCA is the same in absolute value for wavelengths λ_m and λ_M – i.e. $f(\lambda_0)$ is situated at half-distance between $f(\lambda_m)$ and $f(\lambda_M)$ – but the optical efficiency is greater for λ_M focusing behind the absorber.

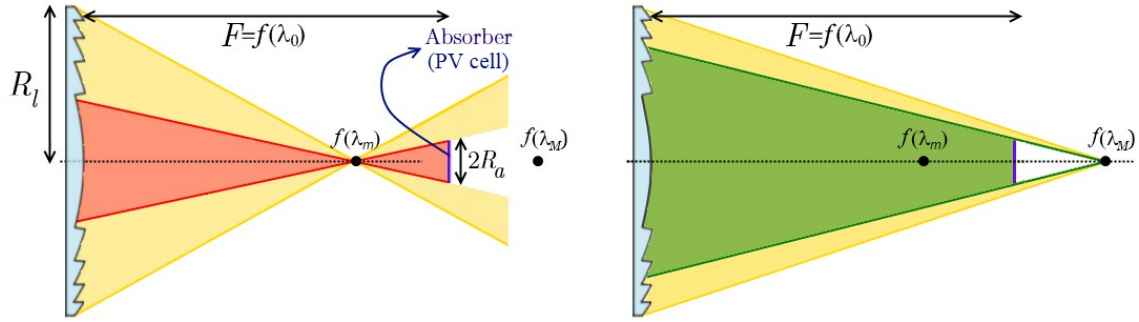

Fig. 3.19: Representation of the optical efficiency for two wavelengths: λ_m and λ_M having the same LCA in absolute value but of opposite sign. Beams with a wavelength λ_m situated in the red cone reach the solar cell, the beams in yellow miss it. While a higher amount of beams with a wavelength λ_M reaches the solar cell (green cone in the right part).

Using the following hypothesis

- normal incidence,
- collimated incoming beams (θ_S=0),
- every beam reaches its focal point,
- $f(\lambda_m)$ and $f(\lambda_M)$ have respectively the minimum and maximum LCA, that are equal in absolute value,

we can deduce from Fig. 3.20 that the smaller radius of the absorber, R_a, situated at $f(\lambda_0)$ which allows to collect all the beams follows Eq. (3.27)

$$\tan(\theta)=\frac{R_l}{f(\lambda_0)-LCA}=\frac{R_a}{LCA} \tag{3.27}$$

The two-dimensional geometrical concentration is thus given by

$$C_{geo}^{2D}=\left(\frac{R_l}{R_a}\right)^2=\left(\frac{1-LCA^*}{LCA^*}\right)^2 \tag{3.28}$$

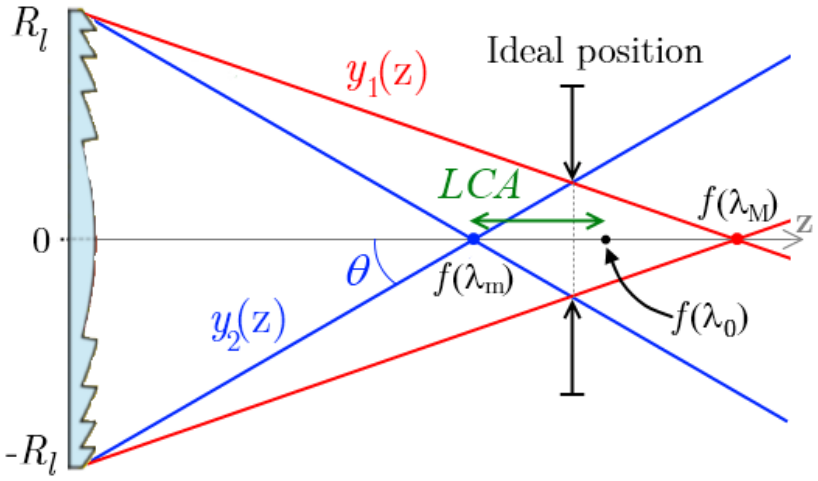

Fig. 3.20: Ideal position of the absorber is closer to $f(\lambda_m)$ than $f(\lambda_M)$

However, it clearly appears that placing the absorber in the middle of the two extreme focal points is not optimal: it should better be placed closer to $f(\lambda_m)$ than $f(\lambda_M)$ to minimize the lateral chromatic aberration. The ideal position is determined by the intersection of the end-rays of wavelengths λ_m and λ_M, represented by the function $y_1(z)$ with $y_2(z)$ as illustrated with Fig. 3.20

$$\begin{cases} y_1(z) := \dfrac{-R_l}{f(\lambda_0)(1+|LCA^*|)} z + R_l \\ y_2(z) := \dfrac{R_l}{f(\lambda_0)(1-|LCA^*|)} z - R_l \end{cases} . \tag{3.29}$$

The intersection occurs at a value z_{int} given by

$$z_{int}\left(\frac{1+|LCA^*|+1-|LCA^*|}{1-LCA^{*2}}\right) = 2f(\lambda_0) \tag{3.30}$$

thus,

$$z_{int} = f(\lambda_0)(1-LCA^{*2}). \tag{3.31}$$

Using Eq. (3.31), the minimum size of the absorber can be deduced

$$y(z_{int}) = \frac{f(\lambda_0)(1-LCA^{*2})(-R_l)}{f(\lambda_0)(1-LCA^*)} + R_l \ . \tag{3.32}$$

Since $A^2–B^2=(A+B)\cdot(A–B)$,

$$y(z_{int}) = R_l \cdot LCA^* \tag{3.33}$$

And the optimized maximum geometrical concentration ratio is

$$C_{geo}^{opt}(LCA^*) = \left(\frac{R_l}{y(z_{int})}\right)^2 = \left(\frac{1}{LCA^*}\right)^2 \tag{3.34}$$

Comparing Eq. (3.28) with (3.34) we see that this optimisation is particularly useful for large LCA^*s. The concentration factor for both positions and the gain obtained by moving the detector from the central position to the ideal position is represented in Fig. 3.21.

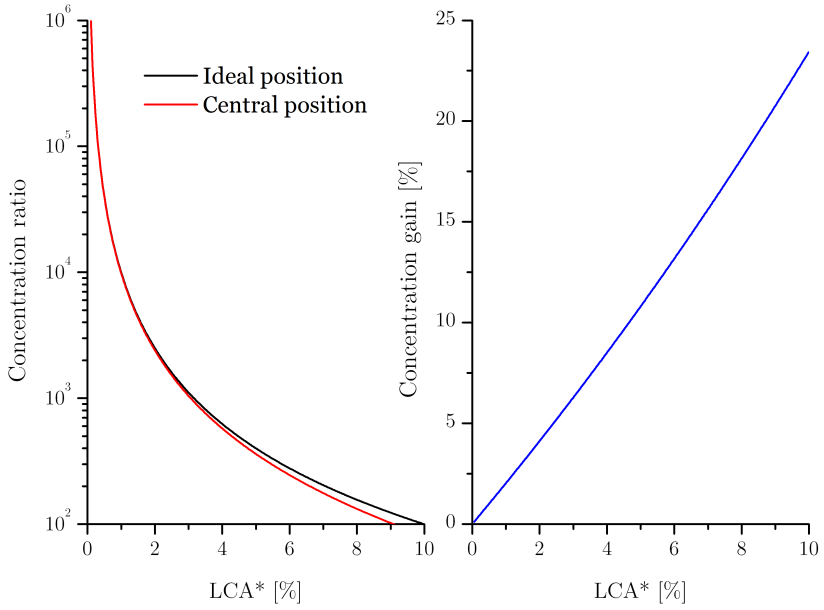

Fig. 3.21: Concentration factor as a function of the LCA* for the ideal and central position of the absorber (left) and gain obtained while moving the absorber from the central position to the ideal position (right).

However it may happen that the size and/or the position of the detector and the lens are imposed. If the imposed geometrical concentration is higher than the maximum concentration given by Eq. (3.34) then Eq. (3.31) no longer applies. The ideal position of the detector may be even before or after $f(\lambda_0)$. Assuming that the position of the detector is imposed at a distance z_{det} of the lens, let's determine the ideal focal distance of λ_0. If the optical efficiency does not achieve 100% due to the fast converging rays, increasing $f(\lambda_0)$ allows for a higher optical efficiency.

On the other hand, if the optical efficiency is low, it is better to decrease $f(\lambda_0)$ since a higher amount of slow converging rays will be intercepted by the absorber while a lower amount of fast converging rays will be lost.

So, to put it in a nutshell, if the optical efficiency does not achieve 100% owing to fast converging rays missing the absorber only, then $f(\lambda_0)$ should be increased. On the contrary, if the optical efficiency is low, decreasing $f(\lambda_0)$ increases the optical efficiency as can be deduced from the following figures. The ideal position of $f(\lambda_0)$ as a function of the geometrical concentration and the LCA^* is presented in Fig. 3.22 and the corresponding optical efficiency is presented in Fig. 3.23.

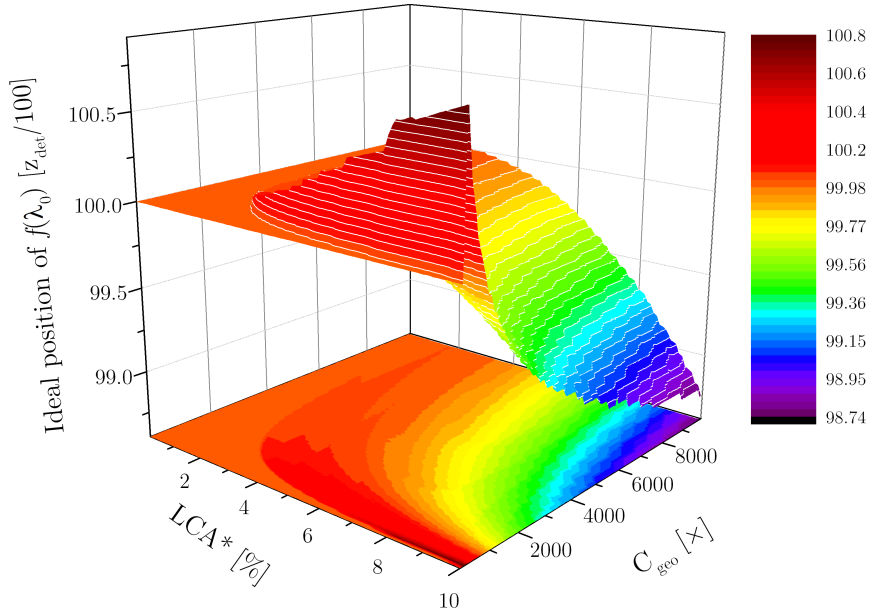

Fig. 3.22: Ideal position of $f(\lambda_0)$ normalized to the detector position as a function of the LCA^* and the geometrical concentration ratio

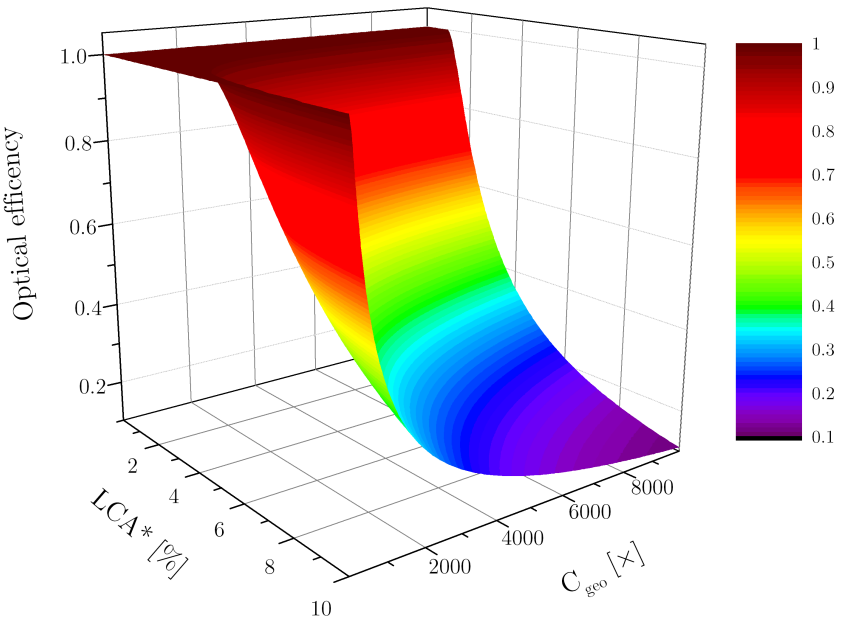

Fig. 3.23: Optical efficiency corresponding to the ideal position of $f(\lambda_0)$ as a function of the LCA^* and the geometrical concentration ratio

3.3.1.3. Comparison between *f*-number and LCA

Which is finally the main limiting factor? The *LCA* or the *f*-number and the angular size of the source?

The maximum concentration ratio is limited by the smallest upper limit of concentrations, that is

$$C_{geo}^{2D} = min\left\{\left(\frac{1}{LCA^*}\right)^2, \left(\frac{1}{2\mathrm{F}\#\tan\theta_S}\right)^2\right\}. \tag{3.35}$$

If we consider the angular size of the Sun, we are able to establish a simple rule to determine which is the limiting factor. Indeed, since $\tan(0.265\,^\circ) \simeq 0.005$, Eq. (3.38) can be rewritten as

$$C_{geo}^{2D} = min\left\{\left(\frac{1}{LCA^*}\right)^2, \left(\frac{1}{0.01\ \mathrm{F}\#}\right)^2\right\} \tag{3.36}$$

If the LCA^* is expressed as a percentage, we just have to compare it with the F#:

$$LCA^*[\%] \overset{?}{>} \mathrm{F}\# \tag{3.37}$$

If the F# is smaller, then and the *LCA* is the limiting factor and vice versa.

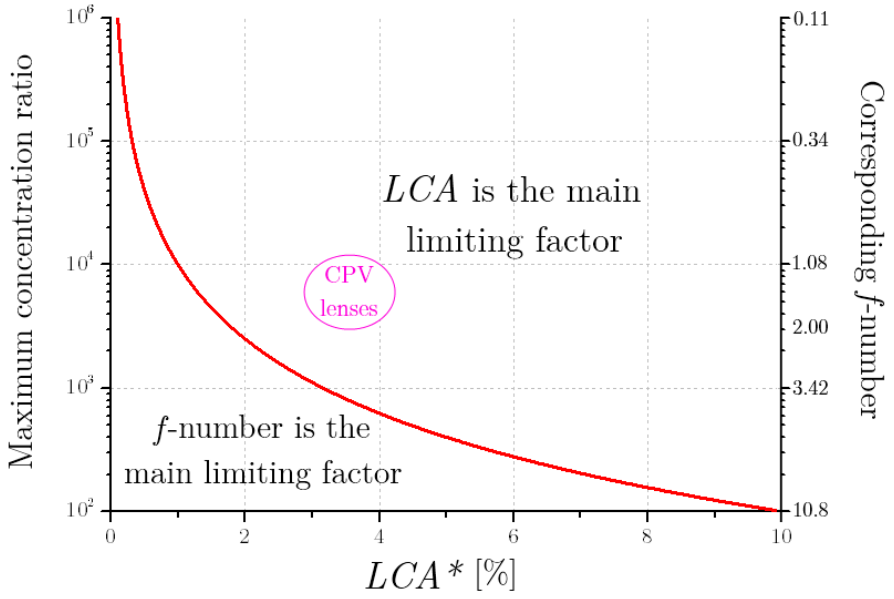

Fig. 3.24: Three axis graph to determine the factor limiting the concentration ratio

Fig. 3.24 shows the maximum concentration ratio as a function of the LCA^*. A third axis, on the right part of the graph, indicates the *f*-number corresponding to the concentration ratio of the left axis. In this case, the x and y coordinates of each point of the curve are almost equal, as expected. Any lens described by an LCA^* and an *f*-number can be characterized using this graph. If its position (LCA^*, *f*-number) is under the red curve then the *f*-number limits the concentration ratio. Otherwise, the LCA^* is the main limiting factor as is the case for typical lenses used in CPV.

3.3.2. Optical losses

The full determination of optical losses by the mean of equations is fastidious and changes with every design. The use of a ray-tracing program provides the optical performance without turning to these equations. However, it is important to classify the losses in order to determine what the predominant factors are.

3.3.2.1. Fresnel reflections

When light beams enter or exit a lens, they suffers from Fresnel reflections. Since the refractive index varies with wavelength, so does the reflection coefficient r. Under normal incidence, the reflectance coefficient R_{FR} (the square of the reflection coefficient r_{FR}) is independent of the polarization state and is given by

$$R_{FR}(\lambda)=r_{FR}^2(\lambda)=\left(\frac{n_1(\lambda)-n_2(\lambda)}{n_1(\lambda)+n_2(\lambda)}\right)^2 \tag{3.38}$$

For other incidence angles, refer to Chap 2.4. If a lens with a refractive index n_2 is immersed into a medium with a refractive index n_1, light passes through two interfaces and the Fresnel transmittance coefficient is

$$T_{FR}(\lambda)=(1-R_{FR(\lambda)})^2 \tag{3.39}$$

Typically, with n_1=1 and n_2=1.5, the average transmittance over a full flat Fresnel lens remains about 92%. Surface texturation (e.g. moth eyes) or anti-reflection coatings can improve the transmittance but the manufacturing cost increase is usually not compensated by the optical gain.

3.3.2.2. Absorption and diffusion

The radiant energy, Q_e, is subject to exponential decay inside the lens material, whose argument is the product of the absorption coefficient, μ_a, with the distance, x ,travelled inside the medium:

$$Q_e = Q_{e0} \exp\left(-\mu_a x\right) \tag{3.40}$$

Typically, the attenuation coefficient of PMMA is around 0.02 m^{-1} (~100dB/km) [Roc09] which is negligible for typical thickness of Fresnel lenses in the range of 2.5 to 5.5 mm. Unfortunately, no information about the diffusion coefficient of optical grade PMMA was found in literature. Since, the total transmission a 3 mm thick PMMA sample is about 91% about 1% should be lost by diffusion.

3.3.2.3. Draft facets

Mass production processes, like injection moulding and embossing, require a draft angle to release the lens from its mould, which causes an optical dead zone at each draft facet (see Fig. 3.25). The optical losses due to draft facets are different if the lens is linear (1D) or is a surface of revolution (2D).

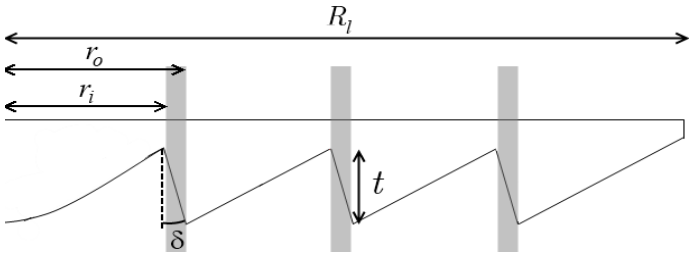

Fig. 3.25: Transversal view of a half Fresnel lens. Dead zones are represented by grey strips.

In the first case, the relative dead zone, dz^*, corresponds to

$$dz^*_{1D} = \frac{\left(n_{teeth} - 1\right) \times t \tan\delta}{R_l} \times 100\,\% \tag{3.41}$$

while for the two dimensions case the dead zone is given by

$$dz^*_{2D} = \frac{\sum_{m=2}^{n_{teeth}} \pi r_{om}^2 - \pi r_{im}^2}{\pi R_l^2} = \frac{\sum_{m=2}^{n_{teeth}} \left(r_{im} + t\tan\delta\right)^2 - r_{im}^2}{R_l^2} \times 100\,\% \tag{3.42}$$

where r_o and r_i are respectively the radii of the outmost and inmost part of the draft facet as shown in Fig. 3.25.

3.3.2.4. Peak and valley

The determination of the optical losses due to peaks and valleys is quite easy to achieve. To do this, we must determine the coordinates (x_c, y_c) of the transition point between the ideal profile and the real profile (see Fig. 3.26).

This is done by finding the point whose tangent matches the tangent to the circle of the peak or the valley. Detailed equations are available in Chap. 4.6.1. Usually peak and valley radii are smaller than 30 µm. Depending on the number of teeth, the total dead zone created is usually about 2% of the lens surface.

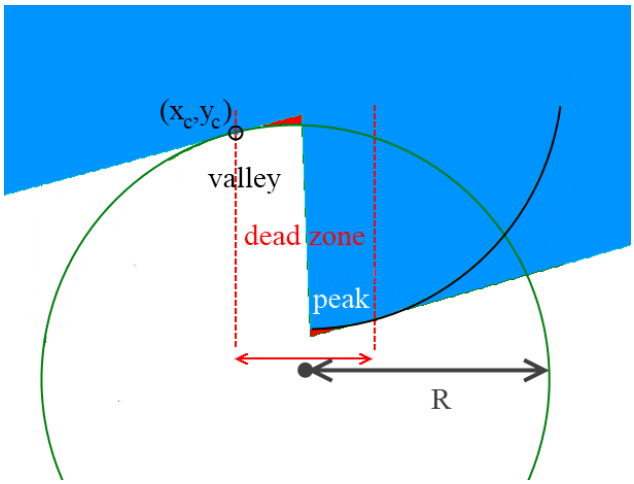

Fig. 3.26: Dead zone due to rounding tips: peak and valley. Fresnel lens is filled with blue and error profile in red.

3.3.3. Refractive index and shape error due to manufacturing or temperature variation

The temperature affects solar concentrators in two ways: the refractive index changes (thus so do the focal distance and the size of the focal spot) and the lens suffers from thermal expansion causing a deformation of its profile. It is therefore preferable to design a lens while taking into account the operating temperature of the optical material. Van Riesen *et al.* [Van11], calculated an optimized design temperature of 40°C. Hornung *et al.* estimated the absolute drop of energy production to be about one percent due to temperature variation during one year using a concentrator made of PMMA with a geometrical concentration ratio of 400× [Hor12].

What is the predominant factor? Is it the thermal expansion or the variation of the refractive index?

Schult *et al.* [Sch09] claimed that their simulations showed a reduction of the short circuit current in the same order of magnitude as the decrease of the refractive index. As a magnitude order, with a thermal variation of refractive index of -1.05×10^{-4} (see Table 3.1), when the temperature increases by 20°C, the refractive index of PMMA decreases by 0.0021 ($\Delta n/n = -0.15\%$).

The influence of the refractive index error and of the shape error on the focal length can be approximately determined using the focal length formula of thin lens in the paraxial approximation:

$$f(\lambda)\simeq\frac{RoC_{eq}}{n(\lambda)-1}. \tag{3.43}$$

When a lens is designed for a refractive index n, the use of another refractive index n' turns the focal distance f into f' following

$$f'(\lambda)\simeq\frac{n(\lambda)-1}{n'(\lambda)-1}f(\lambda). \tag{3.44}$$

On the other hand, a manufacturing error or a dilatation of the lens material could lead to a radius of curvature error, turning the RoC_{eq} into $RoC_{eq}^{''}$ conferring a focal distance to the lens given by

$$f^{''}(\lambda)\simeq\frac{RoC_{eq}^{''}}{RoC_{eq}}f(\lambda) \tag{3.45}$$

Truly speaking, the coefficient of thermal defocus, α_{TD} defined as

$$\alpha_{TD}=\frac{1}{f}\frac{df}{dT} \tag{3.46}$$

is affected by three parameters: the thermal variation of the refractive index of the lens and of the air (negligible), and the linear thermal expansion coefficient α_L:

$$\alpha_{L}=\frac{1}{R}\frac{dR}{dT} \tag{3.47}$$

Considering a homogeneous variation of the temperature with only linear effects, the coefficient of thermal defocus is determined by the derivation of Eq. (3.43), that is

$$\alpha_{TD} = \frac{1}{f}\frac{df}{dT} = \frac{1}{RoC_{eq}}\frac{dRoC_{eq}}{dT} - \frac{1}{n-1}\frac{dn}{dT} \tag{3.48}$$

that can be rewritten in a more practical form:

$$\alpha_{TD} = \alpha_L - \frac{1}{n-1}\frac{dn}{dT}. \tag{3.49}$$

Introducing the values corresponding to the PMMA (see Table 3.1), Eq. (3.49) provides a value of ~2.7 $\times$ 10^{-4} K^{-1} to the coefficient of thermal defocus. Contrary to glasses like BK7 and fused silica, the focal length increases with temperature. The contribution of the thermal expansion is almost negligible in Eq. (3.49) since its value lies around 6 $\times$ 10^{-5} K^{-1}.

3.4. Chapter conclusions

In a first step, several lens design parameters have been investigated. We found that lenses are more tolerant to manufacturing errors than mirrors. In CPV, lenses are required to be "fresnelized" to achieve a cost-effective concentrator. As for lens materials, PMMA is, up to now, the best optical plastic for CPV. The ideal *f*-number is in-between 1.2 and 2 depending mainly on the material dispersion, the tracking error and the shape of the concentrator. The optimal number of teeth and the size of the lens result in a trade-off between shading, absorption, weight and cost of production.

In a second step, after determining the design parameters, we applied Newton's method to design nonimaging Fresnel lenses. The method we developed, based on the symmetry of the edge-rays, ensures a maximal concentration and is particularly powerful for high acceptance angles and small *f*-numbers.

Thirdly, we investigated the longitudinal chromatic aberration. To our knowledge, this is the first time that the effects of the LCA are quantitatively investigated. The concentration ratio is strongly affected by the LCA: it varies as $1/LCA^{*2}$. Consequently, the chromatic effects are not negligible and play an important role in the optical design of concentrators for both the concentration ratio and the spectral homogeneity.

Regarding the concentration ratio, we distinguished the roles of the *f*-number and the LCA^*. On the one hand, the limitation by the *f*-number is due to the angular size of the source. On the other hand, the LCA is an on-axis aberration and is not affected by the angular size of the source. Its value depends only on the variation of its refractive index. In the focal plane, the longitudinal chromatic aberration

produces a lateral chromatic aberration. Hence the need for a wider absorber than for monochromatic applications.

Finally, optical losses were investigated. Compared to continuous lenses, the fresnelization of lenses generates additional optical losses due to the draft facet and the pick and valley radii, in addition to absorption, diffusion and reflections losses. Finally, it is worth noting that optical losses due to thermal effects are much more influenced by the alteration of the refractive index than by the thermal expansion.

4 Design of broadband high-efficiency diffractive lenses

Achromatic lenses, i.e. lenses that are almost free of chromatic aberration, can be achieved with the combination of a diffractive lens with a refractive lens, namely a hybrid lens. Diffraction laws imposes that long wavelengths are more diffracted than short wavelengths. Therefore, as shown in Fig. 4.1, converging diffractive lenses make long wavelengths converge faster than short wavelengths, contrary to refractive lenses. So, adequately combined together, they can result in an achromatic hybrid lens. Moreover, the focal distance of a diffractive lens is independent of the lens material, which implies that an achromatic hybrid lens can be made in only one piece, in a single material.

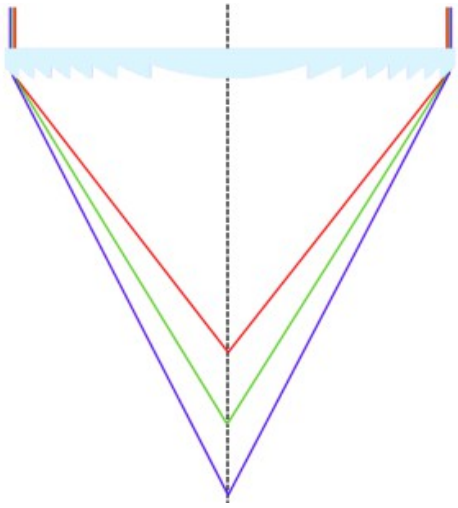

Fig. 4.1: Sketch of a diffractive lens.
Long wavelengths converge faster than short wavelengths

A diffractive lens may be seen as a series of local diffraction gratings. In other words, it looks like a diffraction grating with a variable period, changing with the radial coordinates. Typically, the thickness of the teeth of a diffractive lens is constant over the full radius and is about 1 µm thick (a few hundreds of microns for usual refractive Fresnel lens used in CPV). The teeth, also called "zones", are therefore a hundred times more numerous in a diffractive lens than in refractive Fresnel lens.

After some historical considerations we will present an approximated theory, namely the scalar theory, to optimize the shape of the diffraction gratings. Indeed, it is much easier to first investigate diffraction gratings and then use the results to design a diffractive lens. A particular attention will be paid to the diffraction efficiency. This will lead to the investigation of broadband high efficiency multilayer blazed gratings.

4.1. Diffraction in CPV

Optics for solar concentration sounds either like reflection either like refraction but almost never like diffraction. Diffraction was defined by Sommerfeld as [Som54 in Goo96]

> *"Any deviation of light rays from rectilinear paths which cannot be interpreted as reflection or refraction."*

Diffractive patterns are however used in solar concentration since the early 1960s mainly for light trapping and spectral beam splitting for thermal applications [Gom04, Ime04]. Separation of spectral bands to improve solar cell photoconversion with matching bandgaps appears in the '90s [Frö94, Lud97] mainly with the investigations of Stojanoff *et al.* [Sto94]. In the same time, imaging optics is rediscovering diffractive lenses [Les69, Jor70] already invented in 1875 by I. L. Solet [Mot11]. But the lack of diffraction efficiency over a broad spectral band [Mor97] makes the use of diffractive lenses inopportune. This deficiency has been overcome with the invention of multilayer diffractive optical elements, first patented by Olympus in 1995 [Oha98, Ish00]. Lenses from Canon including multilayer diffractive lens have been commercially available for several years (e.g. Canon EF 70-300mm *f*/4.5-5.6 DO IS USM). But for now, this technology has not been implemented for solar concentration yet. This chapter aims at the design of high efficiency broadband diffractive lenses as well as the determination of critical parameters that could undermine the use of cost-effective multilayer diffractive lens for solar concentration.

4.2. Rigorous diffraction software: RCWA and PCGrate

Rigorous, or exact, theories are based on Maxwell's equations and exact boundary conditions to solve diffraction problems. Their only limiting factors resides in the way they are computed (discretization step, numerical value...). In other words, rigorous models are not vitiated by theoretical approximations.

Although we will develop two approximate theories in the next sections and use it in order to speed up the calculations time, the need for rigorous theories remains for two reasons. Firstly, it is of high importance to determine the validity domain of the approximate theories. How could we determine this validity domain without comparison with a rigorous theory? Secondly, a rigorous model has to be used when the conditions differs from the validity domain.

Several rigorous theories coexist to tackle Maxwell's equations in combination with the boundary conditions (that is, for dielectric materials, the continuity of the tangential components at the interface). For examples the integral method, the classical differential method, the modal method, the coupled-wave method, the finite-element or finite-difference approaches which included the finite-difference time domain (FTDT) method...

We present briefly two different software applications: PCGrate, commercial software based on an integral method and home-made RCWA software (computed by Cédric Lenaerts). PCGrate was used for its calculation speed, its high amount of parameters and its ease of use. RCWA was used to reinforce results obtained with PCGrate or to implement some tricky profiles that would have been very complicated, even impossible, to implement with PCGrate.

Since both PCGrate and the RCWA were used as black boxes, only a quick overview of the numerical methods and their limitations will be presented.

4.2.1. PCGrate ®

In 1989, Dr Leonid I. Goray and its team computed the first PCGrate software and sold it from 1990. From that time, PCGrate has been steadily improved thanks to the collaboration between experts in computer sciences, mathematics and theoretical physics.

PCGrate uses an accurate boundary integral equation method which is described with numerous references available on the website of PCGrate:

> *"The integral method is an approach which allows us in a rigorous manner to reduce a problem of diffraction by grating to solving a*

> *linear boundary integral equation or a system of such equations. In general the integral approach, as well as the similar finite-element method, implies two-dimensional integration. However, in actual practice, a one-dimensional curvilinear integration easily reduced to ordinary integrals is used. Then the linear integral equations so obtained are reduced to a system of linear algebraic equations by the collocation method or by Galerkin's method. In our realization, we use a rather simple but robust and universal technique, the so-called classical Nyström* ***collocation method****. The process of numerical solution of integral equations is based on collocation with piecewise constant basis functions. The principal parameter, in which the convergence is estimated, is the number N of collocation points on each boundary. [...]"*

The description of the underlying theories of PCGrate implies the use and the understanding of a high number of mathematical tools that do not find their place in this thesis.

All we have to understand regards the collocation method, which is a method for solving numerically integral equations. The number of collocation points (quadrature nodes) at each interface defines the dimension of the linear system of equations which is the major accuracy parameter. Usually a collocation number between 100 and 1000 is sufficient to achieve the convergence. In the main majority of cases, the accuracy is revealed by the energy balance (which must be close to one). In this case, the accuracy may be an order of a magnitude of a numerical computation error. It is about 10^{-6} - 10^{-4}, for efficiencies in principal orders for usual resonance diffractions cases.

For extreme diffraction gratings (very high wavelength-to-period ratio, very high depth-to-wavelength, grazing incidence...), the number of collocation points must probably be increased. If this is not sufficient, PCGrate provides different calculations mode that should be able to achieve an efficiency accuracy of 10^{-4} - 10^{-2}. Anyway, we are not concerned by these extreme cases.

So, what our concerns, the accuracy of the simulations is very high compared to manufacturing errors (this will be discussed later).

Much more references and explanations are available on PCGrate website [http://www.pcgrate.com] or in the PCGrate user's guide.

4.2.2. RCWA

The rigorous coupled wave analysis (RCWA) was originally developed by M. G. Moharam and T. K. Gaylord in 1980 for solving the diffraction produced by phase sinusoidal plane grating [Mor81]. This theory was then extended to surface relief profiles [Mor82]. Although the RCWA suffered from convergence issues in certain conditions [Li93, Lal96] it is now able to deal with lots of kinds of gratings (conical incidence, 2D gratings, metallic gratings) even aperiodic structures [Pis11].

RCWA is a semi-analytical method: the wave equation is analytically solved in the longitudinal (z axis) direction. To implement the RCWA, the diffractive structure must be divided into rectangular slices with constant properties along the longitudinal axis (see Fig. 4.2).

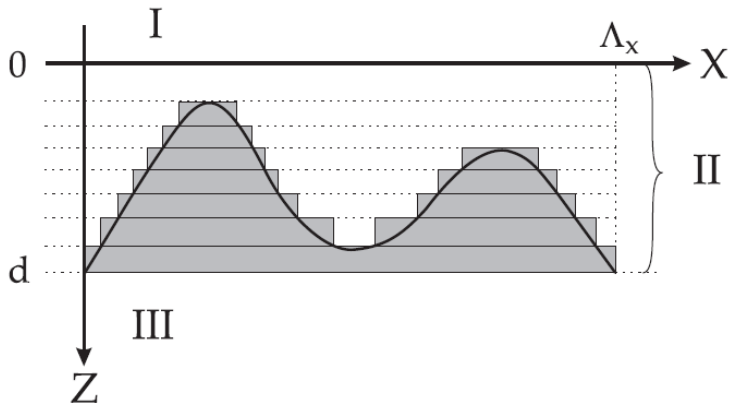

Fig. 4.2: [Len05] Discretization of the diffractive profile along the longitudinal axis for RCWA

RCWA is also called the Fourier Modal Method (FMM) since it involves a Fourier expansion of the fields inside each layer into a finite number of coupled space harmonics. This technique is easier to implement than the integral method, but has a significant drawbacks like Gibb's phenomena due to the Fourier transform of staircase profile, the need of high slicing level for curved or obliques structures and convergence issues in TM modes due to boundaries always vertical [Pop02].

The RCWA software used in this thesis was computed in LabView® by Cédric Lenaerts during its PhD thesis. The source code being available, its implementation may be easily performed to introduce new personnalized profiles. It is worth noting that to obtain faster calculations, the TE and TM cases are treated independently (due to a development based on Helmoltz's equation of the second order [Len05]), which makes impossible to process conical incidence calculations.

The number of slices needed to achieve accurate diffraction results with RCWA for the case of blazed gratings can be determine in two ways. The first consists in increasing the number of slices for each simulation up to the observation of a constant value of the diffraction efficiency in the orders of interest... However, the scalar diffraction efficiency of multi-level blazed grating given by

$$\eta_m^N(\lambda)=\left[\operatorname{sinc}\left(\frac{k\lambda_0}{\lambda}-m\right)\right]^2\left[\operatorname{sinc}\left(\frac{k\lambda_0}{N\lambda}\right)\right]^2 \tag{4.1}$$

where λ_0 is the design wavelength optimized for the k^{th} order, m is the diffraction order considered and N the number of steps used to discretize the grating, as depicted in Fig. 4.3 for N=4.

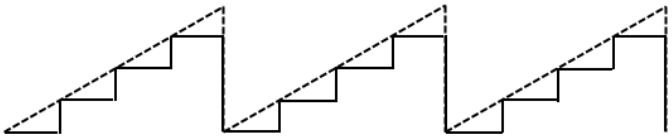

Fig. 4.3: Discretization of a blazed grating into four levels

For the first diffraction order at the design wavelength, Eq. (4.1) reduces to

$$\eta_1^N=\left[\operatorname{sinc}\left(\frac{1}{N}\right)\right]^2. \tag{4.2}$$

Already for 8 levels, the diffraction efficiency reaches 95% and 99% for a 16-level blazed grating [Swa89].

Finally, it should be noted that RCWA is well-known for its stability and accuracy regarding dielectric gratings which need few Fourier orders.

4.3. Scalar theory for diffraction gratings

Nowadays, rigorous theories describing the behaviour of light in complex situations are commonly used. The fact remains that they are time consuming and not easy to implement. In certain conditions, a scalar theory is therefore more convenient. Namely a theory that ignores the vectorial aspect of light but provides results comparable with those obtained with the rigorous theory while being less time consuming and easier to implement. Moreover, the scalar theory allows for an easier approach to optimize diffraction gratings, while rigorous theories sound more like tools to check the diffractions characteristics for the gratings designed. This chapter explains how it is possible to start from Maxwell's equations to

achieve a scalar theory. Secondly, this theory will be harnessed to obtain broadband high diffraction efficiency gratings. Finally, the scalar theory will be extended to take shading effects into account, allowing to achieve results even closer to rigorous theories.

4.3.1. Diffraction grating equation

The dispersion of a diffraction grating is governed by the so-called diffraction grating equation presented in Eq. (4.3). For gratings with a period Λ immersed in a medium of refractive index n_{ext}, the incident beam of wavelength λ coming with an angle θ_i relative to the normal, will be diffracted into discrete orders ($m \in \mathbb{Z}$ is called diffraction order) with an angle θ_d given by

$$\frac{m\lambda}{\Lambda} = n_{ext,d} \sin\theta_d + n_{ext,i} \sin\theta_i \tag{4.3}$$

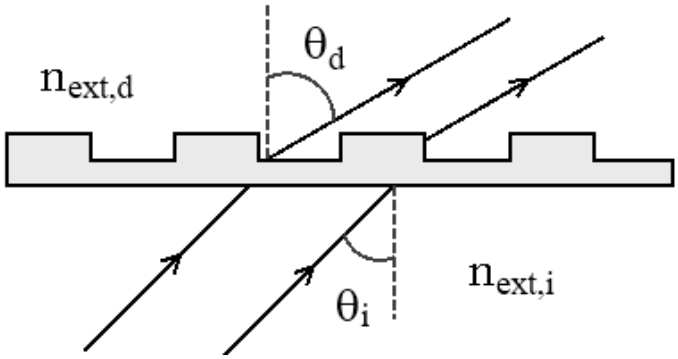

Fig. 4.4: Diffraction grating geometry

This equation is valid in reflection and refraction provided that the diffraction angle is counted positively if situated on the same side from the normal to the grating as the incoming angle and negatively otherwise [Pal00]. The geometry of diffraction grating is depicted in Fig. 4.4. The usefulness of diffraction gratings from a chromatic point of view becomes obvious from Eq. (4.3): diffraction gratings allow for a high chromatic dispersion and offer other design possibilities than purely refractive optics.

4.3.2. Scalar diffraction integral

One of the main issues regarding diffraction gratings lies in the determination the diffraction efficiency which depends on the grating characteristics but also on the polarization state of light and its wave vector (i.e. the wavelength and the incidence angle) as well as on the surrounding medium. Moreover, among the

science community the definition of diffraction efficiency for the k^{th} order (η_k) is not clearly established. Indeed, it is usually defined as the fraction of the *total* incoming intensity (I_{inc}) that is diffracted in the k^{th} (I_k) order i.e.

$$\eta_k^{tot} = \frac{I_k}{I_{inc}}. \tag{4.4}$$

However, it is sometimes defined as the ratio of the intensity into the k^{th} order *relatively* to the sum of the intensity lying in every existing diffraction order, in order to neglect absorption and scattering:

$$\eta_k^{rel} = \frac{I_k}{\sum_j I_j}. \tag{4.5}$$

Finally, for *transmission* gratings, it may also refer to the ratio of I_k to the sum of every intensity of the transmitted orders

$$\eta_k^{trans} = \frac{I_k}{\sum_j I_j(trans)}. \tag{4.6}$$

The efficiency provided by the scalar efficiency corresponds to this last definition of the efficiency, since the scalar model for transmission gratings does not consider any optical losses (thus no reflection, no absorption and no diffusion).

Anyway, to determine the intensity in a given order one normally needs to solve Maxwell's equations. A rigorous solution requires long and complex mathematical developments. Considering a diffracting material with a permittivity ε and a permeability μ, and assuming that

i. the material is linear (i.e. μ and **ε** do not change in the presence of magnetic and electric field);

ii. the material is isotropic (i.e. μ and **ε** do not depend on the polarization state);

iii. the material is homogeneous and uniform (i.e. μ and **ε** do not vary with position and time)

iv. the temporal component of the electric field may be ignored

v. the light passes through an aperture plane where light properties are known

vi. the aperture size is greater than the wavelength: $Z \gg \lambda$.

the solution of Maxwell's equation lead to a scalar equation [OSh03]. Indeed, we show in Appendix III.1 that the diffracted field U can be simply obtained by the Fourier transform $\mathscr{F}$ of the complex amplitude in the aperture plane u_0, which introduce a position dependent phase shift ϕ_0:

$$U(X,Y,Z)=\mathscr{F}\left\{u_0(x,y)\,\exp\left[i\,\phi_0(x,y)\right]\right\}. \tag{4.7}$$

where x and y are the coordinates in the aperture plane and X, Y are the coordinates of the observation plane situated at a distance Z.

From a practical point of view it is much easier and less time consuming to use the scalar theory than a rigorous theory.

4.3.3. Scalar diffraction grating efficiency

As regards diffraction gratings, the amplitude transmission function is periodic, and the Fourier transform becomes a Fourier series. The diffraction efficiency of the m^{th} order is given by the modulus of the m^{th} coefficient of the Fourier series to the square (provided that the Fourier series has been normalised).

$$\eta_m^{trans}=c_m\,\bar{c}_m \tag{4.8}$$

where c_m is given by

$$c_m=\frac{1}{\Lambda}\int_{-\Lambda/2}^{\Lambda/2} g(x)\,e^{-i\frac{2\pi m}{\Lambda}x}\,dx \tag{4.9}$$

and $\bar{c}_m$ denotes the complex conjugate of c_m. Since the scalar theory considers only the transmission function, the diffraction efficiency is related to the transmission efficiency defined in Eq. (4.6). The superscript "*trans*" will intentionally be omitted for the rest of the thesis.

4.3.4. Limits of the scalar theory

In the penultimate section, seven assumptions have been established. Among these assumptions, iii. and vi. are less often encountered in microstructure diffractive patterns. If the refractive index changes with position, the first of Maxwell's equations (Gauss'law) can be written as

$$\vec{\nabla}\cdot\varepsilon\vec{E}=\varepsilon\left(\vec{\nabla}\cdot\vec{E}\right)+\vec{E}\cdot\vec{\nabla}\varepsilon=0 \tag{4.10}$$

thus,

$$\vec{\nabla}\cdot\vec{E}=-\vec{E}\cdot\frac{\vec{\nabla}\varepsilon}{\varepsilon}=-\vec{E}\cdot\vec{\nabla}\ln\varepsilon \tag{4.11}$$

Eq. (3.37) no longer applies and shall be replaced by

$$\nabla^2\vec{E}+2\vec{\nabla}\left(\vec{E}\cdot\vec{\nabla}\ln n\right)=\frac{n^2}{c^2}\frac{\partial^2\vec{E}}{\partial t^2} \tag{4.12}$$

This results in a coupling between the components (E_x, E_y, E_z) of the electric field. The problem can be bypassed by first calculating the transmission function and secondly applying the scalar theory [OSh03]. Regarding assumption vi., the scalar theory does not take into account the electromagnetic coupling at the boundaries. Scalar theory is considered to be accurate when the grating period is larger than five times the wavelength, relying on Swanson's sentence [Swa89]:

> *"The scalar theory is, in general, accurate when the grating period is greater than five wavelengths."*

Other authors mention about ten [Kal00, Gre93] or twenty wavelengths [Pom94], depending mainly on the polarization, grating thickness and tolerances. This will be further investigated in the Chap. 4.5. "Extended scalar theory".

4.4. High diffraction efficiency grating

Diffraction gratings are particularly useful if the diffraction efficiency can be controlled. From a given thickness profile $z(x)$ of refractive index $n_g(x)$, immersed in a medium of refractive index n_{ext}, the phase modulation function $\phi(x)$ introduced for a wavelength λ_0 is related to the thickness and the refractive difference of refractive indices:

$$\phi(x)=\frac{2\pi}{\lambda_0}\Delta n(x)\,z(x) \tag{4.13}$$

and the transmission $t(x)$ function is thus expressed as

$$t(x)=\exp\left\{i\,\phi(x)\right\}=\exp\left\{i\,\frac{2\pi}{\lambda_0}\Delta n(x)\,z(x)\right\} \tag{4.14}$$

which does not take into account the reflection and absorption losses. These effects will be ignored in this chapter. From the Fourier theory, if $t(x)$ has a periodicity Λ, it may be established as a sum of oscillating functions

$$t(x)=\sum_{m=-\infty}^{\infty} c_m \exp\left\{-i\,\frac{2\pi}{\Lambda}m\,x\right\} \tag{4.15}$$

with c_m the Fourier coefficients. From Eq. (4.8), the diffraction efficiency is given by the square modulus of the Fourier coefficients. The function $t(x)$ can be thus conceived in order to have the desired diffraction efficiency in every diffraction order. For example, to have a hundred percent diffraction efficiency to the j^{th} order, one fixes

$$\begin{cases} c_j=1 \\ c_m=0 \qquad \text{for } m\neq j \end{cases} \tag{4.16}$$

The phase function optimizing the diffraction efficiency to the first order is thus simply

$$t_{\eta_j=1}(x)=\exp\left\{-i\,\frac{2\pi j}{\Lambda}x\right\} \tag{4.17}$$

At a constant thickness, the modulation of the refractive index allowing for a maximum efficiency at the j^{th} order is

$$\Delta n(x) = j\frac{\lambda_0}{\Lambda}\frac{x}{z}, \tag{4.18}$$

this can be achieved by holographic recording. However high performance will be more easily attained with a constant refractive index and a variable thickness [Pop95]

$$z(x) = j\frac{\lambda_0}{\Lambda}\frac{1}{\Delta n}x \tag{4.19}$$

This metric profile has the shape of a sawtooth grating and is presented in the following section dedicated to blazed grating.

4.4.1. Efficiency-optimized monolayer grating: the blazed grating

Blazed gratings – also called echelette – are diffractive optical elements (DOEs) with a sawtooth profile described by Eq. (4.19), as depicted in Fig. 4.5. Theoretically, they allow for a 100% diffraction efficiency at a given diffraction order, j, for a design wavelength, λ_0.

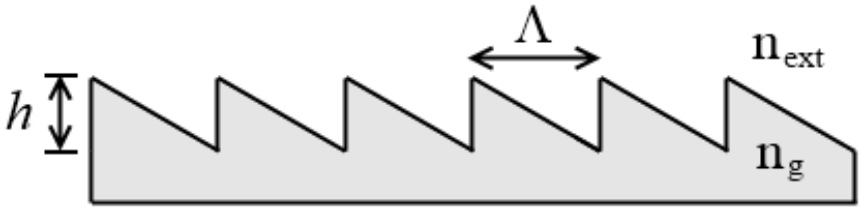

Fig. 4.5: Blazed grating with a thickness h, a period Λ and with a refractive index n_g which is immersed in a material of refractive index n_{ext}

Still following Eq. (4.19), the optimal thickness of the teeth to obtain a 100% diffraction efficiency with λ_0 to the j^{th} order is given by

$$h = z_{max} = z(\Lambda) = j\frac{\lambda_0}{n_g(\lambda_0) - n_{ext}(\lambda_0)} \tag{4.20}$$

which is independent of the period. In this case, on the inner side of the draft facet, the phase modulation is $j2\pi$ and 0 at the outer size, thus ensuring a continuity of the wavefront. While illuminated with another wavelength, the transmission function changes and so does the diffraction efficiency, but to which extent?

The phase delay introduced at the draft facets is calculated as follows:

$$\Delta\phi = ik\left(n_g h - n_{ext} h\right) = i\frac{2\pi}{\lambda} h\left(n_g - n_{ext}\right) \tag{4.21}$$

where $n_g h$ and $n_{ext} h$ are respectively the optical path lengths at the inner and outer side of the diffraction grating. Now let's introduce a parameter which we will regularly use in this chapter: the *design parameter*, α, defined as

$$\alpha(\lambda) = \frac{h}{\lambda}(n_g - n_{ext}) = j\frac{\lambda_0}{\lambda}\frac{n_g(\lambda) - n_{ext}(\lambda)}{n_g(\lambda_0) - n_{ext}(\lambda_0)}. \tag{4.22}$$

It corresponds to the fraction of the 2π phase delay that is introduced by the blazed grating of thickness h and illuminated with a wavelength λ_0: $\Delta\phi = i\,2\pi\alpha$.

Investigating the Fourier transform of the transmission function will allow us to describe quantitatively the drop of diffraction efficiency. Since the transmission function is periodic it can be written in the form of

$$t_{blazed}(x) = \sum_{m=-\infty}^{\infty} c_m \exp\left\{i\frac{2\pi}{\Lambda}x\right\} \tag{4.23}$$

where

$$c_m = \frac{1}{\Lambda}\int_0^{\Lambda} \exp\left\{i\frac{2\pi}{\lambda}(n_g - n_{ext})\,z(x)\right\}\exp\left\{i\frac{2\pi}{\Lambda}m\,x\right\}dx. \tag{4.24}$$

Introducing the blazed profile given by Eq. (4.19) in (4.24) we obtain

$$c_m = \frac{1}{\Lambda}\int_0^{\Lambda} \exp\left\{i\frac{2\pi}{\lambda}(n_g - n_{ext})\,h\frac{x}{\Lambda}\right\}\exp\left\{-i\frac{2\pi}{\Lambda}m\,x\right\}dx \tag{4.25}$$

Using the design parameter α, defined in Eq. (4.22), the c_m coefficients equation becomes

$$c_m = \frac{1}{\Lambda}\int_0^{\Lambda} \exp\left\{i\frac{2\pi}{\Lambda}x\left(\alpha - m\right)\right\}dx. \tag{4.26}$$

The resolution of this integral provides as solution

$$c_m = \frac{1}{\Lambda}\left[\frac{\exp\left\{i\frac{2\pi}{\Lambda}x\left(\alpha-m\right)\right\}}{i\frac{2\pi}{\Lambda}\left(\alpha-m\right)}\right]_0^{\Lambda}. \tag{4.27}$$

Taking the interval into account, this takes the form of

$$c_m = \frac{\exp\left\{i\,2\pi\left(\alpha-m\right)\right\}-1}{i\,2\pi\left(\alpha-m\right)}. \tag{4.28}$$

The diffraction efficiency may be now calculated as follows

$$\eta_m = c_m \bar{c}_m = \frac{2-2\cos\left\{2\pi\left(\alpha-m\right)\right\}}{\left[2\pi\left(\alpha-m\right)\right]^2} \tag{4.29}$$

$$\eta_m = \frac{2-2\left[1-2\sin^2\left\{\pi\left(\alpha-m\right)\right\}\right]}{\left[2\pi\left(\alpha-m\right)\right]^2} \tag{4.30}$$

$$\eta_m = \frac{4\sin^2\left\{\pi\left(\alpha-m\right)\right\}}{4\left[\pi\left(\alpha-m\right)\right]^2}. \tag{4.31}$$

Finally, the diffraction efficiency is simply expressed in the form of

$$\eta_m = \mathrm{sinc}^2\left(\alpha-m\right) \tag{4.32}$$

with *sinc*, the cardinal sine function. This function is comprised between 0 and 1 and equals 1 only if α equals m as depicted in Fig. 4.6. The meaning of the *design parameter,* α, becomes clear: the maximum efficiency to the m^{th} order is achieved when $\alpha=m$.

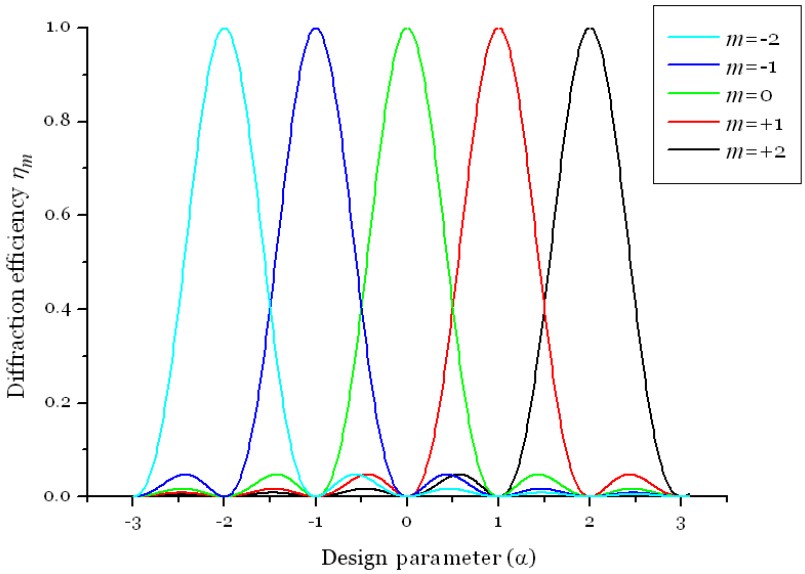

Fig. 4.6: Diffraction efficiency for orders -2 to +2 as a function of the design parameter.

One may erroneously think that choosing the first order of diffraction or any higher order results to the same diffraction efficiency. This is true for the design wavelength, but for wavelength other than λ_0, the drop of diffraction efficiency is faster in higher diffraction orders than for the first order. Indeed, the higher the diffraction order, the higher the optical path difference at the draft facet for a small variation of the wavelength. For instance, two gratings immersed in the air and optimized for the same wavelength λ_0 but designed for j=1 and j=2 (i.e. the gratings have been optimized for the first and second order of diffraction) have as efficiency equations Eq. (4.33) and Eq. (4.34) respectively.

$$\eta_1(\lambda)=\mathrm{sinc}^2\left(\frac{\lambda_0}{\lambda}\frac{n(\lambda)-1}{n(\lambda_0)-1}-1\right) \tag{4.33}$$

$$\eta_2(\lambda)=\mathrm{sinc}^2\left(2\frac{\lambda_0}{\lambda}\frac{n(\lambda)-1}{n(\lambda_0)-1}-2\right) \tag{4.34}$$

These equations have been plotted in Fig. 4.7 for two blazed gratings made of PMMA optimized for λ_0=550 nm at the first and second orders with a thickness of 1.1 µm and 2.2 µm respectively.

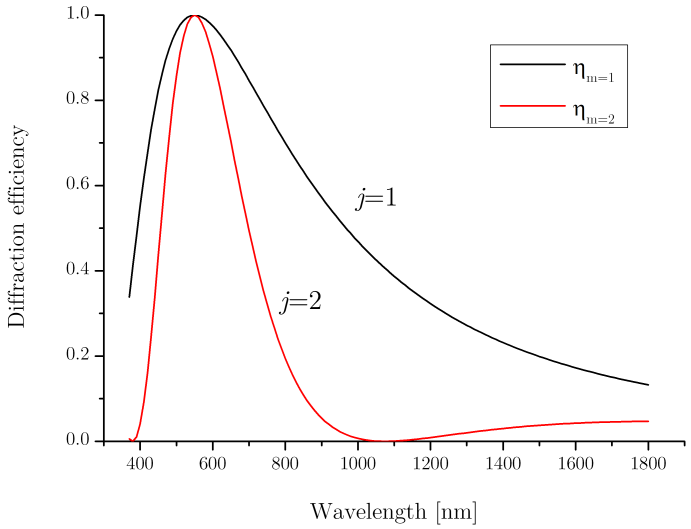

Fig. 4.7: Comparison of the diffraction efficiencies for two blazed gratings of PMMA immersed into the air and optimized for the first (j=1) and the second (j=2) order of diffraction.

Due to the principle of energy conservation, the energy that is not diffracted in the 1st order is diffracted in spurious diffraction orders. Wavelengths shorter than λ_0 will be diffracted preferentially in higher orders of diffraction. For example, with a constant refractive index, all the light at $\lambda_0/2$ will be diffracted in the second order. Conversely, higher wavelengths will be diffracted in lower diffraction orders. This is illustrated in Fig. 4.8 for a blazed grating made of PMMA, with λ_0=550 nm optimized for the first diffraction order.

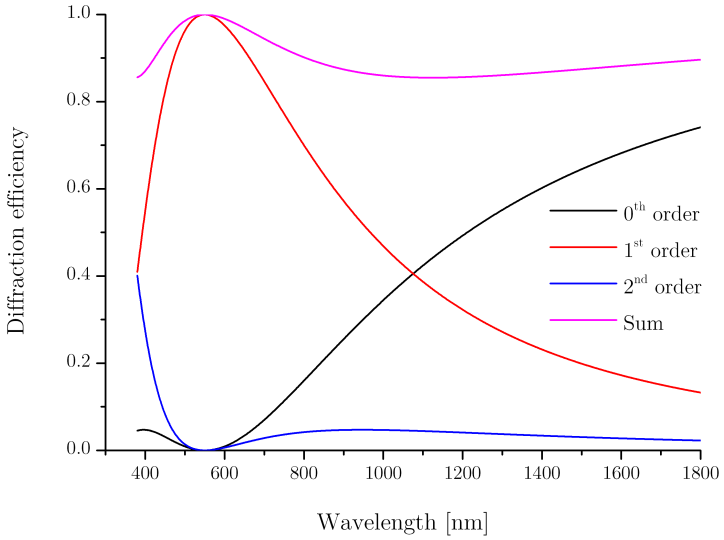

Fig. 4.8: Diffraction efficiency for a blazed grating made of PMMA and optimized for λ_0=550 nm. The diffraction efficiency of the 0th, 1st and 2nd order are shown as well as the sum of the efficiencies in these three orders.

4.4.2. Multilayer blazed grating

The main issue of blazed diffraction gratings resides in the strong sensitivity of the diffraction efficiency to the wavelength, especially for diffraction orders other than 1. To get broadband high diffraction efficiency, it is preferable to maximize the first diffraction order.

The strong wavelength dependence comes from the first term of the cardinal sine in Eq. (4.32), α, the design parameter. It shows a decreasing dependence with the wavelength due to the presence of λ in the denominator. When the grating is immersed in the air (i.e. n_{ext}=1) this is even reinforced by the behaviour of n_g, which decreases when λ increases.

$$\eta_1(\lambda)=\mathrm{sinc}^2(\alpha-1)=\mathrm{sinc}^2\left(\frac{n_g(\lambda)-n_{ext}(\lambda)}{\lambda}h-1\right) \tag{4.35}$$

However it is has to be pointed out that a blazed grating may be conceived with more than one layer. In this case, the design parameter consists in the sum of each sublayer design parameter

$$\alpha=\sum_i \alpha_i=\sum_i \frac{\left[n_i(\lambda)-n_{i+1}(\lambda)\right]h_i}{\lambda} \tag{4.36}$$

where n_i must be always taken from the same side as the draft facet. For example, the design parameter corresponding to Fig. 4.9 is

$$\alpha = \frac{n_0(\lambda) - n_1(\lambda)}{\lambda} h_1 + \frac{n_2(\lambda) - n_0(\lambda)}{\lambda} h_2 \,, \tag{4.37}$$

and <u>not</u> $\frac{n_0(\lambda) - n_1(\lambda)}{\lambda} h_1 + \frac{n_0(\lambda) - n_2(\lambda)}{\lambda} h_2$.

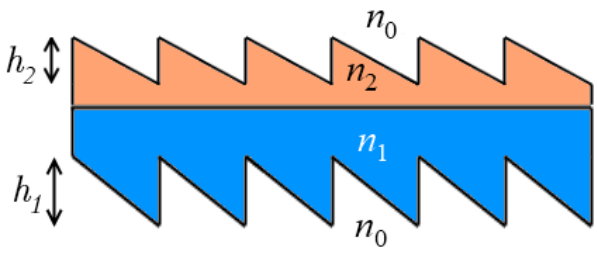

Fig. 4.9: Example of equivalent bilayer diffractive grating

This equation is also valid for the three diffraction gratings presented in Fig. 4.10

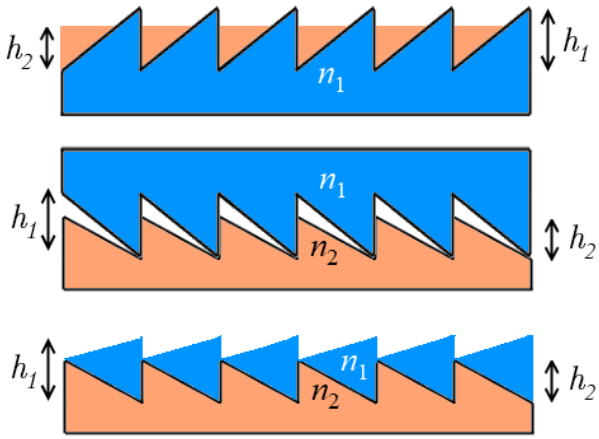

Fig. 4.10: Three diffraction gratings equivalent to the diffraction grating depicted in Fig. 4.9

If we now consider the surrounding medium as air, i.e. n_0=1, we may benefit from two parameters (h_1 and h_2) to maximize the diffraction efficiency to the first order (i.e. α must be equal to 1) for two selected wavelengths. The system to be resolved is thus

$$\begin{cases} \alpha(\lambda_1) = 1 = \dfrac{n_1(\lambda_1) - 1}{\lambda_1} h_1 + \dfrac{n_2(\lambda_1) - 1}{\lambda_1} h_2 \\ \alpha(\lambda_2) = 1 = \dfrac{n_1(\lambda_2) - 1}{\lambda_2} h_1 + \dfrac{n_2(\lambda_2) - 1}{\lambda_2} h_2 \end{cases} \tag{4.38}$$

and the calculation of the thicknesses fulfilling this system leads to

$$\begin{cases} h_1 = \dfrac{\lambda_1 n_{22}^* - \lambda_2 n_{21}^*}{n_{11}^* n_{22}^* - n_{12}^* n_{21}^*} \\ h_2 = \dfrac{\lambda_2 n_{11}^* - \lambda_1 n_{12}^*}{n_{11}^* n_{22}^* - n_{12}^* n_{21}^*} \end{cases} \tag{4.39}$$

where we made use of the following notation

$$n_{ij}^* \overset{\text{def}}{=} n_i(\lambda_j) - 1 \tag{4.40}$$

For wavelengths λ_1 and λ_2, the diffraction efficiency is maximum, elsewhere diffraction efficiency drops but could easily remain above 97% in the visible region. Kleemann *et al.* [Kle08] shown that, in a certain approximation (that is the dispersion curve obeying a second order Cauchy series[6]), the diffraction efficiency is independent on the materials used (see Appendix III.4). More precisely, both medium have a refractive index obeying

$$n_i(\lambda) = A_i + \frac{B_i}{\lambda^2} \tag{4.41}$$

whatever the values of A_i and B_i, the design parameter depends only on the design wavelengths λ_1 and λ_2 and the illumination wavelength λ:

$$\alpha(\lambda) = \frac{\lambda_1^3 \lambda^2 - \lambda_2^3 \lambda^2 + (\lambda_2 - \lambda_1)\lambda_2^2 \lambda_1^2}{\lambda^3 (\lambda_1^2 - \lambda_2^2)}, \tag{4.42}$$

what Kleeman *et al.* call the *generic case*. In the figure below, the diffraction efficiency for this generic case optimized for λ_1=405 and λ_2=650 nm is shown (which are typical values to reach a diffraction efficiency higher than 90% over the full visible spectrum). Fig. 4.11 compares the generic case with a bilayer optimized for the same wavelengths but made of PC and PMMA, and compares it also with a monolayer made of PMMA optimized for 550 nm.

6 We recall the inaccuracy on the refractive index of 10^{-2} to 10^{-3} in this approximation (see Chap. 2.4.)

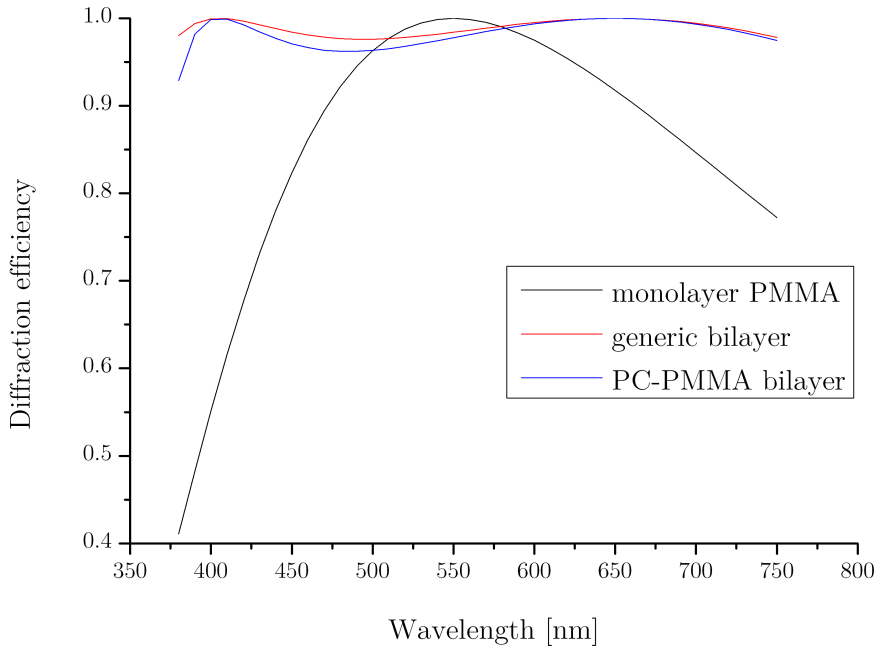

Fig. 4.11: Diffraction efficiency at first order for a monolayer made of PMMA, a bilayer made of PC and PMMA and the generic case. Both bilayers have been optimized for λ_1=405 nm et λ_2=650 nm

We observe that the generic case and the realistic case are in good agreement despite that the refractive indices where approximated by a second order Cauchy series. But most importantly, we observe that the diffraction efficiency remains higher than 92% in the visible region. The thicknesses used for the second bilayer grating are 16.3 µm for the PMMA and 13.1 µm for the PC. These values were calculated using Eq. (4.39).

Strictly speaking, Eq. (4.39) provides as solutions 16.3 µm for the PMMA layer and -13.1 µm for the PC layer, meaning that the PC layer is inverted compared to the PMMA layer (see Fig. 4.12).

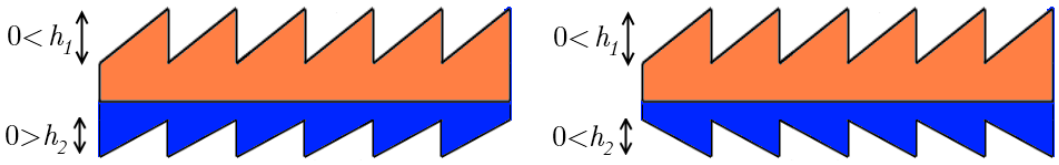

Fig. 4.12: Meaning of a negative layer thickness

Let's take a more detailed look at the contribution of each layer of the bilayer presented in the left part of Fig. 4.12. If the top layer is made of PMMA with a thickness of 16.3 µm, then the diffraction efficiency under normal incidence presented in Fig. 4.14 (page 105) goes mainly in the 12th order of diffraction for the design wavelength λ_2=650 nm. With a thickness of -13.1 µm the PC diffracts mainly in the -11th order. Thus, on the whole, the energy is diffracted to the first

diffraction order. Neglecting the diffraction angle due to the PMMA and the Fresnel losses at the PMMA/PC interface one may erroneously deduce that the diffraction efficiency may be determined by the convolution of the diffraction efficiency of each layer. So that the diffraction efficiency to the first order should be around 0.954 × 0.955 = 91.1%, using only the combination of order 12 with order -11. *But a bilayer diffraction grating could not be considered as two diffraction gratings in series.* The total phase modulation is given by the sum of the individual phase modulations

$$\phi_{tot}(x)=\phi_{PMMA}(x)+\phi_{PC}(x) \tag{4.43}$$

and the transmission function is

$$t(x)=\exp\left[i\,\phi_{tot}(x)\right]=\exp\left[\phi_{PMMA}(x)\right].\exp\left[\phi_{PC}(x)\right] \tag{4.44}$$

Thus, the Fourier coefficients obtained with the Fourier transform can be also obtained with the convolution of the Fourier coefficients of each layer:

$$\mathscr{F}\left\{t(x)\right\}=\mathscr{F}\left\{t_{PMMA}(x).t_{PC}(x)\right\}=\mathscr{F}\left\{t_{PMMA}(x)\right\}\otimes\mathscr{F}\left\{t_{PC}(x)\right\}. \tag{4.45}$$

This has been graphically represented in Fig. 4.14.

The use of more than two layers would of course lead to a higher number of diffraction maxima. In the following example, we calculated the thickness of a trilayer made of PMMA, PC and BK7 to achieve 100% of diffraction efficiency for wavelengths 400, 535 and 1050 nm. The system to be solved with units in nm is

$$\begin{cases} 400=h_{PMMA}\,n^{*}_{PMMA}(400)+h_{PC}\,n^{*}_{PC}(400)+h_{BK7}\,n^{*}_{BK7}(400) \\ 535=h_{PMMA}\,n^{*}_{PMMA}(400)+h_{PC}\,n^{*}_{PC}(400)+h_{BK7}\,n^{*}_{BK7}(400) \\ 1050=h_{PMMA}\,n^{*}_{PMMA}(1050)+h_{PC}\,n^{*}_{PC}(1050)+h_{BK7}\,n^{*}_{BK7}(1050) \end{cases} \tag{4.46}$$

where the notation $n^{*}(\lambda)\overset{\text{def}}{=}n(\lambda)-1$ has been used. With this wavelengths selection, a diffraction efficiency higher than 95% can be achieved from 390 nm to 1220 nm as depicted in Fig. 4.13. The thickness of the teeth for PMMA, PC and BK7 reaches 330 µm, -44 µm and -266 µm respectively...

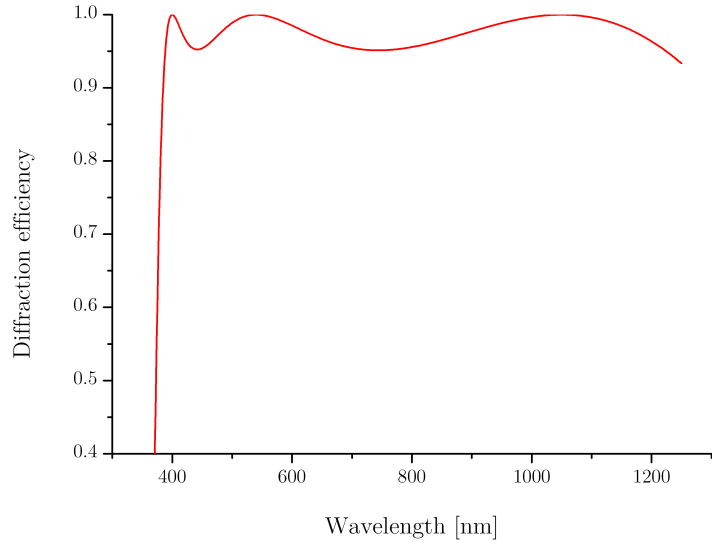

Fig. 4.13: Diffraction efficiency for a trilayer made of PMMA, PC and BK7 optimized for 400, 535 and 1050 nm.

So, the higher the number of layers, the higher the thickness of the diffractive structure which becomes very high compared with the period causing manufacturing difficulties and shading effects that are not taken into account in scalar theory. However, this affects the diffraction, hence the need of an extended scalar theory to take shading effects into account.

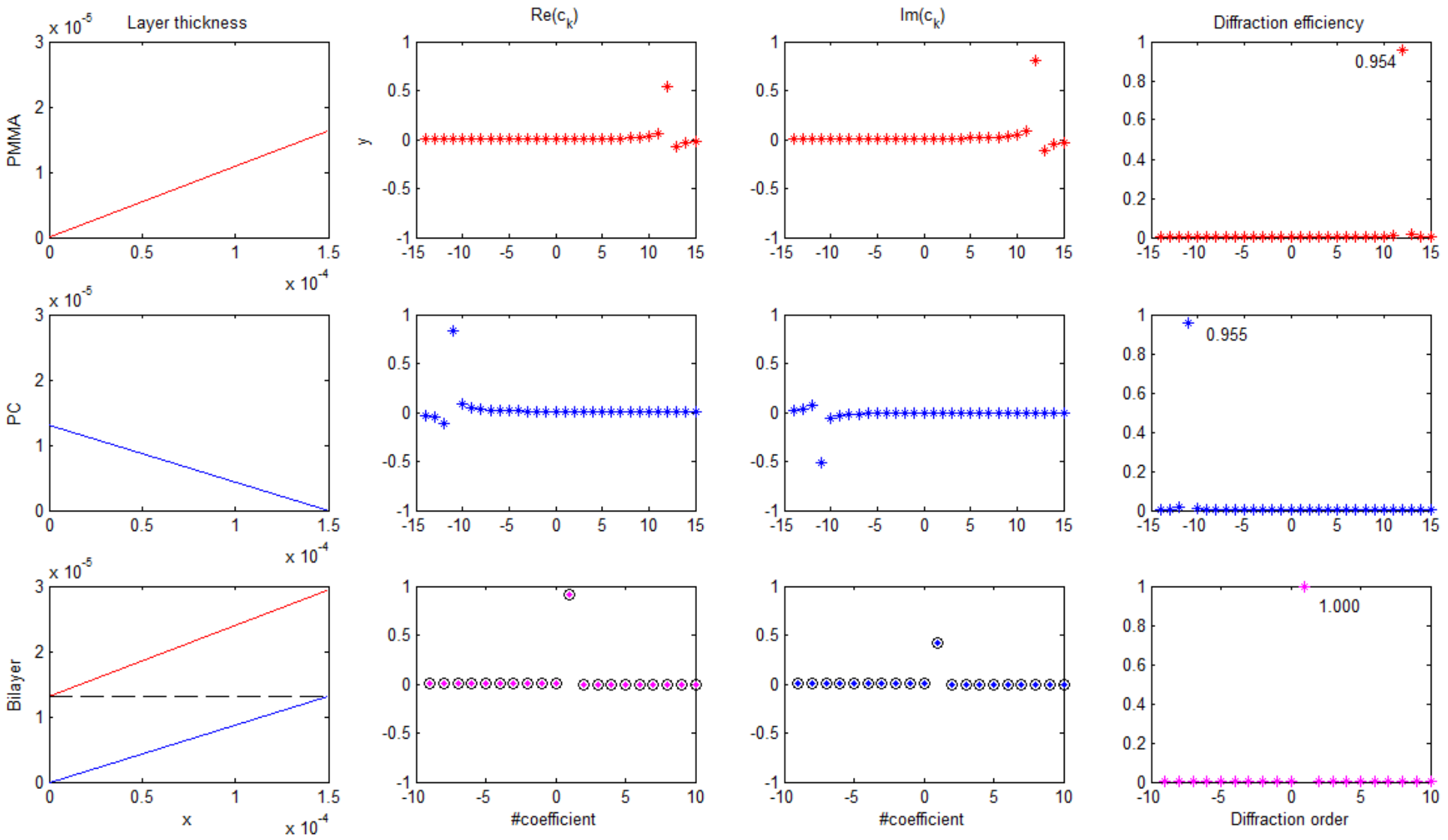

Fig. 4.14: Profile, real and imaginary part of the Fourier coefficients and diffraction efficiency for the PMMA layer, the PC layer and the bilayer (at the design wavelength, λ_2=650 nm). The Fourier coefficients of the bilayer were obtained by Fourier series of the bilayer (dots) and by convolution of the Fourier coefficients of the PMMA with the PC (circles).

4.5. Extended scalar theory

Simulations performed with rigorous theories are time consuming, which is a major inconvenient. On the other hand, as will be shown, the scalar theory is only valid for high period-to-wavelength ratios. Between the time consuming rigorous methods and the hardly simplified scalar theory, an intermediate theory fills the gap: the extended scalar theory.

Besides the scalar theory, only the transmitted phase has been investigated independently of the polarization state: the grating was considered as infinitely thin and the reflections occurring at every interface were not considered. A first simple improvement would consist in taking into account the Fresnel reflections at each interface (see Chap. 2.4.). A second improvement can be achieved taking into account the shading caused by the thickness of the teeth [Lal99, Lev04, Wan08]. This improved scalar theory is known as the extended scalar theory, brought to light by Swanson [Swa91].

When light is coming from the textured side of a blazed grating (see Fig. 4.15), a certain amount will be refracted towards the draft facet and will therefore be lost.

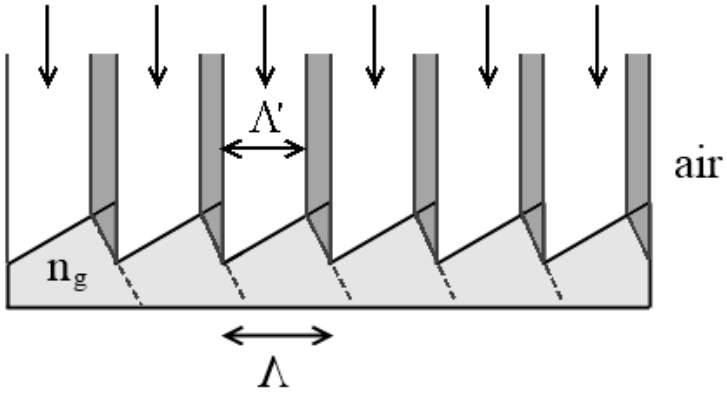

Fig. 4.15: shading for light coming from the teeth side

It is shown in Appendix III.5.1a that the active part of the period, Λ', may be approximated by [Lal99]

$$\frac{\Lambda'}{\Lambda} \simeq 1 - \left[\frac{\lambda^2}{\Lambda^2} \frac{1}{n_g\left(n_g - 1\right)} \right]. \tag{4.47}$$

We have also determined an exact value of the shading effect in Appendix III.5.1b:

$$\frac{W_0}{\Lambda}=1-\left[\frac{\lambda^2}{\Lambda^2}\frac{1}{n_g(n_g-1)}\frac{1}{\sqrt{1-\left(\frac{\lambda}{n_g\Lambda}\right)^2}+\left(\frac{\lambda^2}{\Lambda^2}\frac{1}{n_g(n_g-1)}\right)}\right]. \tag{4.48}$$

If the light comes from the substrate side, as shown in Fig. 4.16, a void appears between two neighbouring teeth [Lev04]. This reduces the diffraction effect and therefore the diffraction efficiency, like shading does [Hes98]. In this case, we demonstrate in Appendix III.5.2 that the active period to period ratio is

$$\frac{\Lambda'}{\Lambda}=1-\left[\frac{(m\lambda_0)^2}{(n_g-1)\Lambda^2}\frac{1}{\sqrt{1+\left(\frac{m\lambda_0}{\Lambda}\right)^2}}\right]. \tag{4.49}$$

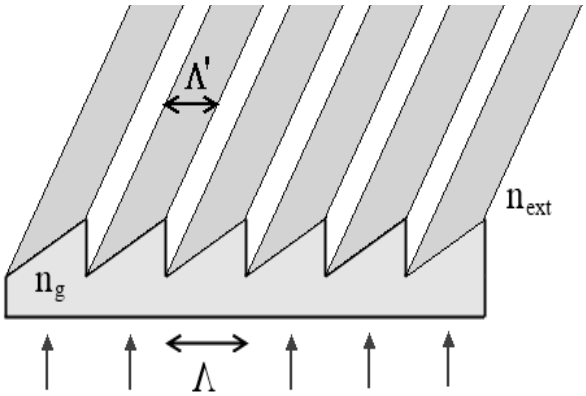

Fig. 4.16: Presence of a void between two adjacent teeth when light is coming from the flat side

Once the shading effect known, the diffraction efficiency in the extended scalar theory (EST) compared to the scalar theory (ST) becomes $\eta_{EST}=\eta_{ST}\ \Lambda'/\Lambda$. However, this equation is valid for a theoretical blazed grating with a *perfectly* linear slope. A real grating can be approximated by a multilevel staircase blazed gratings. Therefore, the sum of the shadows at each stair equals the shadow produced by the draft facet [Swa91, OSh03]. An example for a four-level blazed grating is depicted in Fig. 4.17. Whatever the number of levels, the total shading due to the stairs is equivalent to the shading produced by the draft facet. Therefore, the diffraction efficiency becomes

$$\eta_{EST}=\eta_{ST}\left(\frac{\Lambda'}{\Lambda}\right)^2 \tag{4.50}$$

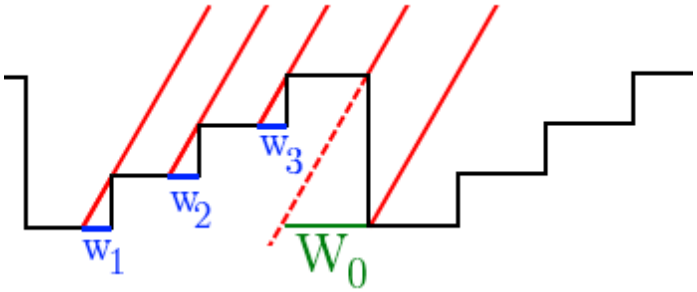

Fig. 4.17: The total shading due to the three stairs is equivalent to the void between two periods: $w_1+w_2+w_3=W_0$

In order to observe the improvement brought by the EST, Fig. 4.18 compares the diffraction efficiency at the design wavelength as a function of the period-to-wavelength ratio obtained by

- the scalar theory including Fresnel reflections,
- the extended scalar theory including Fresnel reflections,
- two different software tools based on a rigorous theory (RCWA and PCGrate).

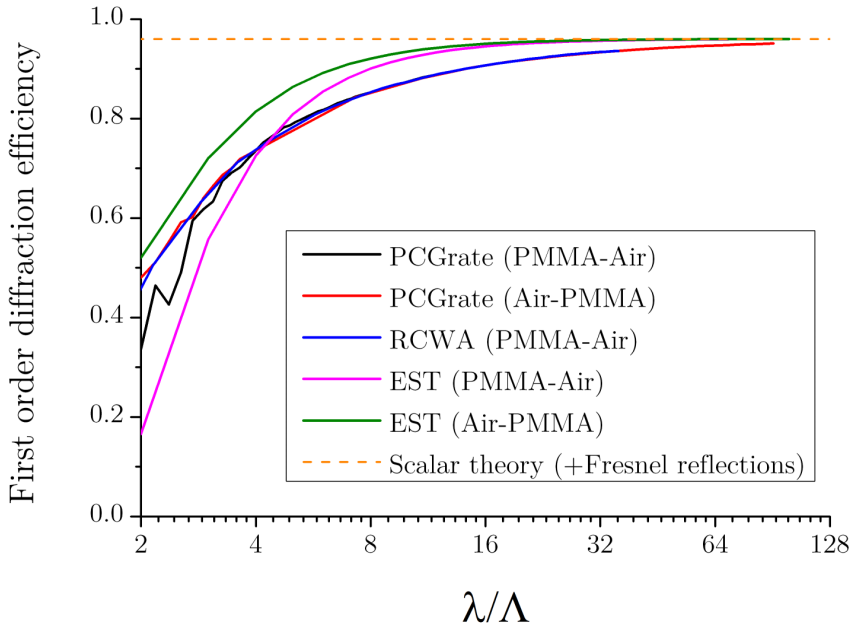

Fig. 4.18: Comparison of diffraction efficiency curves get by scalar theory, extended scalar theory and rigorous theories

It is worth noting that the results of EST fill the gap between the scalar theory results and those obtained with rigorous theories without managing to reproduce the same results. Sandfuchs *et al.* [San06] explain that the quadratic dependence of the λ–to-Λ ratio has to be challenged. And, as far as we know, the limits of the EST have been reached.

Fig. 4.18 shows why the scalar theory is considered to be accurate if the period of the grating is greater than 10 wavelengths. However it is of high importance to notice that this assumption only concerns monolayers designed for the first diffraction order. Blazed gratings designed for a higher order m have higher shading, m times higher in first approximation. The case of bilayers is more complex since it depends on the two design wavelengths. However we can deduce an order of magnitude for the domain of validity of the scalar theory for bilayers, considering that layers are about 10 times thicker than monolayer. The period of the grating should therefore be 10 times larger than for monolayers, i.e. the period should be greater than 100 times the wavelength. This assumption is in good accordance with rigorous calculations depicted in Fig. 4.19.

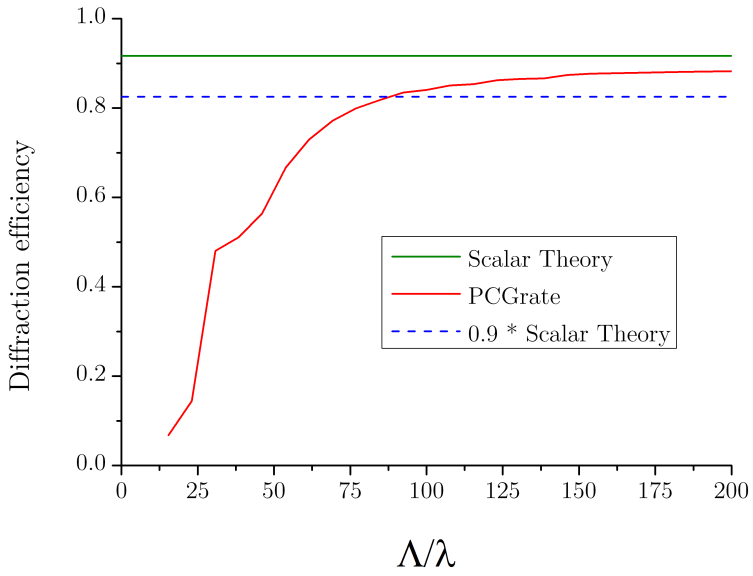

Fig. 4.19: Diffraction efficiency evolution with period-to-wavelength ratio for a bilayer made of PMMA (16.3 µm thick) and PC (13.1 µm thick)

Let's finish this section with a last improvement achieved by the EST regarding the ideal thickness of blazed gratings. We can actually show (Appendix III.5.3) that the grating thickness h, so far considered as equal to $\lambda_0/(n-1)$, is in fact dependent on the grating period [Swa91]:

$$h_{EST} = \frac{\lambda}{n_g - \sqrt{1-\left(\frac{\lambda}{\Lambda}\right)^2}}. \tag{4.51}$$

Obviously, in the limit of the period going to infinity, one finds the well-known value of the scalar theory.

4.6. Some practical additional investigations on blazed gratings

4.6.1. Tip radius influence on the blazed gratings efficiency

As discussed earlier for refractive Fresnel lenses, blazed gratings also suffer from manufacturing errors. While the draft angle should be around two degrees for a refractive lens (with a thickness of a few hundred microns), the draft angle of diffractive lenses (a few microns thick) may be decreased under 0.5° since the draft facet in contact with the mould is so small that it does not hinder the ejection. And, as far as we know, no specific optimization can be performed to reduce the losses induced by the draft angle itself. Regarding the peaks and valleys, they do decrease the diffraction efficiency but not in the same way as they reduce the optical efficiency for refractive teeth. Indeed, the diffraction efficiency is governed by the coefficients of the Fourier transform and not by the "ideal active design". A common cutting tool to manufacture blazed gratings and Fresnel lenses is made of a planar edge and circular edge, called half-radius tool. It is illustrated with a photograph in Fig. 4.20. This tool is used instead of a V-tool (tool presenting a V-shape with a nose radius smaller than 250 nm) to reduce the machining time: with an half radius, more matter is cut per second.

Fig. 4.20: half-radius (R=55µm) tool

The consequence of the use of a half-radius tool is a non-ideal profile of the blazed grating, which has the same form as presented in Fig. 4.21.

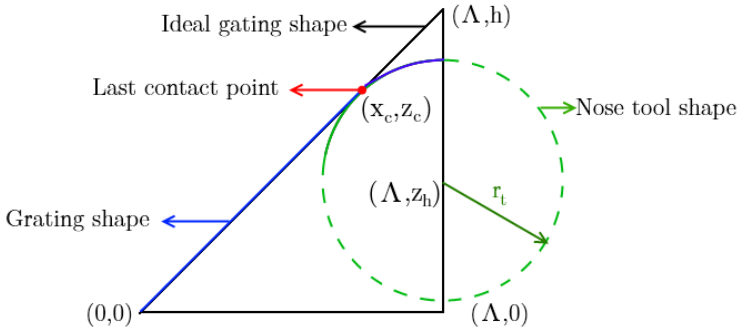

Fig. 4.21: non-ideal blaze grating shape due to the use of a half-radius tool

The contact point (x_c,z_c) between the profile of the diffraction grating and the cutting tool takes place where the tangents are equal. Using the geometry presented in Fig. 4.21, the equation of circle representing the tool edge is

$$\left(z_t(x)-z_h\right)^2=r_t^2-(x-\Lambda)^2 \tag{4.52}$$

where the subscript t refers to the tool. The tangent equation is obtained by derivation of Eq. (4.52)

$$\frac{dz_t}{dx}=\tan_t(x)=+\frac{\Lambda-x}{\sqrt{r_t^2-(x-\Lambda)^2}} \tag{4.53}$$

Thus the condition allowing to find x_c, the last contact point abscissa, is

$$\frac{h}{\Lambda}=\frac{\Lambda-x}{\sqrt{r_t^2-(x-\Lambda)^2}} \tag{4.54}$$

which leads to

$$\begin{cases} x_c=\Lambda-\dfrac{r_t h^2}{\Lambda^2+h^2} \\ z_c=\dfrac{h}{\Lambda}x_c \end{cases} \tag{4.55}$$

Thus, the Fourier series coefficients of this profile illuminated with λ_0 are

$$c_m(\text{non ideal})=\frac{1}{\Lambda}\left\{\int_0^{x_c} e^{i\frac{2\pi}{\Lambda}x}e^{-i\frac{2\pi}{\Lambda}mx}+\int_{x_c}^{\Lambda} e^{i\frac{2\pi}{\lambda_0}z(x)}e^{-i\frac{2\pi}{\Lambda}mx}\right\}dx \tag{4.56}$$

still with a slope h/Λ (and h given by Eq. (4.20) with j=1) before the contact point, and after this point, $z(x)$ is a function of the circle segment centred on (Λ, z_h)

$$z(x) = z_h + \sqrt{r_t^2 - (x-\Lambda)^2} \tag{4.57}$$

with

$$z_h = z_c - \sqrt{r_t^2 - (x_c - \Lambda)^2} \tag{4.58}$$

With this profile the thickness error occurring at the draft facet is

$$\Delta h = h - (z_h + r) \tag{4.59}$$

This profile avoids discontinuity along a single tooth but – contrary to the ideal profile – the thickness error (see Fig. 4.22) introduces a phase discontinuity between two adjacent teeth. Consequently, higher diffraction orders appear.

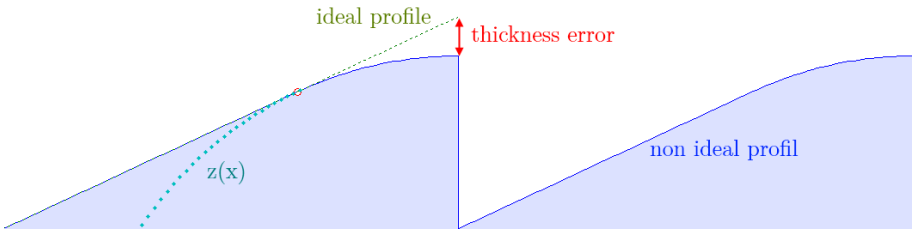

Fig. 4.22: Shape error introducing a phase-shift error between two adjacent teeth

Still using the same half-radius tool, the profile can be optimized to enhance the first diffraction order efficiency. Cutting more deeply along the draft facet would decrease the concordance with the ideal profile but will reduce the phase-shift between two adjacent zones. So the first optimisation makes the profile take a shape as presented in Fig. 4.23. Regarding the Fourier coefficients equation, Eq. (4.56) still applies by changing x_c and z_h in Eq. (4.57).

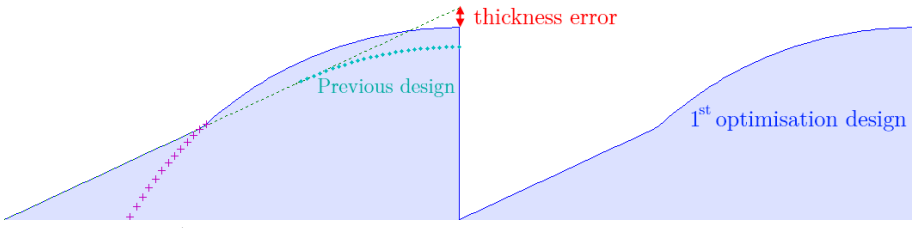

Fig. 4.23: 1st optimisation process. Reduction of the thickness error with deeper etching.

A last optimisation may be performed since the first optimisation is limited by the discontinuity introduced between the curved and the flat shape. Increasing the

slope of the grating allows decreasing this discontinuity and thus a deeper penetration of the tool along the draft facet, which decreases the thickness error and enhances the diffraction efficiency.

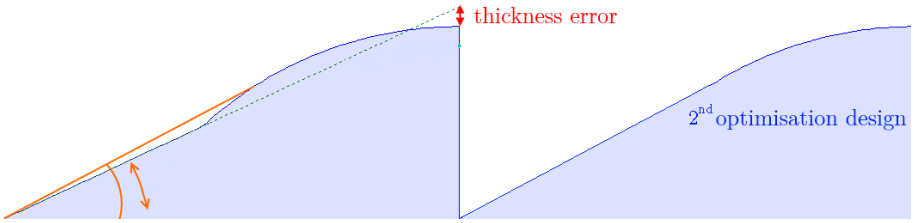

Fig. 4.24: 2nd optimisation process. Both the deepness of the tool and the grating slope are optimized

The four profiles immersed in the air have been compared, using a design wavelength λ_0=550 nm, a refractive index of 1.494 and a period of 20 µm. The radius of the half-radius tool is 150 µm, the diffraction efficiency has been calculated for 550 nm using the scalar theory. All results are graphically presented in Fig. 4.25 on page 115, and are summarized in Table 4.1.

Table 4.1 Comparison of four kinds of blazed gratings

Grating	Thickness	Concordance with ideal grating [%]	Slope	Grating efficiency for first order
Ideal (h=λ_0/0.494)	1.11 µm	100	h/Λ	1.000
Non optimized	0.88 µm	60	h/Λ	0.898
1st optimisation	0.94 µm	38	h/Λ	0.924
2nd optimisation	0.96 µm	0	1.099 h/Λ	0.929

Since Eq. (4.56) exhibits a dependence on the refractive index, on the period, on the thickness, on the illumination wavelength and on the tool radius, no direct solution of the ideal profile may be proposed. The gain obtained in the above example is only 3%. The gain would be even lower with a larger period or thinner tools. But it is interesting to point out that, contrary to refractive Fresnel lenses, the concordance with the ideal grating is not that important for the diffraction efficiency.

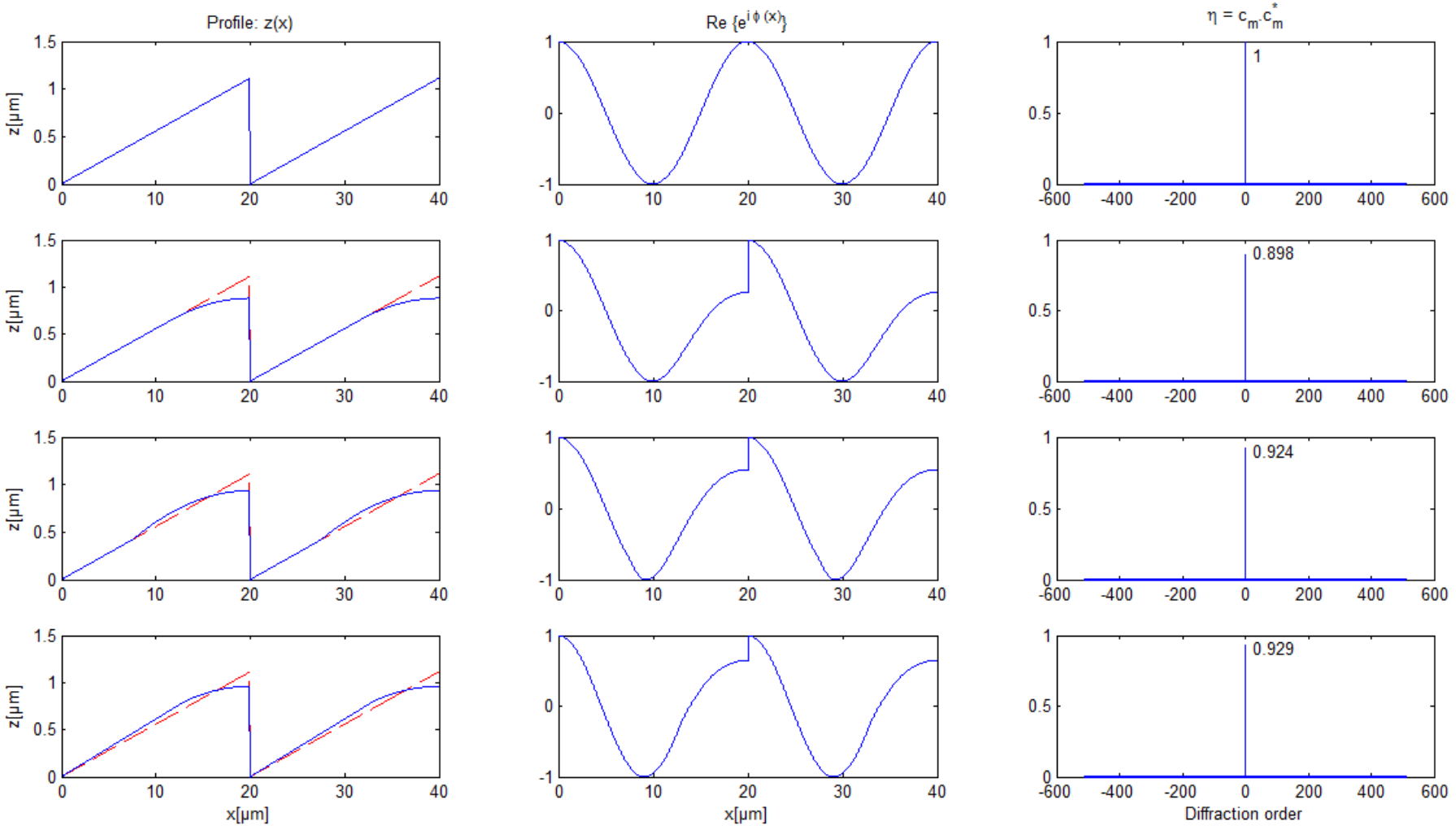

Fig. 4.25: Optimisation of a blazed profile. Column 1 contains the blazed profiles, Column 2 is the real part of the transmission function and Column 3 shows the diffraction efficiencies (the peaks correspond to the first order). Line 1 is the ideal profile, Line 2 is the curved profile without optimisation, Line 3 shows the profile with optimisation of the deepness of the tool and on Line 4 both the slope and deepness of the profile have been optimized. Each profile has a period of 20 µm, a refractive index of 1.494, is illuminated with a wavelength of 550 nm and the radius of the half-radius is 150 µm.

4.6.2. Non-null incidence

So far, only the normal incidence has been considered. The introduction of a non-null incidence angle makes the calculations a little more complex but, mostly, period dependent. Moreover, because of the asymmetry of the blazed grating, two angles with the same absolute value but of opposite signs will not affect the efficiency in the same way. We will consider a positive angle inside the grating if the diffracted beam remains on the same side of the grating normal.

Let's examine the evolution of the diffraction efficiency for a blazed grating designed for normal incidence but illuminated with an incidence angle. The effective thickness for the positive case h^+ is given

$$h^+ = \frac{h}{\cos\left(\theta_1^+\right)} \tag{4.60}$$

with θ_1^+, the incoming angle *inside the grating* (see Fig. 4.26).

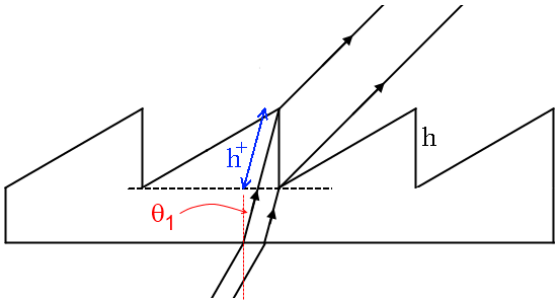

Fig. 4.26: Effective thickness for positive incoming angles

Hence, the diffraction efficiency becomes

$$\eta\left(\theta_1^+\right) = \mathrm{sinc}^2\left(\frac{1}{\cos\theta_1^+} - 1\right) \tag{4.61}$$

For the negative case (Fig. 4.27), the determination of h^- is not straightforward since it depends on the period of the grating. In a first approximation it is similar to h^+ while being smaller than h^+.

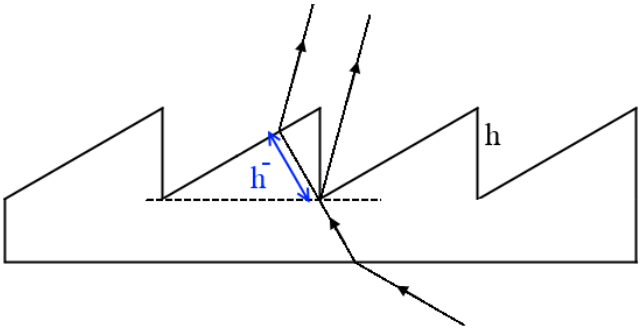

Fig. 4.27: Effective thickness for negative incoming angle

The figure below shows the evolution of the relative diffraction efficiency as a function of the incoming angle for a period of 150 µm and a wavelength of 550 nm. It compares Eq. (4.61) with a rigorous theory for a monolayer. The case of the bilayer was also calculated with the rigorous theory used in PCGrate; the bilayer simulated is the same as already used before (see Fig. 4.11).

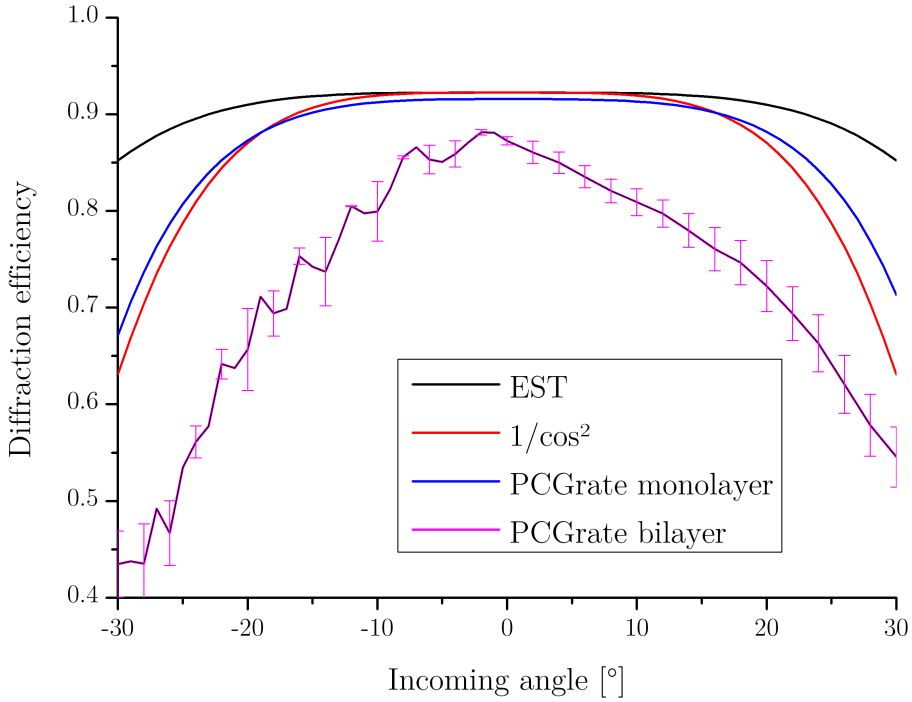

Fig. 4.28: Diffraction efficiency as a function of the incoming angle (inside the grating for monolayers and outside, i.e. in air, for the bilayer)

The EST is not that accurate for angles higher than 10°, and – for an unknown reason – if we use the square of the cosine in Eq. (4.61), we find a curve in much better accordance with the rigorous calculations. Due to a lower period-to-global thickness ratio and higher Fresnel losses, the bilayer has a lower diffraction efficiency.

The bilayer simulated corresponds to Fig. 4.9, which explains the oscillations that appear for the negative incoming angles.

If for some reason, one wishes to optimize the blazed grating for a certain incidence angle θ_i, we show in Appendix III.5.4 that the optimized thickness $h(\theta_i)$ is

$$h(\theta_i)=\frac{\lambda}{n_g\sqrt{1-\sin^2\theta_i}-\sqrt{1-\left(\frac{\lambda}{\Lambda}+n_g\sin\theta_i\right)^2}}. \tag{4.62}$$

From this sub-chapter we may conclude that the EST provides good results for monolayers in the range of -10° to 10° of incidence. In this condition, the diffraction efficiency drops to less than one percent. For the bilayer investigated, the relative drop is less than 10% between -10° and 10°, and less than 5% between -5° and 5° of incidence.

4.6.3. Draft angle

Due to the draft angle imposed for the mould ejection during the manufacturing process, it is impossible to achieve 100% diffraction efficiency under normal incidence. The question that arises is the following: should the draft angle modify preferably the period, the thickness or the slope (see Fig. 4.29)?

Modifying the period changes the diffraction angle without optimizing the diffraction efficiency, and this option has to be rejected.

Fig. 4.29: Draft angle implementation. Left: period modification. Middle: thickness modification. Right: slope modification

Among the two remaining solutions, we observe that the shape of the grating with a modified slope is the same as solution 2 (with a constant slope but a modified thickness) plus an error on the shape. To quantify the loss of diffraction efficiency we calculated the scalar diffraction efficiency for the second and third modified designs at 650 nm for a monolayer made of PMMA and a bilayer made of PMMA and PC. The monolayer was optimized for 650 nm and the bilayer for 405 and 650 nm, resulting in a thickness of 16.3 and 13.1 µm respectively for the PMMA layer and for the PC layer. We compared the results for periods of 50 µm

and 150 µm. Scalar calculations in Fig. 4.30 show that the slope modification option has to be rejected since the diffraction efficiency is always lower than that obtained with the thickness modification option, as expected. The drop of diffraction efficiency is very small for the monolayer: 1% for a draft angle of 10° considering a period of 50 µm but the bilayer loses 20% diffraction efficiency in the same conditions.

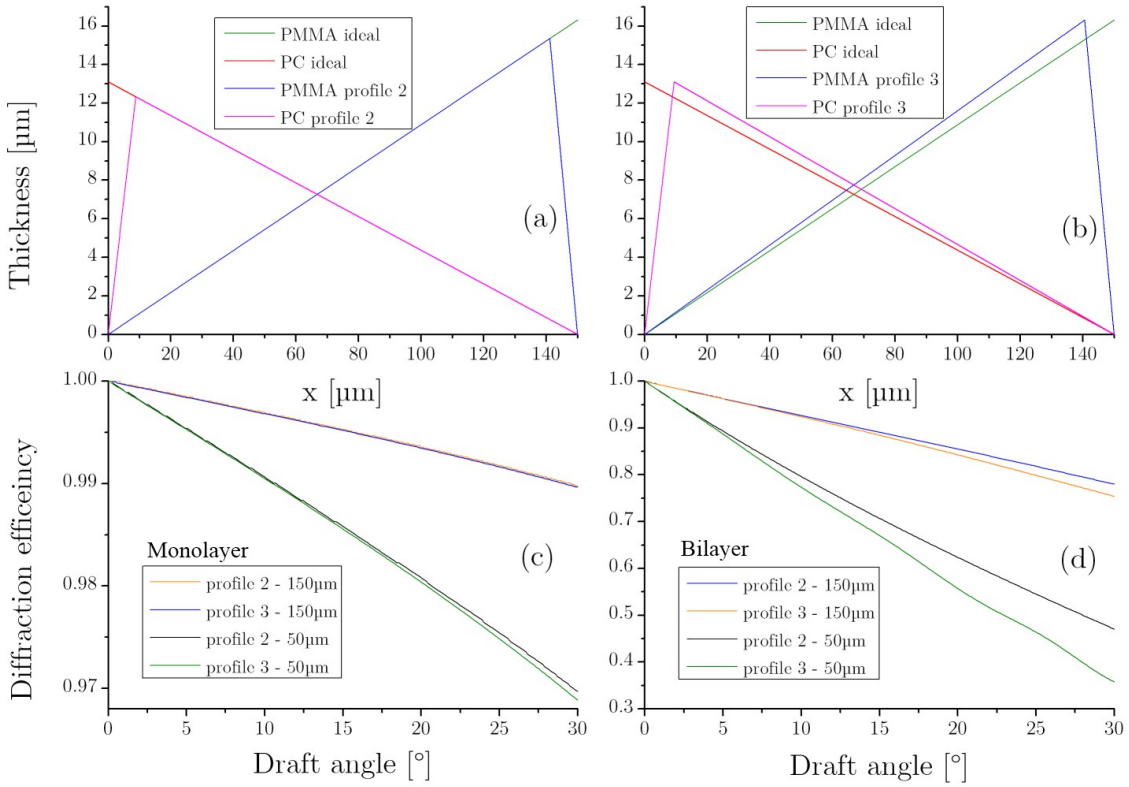

Fig. 4.30 a) Shape of profile 2 compared with the ideal bilayer profile. b) Shape of profile 3 compared with the ideal bilayer profile. c) Comparison of the scalar diffraction efficiency for a monolayer of PMMA with a period of of 50 µm and 150 µm d) Comparison of the scalar diffraction efficiency for a bilayer made of PMMA and PC with a period of 50 µm and 150 µm. All simulations were performed for a wavelength design of 650 nm (n_{PMMA}=1.4829 and n_{PC}=1.5521). The bilayer has a thickness of PMMA of 16.3 µm and a thickness of PC of 13.1 µm

4.6.4. Transversal and lateral shift between layers

The extended scalar theory showed how important it may be to take into account the thickness of the grating. We also deduced from the Fourier theory that a bilayer acts as a single layer and cannot be simply considered as two diffraction gratings in series. But what happens if the layers become physically separated or laterally shifted ?

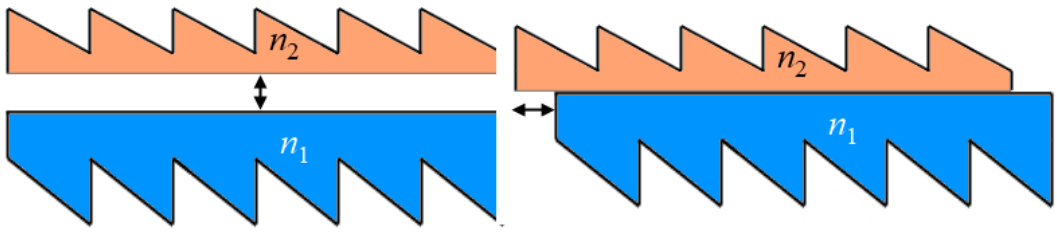

Fig. 4.31: Transversal shift (left) and lateral shift (right) between layers

For a bilayer grating with a period of 100 µm made with PC and PMMA, and optimized for 405 and 650 nm, we simulated the diffraction efficiency by separating the layer up to 4 mm. The diffraction efficiency, calculated with PCGrate, oscillates between 82 and 87% with an approximate period of 1.8 mm following Fig. 4.32. Since the diffractive layer of PMMA diffracts mainly in the 12th order and the refractive index at 650 nm for the PMMA is 1.483, the diffraction angle θ_{12} is

$$\theta_{12}=\text{asin}\left(12\frac{650\ \ 10^{-9}}{n_{PMMA}(650\text{nm})}\frac{1}{100\ \ 10^{-6}}\right)=3.01\,^{\circ}. \tag{4.63}$$

Thus the field diffracted by the nth teeth of PMMA will reach the (n+1)th teeth of PC if the layers are separated by a distance d of

$$d=\frac{100\,10^{-6}}{\tan(\theta_{12})}=1.846\ \text{mm}. \tag{4.64}$$

Therefore the system achieves a new maximum of diffraction which corresponds to the period observed in Fig. 4.32

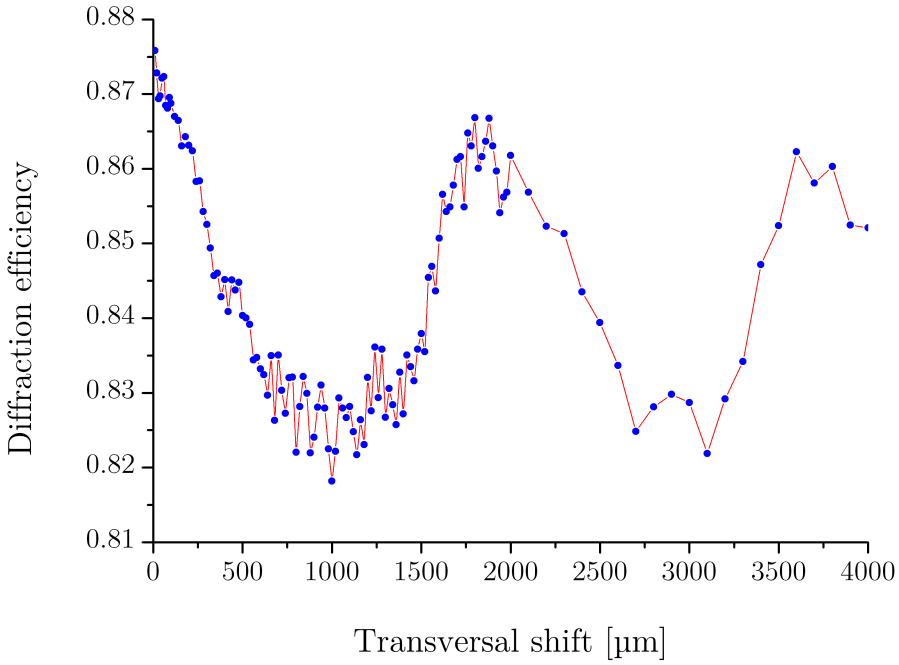

Fig. 4.32: Rigorous diffraction efficiency evolution with transversal shift (filled with PMMA) between layers of the 100 µm period bilayer

Due to this effect, if the distance between layers is imposed, a lateral shift between layers should overcome the drop of diffraction efficiency. This assumption was confirmed by shifting the first layer of a half period relatively to the second layer using PCGrate to obtain the graph shown in Fig. 4.33.

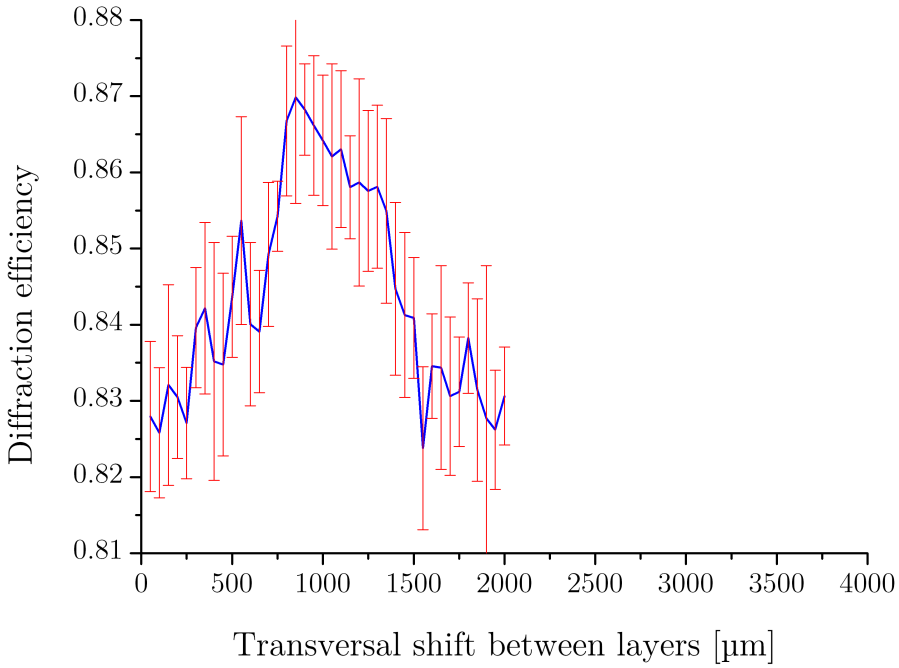

Fig. 4.33: Rigorous diffraction efficiency as a function of the transversal shift between layers for a lateral shift of 1000 µm

4.6.5. Effects of manufacturing errors

During the manufacturing process, many errors will spoil the design and therefore decrease the diffraction efficiency. Hereunder four typical errors are presented as well as the diffraction efficiency formula associated with the manufacturing error [Fuj82]. These errors are: over-etching, swell of the planar facet, draft facet angle and thickness errors. They are depicted in Fig. 4.34

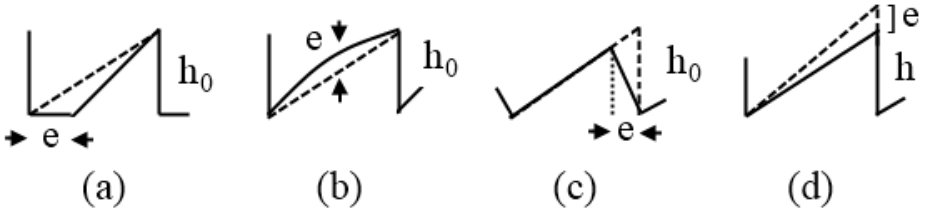

Fig. 4.34: Over/under-etching (a), swelling (b), draft angle (c), thickness error (d)

The diffraction efficiencies turn respectively to

$$\eta = \mathrm{sinc}^2\left(\frac{e}{\Lambda}\right) \tag{4.65}$$

$$\eta \simeq \mathrm{sinc}^2\left(e\frac{n-1}{\lambda}\right) \tag{4.66}$$

$$\eta = \left(1-\frac{e}{\Lambda}\right)^2 \tag{4.67}$$

and

$$\eta = \mathrm{sinc}^2\left(\frac{h}{h_0}-1\right) = \mathrm{sinc}^2\left(\frac{e}{h_0}\right) \tag{4.68}$$

Equations 4.66 and 4.68 are exactly the same. The drop of diffraction efficiency related to the draft angle is faster than over-etching as represented in Fig. 4.35.

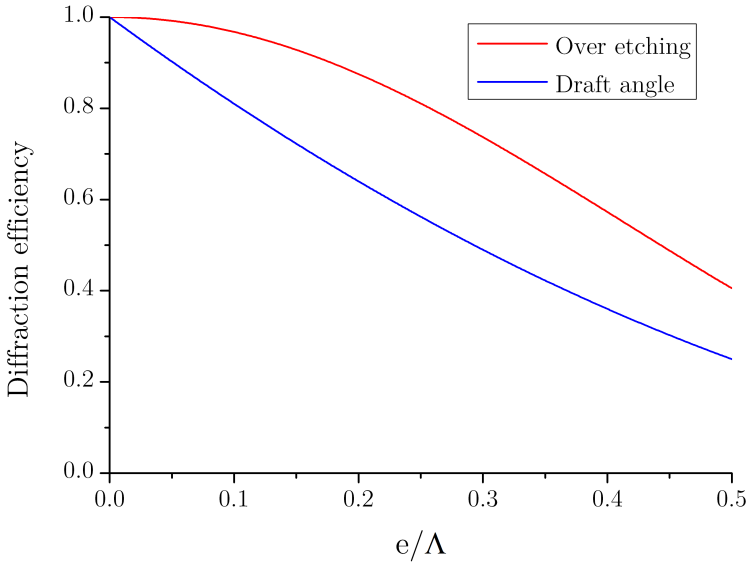

Fig. 4.35: Diffraction efficiency as a function of the error to period ratio. Comparison of over-etching and draft angle errors.

The diffraction efficiency curves for Eq. 4.66 and 4.68 would have been exactly the same as in the draft angle case, only the abscissa label must be changed into "e/h_0".

4.6.6. Layer order

From a scalar point of view, it was concluded that the way layers are stacked has no importance, this is obviously an approximation. If we consider a flat interface, should the most powerful layer be facing the source, is it the contrary, or does it not matter? To overcome this question, the PMMA/PC bilayer optimized for 405 and 650 nm will be used once again. It was said that at 650 nm the PMMA diffracts mainly to the 12^{th} order and the PC to the -11^{th} order for a thickness of 16.3 and 13.1 µm respectively. If the contact between the layers takes place on the flat side, therefore the light first strikes either teeth side. For a grating with a period of 50 µm, the deviation angle is 6.04° in the PMMA and 5.29° in the PC. Since the PMMA has a higher thickness combined with a higher deviation angle, the shading losses are more important if the PMMA is situated on the source side: 3.34% instead of 2.37%, according to Eq. (III.72) modified to take into account the diffraction order. Moreover, if the PMMA layer is on top, the output field will be diffracted towards the draft facet of the PC. This shading does not occur if PC is the top layer. This is depicted in Fig. 4.36.

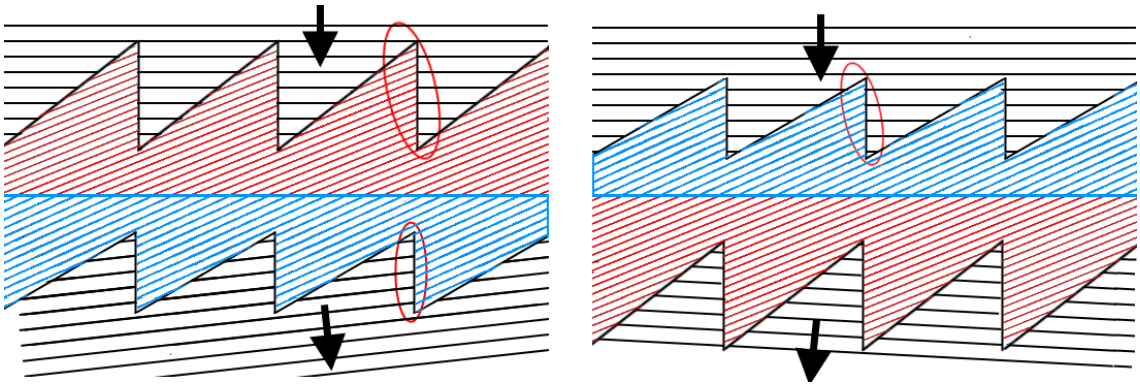

Fig. 4.36: Top layer in PMMA (left) engenders higher shading than PC as top layer (right). shading zones are encircled in red.

Rigorous simulations confirm this assumption. At 650 nm, a diffraction efficiency of 79.9% was found when PMMA is the top layer and 81.9% when PC is top layer.

4.7. Diffractive lens

The diffractive lens is to the Fresnel lens what the diffraction grating is to the prism... By segmenting a prism into teeth series introducing a 2π phase-shift between neighbouring teeth we get a blazed diffraction grating. The shape of refractive lens is obtained by matching the optical path of beams coming from an object towards the desired image point. So, the diffractive lens is designed with a series of zones for which the optical path from the object to the image remains the same, as for the refractive lens. But between two neighbouring segments the optical path differs from a natural number of design wavelengths ($m\lambda_0$). Therefore, both for the blazed diffraction grating and the diffractive lens, the design wavelength may be considered as refracted or diffracted. The diffraction effect occurs only when the diffractive lens is illuminated with a wavelength other than the design wavelength.

4.7.1. Diffractive lens profile

Concretely, let's design an ideal diffractive lens that makes rays coming from infinity converge to the focal point F, situated at a distance f_0 of the lens as depicted in Fig. 4.37.

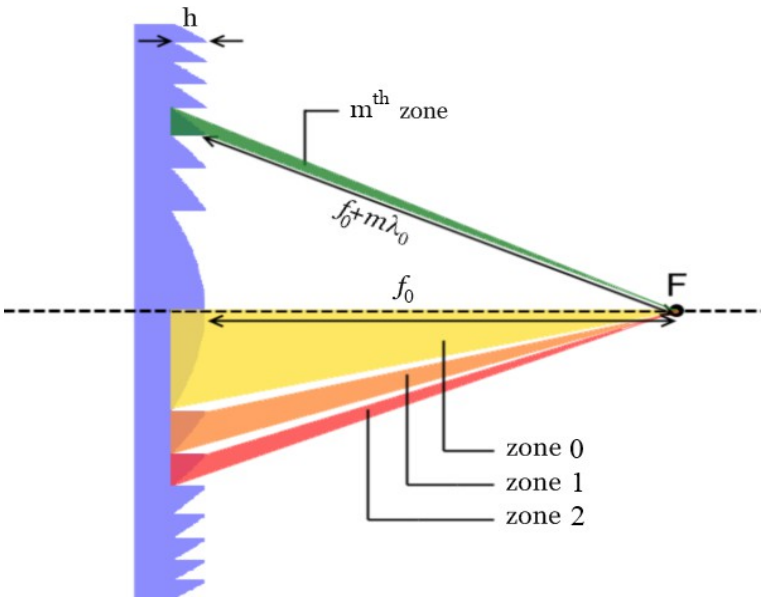

Fig. 4.37: Kinoform diffractive lens

The diffractive lens presented in the above figure with a continuous profile within a zone is called a kinoform lens [Les69, Jor70]. The equation of the shape of diffractive lens is well-known and is described in several works [Bur89, OSh03, Hun12] but the more explicit description was made by Moreno *et al.* [Mor97][7]. Consider the vertex as the axis origin, the z axis as collinear with the optical axis, and the focal point situated to the positive side; any point situated at a distance r of the z axis and lying in the m^{th} zone has the following equation

$$f_0+m\lambda_0-n(\lambda_0)\,s(r)=\sqrt{\left(f_0-s(r)\right)^2+r^2} \tag{4.69}$$

$s(r)$ is the sag profile of the kinoform, always of negative sign. Defining $f_{\text{m}} = f_0+\text{m}\lambda$ and squaring Eq. (4.69), it takes the form of

$$f_m^2+n^2(\lambda_0)s^2(r)-2f_m n(\lambda_0)s(r)=f_0^2-2f_0 s(r)+s^2(r)+r^2 \tag{4.70}$$

The following equation is obtained by dividing by $n^2(\lambda_0)$-1 and rearranging the terms:

$$s^2(r)+\frac{f_m^2-f_0^2}{n^2(\lambda_0)-1}-2s(r)\frac{n(\lambda_0)f_m-f_0}{n^2(\lambda_0)-1}=\frac{r^2}{n^2(\lambda_0)-1} \tag{4.71}$$

Completing the square, it takes the form of

7 Confusion over the numbering of orders takes place in [Mor97]. The distance between a point of the draft facet and the focal point is erroneously given on the figures of [Mor97] and [Hun12], the sag thickness should be added

$$\left\{ s(r) - \frac{n(\lambda_0) f_m - f_0}{n^2(\lambda_0) - 1} \right\}^2 + \frac{f_m^2 - f_0^2}{n^2(\lambda_0) - 1} - \left\{ \frac{n(\lambda_0) f_m - f_0}{n^2(\lambda_0) - 1} \right\}^2 = \frac{r^2}{n^2(\lambda_0) - 1} \tag{4.72}$$

which can be stated as

$$\left\{ s(r) - \frac{n(\lambda_0) f_m - f_0}{n^2(\lambda_0) - 1} \right\}^2 - \left\{ \frac{n(\lambda_0) f_0 - f_m}{n^2(\lambda_0) - 1} \right\}^2 = \frac{r^2}{n^2(\lambda_0) - 1} \tag{4.73}$$

it becomes clear that, as for refractive lenses [Hec02], the profile of diffractive lenses has the shape of a hyperbola [Hun10]. It can be thus recast into

$$\frac{\left[s(r) - s_0 \right]^2}{a^2} - \frac{r^2}{b^2} = 1 \tag{4.74}$$

where

$$s_0 = \frac{f\left[n(\lambda_0) - 1 \right] + n\, m \lambda_0}{n^2(\lambda_0) - 1} \tag{4.75}$$

$$a = \frac{f\left[n(\lambda_0) - 1 \right] - m \lambda_0}{n^2(\lambda_0) - 1} \tag{4.76}$$

$$b = \frac{f\left[n(\lambda_0) - 1 \right] - m \lambda_0}{\sqrt{n^2(\lambda_0) - 1}}. \tag{4.77}$$

This hyperbola has an eccentricity equivalent to the refractive index:

$$\varepsilon = \sqrt{1 + \frac{b^2}{a^2}} = n(\lambda_0). \tag{4.78}$$

An expression of the sag equation may be drawn from Eq. (4.74)

$$s(r) = s_0 - a\sqrt{1 + \frac{r^2}{b^2}} \tag{4.79}$$

Substituting term to term with Eqs. 4.75 to 4.77 gives

$$s(r)=\frac{f_0(n(\lambda_0)-1)+n\,m\lambda_0}{n^2(\lambda_0)-1}-\frac{f_0(n(\lambda_0)-1)-m\lambda_0}{n^2(\lambda_0)-1}\sqrt{1+\frac{r^2}{b^2}} \tag{4.80}$$

which can be rearranged in

$$s(r)=\frac{f_0\left(n(\lambda_0)-1\right)}{n^2(\lambda_0)-1}\left(1-sqr\right)+\frac{m\lambda_0}{n^2(\lambda_0)-1}\left(n(\lambda_0)+1-1+sqr\right) \tag{4.81}$$

which can be separated in two terms: the first independent of r and the second dependent of r

$$s(r)=\frac{m\lambda_0}{n(\lambda_0)-1}+\left(1-sqr\right)\left\{\frac{f_0\left(n(\lambda_0)-1\right)-m\lambda_0}{n^2(\lambda_0)-1}\right\} \tag{4.82}$$

where

$$sqr=\sqrt{1+r^2\frac{n^2(\lambda_0)-1}{\left[f\left(n(\lambda_0)-1\right)-m\lambda_0\right]^2}}. \tag{4.83}$$

The first term in Eq. (4.82) corresponds to the maximum thickness of the diffractive lens like for the blazed grating:

$$h=m\frac{\lambda_0}{n(\lambda_0)-1}. \tag{4.84}$$

The sag equation is valid for a radial position r inside the m^{th} zone:

$$r_m\leqslant r<r_{m+1} \tag{4.85}$$

with

$$r_m=\sqrt{2m\lambda_0 f_0+(m\lambda_0)^2}. \tag{4.86}$$

Since for most diffractive lenses the focal distance is much greater than the radius of the lens, it is common to find the following approximation of Eq. 4.83 in literature

$$sqr \simeq 1 + r^2 \frac{n^2(\lambda_0) - 1}{2\left[f\left(n(\lambda_0) - 1 \right) - m\lambda_0 \right]^2} \tag{4.87}$$

which gives an approximated value for both the sag and the pseudo-period equations. The sag equation previously given by Eq. (4.82) takes the parabolic form described by

$$s(r) \simeq \frac{\lambda_0}{n(\lambda_0) - 1} \left(m - \frac{r^2}{2\lambda_0 f_0} \right) \tag{4.88}$$

and each zone has an approximated pseudo-period of

$$\Lambda_m \simeq \sqrt{2\lambda_0 f_0} \left(\sqrt{m+1} - \sqrt{m} \right). \tag{4.89}$$

4.7.2. Local grating model

Eq. (4.84) makes a first link between diffractive lenses and blazed gratings. But what about the diffraction efficiency? The transmission function is given by

$$t(r) = \exp\left[i\phi \right] = \exp\left[i \frac{2\pi}{\lambda} (n(\lambda) - 1) z(r) \right] \tag{4.90}$$

$$t(r) = \exp\left[i \frac{2\pi}{\lambda} (n(\lambda) - 1) \frac{\lambda_0}{n(\lambda_0) - 1} \left(m - \frac{r^2}{2\lambda_0 f_0} \right) \right]. \tag{4.91}$$

By substituting with $\xi = -r^2/(2\lambda_0 f_0)$, the transmission functions takes the form of a periodic function

$$t(\xi) = \exp\left[i\, 2\pi\alpha \left(m + \xi \right) \right] \tag{4.92}$$

where α the design parameter already introduced in Eq. (4.22). The transmission function can be thus expressed in terms of a Fourier series with coefficients c_k given by

$$c_k = \int_{-1/2}^{1/2} t(\xi)\, e^{-i 2\pi k \xi}\, d\xi \tag{4.93}$$

$$c_k = e^{i2\pi\alpha m}\int_{-1/2}^{1/2} e^{i2\pi\alpha\xi}\ \ e^{-i2\pi k\xi}\,d\xi \tag{4.94}$$

$$c_k = \frac{e^{i2\pi\alpha m}}{2\,i\pi(\alpha-k)}\left[e^{i\pi(\alpha-k)} - e^{-i\pi(\alpha-k)}\right] \tag{4.95}$$

$$c_k = \frac{e^{i2\pi\alpha m}}{\pi(\alpha-k)}\left[\sin\left(\pi(\alpha-k)\right)\right] \tag{4.96}$$

and finally the diffraction efficiency is

$$\eta_k = c_k\,\overline{c}_k = \mathrm{sinc}^2\left(\alpha-k\right) \tag{4.97}$$

The expression of the diffraction efficiency for the diffractive lens or the blazed grating is thus given by the same equation. Moreover, the radius of curvature of the hyperbolic teeth increases rapidly with the zone number, so that they are rapidly approximated by blazed teeth. This means that we can consider a diffractive lens as a collection of local gratings and therefore continuing to use the scalar theory and the extended scalar theory to describe the behaviour of diffractive lenses. Since diffractive lenses have a period of $\xi = -r^2/(2\lambda_0 f_0)$, we will refer to ξ as the "pseudo-period" to avoid confusions with diffraction gratings.

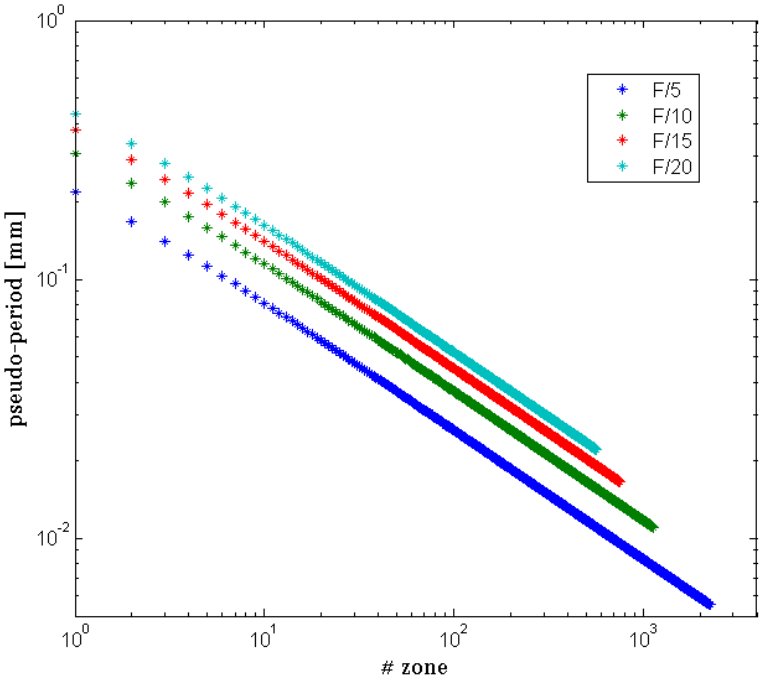

Fig. 4.38: Comparison of four lenses having the same diameter of 5 cm and different *f*-number (5, 10, 15 and 20) for a design wavelength of 550 nm.

To establish some orders of magnitude, the case of a lens with a diameter of 5 cm designed for 550 nm has been arbitrarily chosen. As depicted in Fig. 4.38, the lower the *f*-number the smaller the size of the teeth and the higher the number of teeth. In the present case, lenses with *f*-number smaller than 10 have their last teeth with a pseudo-period smaller than 10 µm which is close to the limit of validity of the scalar theory for monolayers.

Note that all the above equations follow a reasoning that is valid for the first diffraction order. To change the working design diffraction order to j, Eq. (4.69) should simply be modified into

$$f_0 + j\,m\,\lambda_0 - n(\lambda_0)s(r) = \sqrt{\left(f_0 - s(r)\right)^2 + r^2} \tag{4.98}$$

Therefore, the thickness will be j times bigger and the number of teeth j times smaller. It was previously deduced (see Fig. 4.7) that the first diffraction order presents higher performances of diffraction efficiency when illuminated with another wavelength than the design wavelength. However, when the pseudo-period of the diffractive lens becomes too small to be correctly manufactured, higher diffraction orders are preferably used, provided that the pseudo-period remains in the validity domain of the scalar theory (see Fig. 4.39).

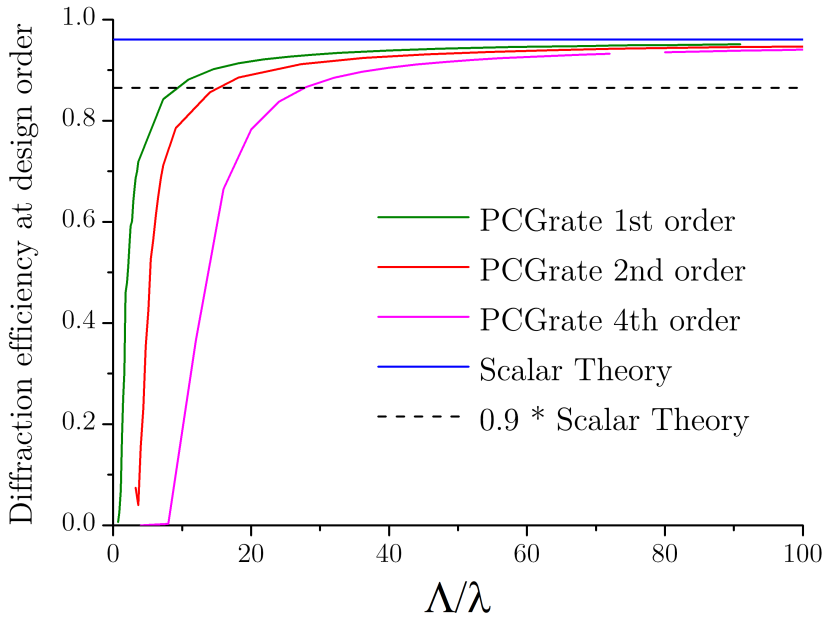

Fig. 4.39: Comparison of the validity domain of the scalar theory for first, second and fourth order for a monolayer made of PMMA

4.7.3. Some properties of diffractive lenses

4.7.3.1. Effects of the refractive index

It is worth noting that the focal distance of a diffractive lens is independent of the refractive index. The refractive index of design will only affect the deepness of the teeth; more precisely the eccentricity of the hyperboloid profile shape, as deduced from Eqs. (4.78) and (4.84). If the effective refractive index differs from the design refractive index, it will alter the design parameter α and therefore diffraction efficiency. Anyway, when the diffractive lens is illuminated with another wavelength than the design wavelength, the wavelength dependence is much more important than the change of refractive index.

4.7.3.2. Effects of the wavelength

When illuminated with another wavelength than the design wavelength, the diffraction efficiency changes but so does the focal distance. Applying the local grating theory allows to determine how the focal distance changes with the wavelength. From any point of the lens at a distance r from the centre that makes the beam converge to a distance focal f_0 at the design wavelength λ_0, the diffraction angle to the first order obeys the gratings equation:

$$\sin\theta_0 = \frac{\lambda_0}{\Lambda}. \tag{4.99}$$

Then, in the domain of validity of the scalar theory, i.e., $\Lambda \gg \lambda$, the focal distance can be approximated by[8]

$$f_0 = f(\lambda_0) = \sqrt{\frac{r^2}{\sin^2\theta} - r^2} = \sqrt{r^2\frac{\Lambda^2}{\lambda_0^2} - r^2} \simeq r\frac{\Lambda}{\lambda_0}. \tag{4.100}$$

When illuminated with another wavelength, the focal distance becomes

$$f(\lambda) \simeq r\frac{\Lambda}{\lambda} = f_0\frac{\lambda_0}{\lambda} \tag{4.101}$$

Therefore the focal distance decreases in λ^{-1} contrary to refractive lenses for which the focal distance increases with the wavelength. Note again that the focal distance remains independent of the refractive index. A more accurate calculation [Mar97] shows that the focal point spreads out and presents a spherical aberration S_I is given by

8 If r is the length of the side opposite to θ, the the hypotenuse is $r/\sin^2\theta$. Th expression of f results from the Pythagorean theorem.

$$S_I = (NA)^4 f\left[1-\left(\frac{\lambda_0}{\lambda}\right)^2\right] \simeq \left(\frac{n}{2F\#}\right)^4 f\left[1-\left(\frac{\lambda_0}{\lambda}\right)^2\right] \tag{4.102}$$

where $NA = n \sin \theta_{max}$ is the numerical aperture with θ_{max} the half angle from the focal point to the lens edge.

4.7.3.3. Abbe number

The deduction of the Abbe number v_d comes from the achromatization condition [Hec02] and corresponds in fact to

$$v_d = \frac{f(\lambda_F) - f(\lambda_C)}{f(\lambda_d)} \tag{4.103}$$

where F, C and d refer to Fraunhofer spectral lines (587.56 nm, 486.13 nm and 656.27 nm respectively). For diffractive lenses it takes simply the form of

$$v_d^{dif} = \frac{\lambda_d}{\lambda_F - \lambda_C} = \frac{587.56}{486.13 - 656.27} = -3.453. \tag{4.104}$$

The value obtained is independent of the nature of the material, is small in absolute value compare to usual Abbe numbers and is negative contrary to Abbe number of refractive glasses. Since the Abbe number is constant for all diffractive lenses it is therefore impossible to obtain an achromatic system using two diffractive lenses. However the combination of a diffractive lens with a refractive lens (called hybrid lens) can lead to an achromatic doublet of faster convergence than two refractive lenses since both the refractive lens and the diffractive lens must be converging for achromatic hybrid lenses. This will be further discussed in chapter 5.4.

4.7.3.4. Size of the focal spot

The diffraction limit is the same for diffractive and refractive optics. The Airy disk in the focal plane is given by

$$r(\lambda) = 1.22 \frac{\lambda f}{D}. \tag{4.105}$$

The wavelength dependence of the focal length for diffractive lenses (Eq. 4.101) leads to a constant value of the Airy disk.

4.8. Sweatt model: modelling a diffractive lens with refraction

Diffractive lenses are hard to simulate and realistic simulations are time consuming. A simple approach was proposed by W. Sweatt to model a diffractive lens using a refractive behaviour [Swe79].

The refractive model must follow the diffractive behaviour. Firstly, the local grating behaviour:

$$\sin\theta_1 - \sin\theta_2 = m\frac{\lambda}{\Lambda}. \tag{4.106}$$

Secondly, the variation of the focal distance must be inversely proportional to the wavelength:

$$f_{dif}(\lambda) = f(\lambda_0)\frac{\lambda_0}{\lambda}. \tag{4.107}$$

Both requirements are fulfilled with a thin lens made with very high refractive index medium (n>10'000) changing proportionally to the wavelength. Indeed, in these conditions the variation of the refractive focal length has a behaviour similar to Eq. 4.107 as deduced in Eq. 4.108

$$f_{ref}^{Sweatt}(\lambda) = \frac{RoC_{eq}}{n(\lambda)-1} \simeq \frac{RoC_{eq}}{n(\lambda)} = \frac{RoC_{eq}}{\lambda\, n(\lambda_0)}. \tag{4.108}$$

Regarding the first condition, W. Sweatt showed [Swe79] that an incoming ray will be refracted by a thin lens of thickness t with very high refractive index n following the relationship

$$\sin\theta_1 - \sin\theta_2 = (n-1)\frac{dt}{dr} \tag{4.109}$$

where r is the radial coordinate of the lens.

Hence, the lens profile is deduced equating Eqs. 4.106 and 4.109

$$m\frac{\lambda}{\Lambda} = (n-1)\frac{dt}{dr} \tag{4.110}$$

which is independent of the incidence angle of the incoming ray. This simple model will be used later, to perform ray-tracing simulations with a diffractive lens.

4.9. Transition between refractive and diffractive optics

To design an ideal diffractive grating or lens, both refractive and diffractive laws were used (see for example Appendix III.5.3). But what happens when the design slightly changes? When can we consider that an optical element acts refractively or diffractively?

First of all, it has to be noted that the classification is purely anthropological and both effects can be described by one single electromagnetic theory. In fact, diffraction and refraction are two limit cases of this electromagnetic theory. Secondly, it is commonly taught that diffraction occurs when light is confined by passing through an object which size is in the order of the wavelength. Blazed gratings are especially relevant to prove that this sentence may lead to erroneous intuitions. Indeed, the diffraction effect is easily described for high period-to-wavelength ratios, and blazed gratings or lenses in the order of the meter are manufactured. The transition between purely diffractive and purely refractive optical elements has been investigated mainly in the middle of the '90s. We propose here a summary of three relevant publications [Sin95, Sal97, Ros95].

Sinzinger and Testof [Sin95] investigated the transmission function in the Fourier plane of light passing through a blazed grating and a lens, the grating being situated in the object focal plane of the lens as shown in Fig. 4.40 hereunder.

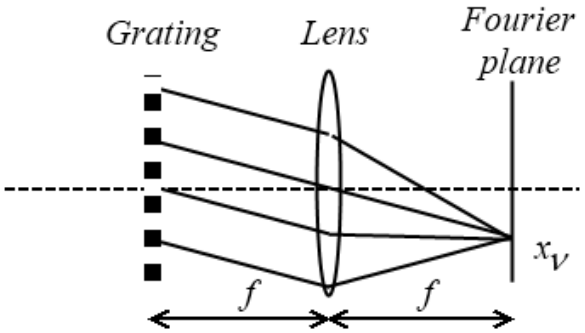

Fig. 4.40: Fourier set-up for the reconstruction of the effect of a blazed grating

They showed that the transmission function in Fourier space $\tilde{t}(\nu)$ can be approximated by the product of a term independent of the diffraction order m $\left(\tilde{t}_{ref}\right)$ with a term varying with the diffraction order $\left(\tilde{t}_{diff}\right)$

$$\tilde{t}(\nu)=\tilde{t}_{ref}(\nu) \times \tilde{t}_{diff}(\nu)= \left\{ sinc\left[\left(\frac{\nu\lambda_0}{\theta_b(n-1)}-\alpha\right)k\right]\right\} \times \left\{\sum_m sinc\left[\left(\nu-\frac{m}{k}\frac{\theta_b(n-1)}{\lambda_0}\right)D\right]\right\} \tag{4.111}$$

where ν is the spatial frequency, k is the design order, θ_b is the blaze angle and D *is* the total width of the grating. The transmission function of the first diffraction order can therefore be evaluated in the focal plane using[9]

$$x_\nu=\lambda f \nu \tag{4.112}$$

This function has been depicted in Fig. 4.41 for different values of D (D=100Λ, D=20Λ and D=4Λ). When $D \gg \Lambda$, $\tilde{t}_{diff}$ is similar to the δ comb function thus the regime is purely diffractive. Peaks enlarge when D decreases and the regime is in-between the refractive and the diffractive regime. At the design wavelength, the maximum of $\tilde{t}_{ref}$ corresponds to one maximum of $\tilde{t}_{diff}$ but the other peaks of $\tilde{t}_{diff}$ correspond to a zero of $\tilde{t}_{ref}$, the total transmission function results thus in a single peak with a width depending on the number of prisms.

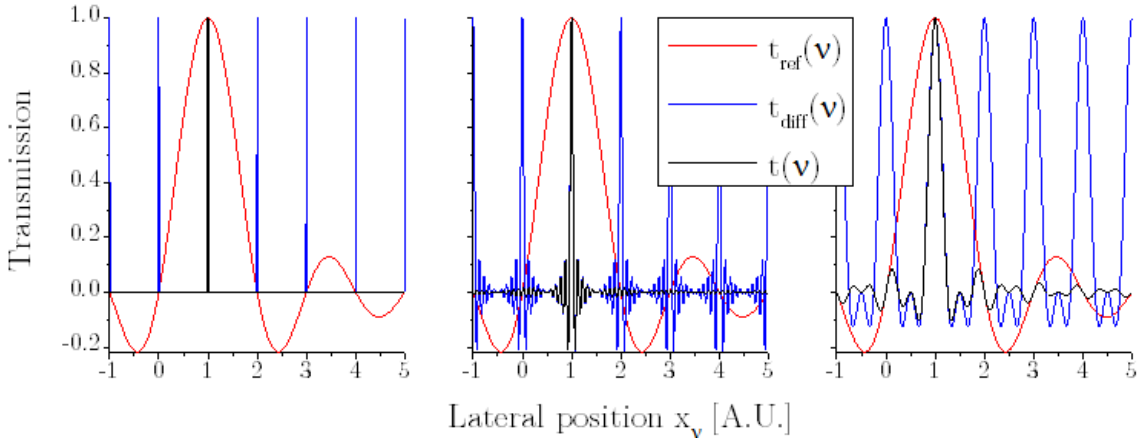

Fig. 4.41: Transmission function for 100 prisms (left), 20 prisms (centre) and 4 prisms (right). Set-up illuminated for the design wavelength (a=1) optimized at the first order (k=1)

When the illumination wavelength differs from the design wavelength ($\alpha \neq 1$), the lateral positions of the refractive peak moves slightly due to the small dependence of the refractive index with the wavelength while the dependence in λ^{-1} of α is

9 Since $\sin\theta \simeq x_v / f$ and $\sin\theta = m\lambda\nu$, with $\nu = 1/\Lambda$

compensated by the lateral variation with wavelength given by Eq. (4.111). To the contrary, the diffractive peaks see their positions change accordingly to Eq. (4.111). Since both variations occur in opposite directions, the achromatization of a blazed grating is impossible. The wavelength detuning leads therefore to the apparition of other diffraction orders and a lateral shift of the diffraction orders, see Fig. 4.42.

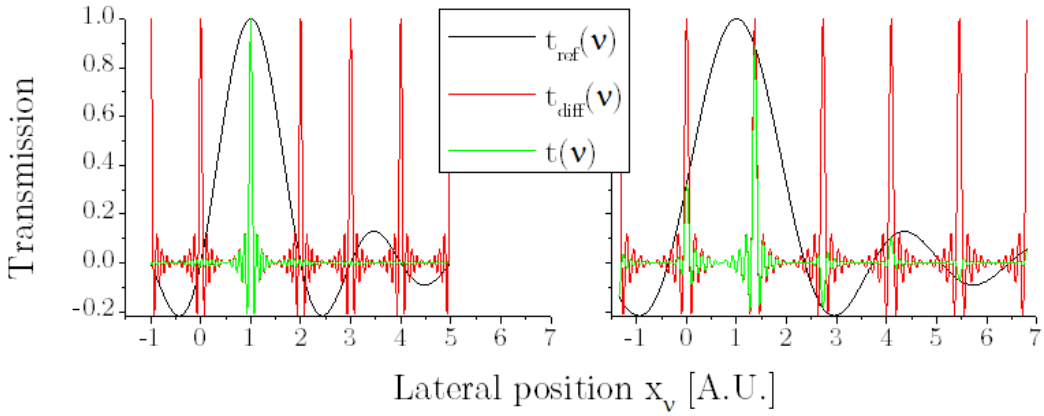

Fig. 4.42: Peaks shift with wavelength variation. Design wavelength = 550 nm and illumination wavelength = 550 [left] and 750 nm (α=0.73) [right]

In 1997, T.R.M. Sales and G.M Morris, gave an expression of the on-axis scalar field produced by a diffractive lens. Each zone produces a refractive field with a contribution modulated by the neighbouring zones. The total field can therefore be seen as "*interference pattern of associated refractive lenses related to each individual zone and modulated by a zone-dependent complex-valued coefficient*" [Sal97].

An interesting approach was proposed by Rossi *et al.* in 1995 [Ros95]. They compared the irradiance along the optical axis of several lenses made of 1 to 8 segments but all with the same numerical aperture. Lenses were affected by a non-ideality factor of 10%; namely their thickness is set to 0.9 $q\lambda_0/(n\text{-}1)$ so that the refractive focal length is slightly greater than the diffractive focal length. Designs conceived for order k=1 and k=2, respectively with 8 and 4 segments, don't have any diffraction order focusing near the refractive focal point. These lenses therefore show only one diffractive focus and have a purely diffractive behaviour. For higher order diffractive designs, a second focus corresponding to k-1 appears and the Airy disks stack each other leading to a large focal spot centred close to the refractive focal point. Finally, for the purely refractive lens, i.e. the diffractive lens made of only one segment, the focal length corresponds to the calculated refractive case. This shows that the diffractive behaviour depends only on the number of elements and that a four segment diffractive lens still exhibits properties of a diffractive lens.

Finally, a brand new peer-reviewed article [Lar12] shows that the generalized law of refraction [Yu11]

$$n_i \sin\theta_1 - n_0 \sin\theta_o = \frac{\lambda}{2\pi}\frac{d\varphi(x)}{dx} \tag{4.113}$$

is valid for both refraction and diffraction gratings.

4.10. Chapter conclusions

After some historical background, this chapter determined a simple but useful tool to deal with high period-to-thickness ratios: the scalar theory. The transition from Maxwell's equations to a scalar theory leads to the use of Fourier transforms which is particularly useful in the case of diffraction gratings since the diffraction efficiency depends only on the Fourier series coefficients. Still with the scalar theory, an ideal blazed grating was determined so as to generate the maximum diffraction efficiency in the desired order. Among the infinite choice of diffraction orders, the first order is the least sensitive to wavelength variation – except for the zeroth order which is of no interest in this thesis. However, for broadband applications needing a high diffraction efficiency, one diffractive layer cannot suffice and the use of more than two layers gives rise to technological difficulties and to an alteration of the optical efficiency. In between the two, bilayer gratings allow for high diffraction efficiencies which is practically independent of the materials used. Nevertheless, it is difficult to draw conclusions from the scalar theory. For example the scalar theory is supposed to be valid for periods greater than 10 times the wavelength. This no longer applies for multilayer gratings, hence the need of a validation with rigorous theories or at least the use of an extended scalar theory. This extended theory reflects the drop of diffraction efficiency for short Λ–to-λ ratios through the shading created by the draft facets. From this theory we found an optimized expression of the ideal thickness for blazed gratings, we also explained how to optimize bilayer gratings. We paid attention to the optimisation of the diffraction efficiency related to manufacturing errors, shading, layers arrangement and found that a few percent can be gained in several steps leading to a non-negligible overall gain for small period gratings.

Finally, the ideal profile of a diffractive lens was deduced: it strongly differs from a refractive lens when illuminated at another wavelength than the design wavelength. The focal distance is independent of the refractive index and decreases with the wavelength contrary to refractive lenses. It was deduced that the optimization of the diffractive lens may be performed by local grating theory: the diffractive lens is nothing more than a diffractive grating with a period

decreasing with the distance from the optical axis. Properties of diffractive lenses make them good candidates to be combined with refractive lenses in order to achieve achromatic systems...

5 | Design and comparison of singlet, hybrid lens and refractive doublet for CPV

"Many modern refracting systems intended for use over an appreciable range of wavelengths are ultimately limited in performance by chromatic effects rather than by the monochromatic aberrations"

W. T. Welford

This chapter is dedicated to the reduction of the chromatic aberration of Fresnel lenses. The achromatization process can be performed in two ways: combining the refractive lens with a diffractive lens, or combining the converging refractive lens with a diverging refractive lens. This requires determining with high precision the refractive index of the PC and the PMMA. Optimized theoretical designs of singlet lenses, hybrid (diffractive/refractive) lenses and refractive doublets will be presented and compared. Some tolerances will also be presented.

5.1. History of achromatic doublets

Until the late 1660s, people thought that colours arose from a mixture between light and darkness and that prisms coloured light. By using a lens and a secondary prism, Newton could recompose the rainbow spectrum into white light, proving that white light is made of colours mixture. However, Newton considered that every material had the same constringence (i.e. the same chromatic dispersion) and thus deduced that it was impossible to avoid and correct

chromatic aberrations. This is the reason why only reflective telescopes were used to perform astronomical observations in that time. In the middle of the 18th century J. Dollond and C. Moore showed that Newton was wrong regarding the constance of the media constringence. Indeed, the focal distance variation of lenses made with specific materials are very sensitive to the wavelength while other materials are less sensitive. This variation of the focal distance is due to the variation of the refractive index, simply named dispersion, changing from a medium to another in relation with their chemical and physical properties. Thanks to this reversal, so-called "achromatic doublets" were manufactured and gradually replaced reflective telescopes. Over time, bigger and bigger telescopes were made, up to one meter wide. Beyond this value, the secondary spectrum (i.e. residual chromatic aberration) became too important. Therefore mirrors were reintroduced and are nowadays "*universally used for apertures exceeding one meter*" [Wel89][10]. Meanwhile, scientists keep for searching cost-effective systems with an as small as possible chromatic aberration.

5.2. Design parameters

From Chapter 3.1 "Important Fresnel lenses parameters", the following parameters were chosen:

- all interfaces are flat (excluding teeth texturation)
- lens radius R_l=2 cm
- *f*-number=2 (therefore a focal distance of 8 cm)
- maximum refractive teeth thickness t=400 µm
- draft angle δ=2° for refractive structure, 1° for diffractive structures
- thickness of the lens (teeth excluded) h=2 mm
- peak and valley radius r_{pv}=50 µm for refractive lenses.

Moreover, the characterization of the solar spectrum on Earth and the spectral external quantum efficiency of triple-junction solar cell combined with the transmission spectra of PC and PMMA allow to establish a spectral band of interest: 380-1600 nm [Bet07, Spe12, NREL, Gue01] (see Chap. 2.2., 2.3. and Fig. 3.8).

Note that with an aspect ratio equivalent to an *f*/2 lens, a CPC would have an acceptance angle of 35° but a concentration ratio of 3.1×!

10 The GAW telescope, presented in this thesis is an exception: it is made of a 2.13 meters diameter Fresnel lens. See 8.1.

5.2.1. Refractive index of PC and PMMA

In Chapter 3.1.3., the choice of optical plastics was discussed and it turned out that PMMA was probably the best candidate for singlets and that PC is a good candidate to be combined with PMMA. Since the chromatic aspect is linked to the refractive index, investigating the evolution of the refractive index with the wavelength (called dispersion curve) is of high importance.

Up to now, we spoke about PMMA and PC as a whole. But there can be different forms of PMMA and PC. To see how far PMMAs can differ from one another, we compared dispersion curves from the literature with measurements performed at the CSL by ellipsometry. The same was done for some PCs. Eight OPs were investigated: three from the literature and five from our suppliers, for which we determined the dispersion curve. In total four PCs and four PMMAs listed in Table 5.1 were studied.

Table 5.1 Information about PMMAs and PCs

PMMA	Data source	Provider (P) or Trade Mark (TM)
PMMA-1	[Lyt09]	Unknown
PMMA-2	CSL	Altuglas (TM)
PMMA-3	CSL	Diakon (TM)
PMMA-4	CSL	Evonik (P)
PC-1	[Kas07][1]	Unknown
PC-2	[Lyt09]	Unknown
PC-3	CSL	Calibre 1080 DVD (TM)
PC-4	CSL	Makrolon (TM)

[1] Referenced as PC in [Kas07]

Both Laurent's and Sellmeier's equations were used for each sample, but only the equation giving the smallest error is presented (see Chap 2.4.1.5.). The dispersion coefficients are presented in Table 5.2. Note that these coefficients must be used with the wavelength expressed in microns. The curves of the dispersion curves are shown in Fig. 5.1 and Fig. 5.2 respectively for PMMAs and PCs. The variation of the refractive index from a sample to another might be explained by the industrial process parameters that are not constant [Lee01], the grade used and the packing coefficient [Tan06]. Nevertheless, the curve "PC-1 (old)" exhibits an abnormal behaviour: above 1200 nm the refractive index drops too rapidly compared to any other PC. This is because the dispersion coefficients were retrieved by Kasarova *et al.* [Kas07] from measurements going from 435.8 to 1052 nm and the extrapolation outside of this range gives wrong results. So, we performed another interpolation (PC-1) giving more probable results in the near infrared region. Thus, PC-1 (old) will no longer be considered hereafter.

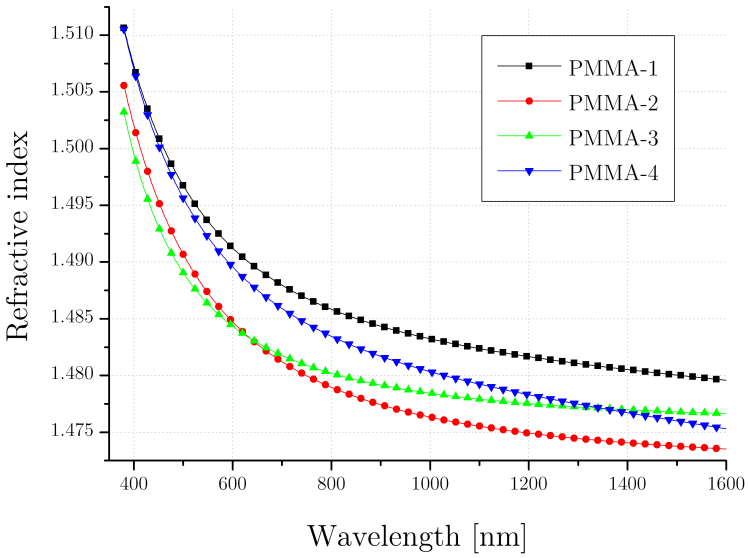

Fig. 5.1: Dispersion curves of some PMMAs

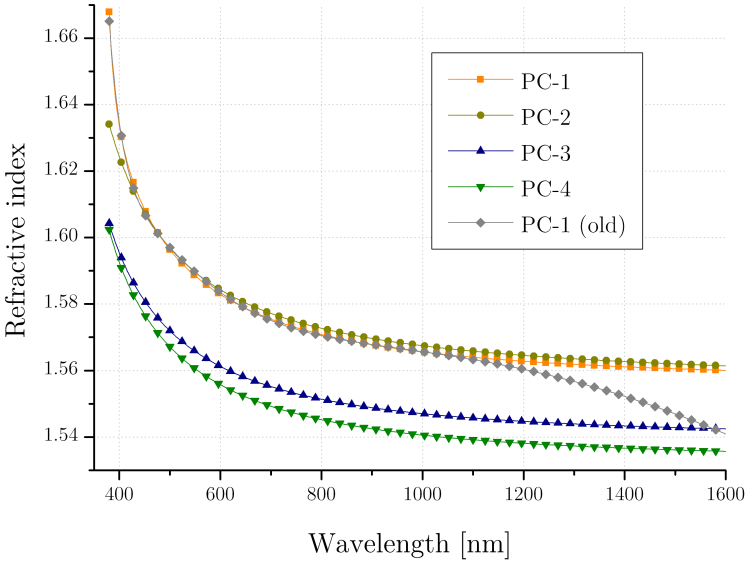

Fig. 5.2: Dispersion curves of some PCs.

Table 5.2 Dispersion coefficients of some PCs and PMMAs

Material (L/S)[1]	Dispersion coefficients					
	A_1 or B_1	A_2 or B_2	A_3 or B_3	A_4 or C_1	A_5 or C_2	A_6 or C_3
PMMA-1 (L)	2.190664	-2.330317e-3	1.122194e-2	4.765210e-4	-5.040529e-5	3.423433e-6
PMMA-2 (S)	4.841120e-1	3.353637e-4	6.815579e-1	1.096254e-2	1.028035e-2	1.184708e-2
PMMA-3 (S)	6.997099e-1	2.731275e-1	2.043425e-1	-5.777416e-4	-5.784644e-4	4.291190e-2
PMMA-4 (S)	1.838458e-1	2.827502e+1	0. 998312e-1	1.127337e-2	6.664339e+3	1.127703e-2
PC-1 (S)[2]	1.341659e-2	2.410966e-1	1.168465	1.329927e-1	1.811373e-2	1.812526e-2
PC-2 (L)	2.430734	-1.343233e-3	2.714995e-2	3.244405e-4	7.013408e-5	5.615956e-6
PC-3 (S)	2.583939e-2	3.675250e-1	9.769463e-1	9.453662e-2	1.483129e-2	1.488111e-2
PC-4 (S)	2.205583e-2	2.532511e-1	1.073656	1.004816e-1	1.630428e-2	1.623521e-2

[1] Dispersion mode: Laurent (L) or Sellmeier (S) (see Chap 2.4.1.5.)

[2] Recalculated dispersion coefficients to get more probable results in the near infrared region

5.2.2. Extinction coefficient of PC and PMMA

Ellipsometric measurements were also used to determine the extinction coefficient k. As a reminder, see Chap 2.4.1.4., k is a dimensionless number representing the imaginary part of the complex refractive index

$$\tilde{n} = n + ik \tag{5.1}$$

and is directly related to the absorption coefficient μ_a

$$\mu_a(\lambda_0) = \frac{4\pi k}{\lambda_0} \tag{5.2}$$

which is used to determine the transmitted light intensity I after passing through a layer with a thickness x

$$I = I_0 \exp\left(-\mu_a x\right) \tag{5.3}$$

However, the measurements performed did not distinguish the absorption coefficient μ_a from the diffusion coefficient μ_d. Therefore, strictly speaking, the "k" measured is not the extinction coefficient but is related to the attenuation coefficient, μ_t, which also includes the diffusion losses. Anyway, since diffused light will in principle not reach the solar cell, both absorbed and diffused can be considered as a whole.

Values of the extinction coefficient and of the transmission coefficient (I/I_0) for a

layer of 2 mm are respectively shown in Fig. 5.3 and Fig. 5.4 for two PMMAs and two PCs.

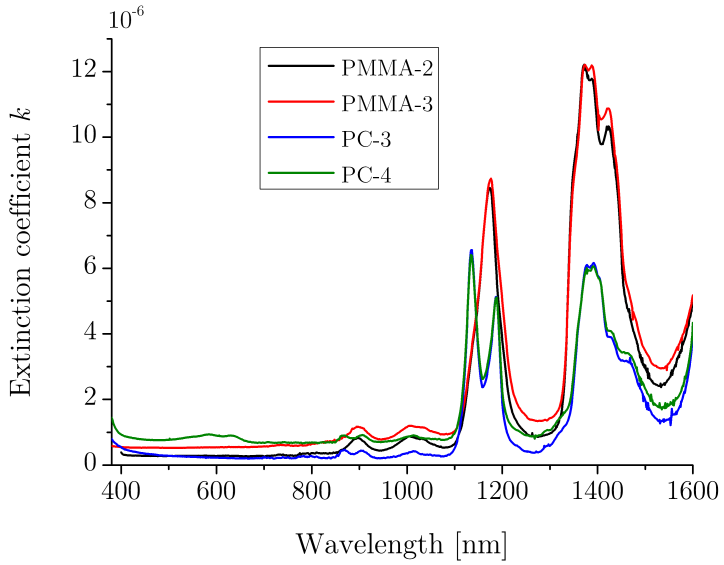

Fig. 5.3 Extinction coefficient of two PMMAs and two PCs

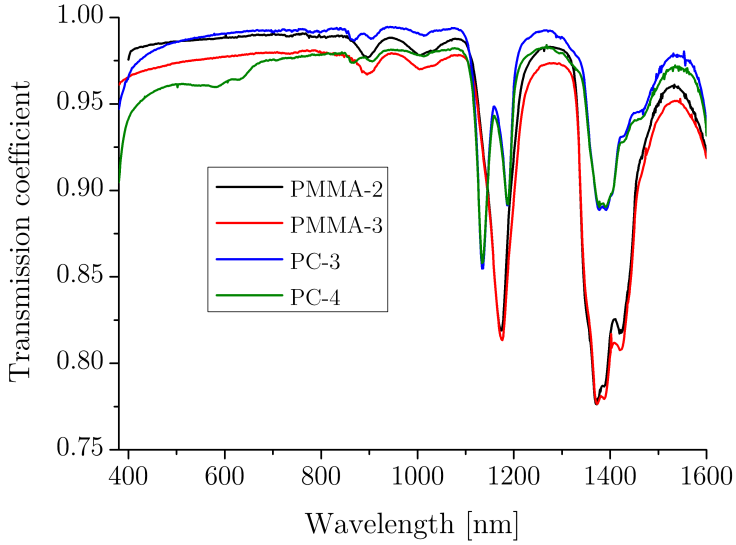

Fig. 5.4 Transmission coefficient of light passing through two millimetres of optical plastic (no interface, no Fresnel losses)

5.2.3. Testing the design

As already mentioned, determining equations in order to establish tolerances and optical performances is hard to achieve. Testing the performances in a ray-tracing program avoids this fastidious work. However, it is important to determine the order of magnitude of the various factors responsible for optical losses. To achieve this, we will afford the following approximations:

- only on-axis beams reach the lens,

- absorption occurs only in the bulk material (i.e. teeth excluded),
- the incoming solar spectrum corresponds to a 5780 K black-body
- prism peak and valley radius, r_{PV}: 50 µm

Refractive index and sag profile error will also be investigated considering

- a variation of the refractive index corresponding to a thermal variation of +20 °C (Δn = -0.0021 for PMMA and -0.0024 for PC)
- a deformation of 5% of the sag profile (only along the optical axis)

The choice of a refractive index variation corresponding to a thermal variation of 20 °C may be justified in two ways. Firstly, the value of the temperature variation is in the order of the working range. Secondly, this corresponds to a typical error due to the use of another grade of PMMA during the plastic injection process as can be deduced from Fig. 5.1.

After the determination of optical losses under normal incidence, ray-tracing simulations will be performed using the angular aperture of the Sun in order to confirm the results obtained under normal incidence but also to investigate the effects of the shape and refractive index error on the focal length and the focal spot. Ray-tracing simulations will be performed using a black-body spectrum at 5780 K for a wavelengths range from 380 to 1600 nm with a step smaller than 50 nm. For every wavelength 48'000 rays are launched. Fresnel reflections are automatically calculated by the ray-tracing program: ASAP ®.

5.3. Flat singlet

The investigation of singlets will allow to determine a reference for the comparison with achromatic doublets in terms of equivalent radius of curvature (RoC^*_{eq}), longitudinal chromatic aberration (LCA^*) and maximum concentration (C_{max}). As a reminder, the asterisk superscript indicates the normalisation with $f(\lambda_0)$. The normalized equivalent radius of curvature depends only on the refractive index:

$$RoC^*_{eq} = \frac{RoC}{f(\lambda_0)} = n(\lambda_0) - 1 \tag{5.4}$$

5.3.1. Focal distances minimizing the LCA and upper limit of concentration factor

In order to adequately compare the focusing performance of all PMMAs and PCs, a central wavelength λ_c was determined for any of the OPs. This central wavelength is determined in such a way that the greatest LCA is minimized,

$$\left|f(\lambda_c)-f(380\text{nm})\right|=\left|f(\lambda_c)-f(1600\text{nm})\right| \tag{5.5}$$

Plotting the focal distance curve which minimizes the LCA as a function of the wavelength directly highlights the PMMA (Fig. 5.5) and the PC (Fig. 5.6) offering the lowest LCA. Relevant data about singlets are provided in Table 5.3.

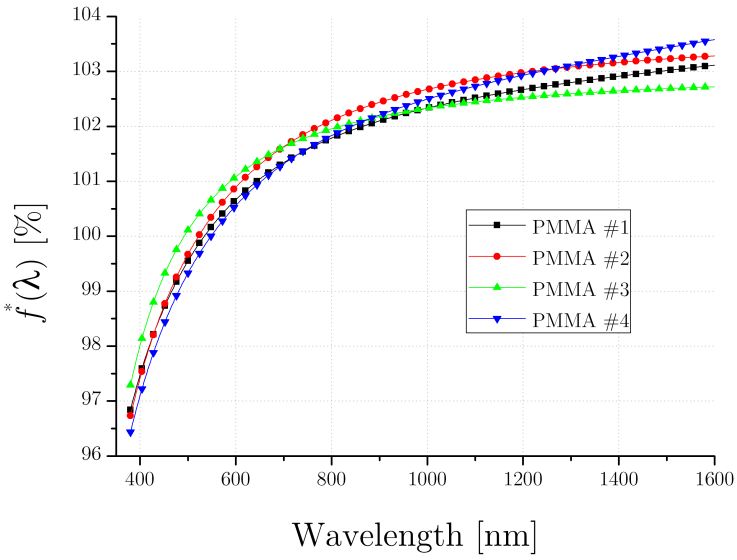

Fig. 5.5: Evolution of the focal distance minimizing the LCA for four kinds of PMMAs.

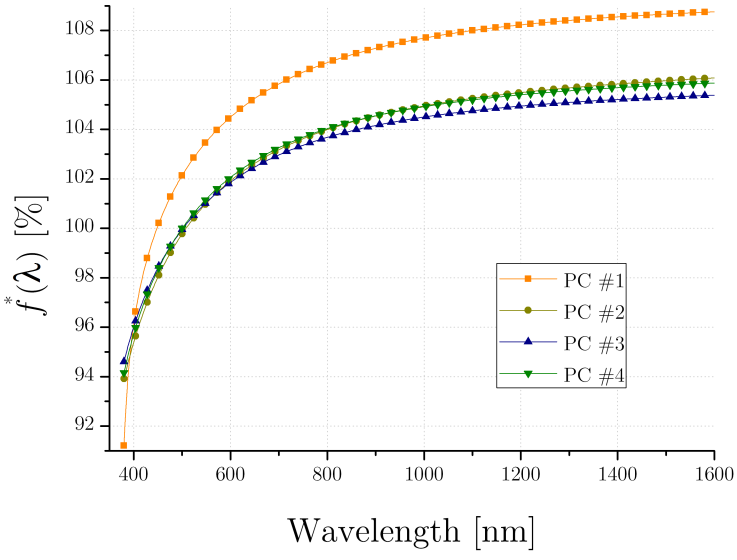

Fig. 5.6: Evolution of the focal distance minimizing the LCA for four kinds of PCs.

Table 5.3 Relevant data about singlets

Material	λ_0 [nm]	RoC^*_{eq} [%]	LCA^* [%]	C_{max}	v_d
PMMA-1	534	49.00	3.159	1002	57.231
PMMA-2	522	48.91	3.282	928	52.270
PMMA-3	492	48.96	2.720	1351	66.522
PMMA-4	548	49.23	3.579	781	51.710
PC-1	448	60.91	8.794	129	27.928
PC-2	508	59.56	6.086	270	29.894
PC-3	502	57.17	5.393	344	33.746
PC-4	500	56.72	5.877	290	33.271

As a reminder, from Eq. (3.34) C_{max} is independent of the focal length and is given by $(1/\text{LCA}^*)^2$

Thus, as expected from the Abbe number, PMMAs present a lower chromatic aberration than PCs. The concentration achieved with PMMAs for collimated beams lies around 1000×. This value has to be compared with the sine law value (~46'000×) and the maximum value that can be achieved with an *f*-number of 2: ~3000× following Eq. (3.3). In this case, it is obvious that the maximum concentration achievable with a singlet is much more limited by the chromatic aberration than by the angular aperture of the Sun.

Among the PMMAs, PMMA-3 exhibits the lowest LCA^*, so this PMMA will be used for our simulations.

5.3.2. Design of the Fresnel singlet

In Chapter 3.2., comparisons between imaging and nonimaging $f/2$ Fresnel lenses showed that for small incidence angles, nonimaging designs provide only a very slight improvement in performance under monochromatic illumination. It is therefore obvious that these improvements become insignificant under polychromatic illuminations, especially if the spectrum of interest extends from 380 to 1600 nm. However, the lens was optimized for an incoming angle of 0.265° and designed for a wavelength of 492 nm (corresponding to the central wavelength of PMMA-3 in Table 5.3). The final lens shape is shown in the figure below.

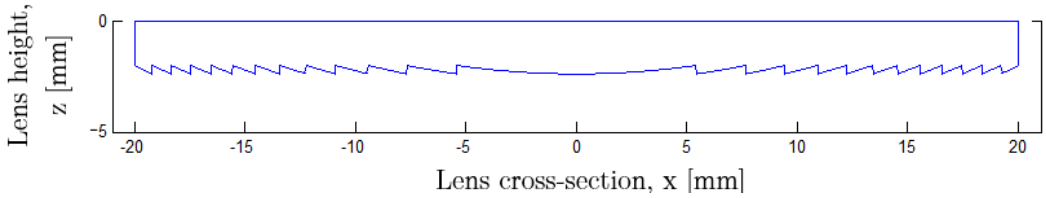

Fig. 5.7: Design of the singlet Fresnel lens

5.3.3. Approximated optical losses

Fresnel reflection losses as well as attenuation losses are wavelength dependent. As shown on Fig. 5.8, Fresnel reflection losses remain close to 8% while the attenuation varies from 1 to 10 % for a 2 mm thick PMMA sample.

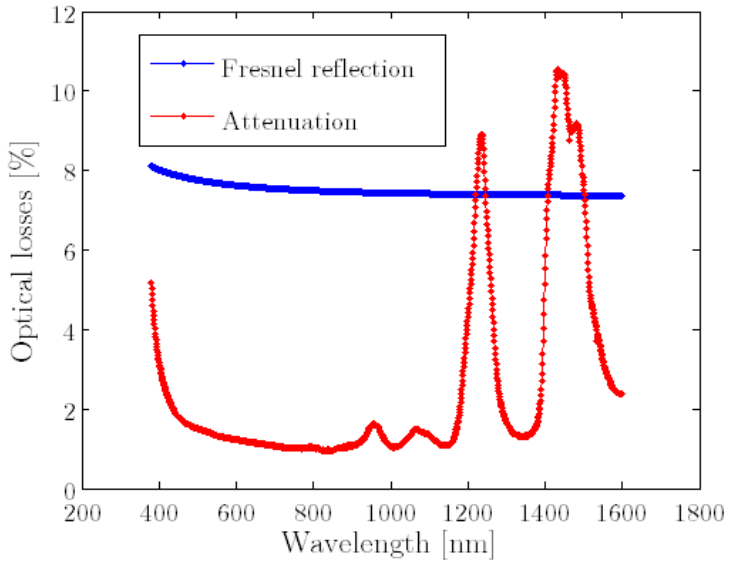

Fig. 5.8: Optical losses due to two Fresnel reflections and attenuation within 2mm of PMMA.

Draft angles, peaks and valleys are responsible for dead zones, the proportion of which depends on the kind of concentration (2D or 3D). Values are given in Table 5.4

Table 5.4 Optical losses due to draft angles, peaks and valleys

Loss factor	Optical losses [%]	
	2D	3D
Draft angles	0.81	1.10
Peaks and valleys	1.84	2.71
Total	2.64	3.82

Grouping all these data while taking into account the 5780 K black-body

radiation yields to the total transmitted spectral power, see Fig. 5.9 for the 3D concentrator. The ratio of the incoming radiant flux to the transmitted radiant flux provides the final optical efficiency: 88.32% and 87.25% respectively for 2D and 3D.

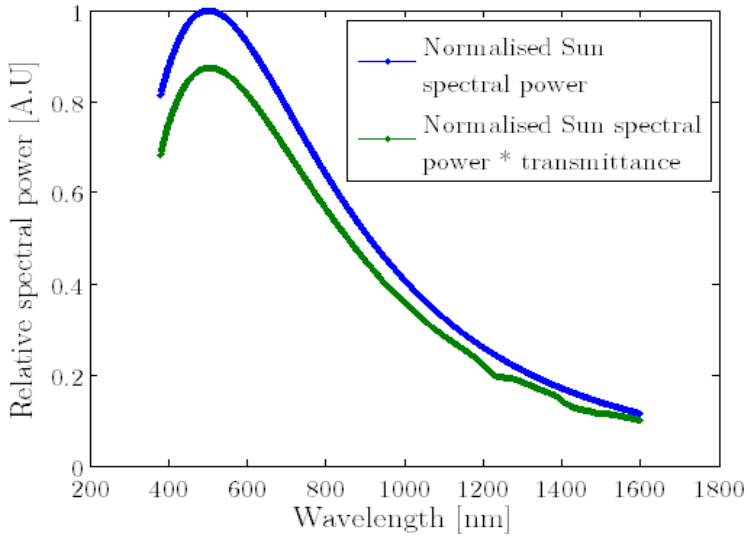

Fig. 5.9 Comparison between the incoming spectral solar power and transmitted spectral power for a 3D concentrator.

Among the 12 percent lost, two third are due to Fresnel reflections. This is why anti-reflective coatings are sometimes proposed [Sch02].

5.3.4. Refractive index and radius of curvature error

Using Eqs. (3.44) and (3.45), we found a variation of the focal distance of -0.05% and 5% respectively for a shift of the refractive index of -0.0021 and for an alteration of 5% of the sag profile. Ray-tracing simulations will be performed to check the validity of the thin lens approximation.

5.3.5. Ray-tracing simulations

Several Fresnel lens profiles have been investigated to determine the influence of the draft facet angle (δ), the Fresnel reflections (R_{Fr}), the pick and valley radius (r_{PV}), the longitudinal error on the sag profile (e) and the variation of refractive index (Δn) on the optical efficiency reaching the absorber of radius R_a placed at a back focal distance, *bfd* (80 mm for the design *bfd*).

Results are summarized in Table 5.5 and the encircled energy (valid for all simulated cases without shape error) is shown in Fig. 5.10.

Table 5.5: Influence of singlet parameters on the optical efficiency, back focal distance and collection radius

Singlet parameters					Optical efficiency [%]	bfd/80mm	R_a
δ [°]	R_{Fr}	r_{PV} [µm]	e [%]	Δn			
0	0	0	0	0.0	99.8	1	0.95
0	0	50	0	0.0	97.1	1	0.95
0	R(λ)	0	0	0.0	92.2	1	0.95
2	R(λ)	0	0	0.0	91.2	1	0.95
2	R(λ)	50	0	0.0	89.6	1	0.95
2	R(λ)	0	-5	0.0	91.2	1.07-1	0.95-1.90
2	R(λ)	0	0	-0.0021	91.2	1	0.95
2	R(λ)	50	-5	-0.0021	88.7	1.07-1	0.95-1.90

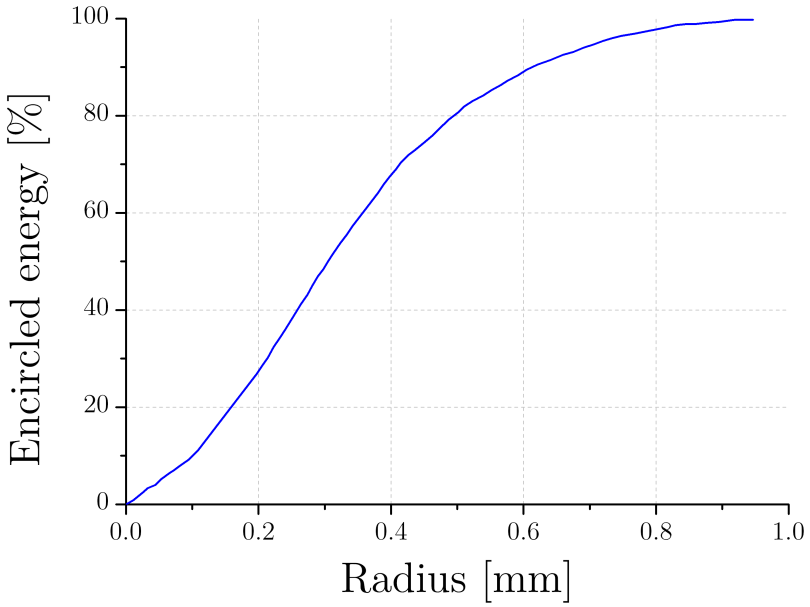

Fig. 5.10: Encircled energy on the absorber for the Fresnel singlet made of PMMA-3

The main contribution to the drop of optical efficiency comes from Fresnel losses: 7.8%. The pick and valley radius of 50 µm is responsible for a drop of 2.9%. The -0.0021 error on the refractive index has no observable influence on the flux reaching the absorber. The sag profile error however doubles the size of the collection radius if the absorber remains at the design focal plane. The sag error of 5% leads to a variation of the back focal distance by 7%. This is the only result that is not in good agreement with the theoretical approximations deduced in sub-chapters 5.3.3. and 5.3.4.. This can be explained by the double approximation performed: the paraxial approximation and the thin lens approximation. In these

approximations we calculated a variation of 5% of the focal distance instead of 7%.

The optical concentration factor lies around 400× if the whole flux reaching the absorber is considered. If we now consider 90% of the enclosed energy, the optical concentration factor is 870× [$=0.9 \cdot 0.9 \cdot (20/0.61)^2$].

5.4. Hybrid (refractive/diffractive) lens

Even though diffractive lenses present a high chromatic aberration, their small and negative Abbe number (-3.45) make them good candidates to be combined with a refractive lens. Contrary to purely refractive doublets, fast achromatic systems can be achieved by the combination of a converging diffractive lens with a converging refractive lens as shown in Fig. 5.11. Moreover, hybrid lenses can be athermalized, i.e., they can be designed to not be affected by temperature variation. But is it possible to design an athermal achromatic hybrid lens?

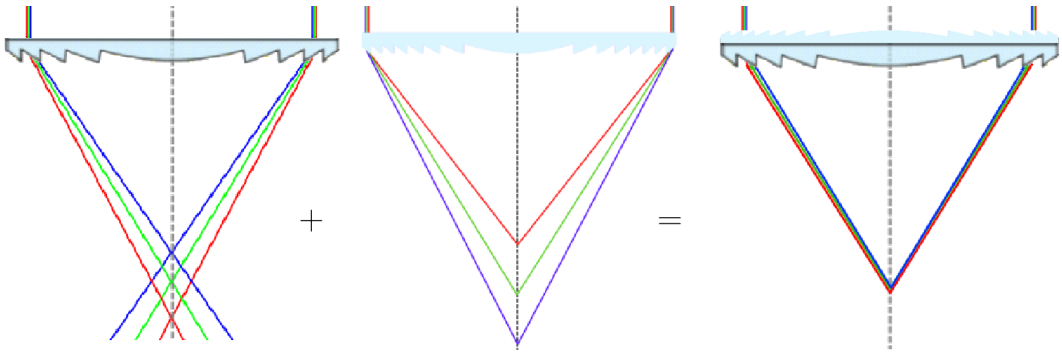

Fig. 5.11: Combination of a refractive lens and a diffractive lens to achieve and hybrid achromat.

5.4.1. New achromatization equation

From literature, it appears that an achromatic doublet is designed following the combination of the well-known achromatization equation

$$f_1 v_1 + f_2 v_2 = 0 \tag{5.6}$$

with the formula of the effective focal length

$$\frac{1}{f_{eff}} = \frac{1}{f_1} + \frac{1}{f_2} \tag{5.7}$$

In the vast majority of cases, the Abbe number is given for the wavelengths corresponding to the Fraunhofer d spectral line

$$v_d = \frac{n_d - 1}{n_F - n_C} \tag{5.8}$$

Implying that the doublet will have the chosen effective focal length at 587.56 nm and that wavelengths 486.13 nm and 656.27 nm will have their own same focal distance but different from the *d*-line and usually bigger [Lan11a]. Thus, not only the given effective focal length corresponds to an extremum (there is therefore no incentive to place the detector there) but nothing indicates that the two wavelengths of the denominator minimize the chromatic aberration especially if the spectral zone of interest is not the visible region. Moreover, Eq. (5.6) and (5.7) do not take into account the distance between the lenses. Hence, it is of interest to directly determine the focal distance of two desired wavelengths taking the thickness of the lens into account.

Before starting the calculation, let's define the geometry of a hybrid doublet,

- design wavelength: λ_1 and λ_2 with $\lambda_1 < \lambda_2$,
- focal length of the first and second lenses: $f_1(\lambda)$ and $f_2(\lambda)$,
- distance between the lenses: d,
- back focal lens: $bfl(\lambda_1) = bfl(\lambda_2) = bfl$.
- lenses are assumed to be thin
- both lenses have the same optical axis
- the incoming light is collimated and parallel to the optical axis

These parameters are depicted in Fig. 5.12.

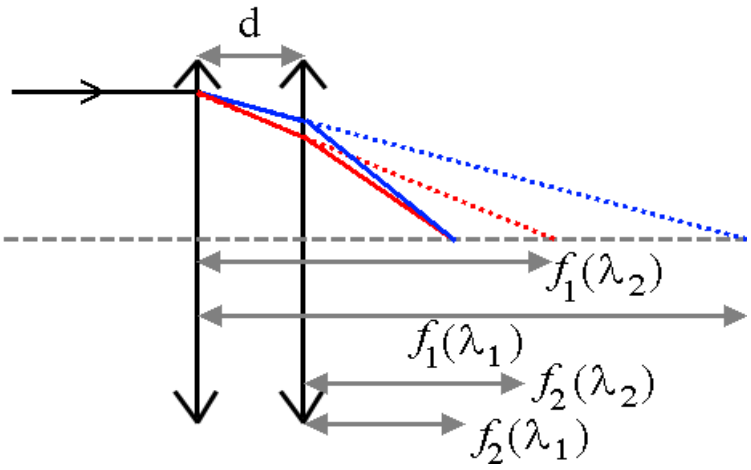

Fig. 5.12: Schematic representation of a hybrid lens

The sign convention used for the mathematical developments is the same as in

many books dedicated to optics like [Hec02]. Therefore the lens formula is

$$\frac{1}{f}=\frac{1}{s_o}+\frac{1}{s_i} \tag{5.9}$$

where s_o is the lens-object distance and s_i is the lens-image distance. No matter if the light strikes the refractive or the diffractive lens first the *bfl* is given by [Lan11a]

$$bfl=s_{i2}=\left(\frac{1}{f_2}+\frac{1}{f_1-d}\right)^{-1}=\frac{f_2(d-f_1)}{d-f_1-f_2} \tag{5.10}$$

For the sake of readability, the following simplified notation will be used

$$\begin{aligned} f_i(\lambda_j) &\stackrel{\text{def}}{\equiv} f_{ij} \\ n_i(\lambda_j) &\stackrel{\text{def}}{\equiv} n_{ij} \end{aligned}. \tag{5.11}$$

Let's also define the focal length variation coefficient γ and ζ with

$$f_{11}=\left(\frac{\lambda_2}{\lambda_1}\right)f_{12}=\gamma f_{12} \tag{5.12}$$

and

$$f_{22}=\left(\frac{n_{21}-1}{n_{22}-1}\right)f_{21}=\zeta f_{21}. \tag{5.13}$$

Combining Eqs. (5.10) and (5.9) leads to

$$f_{11}=\frac{(bfl+d)f_{21}-bfl\,d}{f_{21}-bfl}=\gamma\frac{(bfl+d)\zeta f_{21}-bfl\,d}{\zeta f_{21}-bfl}. \tag{5.14}$$

Performing the cross product and separating terms in f_{21}^2, f_{21}^1 and f_{21}^0, we obtain

$$\begin{aligned} 0=&f_{21}^2\left[(bfl+d)\zeta-(bfl+d)\gamma\zeta\right] \\ &+f_{21}\left[bfl\left(\gamma d+(bfl+d)\gamma\zeta-(bfl+d)-\zeta d\right)\right] \\ &+d\,bfl^2-\gamma\,bfl^2 d \end{aligned} \tag{5.15}$$

Thus

$$f_{21}=\frac{-B\pm\sqrt{B^2-4\,A\,C}}{2\mathrm{A}} \tag{5.16}$$

with

$$\begin{cases} A=(bfl+d)\left(\dfrac{n_{21}-1}{n_{22}-1}\right)\left(1-\dfrac{\lambda_2}{\lambda_1}\right) \\ B=bfl\left[d\left(\dfrac{n_{21}-1}{n_{22}-1}-\dfrac{\lambda_2}{\lambda_1}\right)+(bfl+d)\left(\dfrac{\lambda_2}{\lambda_1}\dfrac{n_{21}-1}{n_{22}-1}-1\right)\right] \\ C=d\,bfl^2\left(1-\dfrac{\lambda_2}{\lambda_1}\right) \end{cases} \tag{5.17}$$

Once f_{21} has been established, all other values can be determined with the above equations. Since $\lambda_1 < \lambda_2$ then $n_{21} > n_{22} > 1$, then A and C are always negative while B is always positive. From Eq. (5.6), f_{21} must be positive because and this system accepts only one solution:

$$f_{21}=\frac{-B-\sqrt{B^2-4\,A\,C}}{2\mathrm{A}} \tag{5.18}$$

5.4.2. Focal distances minimizing the LCA and upper limit of concentration factor

Hybrid (diffractive/refractive) lenses may be designed in one piece, in a single material, the focal distance of the diffractive part being independent of the material used (it only affects the diffraction efficiency). Due to the negative Abbe number of the diffractive lens both the diffractive and the refractive lenses are converging. In addition to being negative, the Abbe number of diffractive lenses is also small (-3.45) compared to the refractive regime. Hence, the focal distance of the diffractive lens is very long (about one order of magnitude higher) compared to the effective focal length of the hybrid lens.

Thanks to the achromatization equations, established in the previous section, we can now choose two wavelengths that focus on the absorber. Selecting adequately these design wavelengths allows to minimize the LCA^* and therefore to optimize the concentration ratio. Design wavelengths λ_0 and λ_0' have been determined for all eight OPs as well as the equivalent radius of curvature of the refractive lens, the LCA^* and the maximum concentration ratio. All these results are presented

in Table 5.6 and a graphical representation of the focal distance variation with wavelength is shown in Fig. 5.13.

Table 5.6 Relevant data about hybrid lenses

Material	$\lambda_0 - \lambda_0'$ [nm]	RoC^*_{eq} [%]	f_R*(550nm)	f_D* (550nm)	LCA^* [%]	C_{max}
PMMA-1	444 – 1239	51.3	1.039	36.57	1.423	4938
PMMA-2	446 – 1247	50.8	1.042	34.99	1.581	4000
PMMA-3	436 – 1223	50.4	1.034	44.21	1.450	4756
PMMA-4	446 – 1236	51.4	1.044	32.37	1.502	4432
PC-1	402 – 1177	66.8	1.136	13.201	4.954	407
PC-2	436 – 1125	63.8	1.081	19.387	2.992	1117
PC-3	434 – 1125	60.7	1.073	21.666	2.731	1341
PC-4	434 – 1123	60.5	1.079	20.139	2.965	1138

Looking at Table 5.6 it is clear that a hybrid lens made of PMMA offers a lower longitudinal chromatic aberration than a hybrid lens made of PC. In this case, ~96% of the focal power is due to the refractive lens (=1/f_R*).

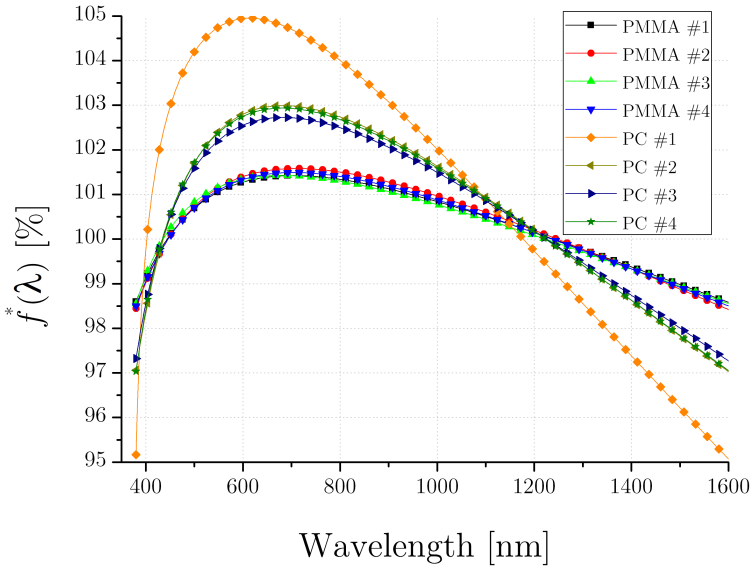

Fig. 5.13 Evolution of the focal distance for hybrid lenses made in PC and PMMA for the case minimizing the LCA^*.

5.4.3. Design of the hybrid doublet

Even if the hybrid lens made of PMMA-1 has a lower LCA^* than the hybrid lens made of PMMA-3, the relative difference is so small (<2%) that we decided to investigate the same material as for the singlet (i.e. PMMA-3).

Two different configurations are possible: the diffractive lens on top (diffractive lens facing the Sun) or the refractive lens on top. Looking at the focal power of both lenses into details, we realize that over the full spectrum of interest, the focal length of the diffractive lens is at least one order of magnitude higher than that of the refractive focal length.

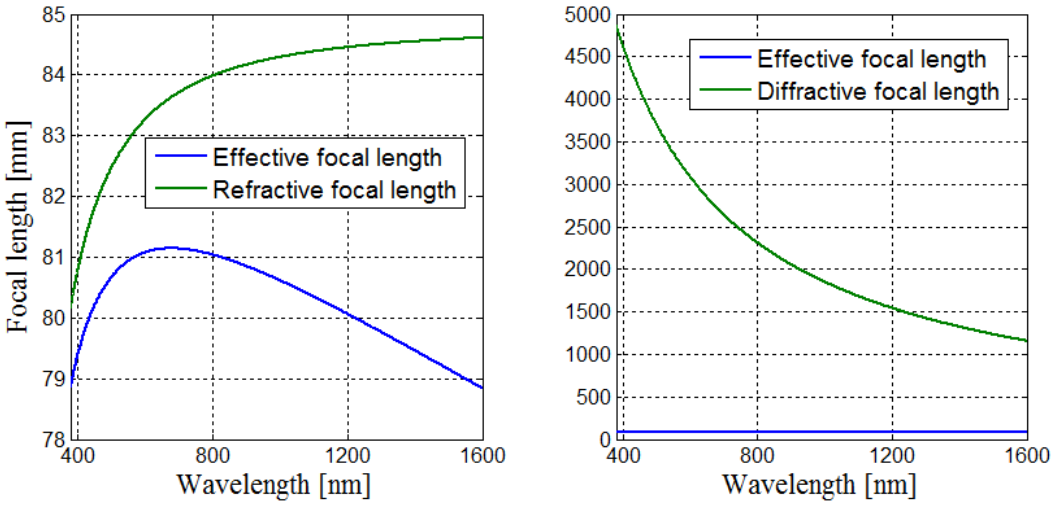

Fig. 5.14 Effective and refractive focal length (left) and effective and diffractive focal length (right)

It is therefore more convenient to have the diffractive lens on top since it was shown in Chapter 4.6.2. that the diffraction efficiency drops when the incidence angle increases.

5.4.3.1. Refractive part

The way of designing the refractive part of a flat hybrid lens is basically the same as for the purely refractive lens. The only thing that changes is the incidence angle of the incoming cone of light that is tilted by the diffractive lens as shown on Fig. 5.15.

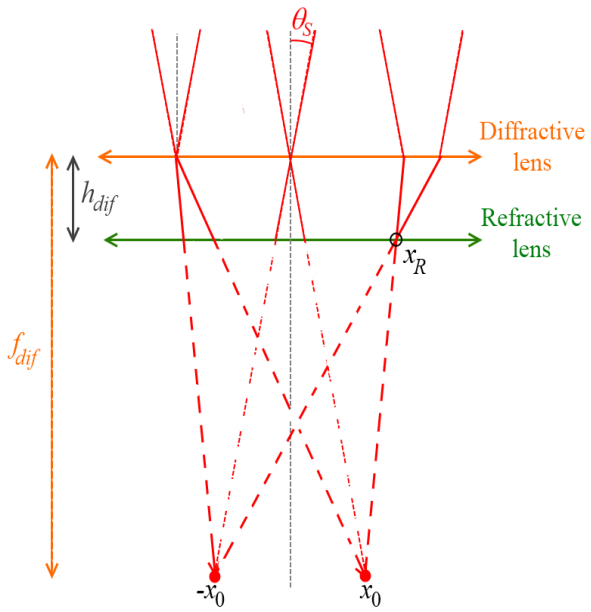

Fig. 5.15: Schematic design of a hybrid lens to illustrate the variation of angular incoming cone of light on the refractive lens (the deviation caused by the refractive lens has not been traced)

From the geometry of the above figure, the new cone of incidence (θ^-,θ^+) at the x_R coordinate becomes

$$\begin{cases} \theta^- = \text{atan}\left(\dfrac{x_R - x_0}{f_{dif} - h_{dif}}\right) \\ \theta^+ = \text{atan}\left(\dfrac{x_R + x_0}{f_{dif} - h_{dif}}\right) \end{cases} \tag{5.19}$$

where $x_0 = f_{dif} \tan \theta_S$. The design of the refractive part of the hybrid is therefore affected but only slightly since, once again, the focal length of the diffractive lens is very long compared to the refractive part.

We chose 680 nm as the design wavelength. This is because, at this wavelength, the hybrid lens made of PMMA-3 has its maximum LCA^*, it is thus better to have the minimum spot size at this wavelength. The design obtained using Newton's method is depicted in Fig. 5.16.

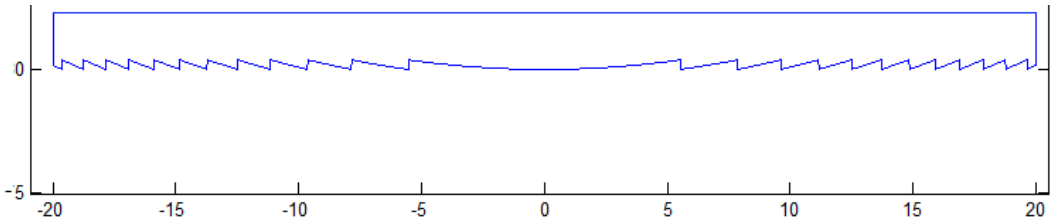

Fig. 5.16: Refractive part of the hybrid lens

5.4.3.2. Diffractive part

Remember that the pseudo-periodicity of the diffractive lens is entirely defined by the focal length and by the design diffraction order (the first order in our case like in most designs), see Eq (4.86). At 680 nm, the focal length of the diffractive lens is 2.722 meters (f/68.05 lens). In this case, the number of zones is 108.

Regarding the diffractive lens, only the diffraction efficiency has to be optimized. We performed the optimization in the scalar regime for a monolayer and a bilayer considering the black-body spectrum of 5780 K. The monolayer is made of PMMA-3 and the bilayer is made of PMMA-3 and PC. The four PCs have been tested for the optimization of the bilayer. Relevant data are shown in Table 5.7

Table 5.7 Relevant data about the efficiency of a monolayer diffractive lens made of PMMA-3 and bilayer diffractive lenses made of PMMA-3 and PC.

Material 1	Material 2	λ_1; λ_2 [nm][1]	h_{PMMA}; h_{PC} [µm][2]	η_{sol} [%][3]
PMMA-3	None	603	1.24	70.5
PMMA-3	PC-1	458; 830	24.29; -19.08	90.7
PMMA-3	PC-2	442; 799	23.67; -18.45	91.3
PMMA-3	PC-3	442; 800	29.58; -23.31	91.1
PMMA-3	PC-4	440; 796	25.26; -20.79	90.8

[1] optimized design wavelengths.
[2] optimized thickness of PC and PMMA
[3] Diffraction efficiency integrated on a 5780 K black-body spectrum

The diffraction efficiency of the different optimized designs is depicted in Fig. 5.17.

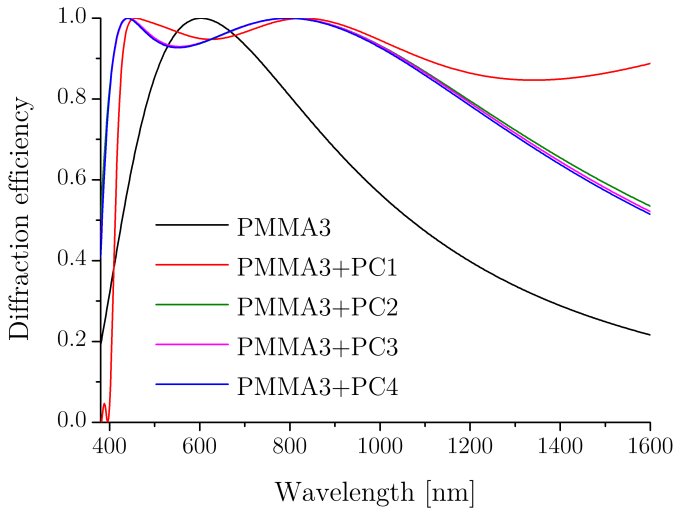

Fig. 5.17: Diffraction efficiency of the optimized designs including PMMA-3

The use of a bilayer diffractive lens is needed to exceed 90% of scalar diffraction efficiency. Among the four combinations of PMMA and PC, it appears in Fig. 5.17 that PMMA3-PC1 has very low diffraction efficiency under 400 nm and has to be rejected. The three other combinations are almost equivalent but the combination of PMMA-3 with PC-2 has the higher diffraction efficiency and the lower teeth thickness, which is easier to manufacture. We will therefore use this combination.

5.4.3.3. Whole design

Two different designs are of interest, each having its pros and cons.

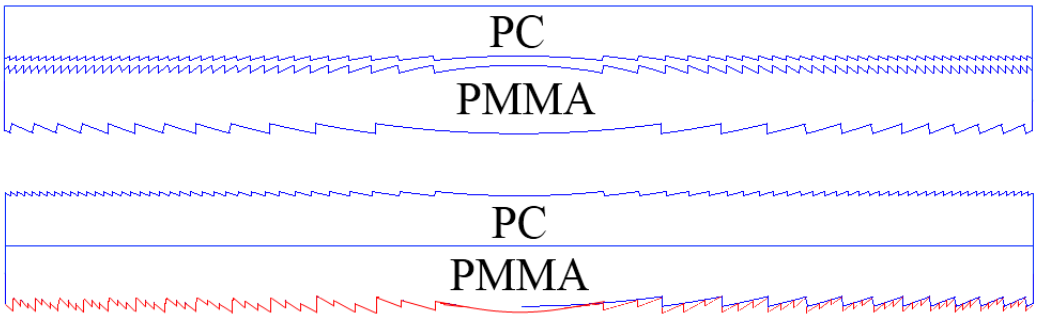

Fig. 5.18: Two different bilayer hybrid lenses. Refractive structure is depicted to scale, and the diffractive structures are purely schematic.

The first design, on the top in Fig. 5.18, has a flat interface facing the Sun avoiding problem of soiling. Moreover the distance between the two diffractive structures can be reduced to a few microns. On the other hand, two new interfaces PC/air, PMMA/air are needed, leading to higher reflection losses.

The second design, at the bottom of Fig. 5.18 has a textured surface facing the Sun which is prone to soiling problem. The other textured surface is superimposed to the refractive surface. Thus, the distance between the two diffractive structures can hardly be reduced to less than 2 millimetres. On the other hand, it suffers from fewer Fresnel reflection losses than the first design and has fewer interfaces to manufacture.

5.4.4. Athermal design

The change of focal distance with temperature is one concern in CPV where solar panels are supposed to work in the summer as well in the winter. Hybrid glass lenses offer the possibility to achieve athermal designs. What about hybrid lenses in polymer? The method we will develop to answer this question is borrowed from London *et al.* [Lon93] and is slightly adapted to be in accordance with our surface relief diffractive lenses.

To obtain an athermal design, the thermal defocus coefficient of the refractive lens given by Eq. (3.49)

$$\alpha_{TD}^{r}=\alpha_{L}-\frac{1}{n-1}\frac{dn}{dT} \tag{3.49}$$

must be compensated by the thermal defocus coefficient of the diffractive lens, α_{TD}^{d}. To determine an equation for α_{TD}^{d} we express the focal length of the diffractive lens as[11]

$$f^{d}(\lambda)=\frac{r_{Z1}^{2}}{2\lambda} \tag{5.20}$$

where r_{Z1} is the radius of the first diffractive zone. The differentiation of the above equation per unit of focal length corresponds to the definition of α_{TD}^{d}:

$$\alpha_{TD}^{d}=\frac{1}{f_{d}}\frac{df_{d}}{dT}=\frac{1}{f_{d}}\frac{r_{z1}}{\lambda}\frac{dr}{dT}=\frac{1}{f_{d}}\left\{\frac{r_{Z1}}{\lambda}\frac{r_{Z1}}{2}\right\}\frac{2}{r_{Z1}}\frac{dr}{dT}=\frac{2}{r_{Z1}}\frac{dr}{dT}=2\alpha_{L} \tag{5.21}$$

It is shown in Annex III.6 that the variation of the refractive index with temperature can be expressed as a function of the linear thermal expansion coefficient α_{L}:

11 According to Eq. (4.86), $r_{m}=\sqrt{2m\lambda_{0}f_{0}+(m\lambda_{0})^{2}}$ so $r_{Z1}=\sqrt{2\lambda_{0}f_{0}+(\lambda_{0})^{2}}$ with $f_{0}\gg\lambda_{0}$

$$\frac{dn}{dT}=-\alpha_L\frac{(n^2+2)(n^2-1)}{2n}. \tag{5.22}$$

So, if we impose that the effective focal length is not affected by a temperature variation

$$\frac{df_{eff}}{dT}=0\Leftrightarrow\frac{d\Phi_{eff}}{dT}=\frac{d\Phi_r}{dT}+\frac{d\Phi_d}{dT}=0, \tag{5.23}$$

we obtain[12]

$$\begin{aligned}\frac{2\alpha_L}{f_d} &= \frac{1}{f_r}\left(\frac{1}{n-1}\frac{dn}{dT}-\alpha_L\right)\\ &= -\alpha_L f_r\left(\frac{(n^2+2)(n^2-1)}{2n(n-1)}+1\right),\end{aligned} \tag{5.24}$$

which reduces to

$$\frac{f_r}{f_d}=-\frac{1}{2}\left(\frac{(n^2+2)(n+1)}{2\mathrm{n}}-1\right) \tag{5.25}$$

or equivalently to

$$\frac{f_r}{f_d}=-\frac{(n^2+2)(n+1)+2n}{4n}. \tag{5.26}$$

For a refractive index of 1.494, f_r/f_d=-2.266. As a result, it is possible to achieve an achromatic hybrid lens made of polymer combining a converging lens and a diverging lens. However, it was calculated that an achromatic hybrid lens is made of two converging components. It is thus impossible to design an athermal achromat in a single hybrid lens made of polymers.

Since losses due to thermal aspects are about 1% (see Chap. 3.3.3.), we will no longer dwell on athermal designs.

[12] $\Phi=\frac{1}{f}\Rightarrow d\Phi=\frac{d\Phi}{df}df=\frac{-1}{f^2}df\Rightarrow\frac{1}{\Phi}d\Phi=\frac{-1}{f}df$

5.4.5. Minimal losses

In addition to the physical phenomena responsible for optical losses in refractive lenses, hybrid lenses suffer from a loss of diffraction efficiency which cannot be calculated as easily as geometrical losses. Indeed, diffraction losses depend on the width of the diffractive teeth which changes depending on its radial position, its shape and the illumination wavelength. Based on certain assumptions, we will estimate the diffraction losses.

At 680 nm, the focal length of the diffractive lens is 2.722 meters (f/68.05 lens). From then on, the diffractive lens is composed of 108 zones whose widths are represented in the figure hereunder.

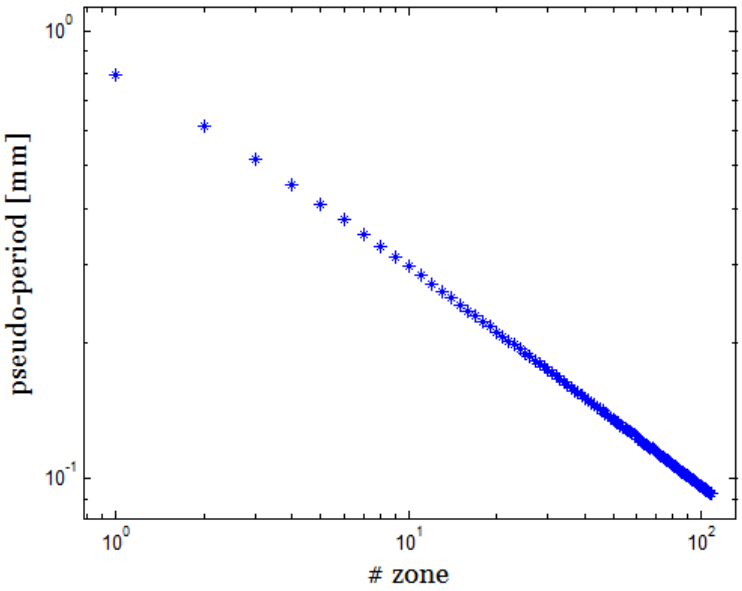

Fig. 5.19: Size of the zones forming the diffractive lens of the f/2 hybrid lens

The first zone and the last zone are respectively 800 µm and 92 µm wide. The smallest pseudo-period-to-wavelength ratio is 92/1.6 = 57.5 which is not in accordance with Fig. 4.19 showing that a ratio of 100 is required to obtain 90% of the maximum diffraction efficiency for a bilayer. For the design on hand, the thicknesses of the two layers are different from those in Fig. 4.19. New simulations results are shown in Fig. 5.20. We can see that the diffraction efficiency reaches 66% of the scalar value for a period-to-wavelength ratio of 57.5.

Thus, the high diffraction efficiency condition, i.e. $\Lambda/\lambda>100$, is not fulfilled for a wavelength of 1600 nm from the 160 µm wide 36$^{\text{th}}$ zone, situated at 1 cm from the centre of the lens. However, for all wavelengths shorter than 920 nm, the above condition is fulfilled for all radial coordinates.

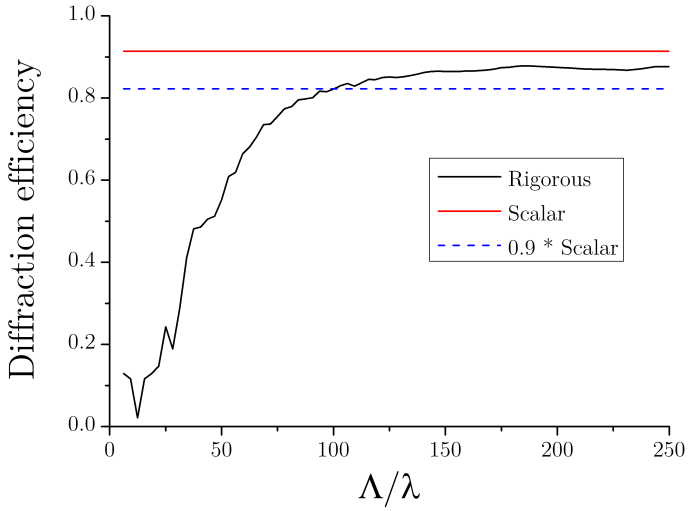

Fig. 5.20: Diffraction efficiency evolution with period for a bilayer made of PMMA (23.67µm thick) and PC (-18.45.µm thick)

To determine the maximum diffraction efficiency value that can be achieved with this $f/2$ hybrid lens, let's assume that all wavelengths have a diffraction efficiency corresponding to the rigorous diffraction efficiency shown in Fig. 5.20. We are thus able to determine the diffraction efficiency in every point of the lens for all wavelengths. Two graphs are shown in Fig. 5.21. On the left side, the mean diffraction efficiency (for wavelengths from 380 to 1600 nm) is given as a function of the radial position and on the right side the mean diffraction efficiency is given for all wavelengths.

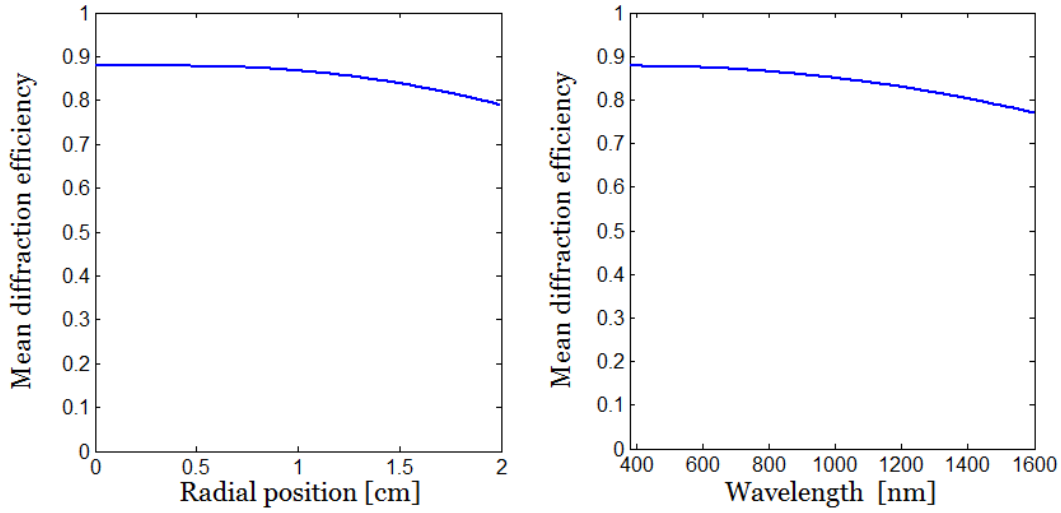

Fig. 5.21: Mean diffraction efficiency as a function of the radial position (left) and as a function of the wavelength (right)

In the worth case, i.e. at 1600 nm, the diffraction efficiency is 11% under the maximum. The diffraction efficiency integrated over the full lens over the full spectrum is 85.95% and 84.92% for a 1D and 2D lens respectively. Note that these

calculations do not take into account the weight of wavelengths due to the black-body spectrum nor the real diffraction efficiency (with draft angle, rounded tip and other manufacturing errors) that would have led to an even lower value of the real global diffraction efficiency due to manufacturing error e.g.

Up to now, only the first diffraction order was considered as optically useful. However, we are dealing with nonimaging optics and every single ray reaching the absorber counts. Indeed, a non-negligible part of the zero and second order of diffraction also reaches the absorber. Let's consider only on-axis beams and a geometrical concentration of 2500×. Depending on their LCA^*, some rays will miss the absorber, some will reach it as shown in Fig. 5.22.

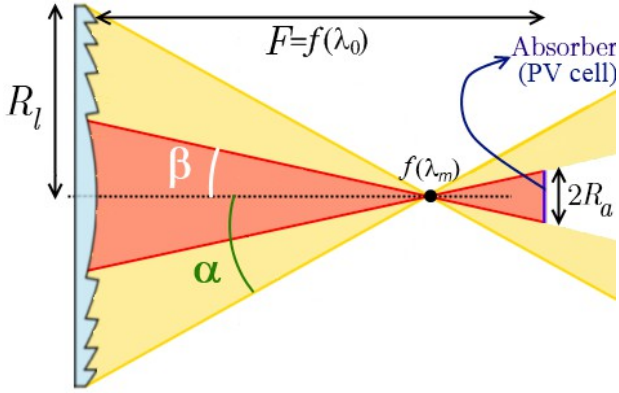

Fig. 5.22: Beams in red, included in a view angle α from the focal point, reach the absorber while beams in yellow, included in a view angle β, miss it.

The geometrical efficiency, that we defined as the optical efficiency divided by the transmittance can be calculated as follows

$$\eta_{geo}(\lambda)=\frac{\eta_{opt}}{T(\lambda,r)}=\frac{\tan(\beta)}{\tan(\alpha)}\bigg|_{\leqslant 1}=\frac{R_a}{R_l}\frac{f(\lambda)}{\left|f(\lambda_0)-f(\lambda)\right|}\bigg|_{\leqslant 1} \tag{5.27}$$

where $f(\lambda_0)$ corresponds to the position of the absorber. The geometrical concentration factor only depends on the geometrical concentration factor and the wavelength. Assuming a geometrical concentration ratio and making use of Eq. (5.27) we are able to determine the optical efficiency as a function of the wavelength. For example, for a geometrical concentration ratio of 2500×, Fig. 5.23 shows the geometrical efficiency of order 0, 1 and 2. Unfortunately, the energy diffracted in orders other than 1 is mainly dissipated in the 0 order for long wavelengths and in the second order for short wavelengths (see Fig. 5.24).

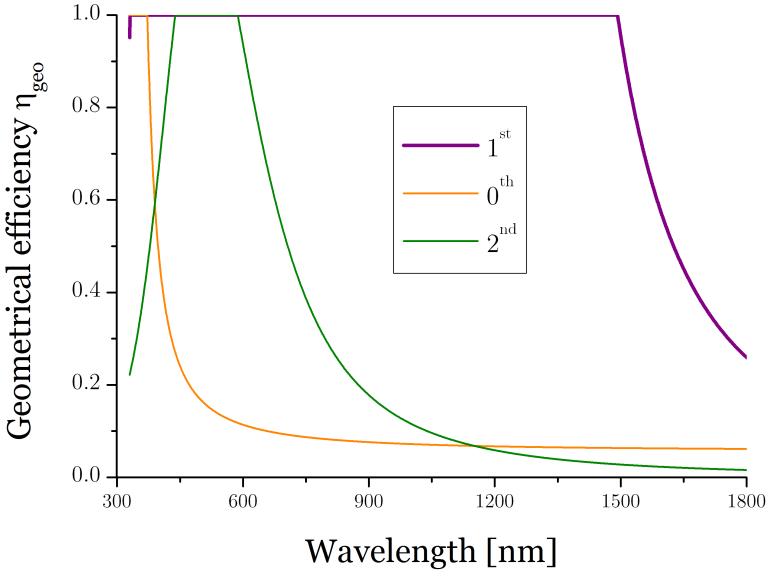

Fig. 5.23: Geometrical efficiency of order 0, 1 and 2 for an optimized hybrid lens made of PMMA-3

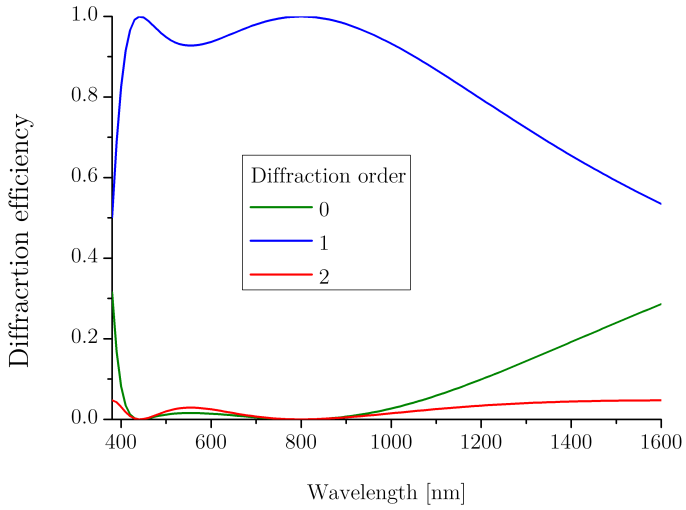

Fig. 5.24: Scalar diffraction efficiency at the 0th, 1st and 2nd order

Anyway, the diffraction efficiency is too critically low to see hybrid lenses compete with the purely refractive designs on the CPV market. The optimal optical efficiency is at best 78%[13], regardless of the shape error and of optical losses due to the refractive Fresnel lens.

13 Obtained by multiplying 0.8492 by 0.91, corresponding to the rigorous diffraction efficiency taking the period-to-wavelength ratio into account and the scalar diffraction efficiency depending on the wavelength and on the weight attributed to each wavelength relative to the black-body spectrum.

5.4.6. Refractive index and shape error tolerance

For the refractive structure, the manufacture tolerance is the same as for the singlet lens. But what about the diffractive structure? Assuming an error of 1% (0.24 µm) only on the thickness of the PMMA teeth, the diffraction efficiency drops from 100% to 88.6%. For an error of 2% the diffraction efficiency drops to 60% and for an error of 5% (1.18 µm) it decreases to almost zero (0.22%)! The bilayer diffractive lens is thus extremely sensitive to shape errors. The error on the refractive part is negligible compared to the drop of diffraction efficiency illustrated in Fig. 5.25.

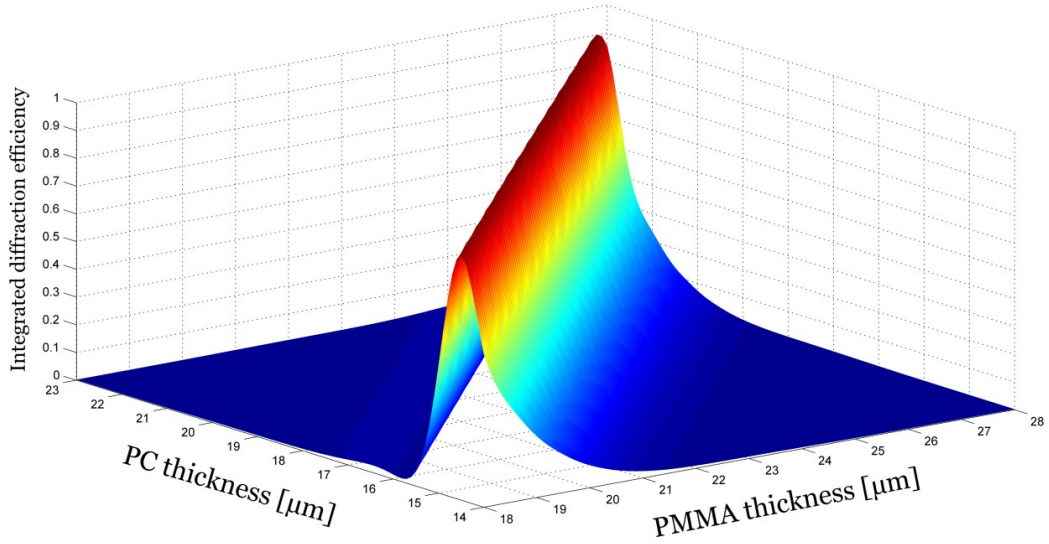

Fig. 5.25: Scalar diffraction efficiency (integrated from 380 to 1600 nm) for a range of PC and PMMA thicknesses

Regarding the refractive index, an alteration of -0.0021 on the PMMA and -0.0024 on the PC lead to a drop of ~6.5% and 3% at the design wavelengths (respectively 442 and 799 nm).

5.4.7. Ray-tracing simulations

In the following results, only the ideal diffractive lens has been simulated. Indeed, although it is possible (but time consuming) to simulate the diffractive behaviour of diffractive lens with ASAP (the ray-tracing software used at Hololab), ASAP does not calculate the diffraction efficiencies. To avoid time consuming calculations we used the Sweatt model to simulate the diffractive lens (see Chap. 4.8.). Moreover, there is no need to perform ray-tracing simulations of the effects of manufacturing error on the diffractive lens: the variation of refractive index affects the diffraction efficiency of the diffractive lens, without affecting the focal length. The shape error also, which is only axial in our simulations, affects the

diffraction efficiency without changing the focal length.

Due to the use of the Sweatt model, the Fresnel losses cannot be taken into account, so the reflection losses are set to zero. Relevant data about hybrid lens performance simulated by ray-tracing are listed in Table 5.8

Table 5.8: Influence of singlet parameters on the optical efficiency , back focal distance and collection radius of an hybrid lens (with an ideal diffractive lens)

Singlet parameters					Optical efficiency [%]	*bfd*/80mm	R_a [mm]
δ [°]	R_{Fr}	Δn	*e* [%]	r_{pv} [µm]			
0	0	0.0	0	0	99.7*	1	0.73
2	0	0	0	0	98.6	1	0.73
2	0	-0.0021	0	0	98.6	1	0.80
2	0	0	-5	0	98.6	1 – 1.0469	1 49 - 0.77
2	0	0	0	50	96.0	1	0.79

*Losses are due to an artefact from ASAP: for profile with high discretization level, beams hitting exactly one point of the profile is lost;

The enclosed energy at the absorber level produced by the perfect hybrid lens is shown in Fig. 5.26 hereunder.

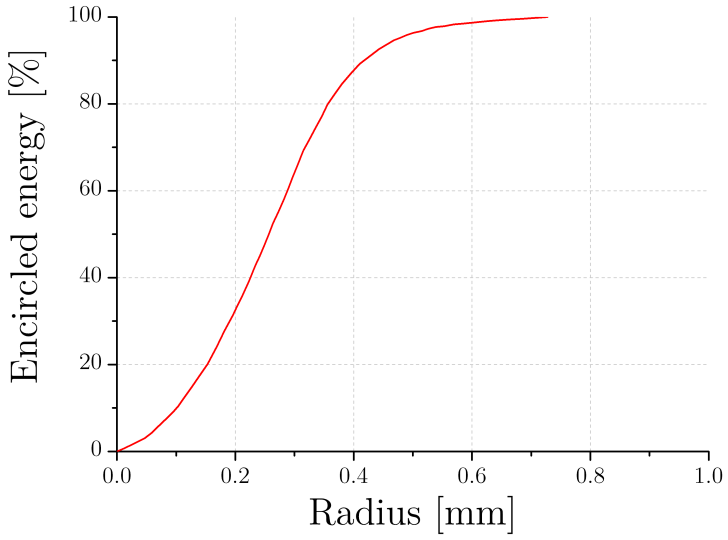

Fig. 5.26: Encircled energy reaching the absorber

The whole energy is enclosed in a radius of 0.73mm, corresponding to a geometrical concentration of 750×. At 90% of the enclosed energy, this ratio rises up to 2270×.

5.5. Refractive doublet

5.5.1. New achromatization equation

The calculations leading to the achromatization equation are considerably similar to the hybrid case. Only Eq. (5.12) will turn into

$$f_{11}=\left(\frac{n_{12}-1}{n_{11}-1}\right)f_{12}=\zeta f_{12} \tag{5.28}$$

The same assumptions as for the hybrid lens are made:

- design wavelength: λ_1 and λ_2 with $\lambda_1 < \lambda_2$,
- focal lens of the first and second lens: $f_1(\lambda)$ and $f_2(\lambda)$,
- distance between the lenses: d,
- back focal lens: $bfl(\lambda_1)=bfl(\lambda_2)=bfl$.
- lenses are assumed to be thin
- the diverging and converging lens have the same optical axis
- the incoming light is collimated and parallel to the optical axis

These parameters are depicted in Fig. 5.27.

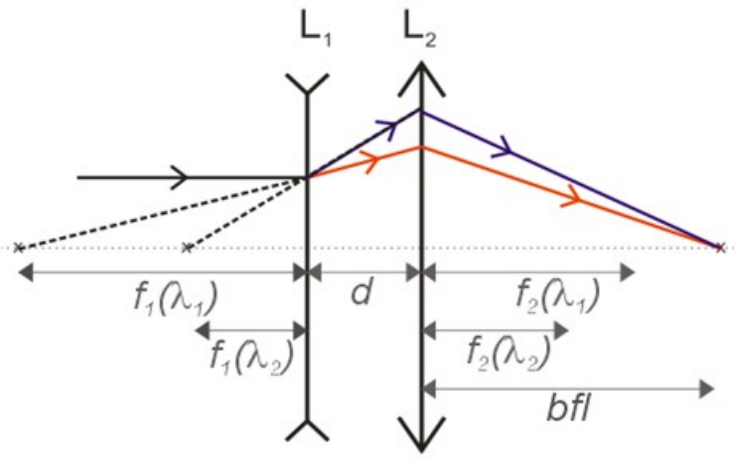

Fig. 5.27: Schematic representation of a refractive doublet

The expression of the second focal distance for the first design wavelength is exactly the same as Eq. (5.16)

$$f_{21}=\frac{-B\pm\sqrt{B^2-4\,A\,C}}{2\mathrm{A}} \tag{5.29}$$

with

$$\begin{cases} A=(bfl+d)\left(\dfrac{n_{21}-1}{n_{22}-1}\right)\left(1-\dfrac{n_{12}-1}{n_{11}-1}\right) \\ B=bfl\left[d\left(\dfrac{n_{21}-1}{n_{22}-1}-\dfrac{n_{12}-1}{n_{11}-1}\right)+(bfl+d)\left(\dfrac{n_{12}-1}{n_{11}-1}\dfrac{n_{21}-1}{n_{22}-1}-1\right)\right] \\ C=d\,bfl^2\left(1-\dfrac{n_{12}-1}{n_{11}-1}\right) \end{cases} \tag{5.30}$$

Once f_{21} has been established, all other values can be determined with the above equations. Since $\lambda_1 < \lambda_2$ then $n_{11} > n_{12} > 1$ therefore A and C are always positive while B depends on the materials used. If the first material – of refractive index $n_1(\lambda)$ – has a dispersion higher than $n_2(\lambda)$, B will be negative and thus $f_2(\lambda)$ will be positive. This system has two solutions depending on the sign chosen in Eq. (5.29). If d is set to zero, then only the plus sign is valid, this solution minimizes the secondary error. If the minus sign was chosen, both f_1 and f_2 would be small compared to the *bfl*. Therefore the use of the minus sign is definitively not the best solution. To get some orders of magnitude, the achromatization of a doublet made of PC and PMMA was performed for λ_1=405 and λ_2=650 nm. Difference of design and performance are given in Table 5.9 and Fig. 5.28.

Table 5.9 Design and performance comparison of two doublets achromatized for the same wavelengths made of the same materials (PC and PMMA)

	minus sign case	plus sign case
*RoC** PC [%]	-4.88	-35.63
*RoC** PMMA [%]	5.91	19.96
Maximum *LCA** [%]	1.52	0.5

* denotes that values are given relatively to the *bfl*

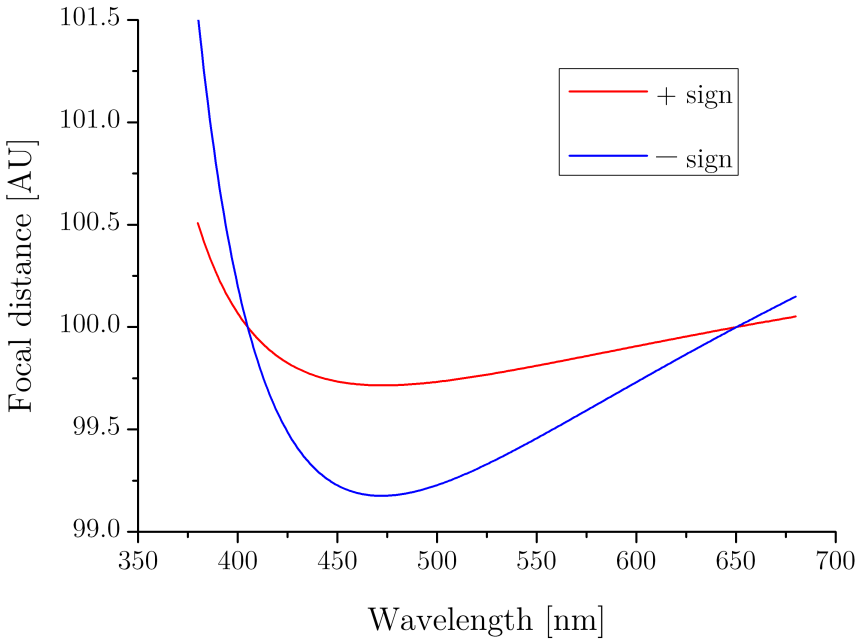

Fig. 5.28: Comparison of the two solutions of Eq. (5.29) regarding the achromatization equation. The doublets were optimized for wavelengths 405 and 650 nm

5.5.2. Focal distances minimizing the LCA and upper limit of concentration factor

We have four different PMMAs and four different PCs available. All 16 combinations of PC/PMMA were tested and optimized to decrease the LCA^*. Results are depicted in Fig. 5.29 and relevant data are provided in Table 5.10.

Table 5.10: Relevant parameters for several combinations of PCs and PMMAs optimized for achromatic doublets

PMMAs	PCs				Best C_{max} (line)
	PC-1	PC-2	PC-3	PC-4	
PMMA-1	1.221 (386 – 711) -114.8, 32.5	0.421 (406 – 1033) -56.4, 24.1	0.570 (402 – 1087) -41.4, 20.8	0.544 (400 – 1063) -49.7, 23.1	56 420
PMMA-2	1.260 (386 – 641) -106.7, 31.3	0.344 (400 – 693) -51.4, 22.7	0.501 (396 – 745) -37.4, 19.4	0.483 (396 – 739) -45.2, 21.7	84 505
PMMA-3	0.788 (386 – 551) -137.9, 34.1	0.124 (432 – 1107) -74.0, 27.1	0.084 (456 – 943) -56.0, 24.2	0.068 (468 – 961) -64.7, 26.1	2 137 410
PMMA-4	1.571 (387 – 806) -94.8, 30.2	0.792 (408 – 1157) -42.4, 20.5	1.081 (404 – 1175) -29.6, 16.9	0.978 (402 – 1159) -37.0, 19.5	15 942
Best C_{max} (column)	16 105	650 360	1 417 233	2 137 410	

The five values in a single cell are: $|LCA^*_{max}|$ [%] (λ_0 – λ'_0 [nm]), RoC^*_{eq}(PC), RoC^*_{eq} (PMMA)

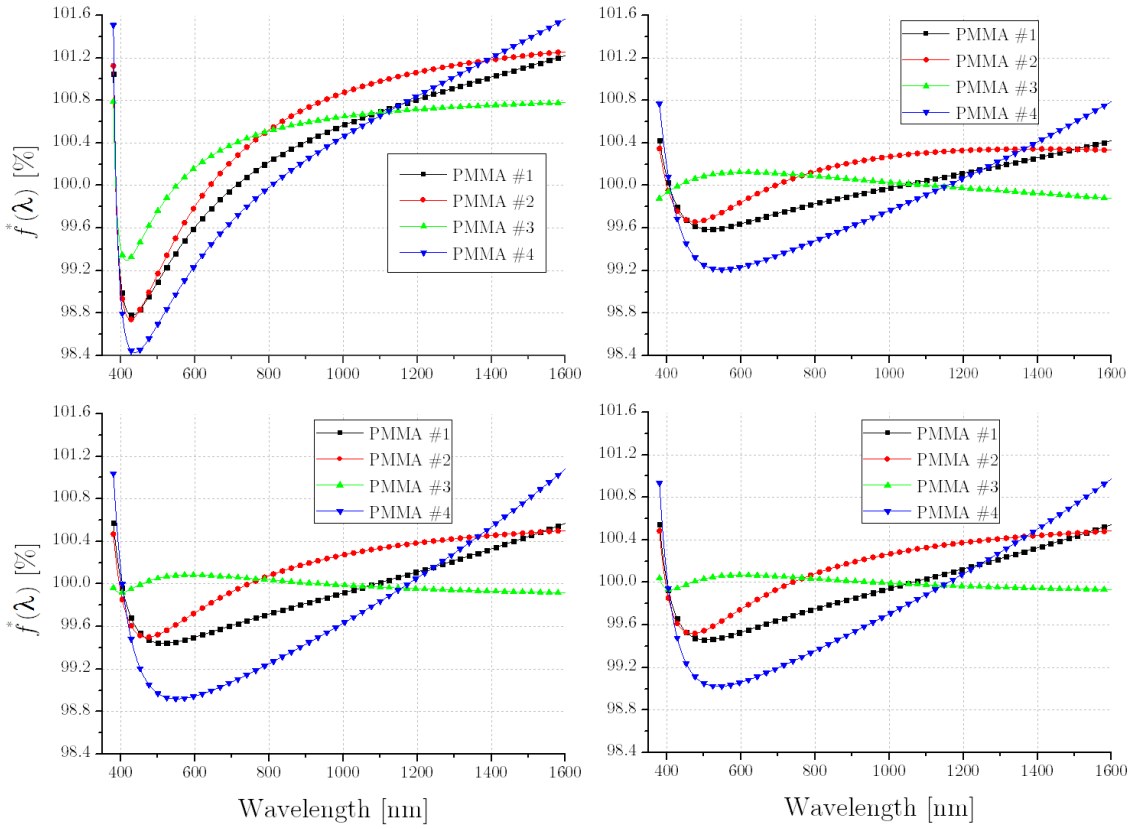

Fig. 5.29: Doublets with PC-1 (top left), PC-2 (top right), PC-3 (bottom left) and PC-4 (bottom).

Table 5.10 clearly shows that achromatic doublets allow for a very high concentration, up to 2 millions for on-axis collimated beams.

5.5.3. Design of flat achromatic Fresnel doublets

Several achromatic Fresnel doublets can be designed. We proposed four different $f/2$ flat Fresnel designs that will be compared with their equivalent non-Fresnel (nF) designs, see Fig. 5.30. All doublets are composed of a converging lens in PMMA and a diverging lens in PC.

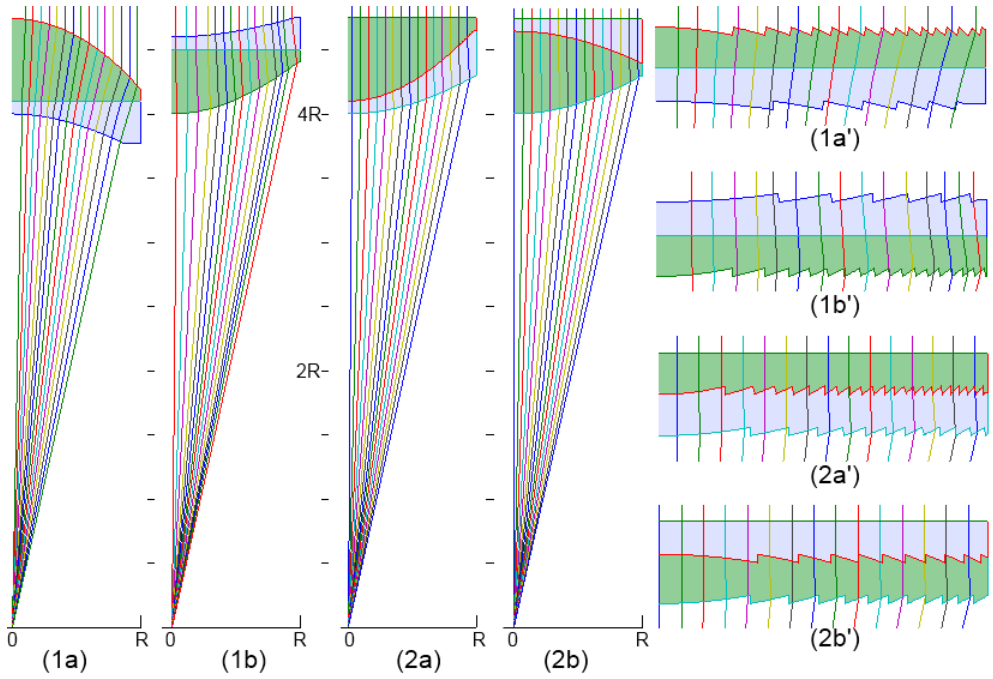

Fig. 5.30: Four kinds of non-Fresnel doublets [(1a) to (2b)] and their Fresnel equivalent [(1a') to (2b')]. Green coloration corresponds to PMMA and blue to PC

The doublets are designed for collimated beams under normal incidence. All achromatic doublets have two free parameters: the curvature of the first textured interface and the curvature of the second textured interface. We could therefore impose that two wavelengths focus perfectly on the absorber as shown on Fig. 5.31

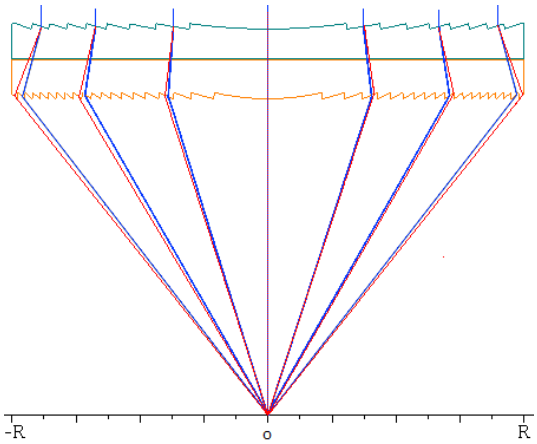

Fig. 5.31: Schematic achromatic Fresnel doublet (not to scale)

The flowchart of the program that designs an achromatic Fresnel lens is given hereunder, with α is the slope angle of the first textured interface, β the angle of the second textured interface and x is the radial position.

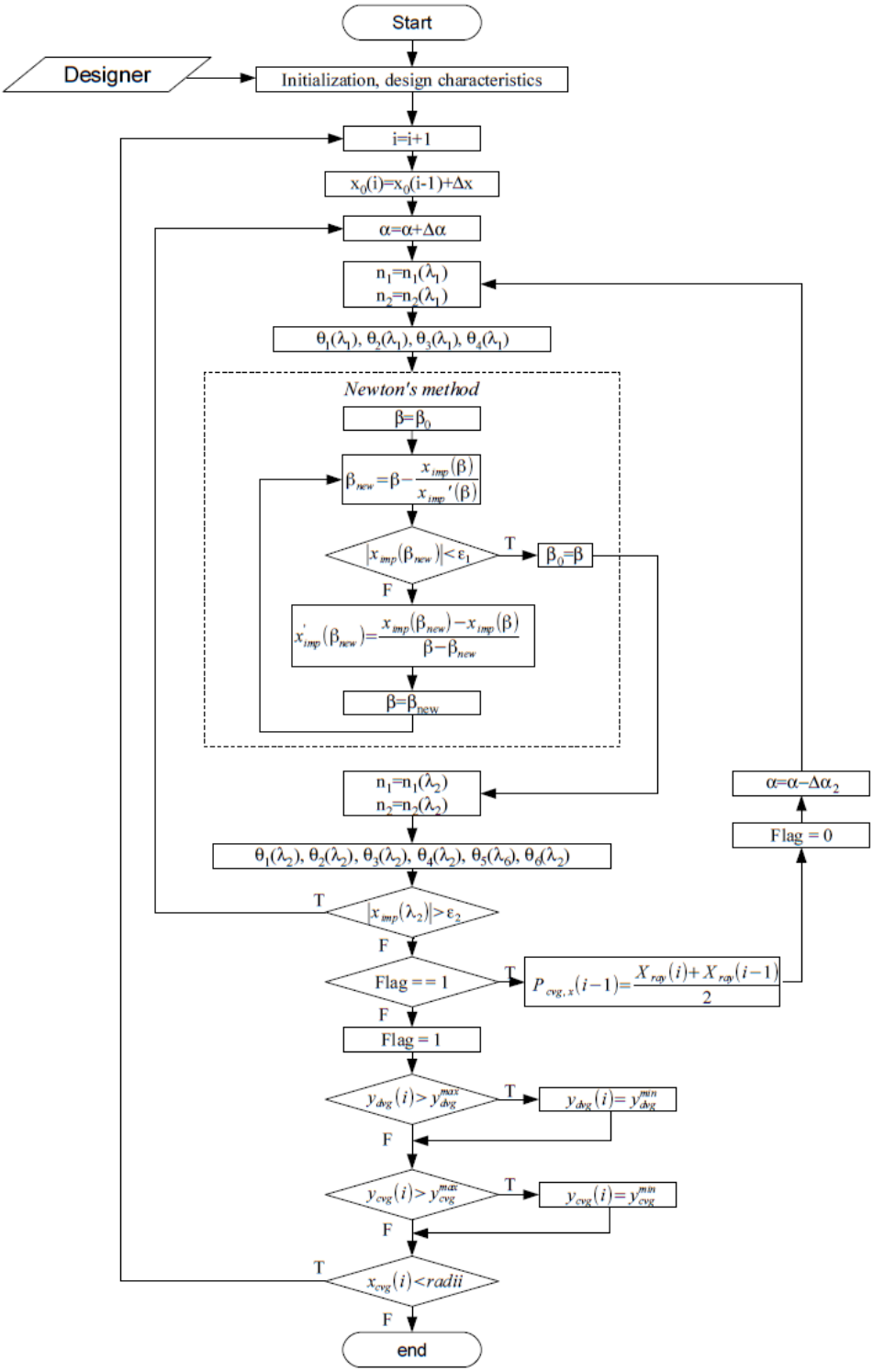

Fig. 5.32: Flowchart of a program designing an achromatic Fresnel doublet

5.5.4. Design comparison and minimal losses for Fresnel and non-Fresnel doublets

There is a concern about the optical losses in Fresnel doublet. Indeed, Fresnel doublets have a smaller radius of curvature compared to a singlet with the same *f*-number. Therefore a higher number of teeth is needed, leading to higher optical losses. Also, sources of optical losses are more numerous: diverging rays inside the lens could reach the border of the lens, moreover on-axis rays could be refracted towards the draft facets of the interface itself. However, the Fresnelization of the last interface does not induce optical losses: incoming rays are always directed towards the active facet (see Fig. 5.30). Moreover, compared to nF achromatic doublets, the distance that rays travel inside the lens is shorter, there is thus less absorption and fewer diverging rays are lost at the edge of the Fresnel lens. Let's take a closer look at these optical losses.

For an easier reading, designs will be denominated following their texturation: TFT for Teeth-Flat-Teeth designs and FTT for Flat-Teeth-Teeth designs. For these two kinds of designs, the first lens may be either converging (in PMMA) either diverging (in PC).

For TFT designs, shown on Fig. 5.33, the first interface refracts the beams towards the draft facet, leading to optical losses. This allows to open the draft angles, facilitating the ejection of the insert during the injection moulding phase. It also implies, to a certain extent, that the pick radius has no influence on the optical efficiency. If the diverging lens is situated on the top, a part of the incoming flux reaches the edge of the lens and will not be focused on the absorber. The thinner the lens the lower the optical losses which is to the advantage of Fresnel lenses compared to nF lenses.

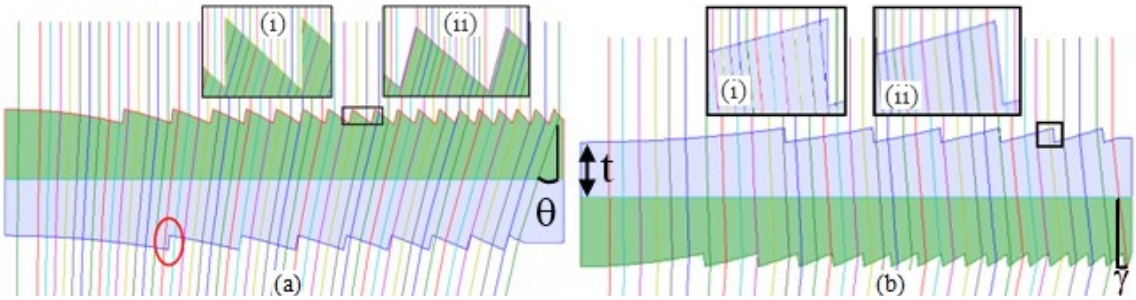

Fig. 5.33: TFT designs. (a) PMMA-top and (b) PC-top. The draft angle of the top lens may be open: zooms (i) and (ii). No optical loss due to the bottom draft angle (encircled in red)

Regarding FTT designs, depicted in Fig. 5.34, both suffer from losses due to diverging rays. However, the divergence angle is smaller than for TFT and the losses occur only inside the second lens. The design with PMMA on top presents

optical losses at the PMMA/PC interface which is not the case for the other design. As well as for the TFT designs, there is no optical loss due to the draft facet of the bottom lens.

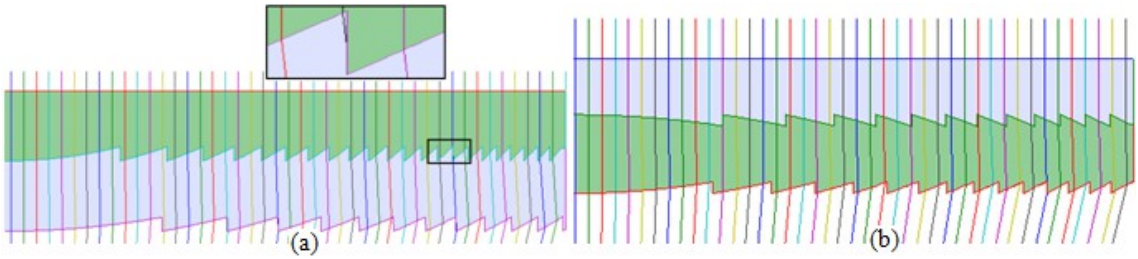

Fig. 5.34: FTT doublets: (a) PMMA-top and zoom on the intermediate teeth, (b) PC-top.

Regardless of the pick and valley radii, FTT designs have fewer optical losses than a TFT design (with the same design parameters). FTT also experience fewer optical losses for diverging border rays than TFT with PC on top, but more than TFT with PMMA on top.

The performance of a doublet is also linked to the discretization of the Fresnel ring (i.e. the segment size) of each lens of the doublet. The top lens may have a discretization as high as desired. The discretization of the bottom lens is limited by the maximum difference of impact ($|P_1P_2|$ in Fig. 5.35) between the rays at the extreme wavelengths coming from the same incoming ray. For a given segment of lens having an angle β with the detector, two wavelengths strike this segment with their own angle of incidence (θ_r and θ_b), that remains the same along the whole segment $|P_1P_2|$ in first approximation. If the detector is centred on the output beams, the detector size must be larger than the lateral spread s given by Eq. (5.31) with parameters in accordance with Fig. 5.35.

$$s = \left(\frac{\sin(\theta_r - \beta)}{\sin(\theta_r)} \frac{\sin(\theta_b - \beta)}{\sin(\theta_b)} \right) \left| P_1 P_2 \right| \tag{5.31}$$

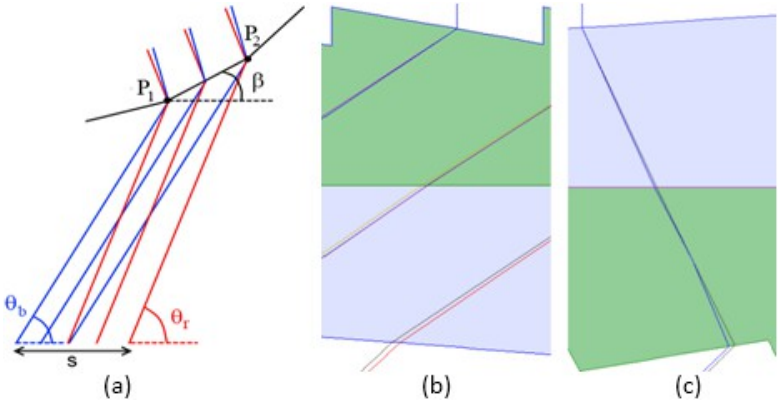

Fig. 5.35: Schematic representation of the chromatic spread on a single segment (a) and representation for both cases of TFT lenses (b and c). Figures (b) and (c) are laterally stretched

Eq. (5.31) has been applied to each of the eight designs considering only the two design wavelengths λ_0 and λ_0' (respectively 468 and 916nm) instead of extreme wavelengths in order to study the chromatic split without being affected by the variation of focal distance. Results are graphically shown in Fig. 5.36. Thanks to their thinner thickness, Fresnel doublets have a lower lateral spread.

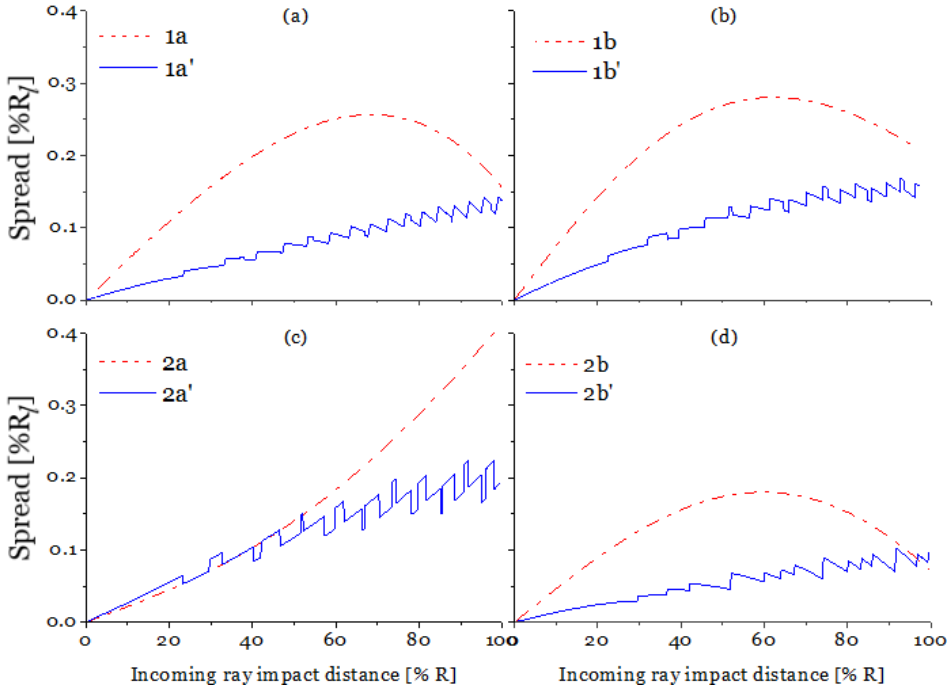

Fig. 5.36: Lateral spread for the Fresnel doublets and their equivalent nF doublets. The spread is expressed as a percentage of the lens radius. The notation of the designs is in accordance with Fig. 5.30. (All figures have the same scale)

To compare the eight designs in Table 5.11, we determined the dead zones geometrically for on-axis beams resulting either from the Fresnelization of the lens (in other words, the shading due to the draft facets) or from the diverging rays reaching the border of the lens. We also compared the higher spread value of the

design in order to know if it could be a cause of reduction of the maximum concentration. We calculated the maximum concentration ratio as follows:

$$C_{max,2D}=\left(\frac{2\mathrm{R}_l}{s}\right)^2\left(1-\frac{dz_{2\mathrm{D}}}{\pi R_l^2}\right)\overset{\text{def}}{=}\left(\frac{2}{s^*}\right)^2\left(1-dz_{2\mathrm{D}}^*\right) \tag{5.32}$$

The global thickness of the lenses is also indicated relatively to its radius:

$$t^*=\frac{t_{PC}+t_{PMMA}+h_{PC}+h_{PMMA}}{R_l} \tag{5.33}$$

Table 5.11 Achromatic doublet performance comparison

Design	dz_{1D}* [%][1]	dz_{2D}* [%][(1)]	s* [%]	t [%]	$C_{max,2D}$[(2)]
1a	0.00+0.00	0.00+0.00	0.257	64.3	0.61e6
1b	0.00+3.25	0.00+6.39	0.280	75.2	0.48e6
2a	0.00+2.25	0.00+2.18	0.406	63.0	0.23e6
2b	0.00+0.53	0.00+1.06	0.180	62.0	1.22e6
1a'	7.88+0.00	11.7+0.00	0.143	25	1.73e6
1b'	1.26+2.40	1.86+4.74	0.168	25	1.32e6
2a'	1.04+0.50	1.54+1.00	0.224	25	0.78e6
2b'	0.00+0.53	0.00+1.06	0.102	25	3.80e6

(1) Expressed as A + B where A is due to the draft facet and B to the finite radius

(2) Takes only the spread into account for on-axis beams with wavelengths λ_0 and λ_0'

From the data in Table 5.11 we deduce that the dead zones are very similar between Fresnel doublets and their equivalent nF doublets, except for designs 1a and 1a'. We also observe that the lateral spread won't be responsible of a drop of the concentration factor since the maximum concentration ratio due to the spread is in the order of $10^6\times$, while it is about $3000\times$ for an $f/2$ lens illuminated with sunlight. The effect of the lateral spread is comparable to the LCA effect (see maximum value of Table 5.10)

5.5.5. Refractive index and shape error tolerance

In the paraxial approximation, two cemented thin lenses have a focal distance given by

$$f_{eff}=\left(\frac{1}{f_{PMMA}}+\frac{1}{f_{PC}}\right)^{-1}=\left(\frac{n_{PMMA}-1}{RoC_{PMMA}}+\frac{n_{PC}-1}{RoC_{PC}}\right)^{-1} \tag{5.34}$$

Introducing the corresponding value of PMMA-3 and PC-4 for the design wavelength 961 nm, we have

$$f_{eff}=\left(\frac{1}{43.549}+\frac{1}{-95.593}\right)^{-1}=\left(\frac{0.4787}{20.847}-\frac{0.5412}{51.735}\right)^{-1}=79.99\text{mm} \tag{5.35}$$

if the temperature increases of 20 °C, the new focal distance becomes

$$f_{eff}(T+20)=\left(\frac{0.4766}{20.847}-\frac{0.5388}{51.735}\right)^{-1}=80.34\text{mm} \tag{5.36}$$

which represents a variation of 0.44%. The variation of power of the converging lens is slightly compensated by the variation of power of the diverging lens.

Regarding the variation of the radius of curvature, the error equally affects the converging and the diverging lenses, so that the same error applies to the effective focal length

$$f_{eff}'=\left(\frac{1}{(1+e)f_{PMMA}}+\frac{1}{(1+e)f_{PC}}\right)^{-1}=(1+e)f_{eff} \tag{5.37}$$

5.5.6. Ray-tracing simulations

In order to confirm what was said above, ray-tracing simulations were performed. This allows taking into account the angular size of the spectrum of the Sun.

As for the singlet, the effects of the Fresnel reflections R_{FR}, the shape error e, the variation of refractive indices and the effects of a pick and valley radius have been investigated. Results for nF doublets and Fresnel doublets have been separated in Table 5.12 and Table 5.13.

Table 5.12: Influence of several parameters on the optical efficiency, back focal distance and collection radius of achromatic nF doublets

nF doublets parameters					Optical efficiency [%]	*bfd*/80mm	R_a [mm]
Model	R_{Fr}	*e* [%]	Δn_{PMMA}	Δn_{PC}			
1a	0	0	0.0	0.0	99.7	1	0.45
1a	R(λ)	0	0.0	0.0	91.1	1	0.45
1a	R(λ)	0	-0.0021	-0.0024	91.1	1 – 1.0050	0.50 – 0.48
1a	R(λ)	5	0.0	0.0	89.9	1 - 1.0625	1.26 - 0.60
1b	R(λ)	0	0.0	0.0	84.8	1	0.54
1b	R(λ)	0	-0.0021	-0.0024	84.8	1 – 1.0125	0.58 – 0.55
1b	R(λ)	5	0.0	0.0	85.0	1 - 1.0638	1.60- 0.60
2a	R(λ)	0	0.0	0.0	89.6	1	0.48
2a	R(λ)	0	-0.0021	-0.0024	89.6	1 – 1.0038	0.54 - 0.50
2a	R(λ)	5	0.0	0.0	89.6	1 – 1.0631	1.60 – 0.56
2b	R(λ)	0	0.0	0.0	90.9	1	0.45
2b	R(λ)	0	-0.0021	-0.0024	91.0	1 – 1.0037	0.55 – 0.50
2b	R(λ)	5	0.0	0.0	91.0	1 – 1.0630	1.61 – 0.52

Table 5.13: Influence of several parameters on the optical efficiency, back focal distance and collection radius of achromatic Fresnel doublets

Fresnel doublets parameters						Optical efficiency [%]	*bfd*/80mm	R_a [mm][(1)]
Model	R_{Fr}	*e* [%]	Δn_{PMMA}	Δn_{PC}	r_{pv} [µm]			
1a'	0	0	0	0	0	86.2	1	0.43 (0.36)
1a'	R(λ)	0	0	0	0	78.8	1	0.43
1a'	R(λ)	0	-0.0021	-0.0024	0	78.8	1 – 1.0055	0.53 - 0.45
1a'	R(λ)	0	0	0	50	72.3	1	0.43
1a'	R(λ)	5	0	0	0	79.1	1 – 1.0528	1.26 – 0.50
1b'	R(λ)	0	0	0	0	84.5	1	0.46 (0.38)
1b'	R(λ)	0	-0.0021	-0.0024	0	84.6	1 – 1.0061	0.58 – 0.51
1b'	R(λ)	0	0	0	50	83.7	1	0.48
1b'	R(λ)	5	0	0	0	84.4	1 – 1.0621	1.62 – 0.55
2a'	R(λ)	0	0	0	0	88.7	1	0.43 (0.36)
2a'	R(λ)	0	-0.0021	-0.0024	0	88.8	1 – 1.0035	0.50 – 0.46
2a'	R(λ)	0	0	0	50	86.2	1	0.50
2a'	R(λ)	5	0	0	0	88.8	1 – 1.0625	1.56 – 0.50
2b'	R(λ)	0	0	0	0	89.9	1	0.46 (0.37)
2b'	R(λ)	0	-0.0021	-0.0024	0	90.0	1 – 1.0032	0.51 - 0.46
2b'	R(λ)	0	0	0	50	89.3	1	0.47
2b'	R(λ)	5	0	0	0	90.1	1 – 1.0575	1.53 – 0.51

(1) Values between brackets correspond to the radius enclosing 90% of the energy on the absorber.

Results from simulations are in good agreements with theoretical calculations: the variation of the refractive index has very little influence on the radius of the encircled energy and the shape error induces a variation of the focal distance of the same order of magnitude. Among the Fresnel designs, the first one, design 1a', has an optical efficiency too weak to be used in CPV. The last one however has a high optical efficiency and is little affected by peaks and valleys. The geometrical concentration ratio is close to 2000× considering 100% of the encircled energy and close to 3000× if we consider 90% of the encircled energy. This last value, 3000×, is the maximum concentration ratio achievable with $f/2$ lenses.

5.6. Performance comparison

Each system was investigated and optimized separately. Now, let's compare the theoretical performances based on paraxial calculations (for collimated beams under normal incidence) and based on ray-tracing simulations with ASAP where the angular size of the Sun was simulated.

From the achromatic point of view, an improvement clearly appears: the LCA^* is about 3% for singlets, 1.5% for hybrid lenses and 0.1% for doublets as shown in Fig. 5.37 where only the best case of each design has been considered.

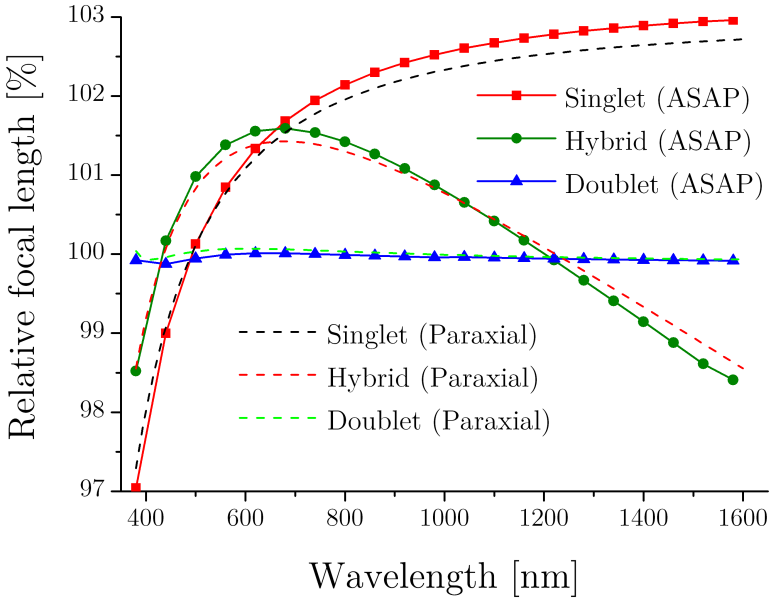

Fig. 5.37: Evolution of the focal distance with wavelength for the optimized singlet, hybrid lens and doublet made of PMMA-3

The reduction of the chromatic aberration leads to a whiter spot (i.e. spectrally homogeneous) but also for higher concentration ratios as depicted in Fig. 5.38.

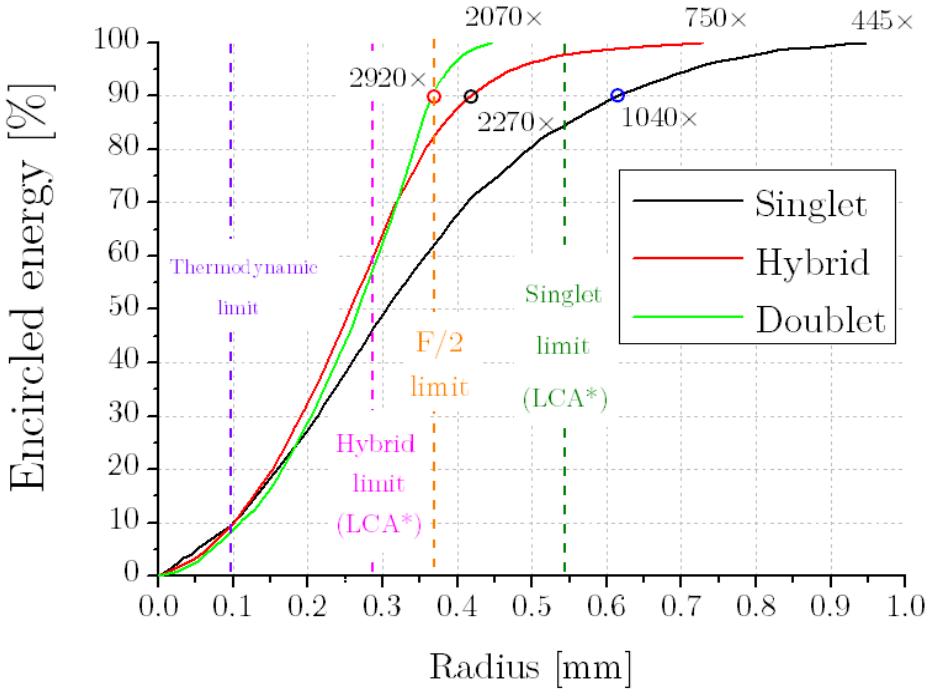

Fig. 5.38: Encircled energy for beams concentrated by a singlet (PMMA-3), an hybrid (PMMA-3) lens and a doublet (PMMA-3/PC-4)

Relevant data regarding optical efficiency and tolerance are provided in Table 5.14.

Table 5.14 Achromatic doublet performance comparison

Design	R_a (n) [mm]	R_a(n+Δn) [mm]	η_{opt} [%]	$\eta_{opt}(r_{pv})$ [%]	$\Delta f/f$ (e) [%]	R_a(e,f) [mm]	R_a(e,f+Δf) [mm]
Singlet	0.95	0.95	91.2	90.6	7.00	1.90	0.95
Hybrid	0.73	0.80	<78	<72	4.70	1.49	0.77
Doublet[(1)]	0.46	0.51	89.9	89.3	5.75	1.53	0.51

with profile error e=5% and peaks and valleys radius r_{pv}=50 µm, the refractive index variation is -0.0021 for PMMA and -0.0024 for PC. The draft angle is always 2°, the lens radius is 20 mm and the f-number is 2.
[(1)] Model 2b'

In terms of optical efficiency, losses go hand in hand with the complexity of design: as the number of layers increases, so do the reflection losses; as the number of teeth increases, so do the losses due to peaks and valleys. This is the reason why hybrid lenses that require a bilayer diffractive lens containing an

important amount of teeth (about 100 for a $f/2$ hybrid lens) are not suitable for CPV. If we compare the refractive doublet with the singlet, the optical efficiency is not that different (1.3% lower for the doublet) for a concentration ratio highly increased. The doublet is however slightly more intolerant to manufacturing errors, while still keeping a higher concentration ratio.

5.7. Chapter conclusions

In this chapter we saw how to design a nonimaging Fresnel lens, a nonimaging hybrid lens and different kinds of achromatic Fresnel doublets. It was deduced that athermal achromatic hybrid lenses are impossible to achieve with plastic materials. It was also deduced that bilayer $f/2$ hybrid lenses suffer from a lack of diffraction efficiency even without manufacturing errors. Moreover, a manufacturing errors of about 1 µm on the thickness of the teeth decreases the diffraction efficiency to almost zero! Refractive doublets show performances highly superior to hybrid lenses in terms of longitudinal chromatic aberration, concentration factor and tolerance to manufacturing errors. The theoretical concentration ratio achieved with an achromatic Fresnel doublet is very close to the maximum limit provided by the angular aperture of the source and the f-number. The optical losses due to the fresnelization of achromatic doublet remain negligible for three designs. However, outwards teeth are subject to soiling problems and designs with a flat air/lens interface constitute a manufacturing challenge.

6 | Solar simulator

6.1. The need for a continuous solar simulator

To avoid tracking problems, cloudy sky hindrance and to ensure constant parameters like irradiance and direct light, having a solar simulator at one's disposal is of huge importance. Several types of solar simulators coexist: continuous, flashed and pulsed. The first category is mainly used in 1 sun applications. The second category allows for very high intensities but suffers from repeatability problems. The third category avoids these problems by using a shutter. For CPV, four parameters have to be taken into account:

- the spectrum (see Chap. 2.2.)
- the angular radius of the Sun (0.265°)
- the spatial uniformity of the output beam
- the radiant exitance (1000 W/m² which is a standard for CPV).

However, the last parameter is only needed to check the performance of a photovoltaic cell. The first parameter, the correspondence between the spectrum of the solar simulator and the Sun's spectrum, may also be unnecessary (see below). Note that, in the case of photovoltaic cell investigations, the room temperature should also be controlled and kept constant at 25 °C.

6.2. Solmacs simulator

The solar simulator used in this thesis in called the “Solmacs simulator”, from a former eponymous project. It has been designed and developed by the CSL. A picture of the whole system is shown hereunder.

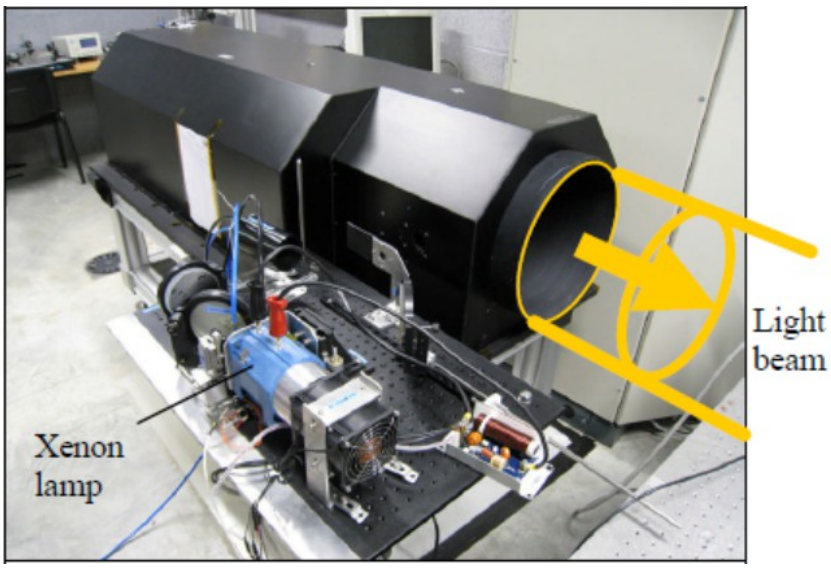

Fig. 6.1: Picture of the Solmacs simulator from CSL

The simulator is comprised of two parts. The first, the source block, contains an air-cooled light source, a water-cooled integrator rod and two mirrors that conduct light to the second part: the collimator. The collimator contains a folding mirror and a 30 cm diameter mirror. A schematic representation of these two parts is depicted in Fig. 6.2

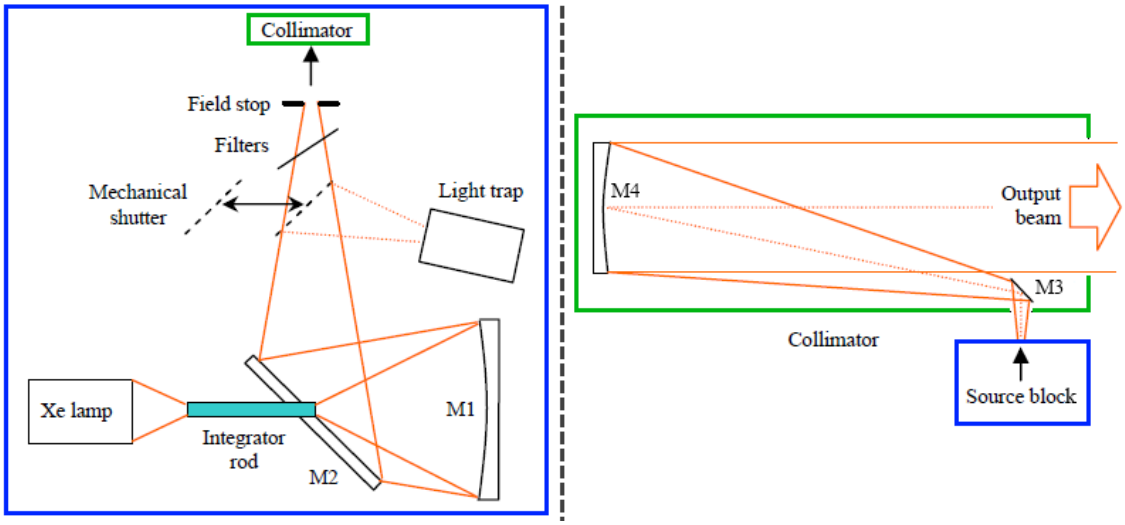

Fig. 6.2: [Thi10] Source block of the solar simulator (left). Collimator of the solar simulator (right)

6.2.1.1. Source block

The light source is a PE700C-13F Cermax ® lamp with a nominal power of 700 watts developed by PerkinElmer. The light is emitted by a continuous xenon arc lamp which is known to reasonably fit the spectrum of the Sun with the exception of some undesirable atomic transition peaks especially at 475 nm and between 800 and 1000 nm as shown in Fig. 6.3.

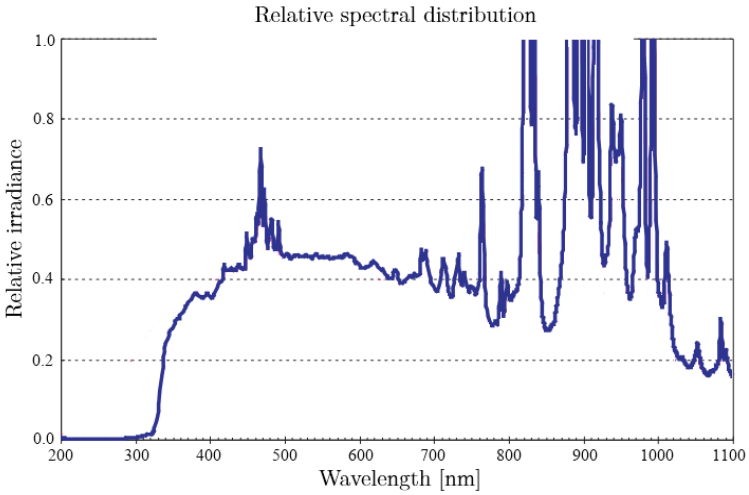

Fig. 6.3: UV-VIS and part of the NIR spectrum of the xenon arc lamp used as source for the Solmacs solar simulator [PE700]

The arc is situated at one focus of a semi-ellipsoid and is thus reflected towards the other focus. The 12mm focal spot contains 180 watts that are collected by the integrator rod passing through the centre of a plane mirror M2 (see Fig. 6.4). The diverging light exiting the barrel is focused towards the field stop with mirror M1 via the folding mirror M2 . A light trap is located on the way between the field stop and M2 to switch off the light without turning off the lamp, in order to increases its lifetime.

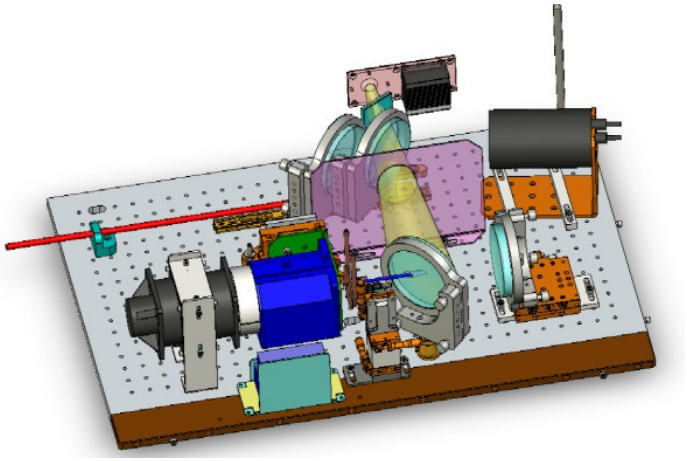

Fig. 6.4: Sketch of the source block

6.2.1.2. Collimator

The collimator has to provide an output beam matching the angular size of the Sun. The field stop must therefore be located in the focal plane of the mirror M4 (since M3 is only a plane folding mirror it does not affect the focal distance) and the radius of the stop, r_{fs}, must correspond to

$$r_{fs} = f_{\mathrm{M4}} \tan \theta_{Sun} \tag{6.1}$$

where f_{M4} is the focal length of the mirror M4.

6.2.2. Characterization

6.2.2.1. Radiant exitance

Thibert *et al.* [Thi10] performed radiant exitance measurements of the output beam. The left image of Fig. 6.5 shows the radiant exitance maps in absolute value, with a maximum around 250 W/m², i.e. one quarter of the solar constant. The black zone observed is due to central hole inside the folding mirror M2.

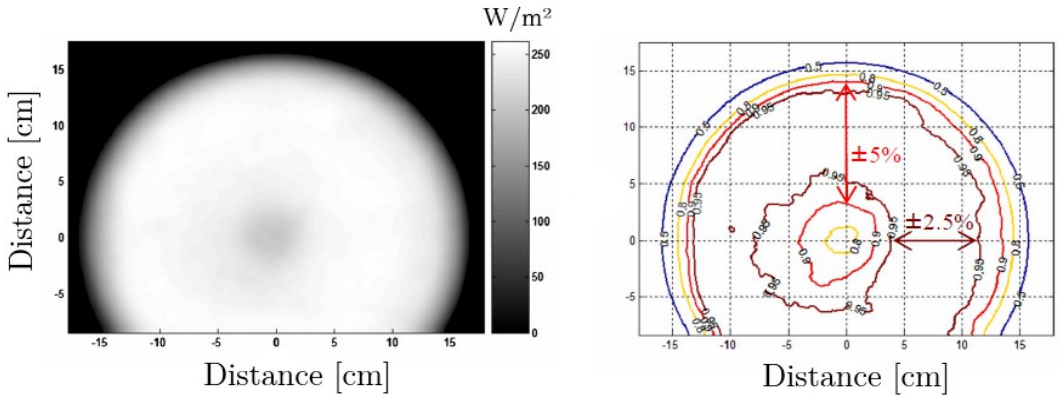

Fig. 6.5: Output beam radiant exitance map (left) and isovalues of the radiant exitance as a percentage of the maximum radiant exitance (right)

The homogeneity is described by the left image of Fig. 6.5: a 6cm by 6cm object may be illuminated with a variation of the intensity smaller than ± 2.5% or a 10 cm by 10 cm with a variation of intensity smaller than ±5%.

6.2.2.2. Angular size

To determine the divergence of the solar simulator, we simply performed one quadruple measurement. We placed a rigid metal sheet in which four holes of different diameters were made at the output of the solar simulator and we measured the shade and light zones of the sheet and holes. A picture of the

experimental setup is shown in Fig. 6.6

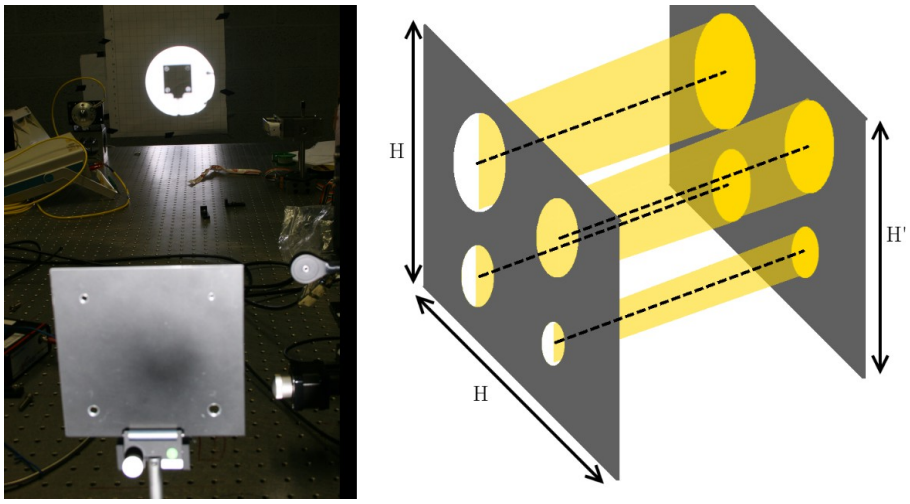

Fig. 6.6. Experimental setup: picture (left) and sketch (right)

The divergence angle of the beams passing through one hole (see Fig. 6.7) can be calculating using

$$\theta = \text{atan}\left(\frac{R_H - R_H^{'}}{L}\right) \tag{6.2}$$

with R_H and $R_H^{'}$ the radius of the field stop and of the image and L the distance separating the field stop and the image plane.

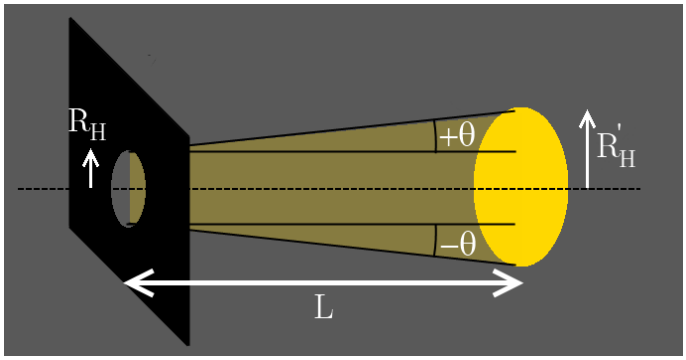

Fig. 6.7: Setup to determine the divergence angle of the beams passing through a hole

It is important to make the difference between the divergence and the angular size of the source. The divergence of a beam is a measure of the spread of the beam radius with the distance. It is calculated from the source (the hole in the sheet is considered here as the source). The value of the divergence is independent of the distance from the point source. The angular size is a measure of the size of the source from an observation point and therefore changes with the distance.

For the simulator to correctly simulate the angular radius of the Sun seen from Earth (0.265°), every single point of the metal sheet must see the light from the source within a cone of angular aperture of ±0.265° (the angle being measured relatively to the optical axis). One simple way to prove this consists in placing a hole and a screen successively at the same place. For example, looking at Fig. 6.8, the light passing through the hole shows that an angle +θ reaches point A and the opaque screen proves that it is also reached by and angle -θ. The smaller the radius, the higher the precision as far as diffractive effects are negligible.

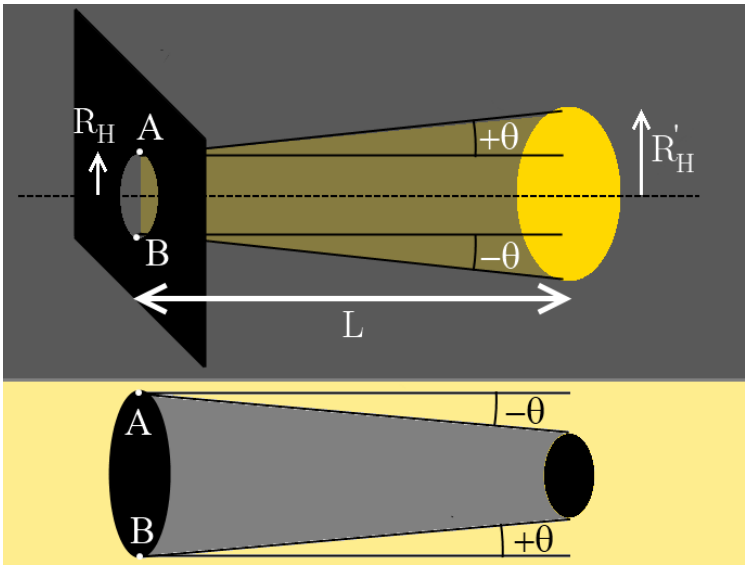

Fig. 6.8: Simple method to show that a point A is reached by a cone of angular radius θ. (Top) Beams pass through a hole (diverging effect). (Bottom) Beams are blocked by an opaque screen (converging effect)

With the setup shown in Fig. 6.6, we obtain the data shown in Table 6.1.

Table 6.1 Determination of the angular size of the solar simulator

	Object size [mm]	Image size [mm]	Δx [mm]	θ [°]
Hole 1	3	24.5	21.5	0.240
Hole 2	5	26.5	21.5	0.240
Hole 3	7	28.5	21.5	0.240
Hole 4	9	30.5	21.5	0.240
Disk 1	23.2	2.0	-21.2	-0.237
Disk 2	25.8	4.5	-21.3	-0.238

Distance between object and image L = 2562.5mm

With a measure error of 1mm, the error on the angular size of the source is ±0.01° which is highly accurate compared to the typical tracking error of 0.1°. A more expensive alternative to determine the angular size of the solar simulator

would have been the use of a theodolite.

6.2.3. Improvement

The datasheets of the xenon arc lamp claim that 180 watts are focused in an aperture of 12mm while, in the end, only 250 W/m² are obtained at the output of the solar simulator, so about a radiant flux lower than 17 watts. Of course each reflection on a mirror causes some losses, but this does not explain why only about 10% of the energy reaches the exit of the simulator. It was rapidly deduced that the integrator rod was not optimal. Indeed, the integrator rod had a conical shape with an entrance radius wider than the output radius, which causes some problems of retroreflection and discretization of the divergence angles, as will be shown hereunder.

To optimize the integrator rod we first simulated the xenon arc lamp on ASAP using the parameters provided by the datasheets (see Fig. 6.9) in order to achieve 180 watts enclosed in a radius of 6mm at the focal plane of the ellipsoid.

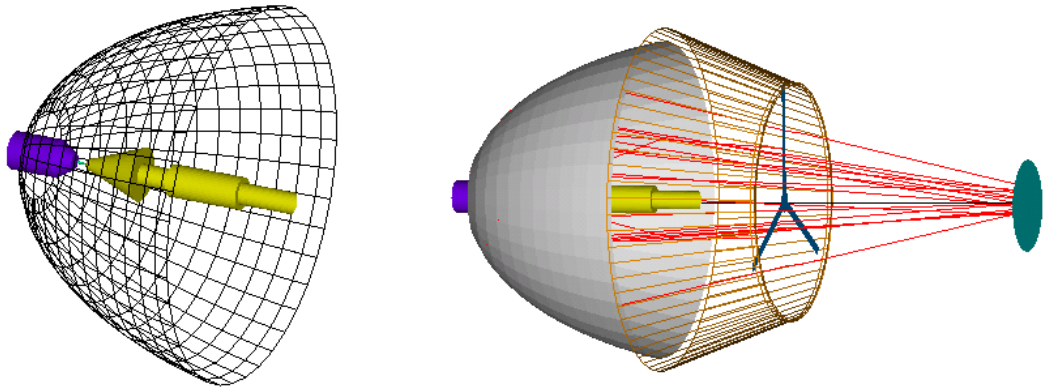

Fig. 6.9: Left: cathode (yellow), anode (purple) and semi-ellipsoidal reflector. Right: Whole emitting system including protection and cathode struts. Some rays are traced up to the focal plane

Light reaching the focus plane is contained in a cone with an angular aperture of 21° without any rays between 0° and 2°. The first barrel we had at to our disposal was 110 mm long and had an entrance and an output diameter of respectively 11 and 4 mm.

To observe what happened to several incidence cones, two of them are depicted. In Fig. 6.10, beams have an incidence angle between +4 and +6°, and between -4 and -6°. The greater the number of reflections inside the barrel the higher the divergence angle which causes a discretization effect on output angles.

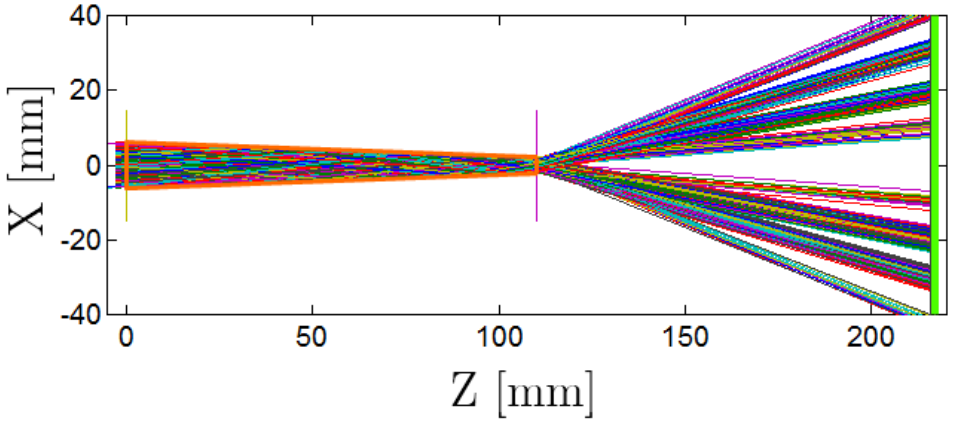

Fig. 6.10: Ray-trace of beams with a divergence comprised between +4 and +6°, and between -4 and-6°. The barrel, in orange, has an entrance diameter of 11 mm and output radius of 4 mm. Mirror M1 is coloured in light green.

In Fig. 6.11, beams have an incidence angle between +10 and +12°, and between -10 and -12°. The same phenomenon of discretization occurs but in addition exiting rays miss their target (M1) due to a too high divergence angle.

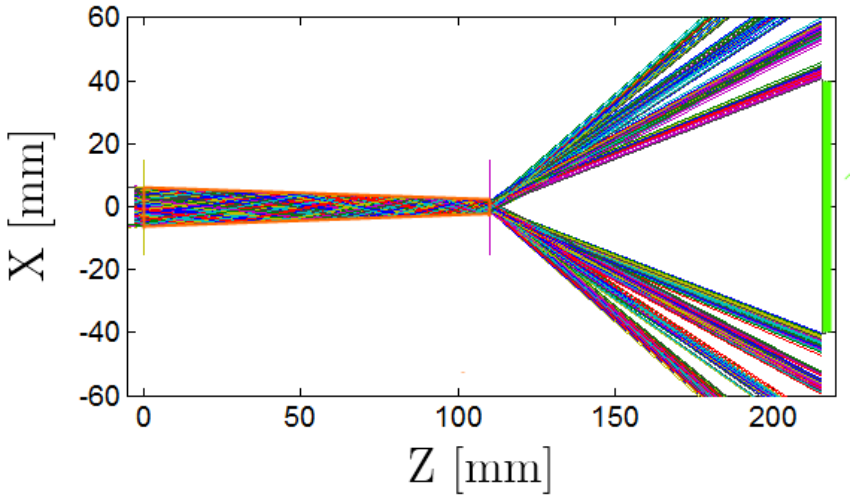

Fig. 6.11: Ray-trace of beams with a divergence comprised between +10 and +12°, and between -10 and-12°.

The distance being fixed between the end of the barrel and the mirror M1 with a radius of 40 mm, the view angle is 21.8°, which corresponds to the highest divergence angle of the source. Therefore any degree of concentration will make high divergence angles miss mirror M1. Indeed, as a reminder, the simplified equation of the étendue conservation, Eq. (2.55), implies that concentrated beams have a higher divergence angle.

$$R_i \sin\alpha_i = R_o \sin\alpha_o \tag{2.55}$$

The only free parameters were the length of the barrel, which has no effect on the

concentration ratio, and the entrance radius (the output radius being fixed at 4 mm). If the entrance radius is also 4 mm wide, then every beam entering in the barrel will reach M1 but the barrel is optically not useful. If the entrance diameter is greater than 4 mm then a higher amount of rays will be collected but also a higher amount will miss M1 due to too high diverging angles as depicted in Fig. 6.12

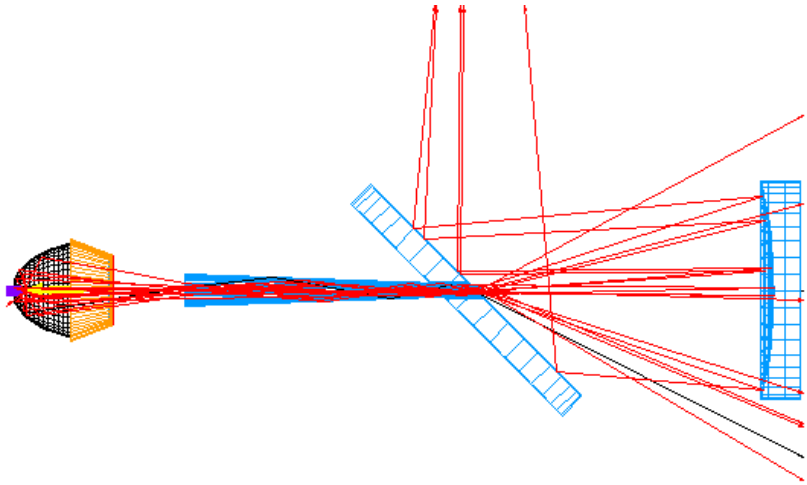

Fig. 6.12: ASAP ray-tracing. High divergence beams miss mirror M1

Following ASAP simulations, changing the aperture radius from 11.0 mm to 5.0 mm increases the optical efficiency from 21% to 31%. Anyway, the better way to enhance the radiant exitance consists in replacing the lamp with another having a lower angular aperture.

6.3. Chapter conclusions

In this chapter, we showed the importance of having a solar simulator. The Solmacs simulator, owned by the Centre Spatial of Liège, is a continuous model fitting reasonably well the spectral properties of the Sun thanks to the xenon arc lamp. The flux provided by the solar simulator exhibits a high homogeneity on surfaces of 6 cm by 6 cm. A simple and cheap method to determine the angular size of the source was used to determine an angular radius of $0.24 \pm 0.01°$, i.e. 94.3% of the Sun's angular radius. On the one hand, the radiant exitance is too weak, about one quarter of the solar constant, to consider Solmacs as a real solar simulator. On the other hand, the focusing properties of lenses to be investigated are not influenced by their irradiance.

7 Experimental performances of a singlet, a hybrid lens and a doublet

7.1. Experimental set-up

The experimental validation of the lenses theoretical designs is a crucial point for their future in CPV. To characterize the chromaticity and the focal properties of the manufactured lenses, the head of an optical VIS/NIR fibre with a core of 50 µm has been mounted on a 3-axis motorized stage as can be seen on Fig. 7.1.

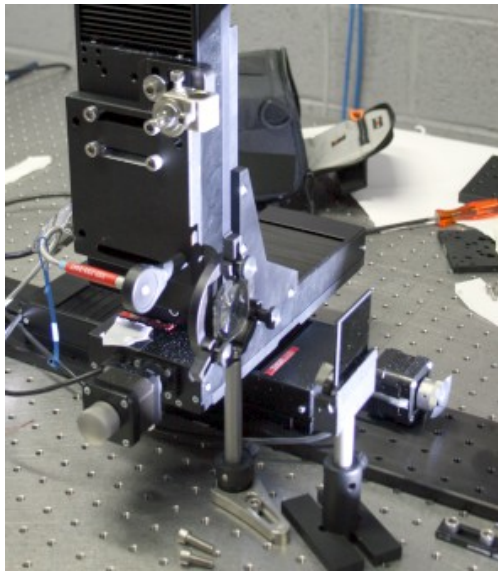

Fig. 7.1: Optical fibre mounted on a 3-axis motorized stage

Each axis has a linear travel of 10 cm and is controlled by means of a stepper motor with an accuracy higher than 5 µm. The other extremity of the optical fibre is connected to a spectrometer (see Fig. 7.2). Two different spectrometers were used to scan the wavelength range from 380 nm to 1600 nm: the AvaSpec-2048 from Avantes (380-1000 nm) and the NIRQuest 512 from Ocean Optics (900-1700 nm).

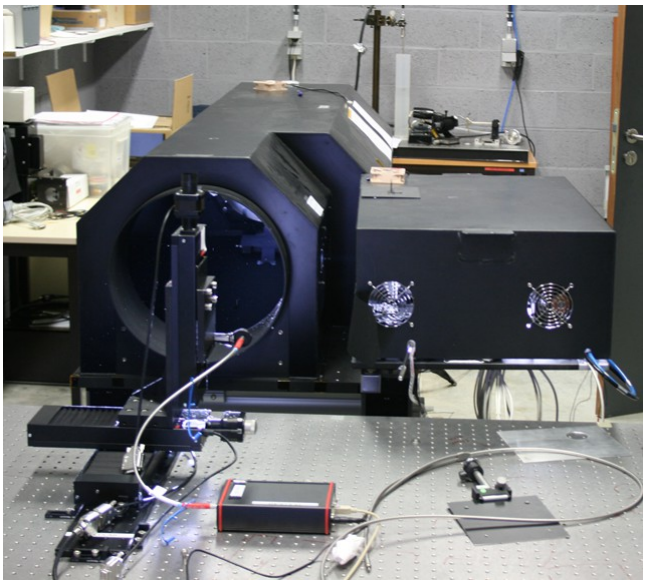

Fig. 7.2. Experimental setup. The optical fibre mounted on the 3-axis motorized stage is connected to a spectrometer

The 3-axis system allows a 3D mapping of the focal spot (see Fig. 7.3), for all wavelengths between 380 and 1600 nm.

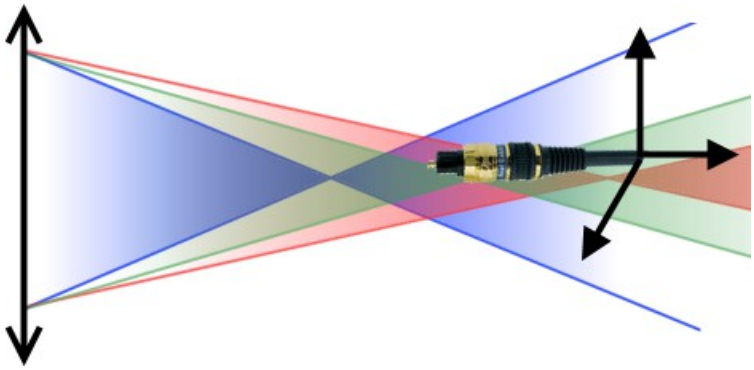

Fig. 7.3: 3D scanning of the focal spot

The whole system is controlled via a home-made Labview® program whose interface is presented in Fig. 7.4. At a given wavelength, the coordinates with the highest number of counts are considered as the focal point. In other words, we consider that the focal point is determined by the highest irradiance in a 50 µm disk with a diameter of 50 µm.

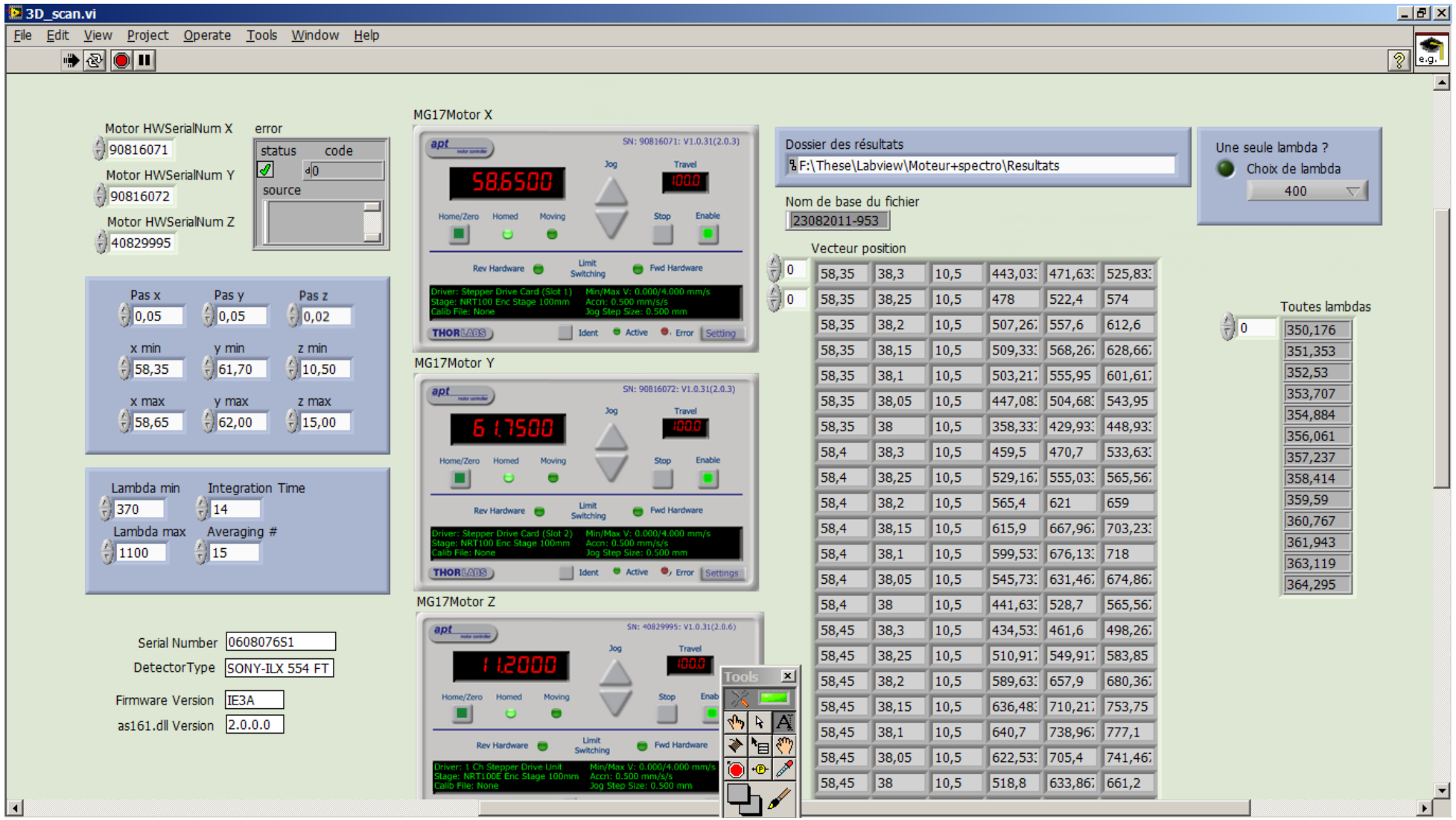

Fig. 7.4: Control interface for the 3D acquisition system

To determine the spot size, several intensity maps were measured perpendicularly to the optical axis. For each map, the acquisition was stopped when the intensity dropped under 1% of the maximum intensity (located on the optical axis). Since the spectrometer used was not calibrated and the lamp spectrum does not exactly correspond to the Sun's spectrum, a relative intensity map was measured for wavelengths between 380 and 1600 nm. A weight (g_λ) was then attributed for each wavelength according to a black-body of 5780 K. Finally the total intensity in one point of the map was considered as being given by the following equation

$$I_{tot} = \sum_{\lambda=380}^{1600} g_\lambda I_\lambda \tag{7.1}$$

7.2. Manufacturing and metrology process overview

Lenses designed by Hololab go through three stages before reaching the solar simulator bench test: the diamond turning, the injection moulding and the metrology.

7.2.1. Single-point diamond turning

Single-point diamond turning or SPDT is a micromachining process used to produce surfaces of optical quality. The substrate to be engraved is attached to a rotating support as it is brought into contact with the tip of the diamond tool, as illustrated in Fig. 7.5.

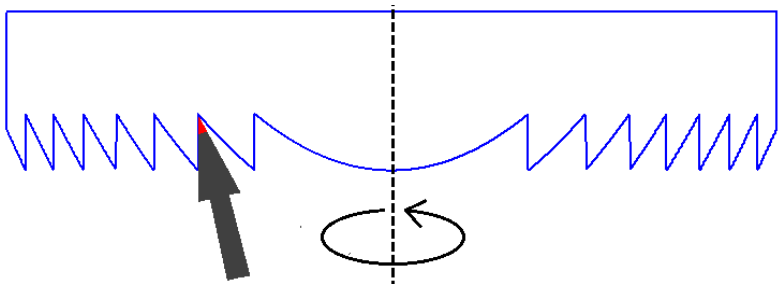

Fig. 7.5: Single-point diamond turning process

A balance must be achieved between the fidelity of the profile and the machining time.

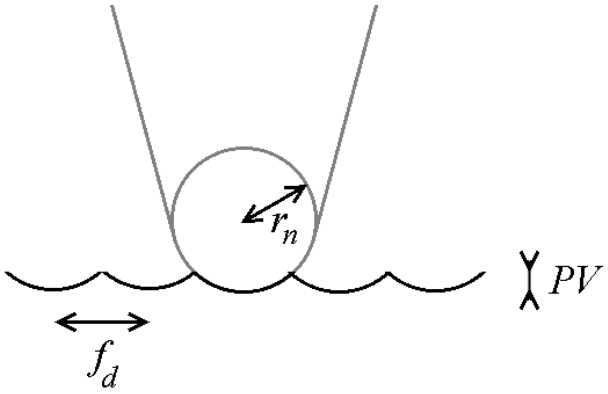

Fig. 7.6: Sketch of the peaks and valleys of a diamond-turned workpiece

Eq. (7.2) expresses, in the parabolic approximation, the relation between the diamond tool nose radius r_n, the feed per revolution f_d and the peak to valley roughness, PV, depicted in Fig. 7.6 [Xia03].

$$PV \simeq \frac{f_d^2}{8\, r_n} \tag{7.2}$$

The diamond turning to realize the mould for our lenses was performed by Amos S.A. (Belgium) owner of a 5-axis diamond turning machine model Nanotech' 350 FG (see Fig. 7.7) from Moore Nanotechnologies Systems.

Fig. 7.7: Nanotech' 350 FG SPDT machine owned by Amos S.A.

7.2.2. Injection moulding

After the diamond turning of the negative profile of the lenses, moulds were sent to Optim Test Center (Belgium) for the injection moulding. A sketch of an injection moulding unit is shown in Fig. 7.8.

Raw plastic, in the form of granules stored in a tank, are poured out in the screw cavity. The rotation of the endless screw provides a molten plastic of homogeneous temperature which is injected in the mould under high pressure. The static and the mobile parts of the mould are kept a certain time under pressure so that the molten plastic takes the form of the mould. The plastic cools down and hardens and is then ejected from to mould. During the cooling process, the plastic shrinks hence the need to manufacture moulds slightly bigger than the desired final shape (see Table 3.1).

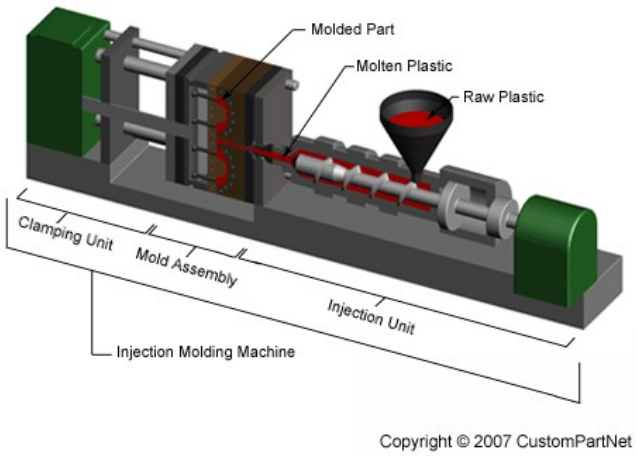

Fig. 7.8: sketch of an injection moulding unit.
Source: CustomPartNet [http://www.custompartnet.com/wu/InjectionMolding]

Injection moulding is a fast and low-cost process for large volume manufacturing. However, accurate replication of the mould is hard to achieve, especially for sharp profile for which melted plastic does not thoroughly fill the mould in the depths.

7.2.3. Metrology

To check the concordance between the designed profile and the manufactured lens profile measurements by optical microscope were performed by the CSL. The roughness was also investigated.

However, a direct measurement of a mould or of a plastic lens could hardly be performed. Indeed the depth of the teeth is too important to use an interferometry process, and mechanical processes cannot achieve an accurate

measurement from the valleys. The CSL processed to negative replications of the lenses and moulds by the means of polydimethylsiloxane (PDMS[14]) replica, as show in Fig. 7.9.

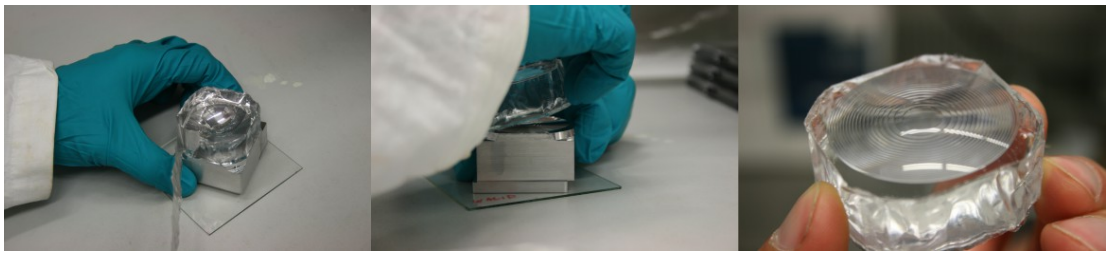

Fig. 7.9: Negative silicone replica of a mould

Casting with silicone rubber is known to have a very high degree of fidelity (less than 100 nm) [Bod08]. The silicone replica can be cut transversally along the diameter to perform a profilometry with an optical microscope. However, demoulding leads to distortion effects [Dal97], cutting may lead to a profile error if the cutting plane does not correspond to the cross sectional plane but also due to mechanical stress. The precision estimated by CSL is in the order of ten microns.

7.3. Singlet manufacturing and optical tests

7.3.1. Manufacturing

For financial reasons, the singlet used experimentally is the refractive component of the hybrid lens. Since the focal distance of the diffractive lens is very long compared to the refractive focal length, the design is only slightly different. But, moreover, the lens radius is only 16 mm instead of 20 mm due to process difficulties[15]. Thirdly, the PMMA used for the injection moulding (PMMA-2 = Altuglas) was different from the PMMA used for the design (PMMA-3 = Diakon CLG356). We took this problem as the opportunity to check the tolerance of the designs.

As a first trial, Amos S.A. manufactured the mould in two steps: a first pass with a 183 µm half-radius tool and a second pass with a 55 µm half-radius tool as illustrated in Fig. 7.10

14 Sometimes simply referred to as silicone

15 However, this problem will be fixed for the refractive doublet

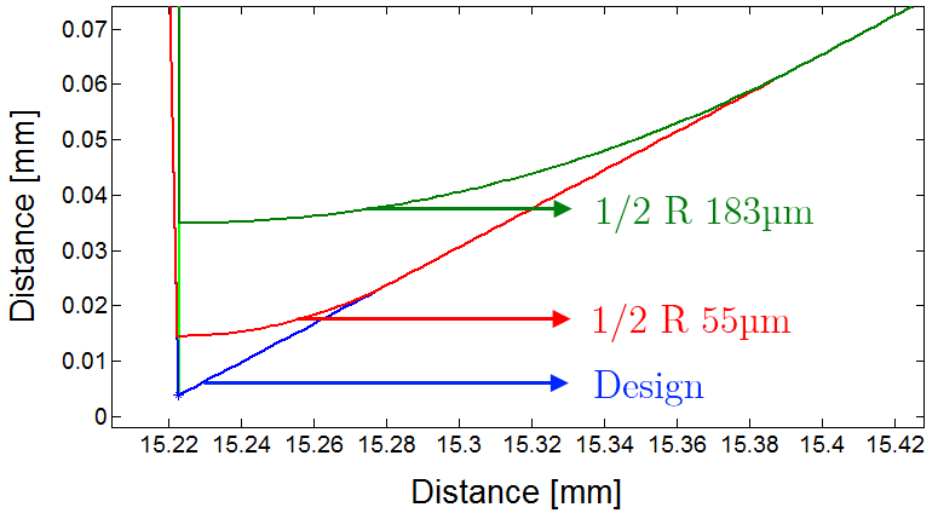

Fig. 7.10: Manufacturing of the mould in two steps: firstly with a half-radius of 183 µm and secondly a half-radius of 55 µm

However this process leads to a premature degradation of the half-radius tool resulting in a matte appearance of the mould. Amos changed his strategy and turned to V-tools which have a nose radius smaller than 250 nm. The mould obtained, shown in Fig. 7.11, has a bright finished and seems to be of high optical quality.

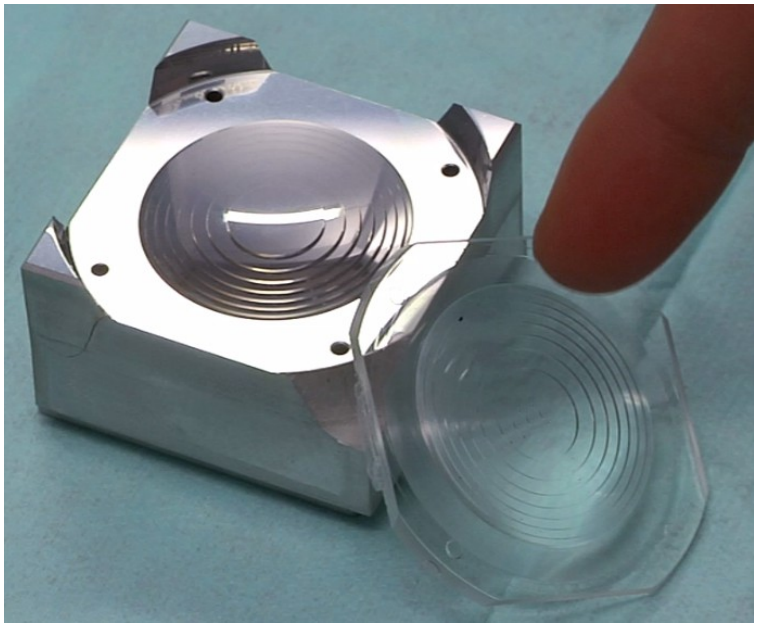

Fig. 7.11: Refractive profile realised with a V-tool on an aluminium substrate

7.3.2. Metrology

Relevant data about the moulds of the singlet regarding the thickness of the teeth and the roughness are presented in Table 7.1.

Table 7.1 Thickness and roughness metrology data for the singlet mould

	Theoretical thickness [µm]	Experimental thickness [µm]	R_{avg} [nm]	R_q [nm]
Teeth 1	386.1	384.9	44.6	75.1
Teeth 2	386.1	385.6	39.2	58.4
Teeth 3	385.9	384.3	33.7	51.8
Teeth 4	386.3	385.7	41.5	64.7
Teeth 5	386.2	381.4	72.6	98.8
Teeth 6	385.8	382.9	67.4	91.1
Teeth 7	385.6	380.1	69.0	94.1
Flat side	Ø	Ø	6.82	8.77

The average error between experimental measurements and theoretical thicknesses is small: 0.28%. However the roughness of the teeth is high compared to optical surface usually produced by diamond turning. This is due to the V-tool used: its nose has a radius smaller than 250 nm. So, referring to Eq. (7.2), a very important number of passes would have been needed to achieve a R_q smaller than 10 nm. As a consequence, the determination of the scattered energy could not be performed using the scalar equation presented in Chap. 2.4., hence the scattered energy will be no longer discussed is this thesis.

We also performed birefringence measurements. Clear fringes were observed only on the border of the sample and mainly at the injection gate (see Fig. 7.12). For the lens itself, there is no notable birefringence.

Fig. 7.12: Birefringence observation. Left: reference (no lens). Right: singlet lens. (the small clear line in the middle of the picture is an artifact)

7.3.3. Optical tests and comparison with theory

The evolution of the focal length with wavelength has been measured and compared with paraxial theoretical calculations and ray-tracing simulations performed with ASAP. To determine experimentally the focal distance of the singlet, the relative intensity for each wavelength was determined, as shown in Fig. 7.13. The focal length corresponds to the maximum of each of these curves.

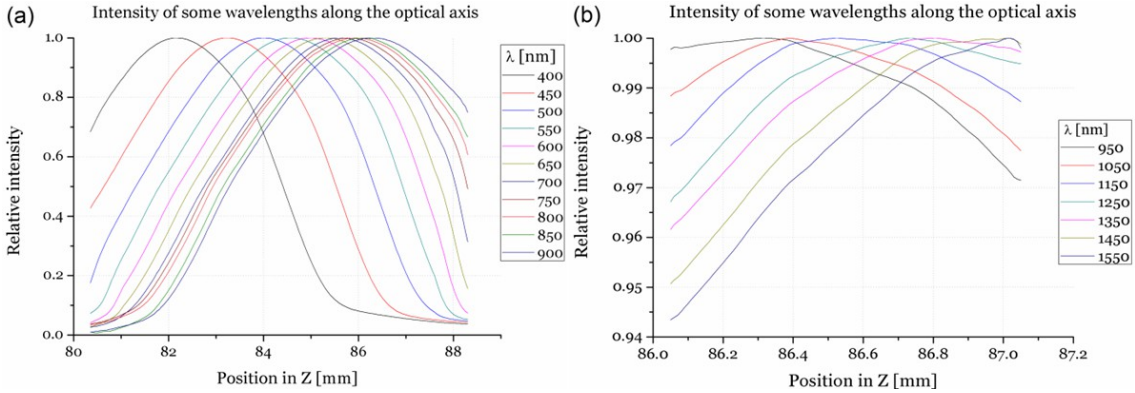

Fig. 7.13: Relative intensity for some wavelengths in the visible (left) and NIR (right) region.

Comparisons were performed between the expected results with the design PMMA (PMMA-3) and the PMMA actually injected (PMMA-2). Results are depicted in Fig. 7.14. We observe that the use of PMMA-2 instead of PMMA-3 changes the focal distance by about 1 mm but the difference between the experimental results and theoretical results remains under 0.25%.

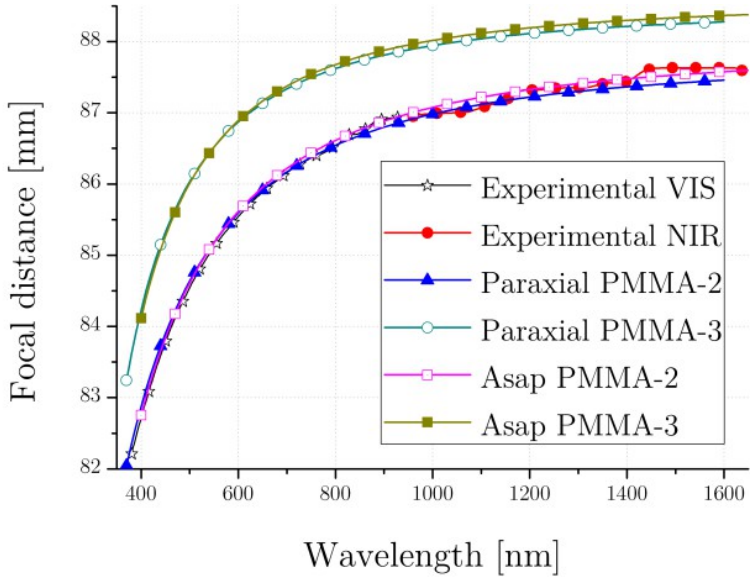

Fig. 7.14: Comparison between focal distances of different kind of singlets: experimental (for PMMA-2) and theoretical results

If we now evaluate the encircled radiant energy, the lens with the design PMMA (PMMA-3) has, theoretically, the smallest radius that encloses 100% of the beams reaching the absorber, as can be seen in Fig. 7.15. However, the simulation with the PMMA-2 actually injected shows a smaller encircling radius up to 98% of the radiant energy. It is not very surprising since the lens used as a singlet was not designed that as such but was designed to work with a front diffractive lens.

The difference between the simulated and the experimental enclosing radius is 4.79% and is maybe due to manufacturing errors or to coma coming from misalignment.

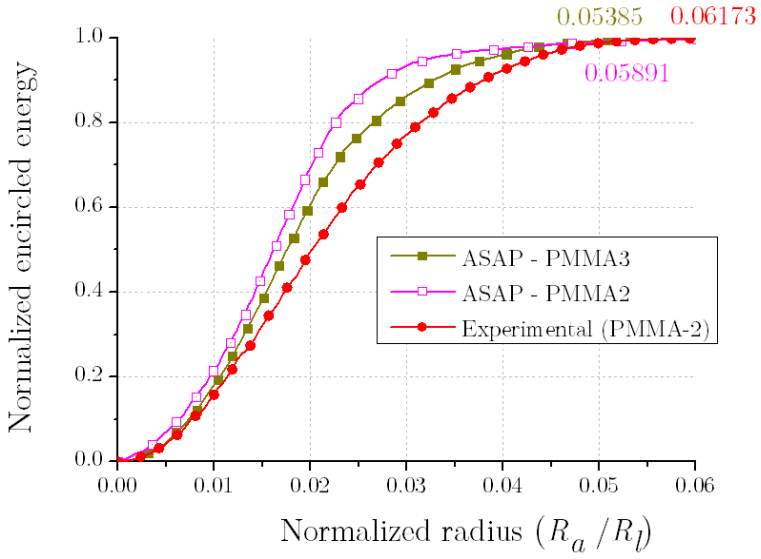

Fig. 7.15: Simulated and experimental normalised enclosed radiant energy

The concentration obtained at 100%, 99%, 95% and 90% of the encircled radiant energy is given in Table 7.2

Table 7.2 Enclosing radius and corresponding geometrical concentration ratio

	R_a(90%) [%]	R_a(95%) [%]	R_a(99%) [%]	R_a(100%) [%]
ASAP with PMMA-3	3.3 (918×)	3.8 (693×)	0.49 (416×)	5.4 (343×)
ASAP with PMMA-2	2.8 (1275×)	3.2 (977×)	0.49 (416×)	5.9 (287×)
Experimental (PMMA-2)	3.8 (693×)	4.3 (540×)	0.50 (400×)	6.2 (260×)

The number in brackets corresponds to the geometrical concentration factor
The radius of the absorber R_a, is expressed as a percentage of the lens radius

The geometrical concentration ratios obtained with this singlet is low for 100% of the enclosed energy: the concentration obtained is at the boundary between medium CPV and HCPV. But the concentration is almost doubled for 95% and tripled for 90% of the enclosed energy. It clearly appears that the concentration ratio rapidly decreases just to collect a few percent more. Note that the three designs are equivalent to collect 99% of the radiant energy of the focal spot.

7.4. Hybrid lens manufacturing and optical tests

7.4.1. Manufacturing

In Chapter 5.4.6., the tolerance of hybrid lens was discussed. It was shown that an error of 1 µm reduces the diffraction efficiency to almost zero! Therefore, it is likely that multilayer hybrid lenses realized by injection moulding will not be efficient. To enhance the concordance between the ideal profile and the manufactured profile, the draft angle (for mould removal after plastic injection) was set to 0.5° and a V-tool was used to perform the diamond turning. A centring nipple was also designed to avoid misalignment of the two diffractive layers forming the diffractive lens. Finally, a spacer was also included in the lens design, maintaining a short distance of 20 µm between the diffractive structures in order to prevent the crashing of the teeth.

A sketch of the bilayer hybrid lens is depicted in Fig. 7.16.

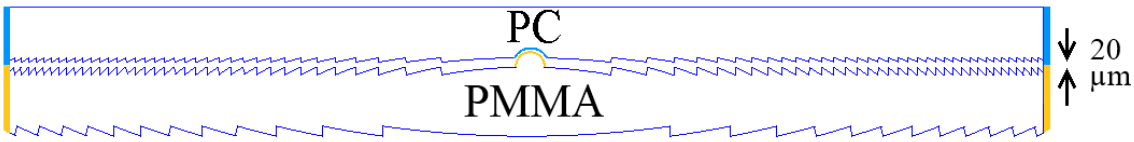

Fig. 7.16: Sketch of the hybrid lens including spacer and centring nipple

As for the singlet, moulds have been replicated with PDMS and characterized. Due to the very high number of teeth composing the diffractive lens, only few relevant metrology results are summarized in Table 7.3.

Table 7.3 Metrology results of the concave mould for the PMMA diffractive component and comparison with the theoretical design

Teeth #	t_{design} [µm]	t_{exp} [µm]	Λ_{design} [µm]	Λ_{exp} [µm]
1	18.935	18.7	644.1	-
10	18.881	18.0	240.0	-
20	18.847	17.8	171.7	-
30	18.821	18.3	140.8	-
50	18.778	18.0	109.4	-
70	18.742	17.8	92.6	-
90	18.712	18.0	81.7	-
110	18.683	17.5	74.0	-
120	18.670	17.5	70.8	71.3
130	18.657	16.8	68.0	67.7
150	18.631	17.0	63.4	63.3
165	18.613	17.0	60.4	60.3

From Table 7.3 we note an increasing error on the teeth thickness from 0.2 µm to 1.6 µm which portends a low diffraction efficiency. However, the widths of the teeth seem in good accordance with the theoretical design even if this cannot be ascertained for two reasons: the small sampling of measurements (only four) and the imprecision of the measurements due mainly to the rounded tip as shown in Fig. 7.17.

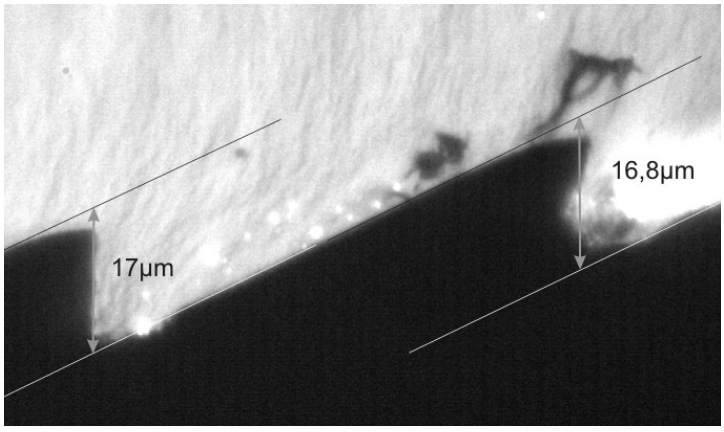

Fig. 7.17: Illustration of measurement performed on a negative silicone replica

As already mentioned, the moulds were designed slightly greater than the desired lens due to shrinkage. A coefficient of 1.0035 was used for the PMMA and 1.006 for the PC.

Metrology results performed on a silicone replica of the PMMA lens obtained by injection moulding are shown in Table 7.4

Table 7.4 Metrology results of the PMMA diffractive component replicated with PDMS and comparison with the theoretical design

Teeth #	t_{design} [µm]	t_{exp} [µm]	Λ_{design} [µm]	Λ_{exp} [µm]
1	18.869	12.2	641.8	-
10	18.815	11.6	239.2	-
20	18.781	11.9	171.1	-
30	18.755	12.2	140.3	-
50	18.712	10.9	109.0	-
70	18.677	10.6	92.3	-
90	18.646	14.1	81.4	-
110	18.618	13.3	73.7	-
120	18.605	11.5	70.5	69.9
130	18.592	11.6	67.7	66.6
150	18.566	9.5	63.1	62.4
160	18.548	8.7	61.1	60.8

The profile degraded even more with the injection moulding process, the thickness error rises up to 10 µm! Looking at Fig. 7.18 the picture taken by CSL for the determination of the width and thickness, it clearly appears that the PMMA did not fill thoroughly the tips.

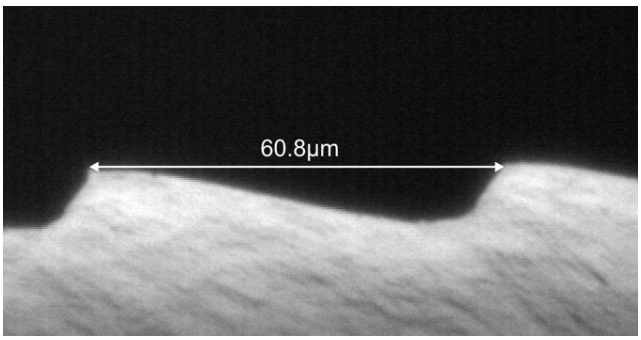

Fig. 7.18: Picture of the 160th teeth of the diffractive component in PMMA replicated by silicone

To improve the quality of the replicated profile as well as to reduce the residual stress inside the lens, Optim Test Center conducted tests with a higher temperature of the mould (~160 °C) so that the injected plastic cools down more slowly and is more flowable to better fill the tips. This high temperature, however, raises other issues like a longer cooling time. Indeed, if the temperature of the tools is higher, the piece takes longer to solidify which drastically increases the cycle time. Moreover, the residence time spent by the polymer into the mould also increases which can cause its degradation. To circumvent this problem, Optim Test Center used a technique called "Pulse cooling" (or variotherm) consisting in a

cyclic variation of the temperature of the mould avoiding the freezing barrier. This process is gaining increasing attention since it allows for an improved quality microreplication while remaining in economically reasonable limits [Gwk12, Che08]. The difference between the classical method and the pulse cooling method is illustrated by Fig. 7.19, a picture from GWK.

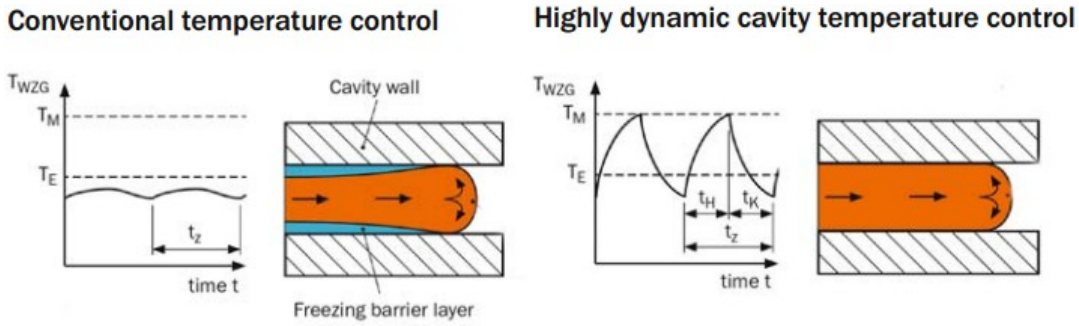

Fig. 7.19: [Gwk12] Illustration of the plastic flow within a conventional mould and a mould using pulse cooling process. t_Z is the cycle time, t_H the heating time, t_K the cooling time, T_{WZG} the cavity wall temperature, T_M the melt temperature, and T_E the demoulding temperature

As shown in Table 7.5, the depth gain with the pulse cooling process is notable, up to 6.4 µm. Compared with the measured thickness of the mould, the error is smaller than 1 µm up to the 110^{th} teeth and the maximum thickness error is 2.9 µm (8.3 µm without pulse cooling).

Table 7.5 Metrology results of the design thicknesses, the measured thicknesses obtained with and without pulse cooling

Teeth #	t_{design} [µm] (lens)	t_{exp} [µm] (mould)	t_{exp} [µm] (lens)	t_{exp} [µm] (lens with pulse cooling)
1	18.869	18.7	12.2	18.6
10	18.815	18.0	11.6	17.6
20	18.781	17.8	11.9	17.6
30	18.755	18.3	12.2	17.0
50	18.712	18.0	10.9	17.0
70	18.677	17.8	10.6	17.0
90	18.646	18.0	14.1	17.0
110	18.618	17.5	13.3	17.0
120	18.605	17.5	11.5	14.6
130	18.592	16.8	11.6	14.3
150	18.566	17.0	9.5	14.2
160	18.548	17.0	8.7	14.5

The conclusion drawn from the investigations on the mould for the PMMA and the lens made of PMMA are also valid for the PC even if not tackled with in this part to avoid redundancy.

7.4.2. Optical tests

Although the diffraction efficiency at the first diffraction order is compromised, the experimental investigation of the diffractive lens is worthwhile. As expected, the search of a bright focal spot at the design distance was totally fruitless. This means that the beams are not diffracted into the first order. As a reminder, the diffraction efficiency depends on the thickness of the lens and its refractive index (see Chap. 4.7.). However, the focal distances are independent of the efficiency but depend only on the pseudo-period of the teeth. In other words, for a given wavelength, the focal distance of the m^{th} order is given by

$$f_m = m f_1 \tag{7.3}$$

were f_1 is the focal distance of the first diffraction order, which is wavelength dependent and can be expressed as

$$f_1(\lambda) = \frac{f_1(\lambda_0)}{\lambda} \tag{7.4}$$

Hence, it is possible to investigate the diffractive behaviour of a refractive lens without the need of high diffraction efficiency to the first order. The converging diffractive lens (made of PMMA) was investigated. Fig. 7.20 shows the pattern produced by light passing through this lens. It clearly shows the superimposition of several diffraction orders.

Fig. 7.20. Superimposition pattern produced by light passing through the converging monolayer diffractive lens.

Introducing the optical fibre in the optical axes, a spectrum made of about fifteen peaks can be observed. At thirteen centimetres from the lens, the spectrum shown in Fig. 7.21 is obtained.

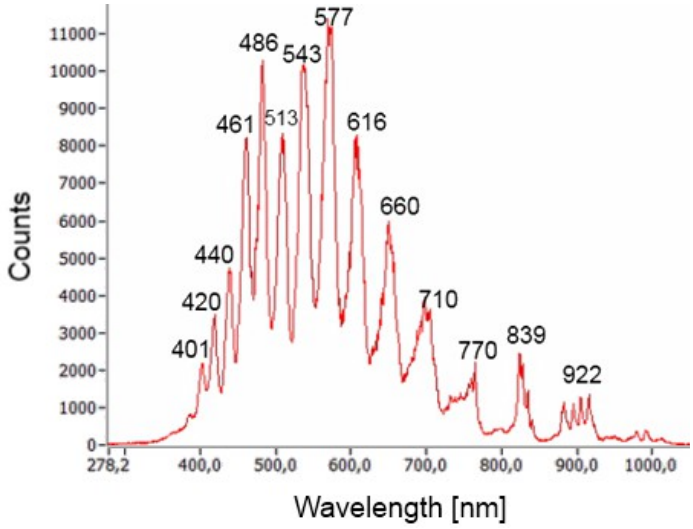

Fig. 7.21: Spectrum of a spot situated at 13cm from the diffractive lens in PMMA.

Now, let's compare this spectrum with the focal distances related to orders from 10 to 23 as a function of the wavelength (other orders are not focusing at 13 cm between 380 and 1600 nm).

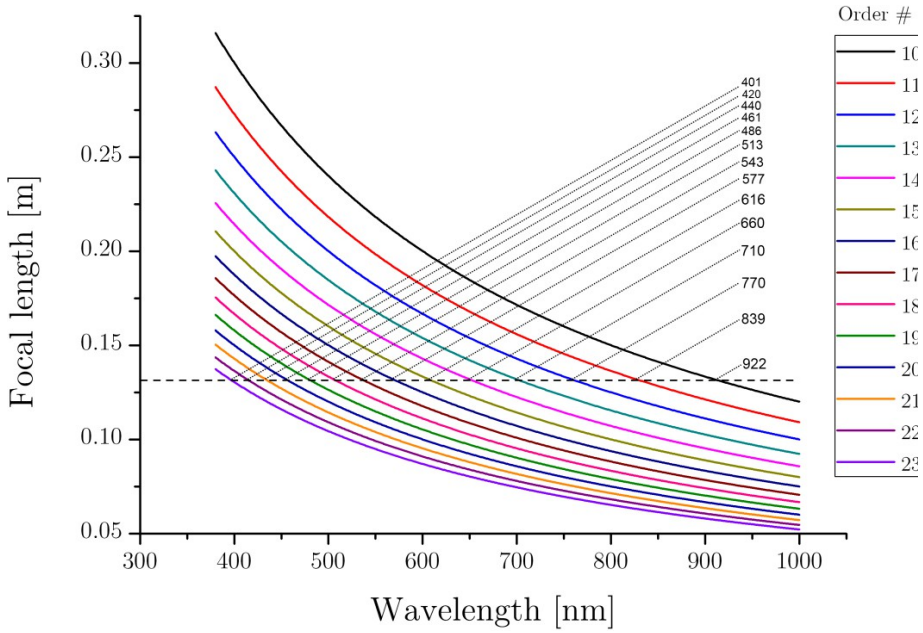

Fig. 7.22: Exponential decay of the focal distance with wavelength for orders from 10 to 23. Wavelengths focusing at 13 cm are highlighted

It clearly appears that wavelengths focused at 13 cm from the lens are the same as the experimental spectrum obtained in the above figure. It can be deduced that the monolayer diffractive structure has a diffractive lens behaviour and hence

has a pseudo-period correctly designed.

7.5. Achromatic doublet manufacturing and optical tests

7.5.1. Manufacturing

Among the four designs of achromatic refractive Fresnel doublets, we decided to manufacture a model with a flat interface between PC and PMMA (namely model 1a' and 1b'). Owing to its higher optical performance, model 1b' shown hereunder, has been selected. An external centring ring has been designed to ensure a good alignment of the lenses.

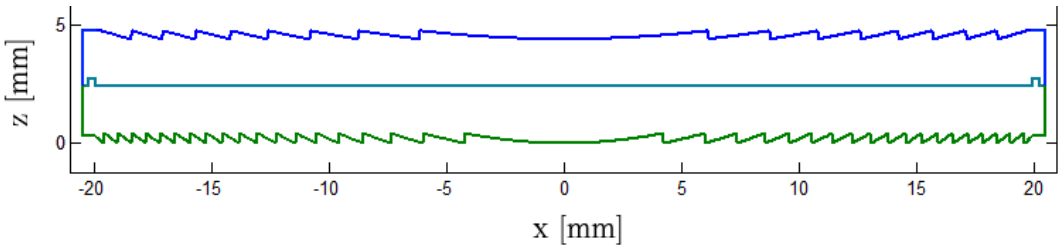

Fig. 7.23: Cross-section view of the achromatic Fresnel doublet (model 1b')

Both moulds have been diamond-turned with a V-tool. The final result is shown in Fig. 7.24.

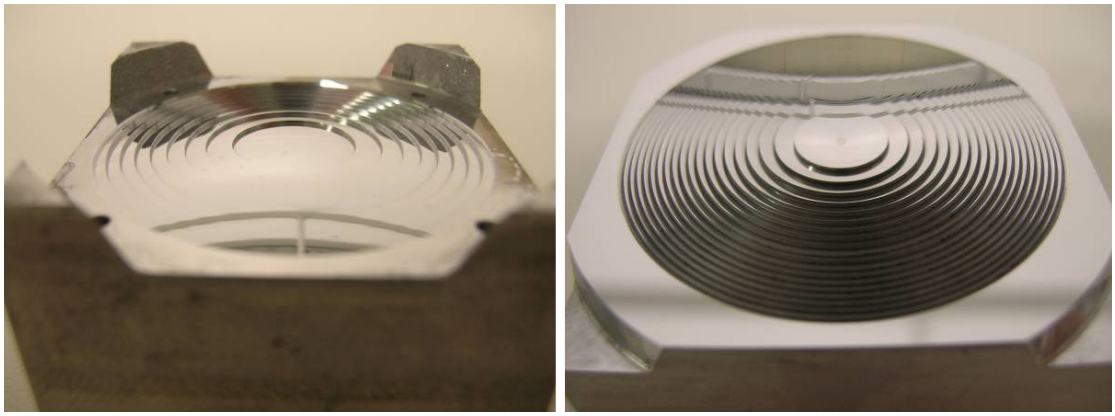

Fig. 7.24: Moulds of the diverging (left) and converging (right) lenses of the achromatic doublet

Experimental measurements of the injected lenses have been compared to the theoretical design. Data are provided in Table 7.6.

Table 7.6 Metrology results comparison between the design thickness and the measured thickness

Teeth #	Designed thickness (PC)	Experimental thickness (PC)	Designed thickness (PMMA)	Experimental thickness (PMMA)
1	352.6	349.2	415.5	403.3
2	356.0	357	417.0	403.7
3	357.7	360.2	415.6	403.6
4	359.6	357.7	420.6	407.6
5	360.1	359.1	415.9	406.8
6	361.6	359.1	419.7	-
7	365.4	365.4	421.7	405.2
8	369.3	368.4	420.4	-
9	-	-	430.9	404.4
11	-	-	426.3	403.6
13	-	-	419.7	404.1
15	-	-	417.7	405.1
17	-	-	424.0	397.2
18	-	-	418.0	388.5
Average	360.3	359.5	420.2	402.8

On the one hand, we observe a strong correlation between the designed thickness and the experimental thickness for the diverging lens in PC-4. The mean error is around 0.2%. On the other hand, the PMMA-2 replication has a lower degree of fidelity, the mean error is about 4.1%. These errors affect the effective focal distance as will be discussed in the next section.

7.5.2. Optical tests and comparison with theory

The original lens was designed to have a focal distance of 80 mm. Due to the use of PMMA-2 instead of PMMA-3, the measured focal distance should have been around 78.5 mm for a wavelength of 961nm (see Fig. 7.25). However, experimental measurements indicate a focal length of about 84 mm (see Fig. 7.26). This might be explained by the shape error described in the above sub-chapter. This error has low influence on the LCA^*: 0.63% for PMMA-2 in paraxial condition, 0.72% for the RoC-2 design and 0.82% for the experimental measurements. Despite the use of another PMMA than that of design, and despite a shape error of the converging lens, the LCA^* remains low: 0.82% to which corresponds a maximum concentration ratio of 15'000×.

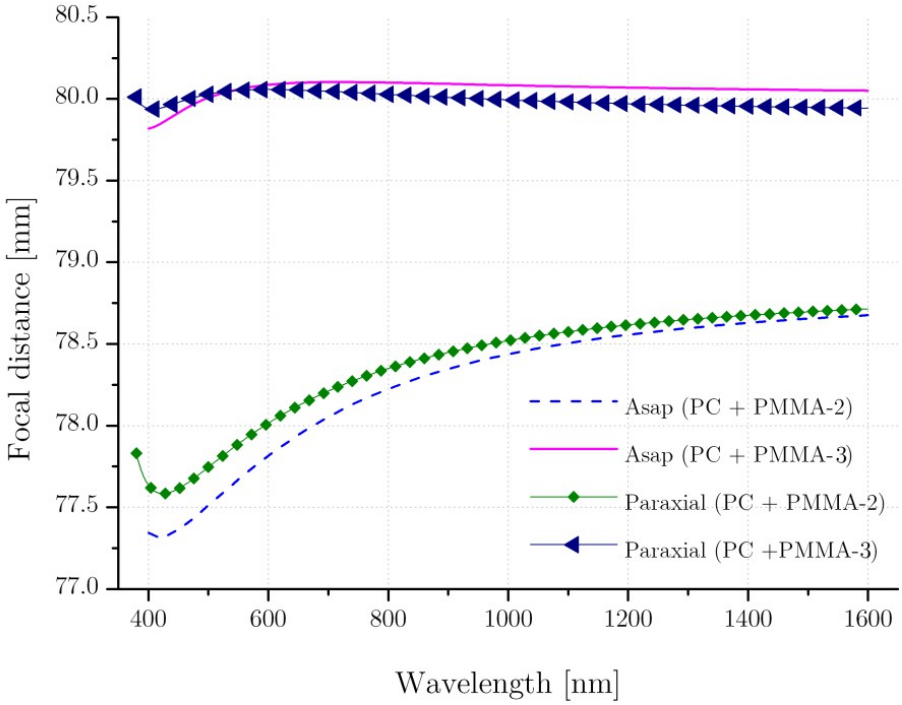

Fig. 7.25: Paraxial focal distances and simulated focal distance for the design doublet (with PMMA-3) and for the designed shape with PMMA-2

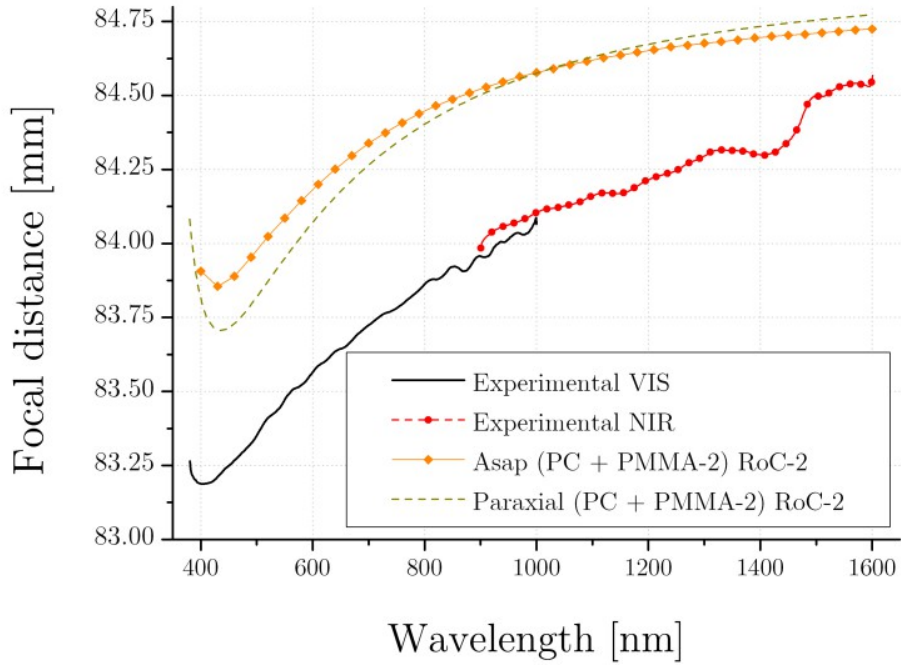

Fig. 7.26: Experimental measurements compared to paraxial calculations and ray-tracing simulations using the modified radius of curvature *RoC*-2

7.6. Doublet and singlet comparison

After the investigation of each design separately, let's compare the performance of the singlet and the doublet. The gain in achromaticity with the doublet is clearly shown in Fig. 7.27. The *LCA** is about 3.2% for the singlet and 0.86% for the doublet. To these *LCAs** correspond maximum concentration factors of about 1000× and 15'000× respectively.

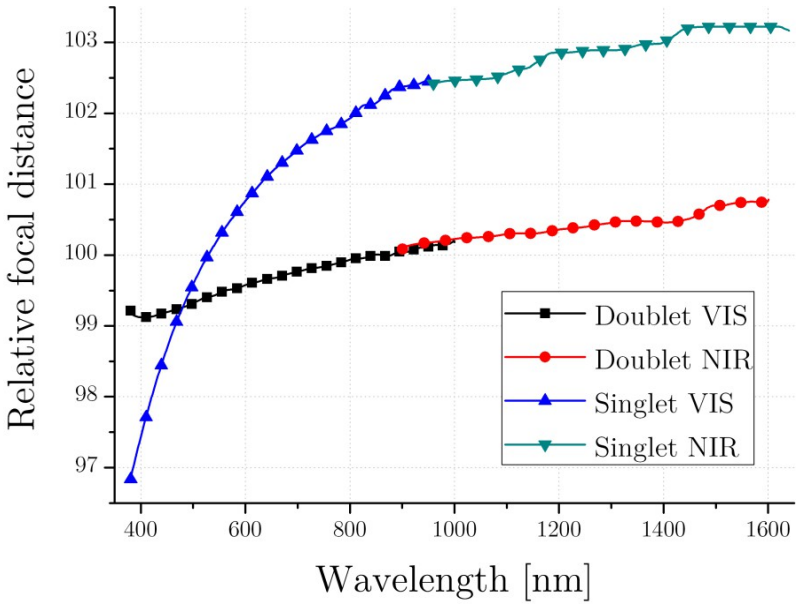

Fig. 7.27: Longitudinal chromatic aberration for the singlet and doublet

To evaluate the performance of the Fresnel doublet, we compared the intensity maps of the focal plane and we calculated the encircled energy and compared it to the ray-tracing simulations using the same angular aperture as the solar simulator (0.24°). While the relative intensity map of the singlet has a large Gaussian shape, the relative intensity map of the doublet is tighter and is much "flat top" as shown in Fig. 7.28.

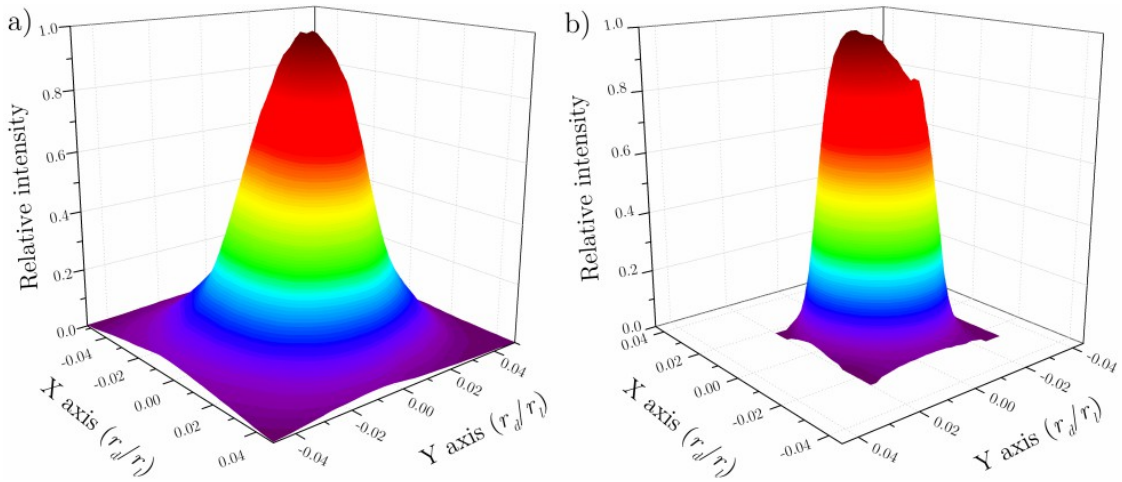

Fig. 7.28: Focal spot relative intensity for the singlet (left) and doublet (right).

Experimental results of the encircled energy are presented in Fig. 7.29. They are in good agreement with the encircled energy obtained with ray-tracing simulations using an illumination source which fits the solar simulator characteristics. The concentration factor of the doublet is almost four times higher than is achieved with a singlet. As predicted by ray-tracing simulations, if the lens had been injected with the design PMMA, the concentration ratio would have been even higher: 3200× for 90% of the encircled energy. Nevertheless, despite the use of another PMMA than initially planned, we reach a very high concentration factor, about 2400× for 90% of the encircled energy.

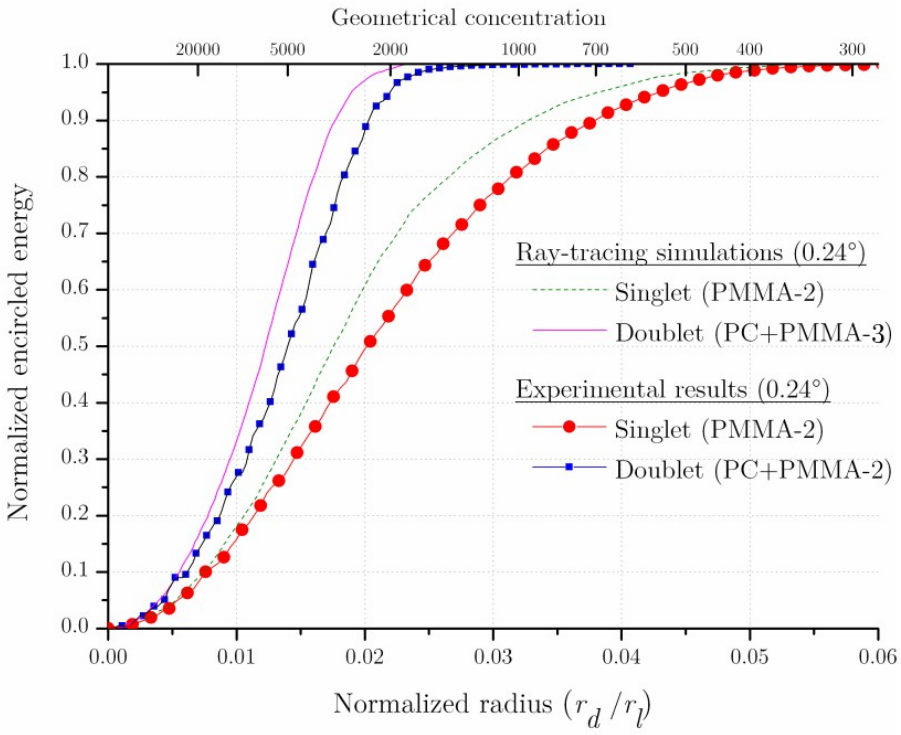

Fig. 7.29: Normalized encircled energy for the singlet and doublet

7.7. Chapter conclusions

In a first step, we developed a simple but efficient set-up to determine the *LCA* of our lenses. Thanks to the metrology performed by CSL we explained the lack of diffraction efficiency for the bilayer diffractive lens. However, the diffractive behaviour was demonstrated in accordance with theoretical calculations. The comparisons between refractive doublet and singlet showed that refractive Fresnel doublets allow for a very high concentration thanks to a highly reduced chromatic aberration. A manufacturing errors – leading to a modification of the curvature of the lens – causes a modification of the focal distance in the same order of

magnitude as the shape error, about 4% in our case. Fortunately, the shape error occurs without significant deterioration of the achromatic behaviour of the Fresnel doublet. The same conclusion may be drawn with the refractive index: an error on the refractive index induces a modification of the focal distance without significant alteration of the chromatic aberration thus retaining a high concentration factor. Refractive Fresnel doublets are thus very tolerant and are suitable in real conditions where the temperature induces a modification of the refractive indices and of the shape of the lenses.

8 | Applications and perspectives

Thanks to the original idea of the combination of refractive and diffractive structures, this PhD thesis already found several industrial applications. Also, the tools developed to act on the chromatic aspect of lenses contributed to new academic researches in the field of solar concentration.

8.1. GAW telescope

Collaborators: Amos S.A., Concentrator Optics GmbH and CSL.

Hololab was asked to contribute to the optical design of a hybrid telescope with a 2.13 m diameter, which is, as far as we know, the greatest refractive telescope[16]. This telescope presents four distinctive features. Firstly, this is a hybrid telescope made of only one material to correct the chromatic aberration (no achromatic doublet). Secondly, the surface is divided in several parts, somewhat like a spider's web. Thirdly, the refractive and diffractive profiles are superimposed in a single component (see Fig. 8.1). Fourth, the lens is made of PMMA and is produced by hot embossing allowing for low-cost reproduction.

Fig. 8.1: Single element hybrid lens with only one textured surface

16 A list of list of the largest optical refracting telescopes is available on http://en.wikipedia.org/wiki/List_of_largest_optical_refracting_telescopes

We calculated the optimal focal distances of the refractive lens and the diffractive lens to obtain a $f/2$ telescope with a reduction of the achromaticity between 300 and 600 nm. The thickness of the diffractive lens was optimized to obtain the highest flux in the first diffraction order. Two pictures of the hybrid telescope are shown hereunder.

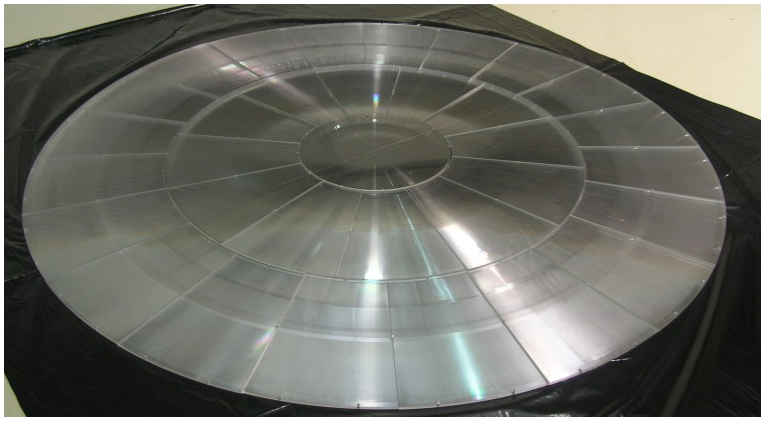

Fig. 8.2: 2.13 meter wide segmented hybrid telescope

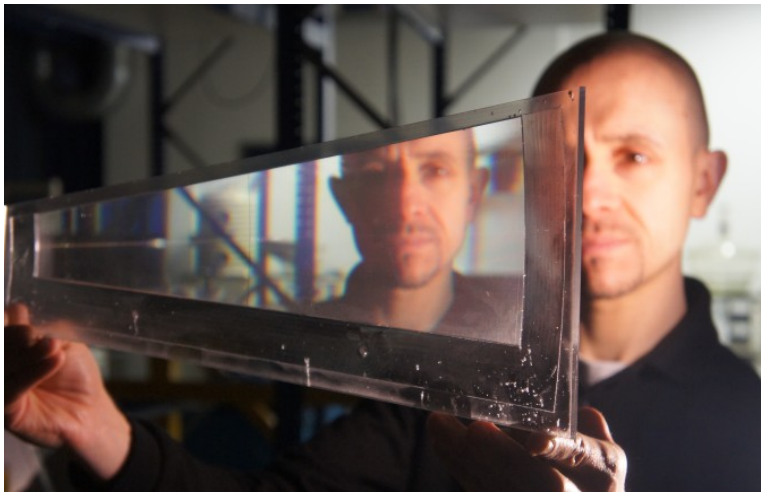

Fig. 8.3: Picture of a segment of the hybrid Fresnel lens

8.2. Hybrid lens for solar concentration in space application

PhD student: Céline MICHEL (Hololab)

Spacecrafts and satellites need a high power supply to makes electrical components work. This is ensures by solar panels. However, it is desirable to provide lighter, cheaper, smaller solar panels with higher efficiency. Solar concentration appears like a compelling solution to reach this target. The concept elaborated by Hololab and developed by Céline Michel with the help of CSL is depicted in Fig. 8.4. It consists in the use of an hybrid optical system made in silicone which is cheaper and lighter than gallium arsenide-based solar cells. The top component of the optical system is a diffraction grating that splits the solar spectrum in diffraction orders. Short wavelengths will be diffracted mainly in the first diffraction order and concentrated by the Fresnel lens towards a first high efficiency solar cell. The majority of wavelengths in the NIR region will be diffracted in the zeroth order (i.e. they will not be diffracted) and will be concentrated on a second high efficiency solar cell suited for NIR wavelengths. Spectrum splitting avoids two important issues: current-matching and lattice-matching. Consequently, higher efficiency can be obtained at lower cost. However, optical losses reduce the performances and a balance must be achieved. Anyway, this technique should increase the performance of space solar panels in terms of W/€ and W/kg.

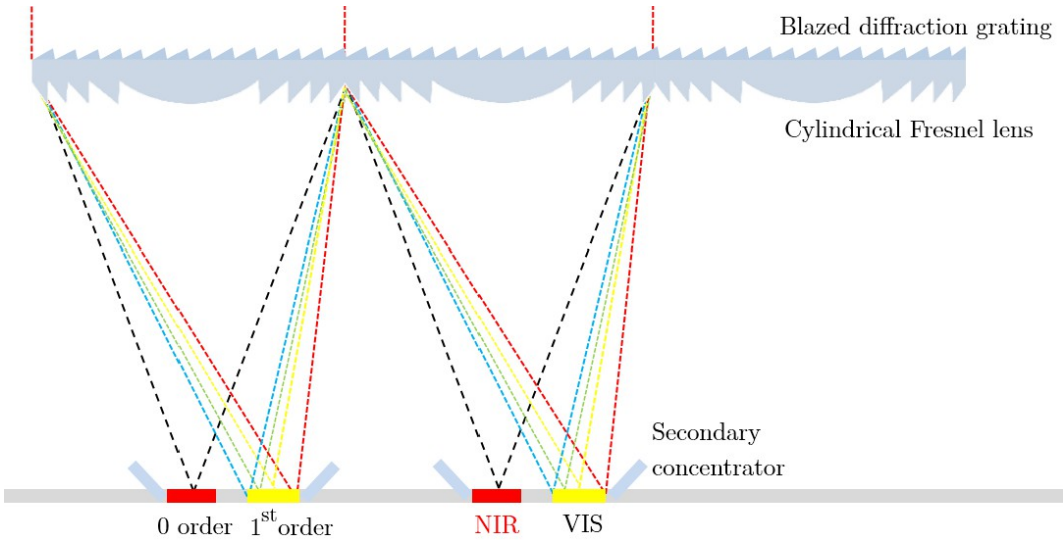

Fig. 8.4: Sketch of hybrid solar concentrator that both splits and concentrates sunlight

8.3. Guide2Dye project

Collaborators: Sirris, GreenMat, CSL.

The Guide2Dye project shares several points in common with Céline Michel's thesis. Here also, the aim consists in light concentration combined with spectrum splitting, using a cylindrical Fresnel lens combined with a diffraction grating. However, the light is not directly focused on the cells but on V-grooves that redirect light within a waveguide towards the cells. Although the optical system can be adapted to any kind of solar cells, dye-sensitized solar cells (DSSC) are investigated in the frame of this project granted by the Walloon Region.

8.4. Hyperspectral spectrometer

Collaborator: Amos S.A.

During our experimental measurements, two spectroscopes were needed. The first one for the visible region, the other one for the NIR region. Spectroscope are spectrally limited for three main reasons. Firstly, the detector used (Si, GaAs, InGaAs, Ge...) has a quantum efficiency different from zero only in a limited spectral band. Secondly, diffraction overlapping occurs from the moment where the longest wavelength is at least two times longer than the shortest wavelength. For example, the diffraction angle to the first order for a wavelength of 800 nm is the same as the angle formed by a wavelength of 400 nm diffracting in the second order, leading to undesirable noise. Thirdly, the diffraction efficiency of usual blazed gratings is optimized for one wavelength (called the blaze wavelength, λ_b). For wavelengths other than λ_b the diffraction efficiency drops significantly (0% for $\lambda_b/2$).

For example, if one wants to optimize the diffraction efficiency between 700 and 5000 nm, the maximum efficiency is obtained for a blaze wavelength of ~2850 nm. However the diffraction efficiency is close to 0% between 700 and 1600 nm as shown in the figure below.

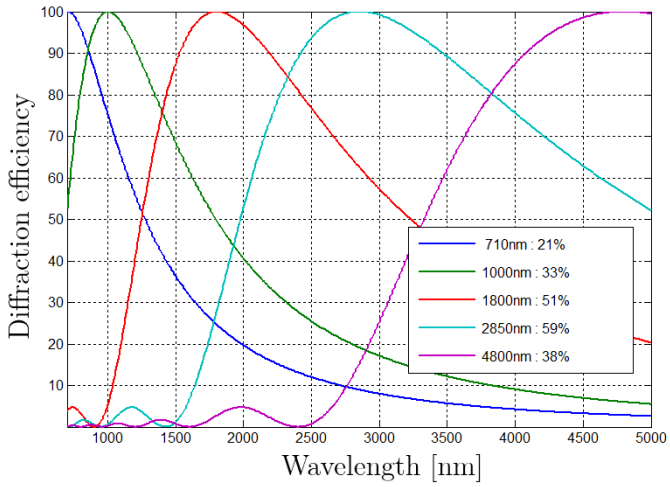

We are currently working on flat shape diffraction efficiency. To achieve this, we are investigating multithickness diffraction gratings as shown in the sketch hereunder.

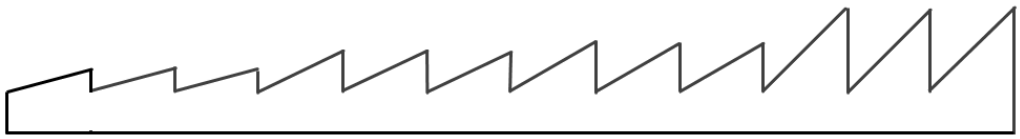

Fig. 8.5: Sketch depicting of a multilthickness diffraction grating

Obtaining a broadband flat-top diffraction efficiency requires optimizing the number of blaze wavelengths needed (i.e. the number of different thicknesses), determining of the corresponding blaze wavelengths and the weight to be assigned to the different blaze wavelengths. The weight is assigned with the number of teeth of a considered thickness.

8.5. To be continued

The investigations on achromatic Fresnel lenses are still going on. To enhance the concentration ratio even more, curved Fresnel lenses are considered. Curved Fresnel lenses are known for their higher acceptance angle than flat Fresnel lenses. Achromatic curved Fresnel lens will be investigated in order to determine if both the acceptance angle and the concentration ratio can be enhanced at the same time.

Although this subject was not treated in this thesis, we have investigated “free-flux” Fresnel lenses. Indeed, an achromatic Fresnel lens is able to provide a very small focal spot under sunlight. So, the shape of the lens can be adapted in order to achieve a particular light pattern on the absorber (e.g. square root intensity shape, Gaussian shape, square shape). People from NREL told us they are particularly interested in this kind of free-flux Fresnel lenses in order to achieve

"avoiding grid" designs, i.e. light pattern that reaches only the active part of the solar cell and avoids the contact grid.

8.6. Chapter conclusions

Despite the relative failure of the multilayer diffractive lens for CPV, the numerous tools developed during this thesis already found several applications: in CPV of course but also in imaging devices and in spectroscopy. The combination of refractive and diffractive structures, one of the innovative aspects of this thesis, seems very promising. We can expect the same for achromatic Fresnel lenses, especially if further investigations show even increased performance.

9 Conclusions

9.1. English version

The use of achromatic lenses in CPV would be a real asset for the production of low-cost green energy.

Indeed, this technology would combine both the advantages of mirrors (i.e. achromaticity and high concentration) with the advantages of lenses (spatial homogeneity and tolerance to manufacturing errors). The advantage of achromatization lens is twofold: first the whiter the flux (spectral homogeneity) the better the quantum efficiency of MJ photovoltaic cells, and secondly it increases the concentration factor. Indeed, we showed that the maximum concentration ratio achieved with a refractive concentrator is not limited by the angular aperture of the Sun but mainly by the variation of the refractive index with the wavelength. In the best case (that is to say for collimated beams under normal incidence) the maximum concentration of a flat lens manufactured with PMMA is about 1000 × for a range of wavelengths from 380 to 1600 nm.

The angular size of the Sun also deteriorates the concentration factor: the higher the *f*-number, the smaller the concentration factor. The use of nonimaging optics for the design of Fresnel lenses allows to manage the angular aperture of the source and optimize the concentration ratio. In particular, thanks to the use of the symmetry condition imposed to the edge-rays. However, the performance difference between an imaging and a nonimaging lens is almost imperceptible when the *f*-number is large and the angular size of the source is small.

In order to achieve an achromatic lens, we investigated hybrid lenses from the prior study of diffraction gratings. We showed that the use of software based on the rigorous theory of light was too time consuming and hard to be implemented for a daily use. The scalar theory helped us to determine the ideal grating shape to achieve a 100% diffraction efficiency in the first diffraction order: the blaze grating. We also showed that the profile of blazed gratings could be optimized taking into account the requirements of manufacturing tools. The optimization was performed in two steps. Firstly, instead of a cutting depth limited by the contact point maximizing the correlation length between the ideal and the manufactured profile, it is best to increase the penetration depth of the tool inside the material. In addition, the slope of the profile should be slightly revised upwards. This is especially true for small periods: the smaller the period, the less reliable the scalar theory. Generally one refers to the famous sentence of Swanson claiming that the scalar theory is accurate if the period of the grating is at least five times larger than the wavelength. For smaller ratios, we had to introduce an extended scalar theory taking into account the effects of shading.

Even if optimized, monolayer diffraction gratings have a too low diffraction efficiency to use only the first order of diffraction in broadband applications like CPV; hence the need for bilayer gratings. These have a second diffraction maximum and a high diffraction efficiency over a broad spectral band. However, shading effects are more important for this type of gratings. We showed that this is not so much the period-to-wavelength ratio that has to be high, but the period-to-thickness. Thus, typically, the period of a bilayer grating must be 100 times larger than the wavelength in order to satisfy the scalar theory. For smaller ratios, the shading is too large so that the diffraction efficiency is low. Thus, the teeth on the outmost edge of a bilayer diffractive lens (that is to say those with the smallest period) suffer from low diffraction efficiency, which is a first drawback for hybrid lenses. For the case on hand, an $f/2$ hybrid lens, we calculated that the diffraction efficiency could not exceed 78%. In addition, the diffractive lens bilayer is extremely intolerant to manufacturing errors. An error of 1 micron on one of the two teeth heights, turns the diffraction efficiency to nearly 0. We can therefore conclude that the bilayer lenses optimized to collect a maximum energy in the first order of diffraction are not suitable for CPV.

Since conclusive results to the disadvantage of hybrid bilayer lenses for achromatization Fresnel lenses were obtained, we turned to purely refractive achromatic Fresnel doublets. Instead of the usual Abbe achromatization equations, we developed a new achromatization equation to achieve better

performances. The determined equation allows to select two wavelengths that perfectly focus on the photovoltaic cell. By properly choosing these two wavelengths, we can drastically reduce the chromatic aberration with two conventional materials, namely PC and PMMA. The chromatic aberration can be reduced to a point where the maximum concentration value becomes much higher than 100 000 ×. In this case, the concentration factor is limited by the *f*-number and the angular aperture of the Sun. For an *f*-number of 2, the maximum value is about 3000 ×. Experimentally, we showed that, for a geometrical concentration ratio we collect 90% of the transmitted flux. Once again, the theoretical and experimental results were in agreement. In addition, we showed by way of theory that the achromatic doublets are tolerant to manufacturing errors. Moreover, the experimental results were obtained with a lens made with another PMMA than that for which it was designed. In this sense, the refractive Fresnel doublets are a success. However, the design studied experimentally is subject to soiling problems since Fresnel teeth are facing outwards. A design with a flat outer surface was proposed but its manufacturing is a real challenge since two textured surfaces are in contact. However, this thesis is not an end, and researches are underway to find a design to achieve the same performance in terms of achromaticity while not being subject to a premature soiling.

Finally, despite the weak performances of the bilayer hybrid lens, experimental results obtained on the diffractive lens were in perfect agreement with the theoretical predictions. So, we participated to the design of a monolayer hybrid telescope with a diameter of 2.13 m, much more tolerant than bilayer structures. This thesis also led to other academic research programs in the field of CPV.

9.2. Version francophone

L'utilisation de lentilles achromatiques en concentration solaire photovoltaïque serait un véritable atout pour la production rentable d'énergie verte.
En effet, cette technologie combinerait à la fois les avantage des miroirs (à savoir l'achromaticité et les haut facteurs de concentration) avec les avantages des lentilles (flux plus homogène spatialement et tolérance quant aux erreurs de fabrication). L'avantage de l'achromatisation de lentilles est donc double: premièrement, plus le flux est achromatique meilleur est le rendement des cellules photovoltaïques, et, deuxièmement, cela permet d'augmenter le facteur de concentration.

Nous avons en effet démontré que les systèmes de concentration par lentilles étaient limités en concentration, non pas par l'ouverture angulaire du Soleil, mais principalement par la variation d'indice de réfraction avec la longueur d'onde. Dans le meilleur des cas (c'est-à-dire sous incidence parfaitement nulle) la valeur maximale de concentration avec une lentille plate en PMMA est de 1000× pour une gamme de longueurs d'onde comprises entre 380 et 1600 nm.

L'ouverture angulaire du Soleil détériore aussi le facteur de concentration. Plus le *f*-number est grand, moins le facteur de concentration est élevé. Le design de lentilles non-imageantes permet de gérer au mieux cette ouverture angulaire pour maximiser le facteur de concentration et notamment en imposant un impact symétrique des « edge-rays ». Cependant, la différence entre une lentille imageante et non-imageante est imperceptible lorsque le *f*-number est grand et la taille angulaire de la source petite.

Pour parvenir à une lentille achromatique, nous avons étudié la piste des lentilles hybrides en passant au préalable par l'étude des réseaux de diffraction. Nous avons montré que l'utilisation de logiciels basés sur la théorie rigoureuse de la lumière était trop lourde en terme de temps d'exécution et d'implémentation. La théorie scalaire nous est venue en aide et a permis de déterminer le profil idéal des réseaux blazés. Nous avons également montré que le profil de réseaux blazés pouvait être optimisé en tenant compte des exigences des outils de fabrication. L'optimisation se fait en deux étapes. Au lieu d'une profondeur de coupe limitée par le point de contact maximisant la longueur de corrélation entre le profil idéal et le profile usiné, nous avons montré qu'il est préférable de creuser plus profondément. De plus, la pente du profil doit aussi être légèrement revue à la hausse. Le gain obtenu étant d'autant plus marqué pour des petites périodes.

Cependant, plus la période est petite, moins la théorie scalaire est fiable. On parle généralement d'avoir une longueur d'onde 5 fois plus grande que la période. D'où la nécessité d'avoir introduit la théorie scalaire étendue prenant en compte les effets d'ombrage.
Même optimisés, les réseaux monocouches possèdent une trop faible efficacité de diffraction sur une gamme telle que 380-1600 nm que pour pouvoir utiliser uniquement le premier ordre de diffraction. D'où la nécessité de recourir à un réseau bicouche. Ceux-ci permettent d'avoir un second maximum de diffraction et d'avoir une haute efficacité de diffraction sur une large bande spectrale. Cependant, les effets d'ombrage sont plus importants pour ce type de réseaux que pour les monocouches. Nous avons montré que pour considérer le régime comme scalaire, ce n'est pas tant la rapport période/longueur d'onde qui doit être élevé mais le rapport période sur hauteur du réseau. Ainsi, typiquement, la période d'un réseau bicouche doit être 100 fois plus élevée que la longueur d'onde pour pouvoir se contenter de la théorie scalaire. Pour de plus petits rapport, l'ombrage est trop important et l'efficacité de diffraction est faible. Ainsi, les dents les plus au bord d'une lentille diffractive bicouche (c'est-à-dire celles ayant les plus petites périodes) souffrent d'un manque d'efficacité de diffraction, ce qui constitue un premier point négatif pour les lentilles hybride. Pour le cas qui nous concerne, une lentille hybride en $f/2$, nous avons calculé que l'efficacité de diffraction ne pouvait excéder 78%. De plus, la lentille diffractive bicouche est extrêmement peu tolérante aux erreurs de fabrication. Une erreur de 1 µm sur l'une des deux hauteurs de dents fait tomber l'efficacité de diffraction à presque 0.
Nous pouvons donc conclure que les lentilles bicouches optimisées pour récolter un maximum d'énergie diffractée à l'ordre 1 ne conviennent pas à la concentration solaire photovoltaïque.

Puisque des résultats concluants mais en défaveur des lentilles hybrides bicouches pour l'achromatisation de lentilles de Fresnel ont été obtenus, nous nous sommes rabattus sur des lentilles achromatiques purement réfractives, à savoir des doublets de Fresnel achromatiques. Pour ceux-ci, nous avons développé une nouvelle équations d'achromatisation, permettant d'atteindre des systèmes plus achromatiques que ceux obtenus sur base de l'équation habituelle d'Abbé. Cette équations permet de choisir librement deux longueurs d'onde venant focaliser parfaitement sur la cellule photovoltaïque. En choisissant correctement ces deux longueurs d'onde, on peut arriver avec deux matériaux usuels, à savoir le PC et le PMMA, à réduire drastiquement les aberrations chromatiques. Ceci à tel point que, sous incidence normale, la valeur de concentration maximale devient alors nettement supérieure à 100 000 $\times$. Dans ce cas, c'est alors le *f*-number et l'ouverture angulaire du Soleil qui limitent le facteur de concentration. Pour un *f*-

number de 2, la valeur maximale est d'environ 3000×. Expérimentalement, nous avons montré que nous obtenions 90% du flux transmis pour un facteur de concentration géométrique de 3000×. Encore une fois, les résultats théoriques et expérimentaux concordaient. De plus, nous avons montré théoriquement que les doublets achromatiques étaient tolérants aux erreurs de fabrication. D'ailleurs les résultats expérimentaux ont été obtenus avec une lentille réalisée avec un PMMA autre que celui pour lequel elle avait été conçue. En ce sens les doublets de Fresnel réfractifs sont un succès. Néanmoins, le design étudié expérimentalement possède des dents côté Soleil, ce qui fait que la lentille est fortement sujette à l'encrassement. Un design avec une surface extérieure plane a été proposé mais s'avère être un challenge technologique au niveau de sa réalisation.
Cependant, cette thèse de doctorat n'est pas un aboutissement, et le recherches vont bon train afin de trouver un design permettant d'atteindre les mêmes performances en terme d'achromaticité tout en n'étant pas sujet à un encrassement prématuré.

Enfin, notons que malgré les performances mitigées de la lentille hybride bichouche, les résultats expérimentaux obtenus sur la lentille diffractive étaient en parfait concordance avec les prédictions théoriques. Les connaissances sur la combinaison réfractif/diffractif acquises durant cette thèse nous ont permis de participer à la conception d'un télescope hybride monocouche conçu pour une gamme de longueurs d'onde s'étendant de 300 à 600 nm. Cette thèse a également débouché sur d'autres programmes de recherches académiques.

Appendix

I References

[Ant01] I. Antón, R. Solar, G. Sala and D. Pachón, "IV Testing of Concentration Modules and Cells with Non-Uniform Light Patterns", in: Proceedings of the 17th European Photovoltaic Solar Energy Conference and Exhibition, Munich, Germany, 611-614 (2001).

[Bac95] H. Bach and N. Neuroth, eds., "The properties of optical glass", Springer, Berlin, 1995.

[Bai12] H. Baig, K.C. Heasman and T.K. Mallick, "Non-uniform illumination in concentrating solar cells", Renewable and Sustainable Energy Reviews **16**, 5890–5909 (2012).

[Ben10] P. Benítez, J.C. Miñano , P. Zamora, R. Mohedano, A. Cvetkovic, M. Buljan, J. Chaves, M. Hernández, "High performance Fresnel-based photovoltaic concentrator", Optics Express **18** (S1), A25-A40 (2010).

[Bet07] A.W. Bett, F. Dimroth and G. Siefer, in "Concentrator Photovoltaics", Chap. 4, Springer, New York, 2007.

[Bih10] Ph. Bihouix and B. de Guillebon, "Quel futur pour les métaux ? Raréfaction des métaux : un nouveau défi pour la société", EDP Sciences, Les Ulis, 2010.

[Bit08] E. Bittmann, O. Mayer, M. Zettl and O. Stern, "Low Concentration PV With Polycarbonate", in: Proceedings of the 23rd European Photovoltaic Solar Energy Conference and Exhibition, Valencia, Spain, 1-5 September 2008.

[Bod08] D. Bodas, J.-Y. Rauch and Ch. Khan-Malek, “Surface modification and aging studies of addition-curing silicone rubbers by oxygen plasma”, European Polymer Journal **44**(7), 2130–2139 (2008).

[Bor03] M. Born and E. Wolf, “Principles of Optics”, 7th Ed., Cambridge University Press, 2003

[Bur89] D.A. Buralli, G.M. Morris and J.R. Rogers, “Optical performance of holographic kinoforms”, Applied Optics **28**(5), 976-983 (1989).

[Car02] C.K. Carniglia and D.G. Jensen, “Single-layer model for surface roughness”, Applied Optics **41**(16), 3167-3171 (2002).

[Car86] J.M. Cariou, J. Dugas, L. Martin and P. Michel, “Refractive-index variations with temperature of PMMA and polycarbonate”, Applied Optics **25**(3), 334-336 (1986).

[Cha05] G. Chartier, “Introduction to Optics”, Springer, 2005.

[Cha08] J. Chaves, “Introduction to Nonimaging Optics”, CRC Press, Taylor and Francis Group, 2008.

[Che08] S.-C. Chen, Y. Chang, T.-H. Chang and R.-D. Chien, “Influence of using pulsed cooling for mold temperature control on microgroove duplication accuracy and warpage of the Blu-ray Disc”, International Communications in Heat and Mass Transfer **35**, 130–138 (2008).

[Cov05] J.S. Coventry, “Performance of a concentrating photovoltaic/thermal solar collector”, Solar Energy **78**, 211-222 (2005).

[Dal97] D.J. Daly, R.A. Ferguson and M.C. Hutley, “Replication of optical components using a silicone rubber intermediate replica”, Proc. SPIE **3099**, 83–88 (1997).

[DeV80] A. De Vos, “Detailed balance limit of the efficiency of tandem solar cells”, Journal of Physics D: Applied Physics **13**, 839-846 (1980).

[Dha81] S. R. Dhariwal, R. K. Mathur and R. Gadre, “Voltage reduction in a non-uniformly illuminated solar cell”, Journal of Physics D: Applied Physics **14**, 1325-1329 (1981).

[Dom12] C. Domínguez, M. Victoria, R. Herrero, S. Askins, I. Antón and G. Sala, “Probing the effects of non-uniform light beams and chromatic aberration on the performance of concentrators using multijunction cells”, in: Proceedings of 8th International conference on Concentrating Photovoltaic Systems (CPV-8), Toledo, Spain, April 16-18, 2012.

[Due10] F. Duerr, Y. Meuret and H. Thienpont, “Miniaturization of Fresnel lenses for solar concentration: a quantitative investigation”, Applied Optics **49**, 2339-2346 (2010).

[Fre11] Fresnel lens brochure of the Fresnel Technologies Inc.: www.fresneltech.com/materials.html, accessed on 2011/06/02.

[Frö94] K. Fröhlich, U. Wagemann, J. Schulat, H. Schütte and C.G. Stojanoff, “Fabrication and test of a holographic concentrator for two color PV-operation”, in: Optical Materials Technology for Energy Efficiency and Solar Energy Conversion XIII, Volker Wittwer, Claes G. Granqvist and Carl M. Lampert Eds., Proc. SPIE **2255**, 812-821 (1994).

[Fth11] V.M. Fthenakis and H.C. Kim, “Photovoltaics: Life-cycle analyses”, Solar Energy **85**(8), 1609-1628 (2011).

[Fuj82] T. Fujita, H. Nishihara and J. Koyama, “Blazed gratings and Fresnel lenses fabricated by electron-beam lithography”, Optics Letters **7**(12), 578-580 (1982).

[Gom04] A. Gombert, “On the suitability of diffractive optical elements in solar applications”, in: Diffractive Optics and Micro-Optics, OSA Technical Digest (Optical Society of America, 2004), paper DTuD3.

[Goo96] J.W. Goodman, “Introduction to Fourier optics”, 2nd edition, McGraw-Hill Book Company, New York, 1996.

[Gre93] D.A. Gremaux and N. C. Gallagher, “Limits of scalar diffraction theory for conducting gratings”, Applied Optics **32**(11), 1948-1953 (1993).

[Gue01] C.A. Gueymard, “Parameterized Transmittance Model for Direct Beam And Circumsolar Spectral Irradiance”, Solar Energy **71**(5), 325-346 (2001)

[Gue04] Ch. Gueymard, “The sun's total and spectral irradiance for solar energy applications and solar radiation models”, Solar Energy **76**(4), 423-453 (2004).

[Gwk12] Gesellschaft Wärme Kältetechnik mbH website, http://www.gwk.com/_pdf/prospect/integrat-evolution_en.pdf, last accessed on 2012/09/28.

[Hec02] E. Hecht, Optics 4th Ed. (Addison-Wesley, 2002), Chap. 5.

[Hes98] T. Hessler, M. Rossi, R.E. Kunz and M.T. Gale, “Analysis and

optimization of fabrication of continuous-relief diffractive optical elements", Applied Optics **37**(19), 4069-4079 (1998).

[Hon02] C.B. Honsberg, S.P. Bremner and R. Corkish, "Design trade-offs and rules for multiple energy level solar cells", Physica E **14**, 136-141 (2002).

[Hor12] T. Hornung, M. Steiner and P. Nitz, "Estimation of the influence of Fresnel lens temperature on energy generation of a concentrator photovoltaic system", Solar Energy Materials and Solar Cells **99**, 333-338 (2012).

[Hun10] H.C. Hunt, "Integrated microlenses and multimode interference devices for microflow cytometers", Doctoral Thesis, University of Southampton, UK, 2010.

[Hun12] H.C. Hunt and J.S. Wilkinson, "Kinoform microlenses for focusing into microfluidic channels", Optics Express **20**(9), 9442-9457 (2012).

[HuyXVII] C. Huyghens, "Traité de la Lumière", Reproduction original text published in 1690, Gauthier-Villars and Cie, Ed., Paris, 1920.

[Ime04] A.G. Imenes and D.R. Mills, "Spectral beam splitting technology for increased conversion efficiency in solar concentrating systems: a review", Solar Energy Materials and Solar Cells **84** (1-4), 19-69 (2004).

[Ish00] T. Ishii, "Diffractive Optical Element", US Patent, 6 157 488 (2000).

[Jor70] J.A. Jordan Jr., P.M. Hirsch, L.B. Lesem and D.L. Van Rooy, "Kinoform lenses", Applied Optics **9**(8), 1883-1887 (1970).

[Kal00] I. Kallioniemi, T. Ammer and M. Rossi, "Optimization of continuous-profile blazed gratings using rigorous diffraction theory", Optics Communications **177**, 15–24 (2000).

[Kas07] S.N. Kasarova, N.G. Sultanova, C.D. Ivanov and I.D. Nikolov, "Analysis of the dispersion of optical plastic materials," Optical Materials **29**(11), 1481–1490 (2007).

[Kle08] B. H. Kleemann, M. Seeßelberg and J. Ruoff, "Design concepts for broadband high–efficiency DOEs", Journal of the European Optical Society - Rapid Publications **3**, 08015 (2008).

[Kuh07] A. Davis, F. Kühnlenz and R. Business, "Optical design using Fresnel lenses", Optik Photonik **4**, 52–55 (2007).

[Lal96] Ph. Lalanne and G.M. Morris, "Highly improved convergence of the

coupled wave method for TM Polarization", Journal of the Optical Society of America A **13**, 779-782 (1996).

[Lal99] Ph. Lalanne, S. Astilean, P. Chavel, E. Cambril and H. Launois, "Design and fabrication of blazed binary diffractive elements with sampling periods smaller than the structural cutoff", Journal of the Optical Society of America A **16**(5), 1143-1156 (1999).

[Lan11a] F. Languy, K. Fleury, C. Lenaerts, J. Loicq, D. Regaert, T. Thibert and S. Habraken, "Flat Fresnel doublets made of PMMA and PC: combining low-cost production and very high concentration ratio for CPV", Optics Express **19**, A280-A294 (2011).

[Lan11b] F. Languy and S. Habraken, "Performance comparison of four kinds of flat nonimaging Fresnel lenses made of polycarbonates and polymethyl methacrylate for concentrated photovoltaics", Optics Letters **36**, 2743-2745 (2011).

[Lar12] S. Larouche and D.R. Smith, "Reconciliation of generalized refraction with diffraction theory", Optics Letters **37**(12), 2391-2393 (2012).

[Lee01] Y.B. Lee and T.H. Kwon, "Modeling and numerical simulation of residual stresses and birefringence in injection molded center-gated disks", Journal of Materials Processing Technology **111**(1-3), 214–218 (2001).

[Len05] C. Lenarts, "Etude et réalisation de filtres spectraux : Application à la résonance de mode guidé et à la résonance de splasmons de surface", Doctoral Thesis, University of Liège, Belgium, 2005.

[Les69] L.B. Lesem, P.M. Hirsch and J.A. Jordan Jr., "The Kinoform: A New Wavefront Reconstruction Device", IBM Journal of Research and Development **13**, 150-155 (1969).

[Leu00] R. Leutz, "Nonimaging Fresnel Lenses for Solar Concentrators", Doctoral Thesis, Tokyo University of Agriculture and Technology, Japan, 2000.

[Leu01] R. Leutz and A. Suzuki, "Nonimaging Fresnel Lenses: Design and Performance of Solar Concentrators", Springer Verlag, New York, 2001.

[Leu09] R. Leutz, H. P. Annen and L. Fu, "Fundamental differences in the design and efficiency of concentrators for solar applications", in: Proceedings of the Workshop on Concentrating Photovoltaic Power Plants: Optical Design and Grid Connection, Darmstadt, Germany,

9-10 March 2009.

[Leu99] R. Leutz, A. Suzuki, A. Akisawa and T. Kashiwagi, “Design of a nonimaging fresnel lens for solar concentrators”, Solar Energy **65**(6), 379-387 (1999).

[Lev04] U. Levy, E. Marom and D. Mendlovic, “Thin element approximation for the analysis of blazed gratings: simplified model and validity limits”, Optics Communications **229**, 11–21 (2004).

[Li93] L. Li and C.W. Haggans, “Convergence of the coupled-wave method for metallic lamellar diffraction gratings”, Journal of the Optical Society of America A **10**, 1184-1189 (1993).

[Liu05] P. Liu and Baïda Lü, “Diffraction of spherical waves at an annular aperture in the use of the boundary diffraction wave theory: A comparison of different diffraction integral approaches”, Optik **116**, 449-453 (2005).

[Lon93] C. Londoño, W.T. Plummer and P.P. Clark, “Athermalization of a single-component lens with diffractive optics”, Applied Optics **32**(13), 2295-2302 (1993).

[Lud97] J.E. Ludman, J. Riccobono, I.V. Semenova, N.O. Reinhand, W. Tai, X. Li, G. Syphers, E. Rallis, G. Sliker and J. Martín, “The optimization of a holographic system for solar power generation”, Solar Energy **60**(1), 1-9 (1997).

[Luq07] I. Luque-Heredia, P.H. Magalhães, G. Quéméré, R. Cervantes, J.M. Moreno, O. Laurent, “CPV tracking systems: performances issues, specifications & design”, in: Proceedings of the 4th International Conference on Solar Concentrators for the Generation of Electricity or Hydrogen, El Escorial, 2007.

[Lyt09] J.D. Lytle, “Polymeric Optics”, in Handbook of Optics, 3rd Edition, Vol. IV, M. Bass, McGraw-Hill, 2009.

[Mak07] J.-T. Mäkinen and R. de Schipper, “How can plastics injection molding help driving down the cost of photovoltaic concentrators?” in: Proceedings of the Workshop on Concentrating Photovoltaic Power Plants: Optical Design and Grid Connection, Marburg, Germany, 2007.

[Mak11] K.G. Makris, D. Psaltis, “Huygens–Fresnel diffraction and evanescent waves”, Optics Communications **284**, 1686–1689 (2011).

[Mar97] S. Martellucci and A.N. Chester, “Diffractive Optics and Optical

Microsystems", Springer, 1997.

[Mas12] H. Mashaal, A. Goldstein, D. Feuermann and J. M. Gordon, "First direct measurement of the spatial coherence of sunlight", Optics Letters **37**(17), 3516-3518 (2012).

[Men05] B. Mendoza, "Total solar irradiance and climate", Advances in Space Research **35**, 882–890 (2005).

[Mil11] D.C. Miller and S.R. Kurtz, "Durability of Fresnel lenses: a review specific to the concentrating photovoltaic application", Solar Energy Materials and Solar Cells **95**, 2037-2068 (2011).

[Mor06] O. Morton, "Solar energy: A new day dawning?: Silicon Valley sunrise", Nature **443**, 19-22 (2006).

[Mor81] M.G. Moharam and T.K. Gaylord, "Rigorous coupled-wave analysis of planar-grating diffraction", Journal of the Optical Society of America **11**(7), 811-818 (1981).

[Mor82] M.G. Moharam and T.K. Gaylord, "Diffraction analysis of dielectric surface relief gratings", Journal of the Optical Society of America **72**, 1385-1392 (1982).

[Mor97] V. Moreno, J. F. Román and J.R. Salgueiro, "High efficiency diffractive lenses: Deduction of kinoform profile", American Journal of Physics **65**(6), 556-562 (1997).

[Mot11] A. Motogaito and K. Hiramatsu, "Fabrication of Binary Diffractive Lens on Optical Films by Electron Beam Lithography", in: *Advances in unconventional lithography*, Gorgi Kostovski ed, InTech, Chap. 7 (2011).

[Mye02] D.R. Myers , K. Emery and Ch. Gueymard, "Revising and validating spectral irradiance reference standards for photovoltaic performance", in: Proceedings of the ASES/ASME solar 2002 conference, Reno, Nevada, June 15–20, 2002.

[Nalux] Nalux Nano Optical website, http://www.naluxnanooptical.com/Clear_Optical_Plastics.html, accessed on 2012/05/11.

[Nil05] J. Nilson, "Optical Design and Characterization of Solar Concentrators for Photovoltaics", Doctoral Thesis, Lund University, Sweden, 2005.

[Nis06] K. Nishioka, T. Takamoto, T. Agui, M. Kaneiwa, Y. Uraok and T.

Fuyuki, “Annual output estimation of concentrator photovoltaic systems using high-efficiency InGaP/InGaAs/Ge triple-junction solar cells based on experimental solar cell’s characteristics and field-test meteorological data”, Solar Energy Materials and Solar Cells **90**, 56-67 (2006).

[NREL] Website for NREL’s AM1.5 Standard Data set: rredc.nrel.gov/solar/spectra/am1.5/ASTMG173/ASTMG173.html, accessed on 2011/06/02.

[Oha98] H. Ohashi, “Diffractive optical element and optical system including the same”, US Patent, 5 737 125 (1998).

[Omn12] Omnexus website: http://www.omnexus.com/, last accessed on 2012/08/05.

[OSh03] D. C. O’Shea, T. J. Suleski, A. D. Kathman and D. W. Prather, “Diffractive optics. Design, Fabrication and Test”, SPIE tutorial texts, vol. TT62. Washington: SPIE Press, 2003.

[Pal00] C. Palmer, “Diffraction Grating Handbook”, Richardson Grating Laboratory, New York, 2000.

[Pat12] J.C. Patra and D.L. Maskell, “Modeling of multi-junction solar cells for estimation of EQE under influence of charged particles using artificial neural networks”, Renewable Energy **44**, 7-16 (2012).

[PE700] PE700C-13F datasheet, http://www.datasheetarchive.com/PE700C-13F-datasheet.html, last accessed on 2012/09/23.

[Pis11] M. Pisarenco, J. Maubach, I. Setija and R. Mattheij, “Modified S-matrix algorithm for the aperiodic Fourier modal method in contrast-field formulation”, Journal of the Optical Society of America A **28**(7), 1364-1371 (2011).

[Pom94] D. A. Pommet, M. G. Moharam and Eric B. Grann, “Limits of scalar diffraction theory for diffractive phase elements”, Journal of the Optical Society of America A **11**(6), 1827-1834 (1994).

[Pop02] E. Popov, M. Nevière, B. Gralak and G. Tayeb, “Staircase approximation validity for arbitrary-shaped gratings”, Journal of the Optical Society of America A **19**(1), 33-42 (2002)

[Pop95] E. Popov, B. Bozkov, M. Sabeva, D. Maystre, “Blazed holographic grating efficiency-numerical comparison with different profiles”, Optics Communications **117**(5–6) 413-416 (1995).

[Pri12] Priyanka Singh, N.M. Ravindra, "Temperature dependence of solar cell performance – an analysis", Solar Energy Materials and Solar Cells **101**, 36–45 (2012).

[Reg10] D. Regaert, "Modelisation, tests numériques et optimisation de lentilles de Fresnel non imageantes utilisées pour la haute concentration solaire", Master thesis in Physics, Facultés Universitaires Notre-Dame de la Paix, 2010.

[Rie94] H. Ries and A. Rabl, "Edge-ray principle of nonimaging optics", Journal of the Optical Society of America A **11(**10), 2627-2632 (1994).

[Roc09] H. Rochholz, P. Battenhausen and P. Marks, "Plastic materials for solar energy applications", in: Proceedings of the Workshop on Concentrating Photovoltaic Power Plants: Optical Design and Grid Connection, Darmstadt, Germany, March 9-10, 2009.

[Ros95] M. Rossi, R.E. Kunz and H.P. Herzig, "Refractive and diffractive properties of planar micro-optical elements", Applied Optics **34**(26), 1995.

[Sal97] T.R.M. Sales and G.M. Morris, "Diffractive–refractive behavior of kinoform lenses", Applied Optics **36**(1), 253-257 (1997).

[San06] O. Sandfuchs, R. Brunner, D. Pätz, S. Sinzinger and J. Ruoff, "Rigorous analysis of shading effects in blazed transmission gratings", Optics Letters **31**(24), 3638-3640 (2006).

[Sas09] T.Sasaki, K.Arafune, W.Metzger, M.J.Romero, K.Jones, M.Al-Jassim b, Y.Ohshita and M. Yamaguchi, "Characterization of carrier recombination in lattice-mismatched InGaAs solar cells on GaAs substrates", Solar Energy Materials and Solar Cells **93**, 936–940 (2009).

[Sch02] U. Schulz, U.B. Schallenberg and N. Kaiser, "Antireflection Coating Design for Plastic Optics", Applied Optics **41**, 3107-3110 (2002).

[Sch09] T. Schult, M. Neubauer, Y. Bessler, P. Nitz and A. Gombert, "Temperature dependence of Fresnel lenses for concentrating photovoltaics", in: Proceedings of the Workshop on Concentrating Photovoltaic Power Plants: Optical Design and Grid Connection, Darmstadt, Germany, March 9-10, 2009.

[Sch12] R.D. Schultz, F.J. Vorster and E.E. van Dyk, "Performance of multi-junction cells due to illumination distribution across the cell

surface", Physica B **407**, 1649-1652 (2012).

[Seg12] G. Segev, G. Mittelman, A. Kribus, "Equivalent circuit models for triple-junction concentrator solar cells", Solar Energy Materials and Solar Cells **98**, 57-65 (2012).

[Sin87] G. Sines and Y. A. Sakellarakis, "Lenses in Antiquity", American Journal of Archaeology **91**(2), 191-196 (1987).

[Sin95] S. Sinzinger and M. Testof, "Transition between diffractive and refractive micro-optical components", Applied Optics **34**(26), 5970-5976 (1995).

[Sol09] D. Feuermann, J.M. Gordon and P. Young, "Unfolded aplanatic optics for high concentration photovoltaics", in: Proceedings of the Workshop on Concentrating Photovoltaic Power Plants: Optical Design and Grid Connection, Darmstadt, Germany, March 9-10, 2009 – http://www.solfocus.com/.

[Som54] A. Sommerfeld. "Optics", Vol. IV of Lectures on Theoretical Physics. Academic Press, New York, 1954.

[Spe12] Spectrolab data sheets, www.spectrolab.com/DataSheets/PV/CPV/CDO-100-C3MJ.pdf, last accessed on 2012/08/29.

[Sto08] A. Stoppato, "Life cycle assessment of photovoltaic electricity generation", Energy **33**, 224-232 (2008).

[Sto94] C.G. Stojanoff, K. Fröhlich, U. Wagemann, H. Schütte, J. Schulat and P. Fröning, "New developments in holographic solar concentrators: a review", in: Proceedings of the Conference on Optical Materials Technology for Energy Efficiency and Solar Energy Conversion XIII, SPIE, Freiburg, Germany.

[Swa89] G.J. Swanson, "Binary optics technology: the theory and design of multilevel diffractive optical elements", Technical Report **854**, MIT Lincoln Laboratory, Massachusetts (1989).

[Swa91] G.J. Swanson, "Binary Optics Technology: Theoretical Limits on the Diffraction Efficiency of Multilevel Diffractive Optical Elements", Technical Report **914**, MIT Lincoln Laboratory, Massachusetts (1991).

[Swe79] W.C. Sweatt, "Mathematical equivalence between a holographic optical element and an ultra-high index lens", Journal of the Optical Society of America **69**(3), 486-487 (1979).

[Tan06] N. Tanio and T. Nakanishi, “Physical Aging and Refractive Index of Poly(methyl methacrylate) Glass”, Polymer Journal **38**(8), 814–818 (2006).

[Thi10] T. Thibert, M.-L. Hellin, J. Loicq, E. Mazy, J.-M. Gillis, F. Languy, S. Habraken, J.-H. Lecat, J.-M. Defise, “Continuous Solar Simulator for Concentrator Photovoltaic Systems”, in: Proceedings of the 25th European Photovoltaic Solar Energy Conference and Exhibition, Valencia, Spain, September 6-10, 2010.

[Tho12] H. Thorsten, M. Steiner and P. Nitz, “Estimation of the influence of Fresnel lens temperature on energy generation of a concentrator photovoltaic system” Solar Energy Materials and Solar Cells **99**, 333-338 (2012).

[Van11] S. van Riesen, A. Gombert, E. Gerster, T. Gerstmaier; J. Jaus, F. Eltermann, A. Bett, “Concentrix Solar’s progress in developing highly efficient modules”, in: Proceedings of CPV-7, Las Vegas, 2011.

[Var69] Y.P. Varshni, “Temperature dependence of the energy gap in semiconductors”, Physica **34**, 149–154 (1967).

[Vic09] M. Victoria, C. Domínguez, I. Antón and G. Sala, “Comparative analisys of different secondary optical elements: effective concentration, acceptance angle and light distribution”, in: Proceedings of 24th European Photovoltaic Solar Energy Conference and Exhibition, Hamburg, Germany, September 20-2, 2009.

[Viv10] M. Vivar, R. Herrero, I. Antón, F. Martínez-Moreno, R. Moretón, G. Sala, A.W. Blakers and J. Smeltink, “Effect of soiling in CPV systems”, Solar Energy **84**(7), 1327-1335 (2010).

[Wan08] H. Wang, D. Kuang and Z. Fang, “Diffraction analysis of blazed transmission gratings with a modified extended scalar theory”, Journal of the Optical Society of America A **25**(6) 1253-1259 (2008).

[Web03] Marvin J. Weber, “Handbook of Optical Materials”, CRC Press, London, 2003.

[Wel89] W.T. Welford, “Aberrations of optical systems”, Adam Hilger L.t.d., Bristol/Boston, 1989.

[Wil09] SunAlign software developed by David Williams, www.green-life-innovators.org/ - www.appropedia.org/Sun_related_calculations, last accessed on 2012/05/02.

[Win05] R. Winston, J. Miñano and P. Benitez, “Nonimaging Optics”,

Elsevier Academic Press, Amsterdam, 2005.

[Wol95] K.B. Wolf and G. Krötzsch, "Geometry and dynamics in refracting systems", European Journal of Physics **16**(1), 14-20 (1995).

[Wur05] P. Würfel, "Physics of Solar Cells, From Principles to New Concepts", WILEY-VCH Verlag GmbH & Co, Weinheim, 2005.

[Xia03] M. Xiao, K. Sato, S. Karube and T. Soutome, "The effect of tool nose radius in ultrasonic vibration cutting of hard metal", International Journal of Machine Tools and Manufacture **43**, 1375-1382 (2003).

[Yu11] N. Yu, P. Genevet, M. Kats, F. Aieta, J.-P. Tetienne, F. Capasso, Z. Gaburro, "Light Propagation with Phase Discontinuities: Generalized Laws of Reflection and Refraction", Science **334**, 333-337 (2011).

[Zha11] L. Zhao, "High Efficiency Mechanically Stacked Multi-junction Solar Cells for Concentrator Photovoltaics", Doctoral Thesis, Katholieke Universiteit Leuven, Belgium, 2011.

II List of acronyms and symbols

II.1 International system of radiometry units

Symbol	Explanation	Unit
Q_e	Radiant energy	J
Φ_e	Radiant flux	W
$\Phi_{e\lambda}$	Spectral power	$W \cdot m^{-1}$
I_e	Radiant intensity	$W \cdot sr^{-1}$
$I_{e\lambda}$	Spectral intensity	$W \cdot sr^{-1} \cdot m^{-1}$
L_e	Radiance	$W \cdot sr^{-1} \cdot m^{-2}$
$L_{e\lambda}$	Spectral radiance	$W \cdot sr^{-1} \cdot m^{-3}$
E_e	Irradiance	$W \cdot m^{-2}$
$E_{e\lambda}$	Spectral irradiance	$W \cdot m^{-3}$
M_e	Radiant exitance	$W \cdot m^{-2}$
$M_{e\lambda}$	Spectral radiant exitance	$W \cdot m^{-3}$

II.2 List of acronyms

AM	Air Mass
AU	Arbitrary Units
BFL	Back Focal Length
°C	Celsius degrees
CPC	Compound Parabolic Concentrator
CPV	Concentrated photovoltaic
CSL	Centre Spatial of Liège
CST	Concentrated Solar Thermal
DNI	Direct Normal Incidence
DOE	Diffractive Optical Element
DZ	Dead Zone
EPBT	Energy payback time
EST	Extended Scalar Theory
F#	F-number
FTT	Flat Teeth Teeth
HCPV	High Concentration Photovoltaic
LCA	Longitudinal Achromatic Aberration
MJ	Multijunction
NIR	Near Infrared
NP	Not Polarized
OP	Optical Plastic
PC	Polycarbonate
PDMS	Polydimethylsiloxane
PMMA	Poly(methyl methacrylate)
PV	Photovoltaic
RCWA	Rigorous Coupled Wave Analysis
RoC	Radius of Curvature
SOG	Silicone on Glass
SPDT	Single-Point Diamond Turning
TE	Transverse electric
TM	Transverse magnetic
TFT	Teeth Flat Teeth
UV	Ultraviolet

II.3 Greek symbols

Symbol	Explanation	Values [Unit]
α	Design parameter of blazed grating	-
α_L	Linear thermal expansion coefficient	[K^{-1}]
α_{TD}	Coefficient of thermal defocus	[K^{-1}]
ε_0	Vacuum permittivity	$8.854187817620 \times 10^{-12}$ [$F \cdot m^{-1}$]
η	Efficiency	-
λ	Wavelength	[m]
μ_a	Absorption coefficient	$4\pi k/\lambda$ [m^{-1}]
μ_d	Diffusion	[m^{-1}]
μ_t	Attenuation coefficient	[m^{-1}]
Λ	Grating period	[m]
π	pi	3.141592654
σ	Stefan–Boltzmann constant	$5.670\ 400 \times 10^{-8}$ [$W \cdot m^{-2} \cdot K^{-4}$]
χ_e	Electric susceptibility	-

II.4 Latin symbols

Symbol	Explanation	Value [Unit]
c	Speed of light	299 792 458 [$m \cdot s^{-1}$]
$\vec{E}$	Electric field	[$N \cdot C^{-1}$]
G	Étendue	[m^2]
h	Planck's constant	$6.62606957 \times 10^{-34}$ [$J \cdot s$]
k	Extinction coefficient (imaginary part of the refractive index $\tilde{n}$)	-
K	Thermodynamic temperature unit	[K]
k_B	Boltzmann's constant	$1.3806503 \times 10^{-23}$ [$m^2 \cdot kg \cdot s^{-2} \cdot K^{-1}$]
m_e	Electron rest mass	$9.10938215(45) \times 10^{-31}$ [kg]
$\tilde{n}$	Complex refractive index $\tilde{n}=n+ik$	-
$\vec{P}$	Polarization density	[$C \cdot m^{-2}$]
q_e	Elementary charge	$1.602176565(35) \times 10^{-19}$ [C]
$r_\odot$	Sun's radius	6.965×10^8 [m]
R_{avg}	Roughness average	[m]
R_q	Root mean square roughness	[m]
sun	Standard irradiance	1000 [$W \cdot m^{-2}$]
$T_\odot$	Effective temperature of Sun's surface	5780 [K]
v_d	Abbe number	
v_ϕ	Phase velocity	ω/k [$m \cdot s^{-1}$]

III Proofs

III.1 Scalar diffraction integral

Let's start from Maxwell's equations

$$\vec{\nabla}\cdot\vec{E}=\frac{\rho}{\varepsilon} \tag{III.1a}$$

$$\vec{\nabla}\cdot\vec{B}=0 \tag{III.1b}$$

$$\vec{\nabla}\wedge\vec{E}=-\frac{\partial\vec{B}}{\partial t} \tag{III.1c}$$

$$\vec{\nabla}\wedge\vec{B}=\mu\vec{J}+\mu\varepsilon\frac{\partial\vec{E}}{\partial t} \tag{III.1d}$$

Where $\vec{E}$ is the electric field [$\mathrm{V\cdot m^{-1}}$], ρ is the charge density [$\mathrm{C\cdot m^{-3}}$], ε the permittivity [$\mathrm{F\cdot m^{-1}}$], $\vec{B}$ the magnetic field [T], μ the permeability [$\mathrm{H\cdot m^{-1}}$] and $\vec{J}$ is the total current density. Only uncharged (ρ=0) dielectric materials ($\vec{J}=\vec{0}$) will be treated hence equations (III.1) become

$$\vec{\nabla}\cdot\varepsilon\vec{E}=0 \tag{III.2a}$$

$$\vec{\nabla}\cdot\vec{B}=0 \tag{III.2b}$$

$$\vec{\nabla} \wedge \vec{E} = -\frac{\partial \vec{B}}{\partial t} \tag{III.2c}$$

$$\vec{\nabla} \wedge \vec{B} = \mu \varepsilon \frac{\partial \vec{E}}{\partial t} \tag{III.2d}$$

Now, let's assume that

i. the material is linear (i.e. μ and ε do not change in the presence of magnetic and electric field);

ii. the material is isotropic (i.e. μ and ε do not depend on the polarization state);

iii. the material is homogeneous and uniform (i.e. μ and ε do not vary with position and time)

Applying the rotational operator to equations (III.2a) and (III.2b) and remembering that

$$\begin{aligned} \vec{\nabla} \wedge (\vec{\nabla} \wedge \vec{A}) &= \vec{\nabla}(\vec{\nabla} \cdot \vec{A}) - (\vec{\nabla} \cdot \vec{\nabla})\vec{A} \\ &= \operatorname{grad}(\operatorname{div} \vec{A}) - \operatorname{div}(\operatorname{grad} \vec{A}) \\ &= \operatorname{grad}(\operatorname{div} \vec{A}) - \nabla^2 \vec{A} \end{aligned} \tag{III.3}$$

where ∇^2 is the vector Laplace operator:

$$\nabla^2 \vec{A} = \left(\nabla^2 A_x, \nabla^2 A_y, \nabla^2 A_z \right). \tag{III.4}$$

we find

$$\nabla^2 \vec{E} = \frac{n^2}{c^2} \frac{\partial^2 \vec{E}}{\partial t^2} \tag{III.5a}$$

$$\nabla^2 \vec{B} = \frac{n^2}{c^2} \frac{\partial^2 \vec{B}}{\partial t^2}. \tag{III.5b}$$

Since the refractive index n and the wave velocity are correlated with

$$n = c/v \qquad\qquad v = 1/\sqrt{\mu \varepsilon} \tag{III.6}$$

For a scalar function f, the Laplace operator in Cartesian coordinates corresponds to

$$\nabla^2 f = \frac{\partial^2 f}{\partial x^2} + \frac{\partial^2 f}{\partial y^2} + \frac{\partial^2 f}{\partial z^2}. \tag{III.7}$$

Because of our above assumptions, both equations (III.5a) and (III.5b) may be broken into three scalar equations in the form of

$$\frac{\partial^2 f_i(r_i,t)}{\partial x^2} + \frac{\partial^2 f_i(r_i,t)}{\partial y^2} + \frac{\partial^2 f_i(r_i,t)}{\partial z^2} = \frac{n^2}{c^2}\frac{\partial^2 f_i(r_i,t)}{\partial t^2}. \tag{III.8}$$

In Eq. (III.7), called the wave equation, f may be replaced by E or B and i may be replaced by x, y or z. For a monochromatic wave, each component of the scalar field may be written as

$$f_i(r_i,t) = A_i(r_i)\, e^{-i 2\pi \nu t}. \tag{III.9}$$

If Eq. (III.8) is injected in (III.7) we obtain Helmholtz's equation

$$\nabla^2 A_i + k^2 A_i = 0. \tag{III.10}$$

with k the wavenumber. Assuming moreover that

iv. the temporal component of the electric field may be ignored

v. the light passes through an aperture plane where light properties are known

vi. the aperture size is greater than the wavelength

One of the most famous solutions is the Rayleigh-Sommerfeld integral [OSh03, Liu05, Goo96, Mak11]

$$f(X,Y,Z) = -\frac{1}{2\pi}\iint_{Aperture} f(x,y,0)\frac{e^{ikr}}{r}\frac{Z}{r}\left(ik - \frac{1}{r}\right)dx\,dy \tag{III.11}$$

where x and y are the coordinates in the aperture plane and X, Y are the coordinates of the observation plane situated at a distance Z. The exponential e^{ikr} refers to Huygens' principle: each point of the aperture plane acts as a secondary emitter of spherical wavelets.

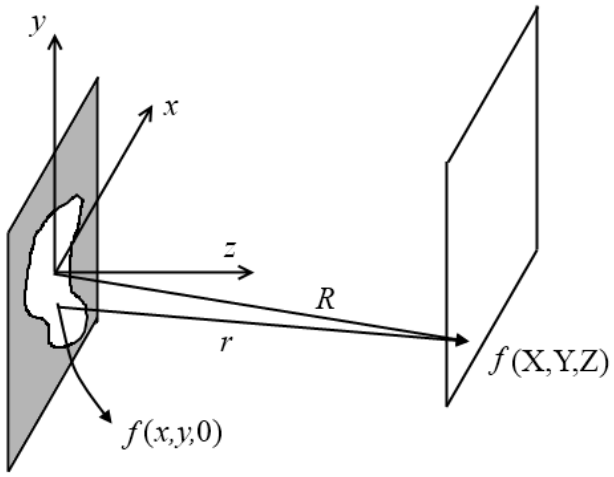

Fig. III.1: Illustration of the relation between the aperture plane and the plane of observation for Rayleigh-Sommerfeld integral

In Eq. (III.6) r is the distance between any point of the aperture plane and the observation plane, i.e.

$$r=\sqrt{(X-x)^2+(Y-y)^2+Z^2} \tag{III.12}$$

and R is the distance from the origin to the same point in the observation plane, as depicted in Fig. III.1. In the far field approximation (assumption vii.), Z/r ≈ 1 and the second term in the parenthesis may be neglected thus

$$f(X,Y,Z)=-\frac{i}{\lambda}\iint_{Aperture} f(x,y,0)\frac{e^{ikr}}{r}dx\,dy. \tag{III.13}$$

By using

$$R=\sqrt{X^2+Y^2+Z^2}, \tag{III.14}$$

let's rewrite Eq. (III.4)

$$r=\sqrt{X^2-2xX+x^2+Y^2-2yY+y^2+Z^2}, \tag{III.15}$$

$$r=\sqrt{R^2-2xX+x^2-2yY+y^2}, \tag{III.16}$$

$$r=R\sqrt{1-2\frac{(xX+yY)}{R^2}+\frac{(x^2+y^2)}{R^2}}, \tag{III.17}$$

$$r\simeq R\sqrt{1-2\frac{(xX+yY)}{R^2}}, \tag{III.18}$$

and finally

$$r \simeq R - \frac{(x\,X + y\,Y)}{R}. \tag{III.19}$$

The last step comes from the Taylor's series expansions to the first order: $\sqrt{1-\varepsilon} \approx 1-\varepsilon/2$. Thus Eq. (III.3) may be approximated by

$$f(X,Y,Z) = -\frac{i}{\lambda} \iint_{Aperture} f(x,y,0) \frac{e^{ikR}}{R} e^{-ik\frac{xX}{R}} e^{-ik\frac{yY}{R}}\, dx\, dy. \tag{III.20}$$

If we now define the complex field $u_0(x,y)$ as

$$u_0(x,y) = u(x,y,0) = -\frac{i}{\lambda} f(x,y,0) \frac{e^{ikR}}{R} \tag{III.21}$$

and if we take into account that the aperture plane may introduce a position dependent phase shift φ_0, the diffracted field $U(X,Y,Z)$ takes the form of

$$U(X,Y,Z) = \iint_{Aperture} u_0(x,y)\, e^{i\varphi_0(x,y)} e^{-ik\frac{xX}{R}} e^{-ik\frac{yY}{R}}\, dx\, dy \tag{III.22}$$

which is simply the Fourier transform $\mathscr{F}$ of the complex amplitude in the aperture plane: $u_0(x,y)$

$$U(X,Y,Z) = \mathscr{F}\left\{ u_0(x,y)\, e^{i\varphi_0(x,y)} \right\}. \tag{III.23}$$

From a practical point of view it is much easier and less time consuming to use a scalar theory than a rigorous theory.

III.2 Deviation angle at a dielectric interface assuming a manufacturing error

What will be the deviation angle D if a prism suffers from a slope error ε? Without slope error, a beam with an incoming angle θ_i would be refracted with an angle θ_r:

$$n_1 \sin(\theta_i) = n_2 \sin(\theta_r) \tag{III.24}$$

With the slope error, Snell's formula becomes

$$n_1 \sin(\theta_i + \varepsilon) = n_2 \sin(\theta_r + D) \tag{III.25}$$

Using trigonometric identities, this last equation turns to

$$\begin{gathered} n_1 \sin(\theta_i)\cos(\varepsilon) + n_1 \cos(\theta_i)\sin(\varepsilon) \\ = \\ n_2 \sin(\theta_r)\cos(D) + n_2 \cos(\theta_r)\sin(D) \end{gathered} \tag{III.26}$$

Let's introduce Eq. (III.24) in (III.26)

$$\begin{gathered} n_2 \sin(\theta_r)\cos(\varepsilon) + n_2 \frac{\sin(\theta_r)}{\sin(\theta_i)} \cos(\theta_i)\sin(\varepsilon) \\ = \\ n_2 \sin(\theta_r)\cos(D) + n_2 \cos(\theta_r)\sin(D) \end{gathered} \tag{III.27}$$

We divide now by $n_2 \sin(\theta_r)$

$$\begin{gathered} \cos(\varepsilon) + \frac{1}{\tan(\theta_i)} \sin(\varepsilon) \\ = \\ \cos(D) + \frac{1}{\tan(\theta_r)} \sin(D) \end{gathered} \tag{III.28}$$

Since ε is a slope error, it is supposed to be small. So the cosine may be approximated by one and the sine by the angle itself and similarly for the deviation angle:

$$1+\frac{\varepsilon}{\tan\left(\theta_i\right)}\simeq 1+\frac{D}{\tan\left(\theta_r\right)}. \tag{III.29}$$

Finally, the deviation angle is

$$D\simeq\frac{\tan\left(\theta_r\right)}{\tan\left(\theta_i\right)}\varepsilon. \tag{III.30}$$

III.3 Relation between deviation angle and prism angle

Using the geometry depicted in Fig. III.2, Snell's law from a medium of refractive index n to air is

$$n\sin(\psi)=\sin(\psi+\beta). \tag{III.31}$$

In can be rewritten in the form of

$$n\sin(\psi)=\sin(\psi)\cos(\beta)+\cos(\psi)\sin(\beta) \tag{III.32}$$

Dividing by $\sin(\psi)$

$$n=\sin(\psi)\frac{1}{\tan(\beta)}+\cos(\psi) \tag{III.33}$$

Placing now, β in the left part of the equation

$$\frac{1}{\tan(\beta)}=\frac{n-\cos(\psi)}{\sin(\psi)} \tag{III.34}$$

gives the final expression for the prism angle,

$$\beta=\operatorname{atan}\left(\frac{\sin\psi}{n-\cos\psi}\right) \tag{III.35}$$

Using Eq. (III.31), we may determine deviation angle ψ as a function of β

$$\psi(\beta)=\operatorname{asin}\left(n\sin(\beta)\right)-\beta \tag{III.36}$$

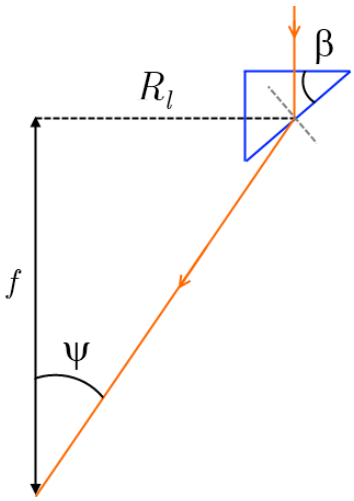

Fig. III.2: Geometry of a prismatic element of a Fresnel lens

III.4 Diffraction efficiency using second order Cauchy series

This mathematical demonstration proof that a blazed grating made of two different refractive indices obeying a Cauchy series of the second order. The proof is mainly picked up from Kleemann *et al.* [Kle08].

In the scalar theory, the diffraction efficiency a the m^{th} order is given by a square cardinal sine function

$$\eta_m = sinc^2(\alpha - m) \tag{III.37}$$

with α the design parameter (also called detuning parameter):

$$\alpha = \sum_i \alpha_i = \sum_i \frac{\left[n_i(\lambda) - n_{i+1}(\lambda)\right] h_i}{\lambda} \tag{III.38}$$

Using a bilayer immersed in the air, α turns to

$$\alpha = \frac{n_1(\lambda) - 1}{\lambda} h_1 + \frac{n_2(\lambda) - 1}{\lambda} h_2 \tag{III.39}$$

using the notation

$$n_{ij}^* = n_i(\lambda_j) - 1 \tag{III.40}$$

The condition to achieve maximum diffraction efficiency with λ_1 and λ_2 is

$$\begin{cases} \lambda_1 = n_{11} h_1 + n_{21} h_2 \\ \lambda_2 = n_{12} h_1 + n_{22} h_2 \end{cases} \tag{III.41}$$

The thicknesses of the two layers obeying this condition are given by

$$\begin{cases} h_1 = \dfrac{\lambda_1 - n_{21}^* h_2}{n_{11}^*} \\ h_2 = \dfrac{\lambda_2 - n_{12}^* h_1}{n_{22}^*} \end{cases} \tag{III.42}$$

Thus,

$$h_2 n_{22}^* = \lambda_2 - \frac{n_{12}^*}{n_{11}^*}\left(\lambda_1 - n_{21}^* h_2\right) \tag{III.43}$$

Putting terms in h_2 together we obtain

$$h_2\left(n_{11}^* n_{22}^* - n_{12}^* n_{21}^*\right) = \lambda_2 n_{11}^* - \lambda_1 n_{12}^* \tag{III.44}$$

Hence,

$$h_2 = \frac{\lambda_2 n_{11}^* - \lambda_1 n_{12}^*}{n_{11}^* n_{22}^* - n_{12}^* n_{21}^*} \tag{III.45}$$

In the same way, we find an expression for h_1

$$h_1 = \frac{\lambda_1 n_{22}^* - \lambda_2 n_{21}^*}{n_{11}^* n_{22}^* - n_{12}^* n_{21}^*} \tag{III.46}$$

If we now express the refractive indices in terms of Cauchy series to the second order,

$$n_i(\lambda_j) = A_i + \frac{B_i}{\lambda_j} \tag{III.47}$$

and use the following notations,

$$n_{ij} = n_i(\lambda_j) \quad \text{and} \quad n_{ij}^* = n_i(\lambda_j) - 1 = A_i + \frac{B_i}{\lambda_j} - 1 = A_i^* + \frac{B_i}{\lambda_j}, \tag{III.48}$$

the design parameter becomes for any wavelength

$$\alpha(\lambda) = \frac{n_1^*(\lambda)\left(\lambda_1 n_{22}^* - \lambda_2 n_{21}^*\right)}{\lambda\left(n_{11}^* n_{22}^* - n_{12}^* n_{21}^*\right)} + \frac{n_2^*(\lambda)\left(\lambda_2 n_{11}^* - \lambda_1 n_{12}^*\right)}{\lambda\left(n_{11}^* n_{22}^* - n_{12}^* n_{21}^*\right)}. \tag{III.49}$$

We may rewrite the denominator (without λ) as

$$
\begin{aligned}
&n_{11}^* n_{22}^* - n_{12}^* n_{21}^* \\
&= \left(A_1^* + \frac{B_1}{\lambda_1}\right)\left(A_2^* + \frac{B_2}{\lambda_2}\right) - \left(A_1^* + \frac{B_1}{\lambda_2}\right)\left(A_2^* + \frac{B_2}{\lambda_1}\right) \\
&= \left[A_1^* A_2^* + \frac{A_1^* B_2}{\lambda_2^2} + \frac{A_2^* B_1}{\lambda_1^2} + \frac{B_1 B_2}{\lambda_1^2 \lambda_2^2}\right] - \left[A_1^* A_2^* + \frac{A_1^* B_2}{\lambda_2^2} + \frac{A_2^* B_1}{\lambda_1^2} + \frac{B_1 B_2}{\lambda_1^2 \lambda_2^2}\right] \\
&= A_1^* B_2 \left(\frac{1}{\lambda_2^2} - \frac{1}{\lambda_1^2}\right) + A_2^* B_1 \left(\frac{1}{\lambda_1^2} - \frac{1}{\lambda_2^2}\right) \\
&= \left[A_1^* B_2 - A_2^* B_1\right]\left(\frac{1}{\lambda_2^2} - \frac{1}{\lambda_1^2}\right)
\end{aligned}
\tag{III.50}
$$

The full denominator is thus

$$
\lambda\left(n_{11}^* n_{22}^* - n_{12}^* n_{21}^*\right) = \lambda\left[A_1^* B_2 - A_2^* B_1\right]\left(\frac{1}{\lambda_2^2} - \frac{1}{\lambda_1^2}\right) \tag{III.51}
$$

Let's also rewrite the first numerator of Eq. (III.49) as

$$
\begin{aligned}
&n_1^*(\lambda)\left[\lambda_1 n_{22}^* - \lambda_2 n_{21}^*\right] \\
&\quad = \left(A_1^* + \frac{B_1}{\lambda^2}\right)\left[\lambda_1\left(A_2^* + \frac{B_2}{\lambda_2^2}\right) - \lambda_2\left(A_2^* + \frac{B_2}{\lambda_1^2}\right)\right] \\
&\quad = A_1^* \lambda_1 A_2^* + A_1^* \frac{\lambda_1}{\lambda_2^2} B_2 - A_1^* \lambda_2 A_2^* - A_1^* \frac{\lambda_2}{\lambda_1^2} B_2 \\
&\qquad + B_1 \frac{\lambda_1}{\lambda^2} A_2^* + \frac{B_1}{\lambda^2}\frac{\lambda_1}{\lambda_2^2} B_2 - B_1 \frac{\lambda_2}{\lambda^2} A_2^* - \frac{B_1}{\lambda^2}\frac{\lambda_2}{\lambda_1^2} B_2
\end{aligned}
\tag{III.52}
$$

Similarly for the second numerator,

$$
\begin{aligned}
&n_2^*(\lambda)\left[\lambda_2 n_{11}^* - \lambda_1 n_{12}^*\right] \\
&\quad = \left(A_2^* + \frac{B_2}{\lambda^2}\right)\left[\lambda_2\left(A_1^* + \frac{B_1}{\lambda_1^2}\right) - \lambda_1\left(A_1^* + \frac{B_1}{\lambda_1^2}\right)\right] \\
&\quad = A_2^*\lambda_2 A_1^* + A_2^*\frac{\lambda_2}{\lambda_1^2}B_1 - A_2^*\lambda_1 A_1^* - A_2^*\frac{\lambda_1}{\lambda_2^2}B_1 \\
&\qquad + B_2\frac{\lambda_2}{\lambda^2}A_1^* + \frac{B_2}{\lambda^2}\frac{\lambda_2}{\lambda_1^2}B_1 - B_2\frac{\lambda_1}{\lambda^2}A_1^* - \frac{B_2}{\lambda^2}\frac{\lambda_1}{\lambda_2^2}B_1
\end{aligned}
\tag{III.53}
$$

We notice that terms in the same colour in Eq. (III.52) and (III.53) cancel each other out. We may also observe that each term is multiplied either $A_2^* B_1$ either $A_1^* B_2$. Thus,

$$
\begin{aligned}
&n_1^*(\lambda)\left[\lambda_1 n_{22}^* - \lambda_2 n_{21}^*\right] + n_2^*(\lambda)\left[\lambda_2 n_{11}^* - \lambda_1 n_{12}^*\right] \\
&\quad = A_1^*\frac{\lambda_1}{\lambda_2^2}B_2 - A_1^*\frac{\lambda_2}{\lambda_1^2}B_2 + B_1\frac{\lambda_1}{\lambda^2}A_2^* - B_1\frac{\lambda_2}{\lambda^2}A_2^* \\
&\qquad + A_2^*\frac{\lambda_2}{\lambda_1^2}B_1 - A_2^*\frac{\lambda_1}{\lambda_2^2}B_1 + B_2\frac{\lambda_2}{\lambda^2}A_1^* - B_2\frac{\lambda_1}{\lambda^2}A_1^* \\
&\quad = \left(A_1^* B_2 - A_2^* B_1\right)\left[\frac{\lambda_1}{\lambda_2^2} - \frac{\lambda_2}{\lambda_1^2} + \frac{\lambda_2 - \lambda_1}{\lambda^2}\right]
\end{aligned}
\tag{III.54}
$$

Finally, the division of (III.54) by (III.51) gives the expression of the design parameter

$$
\alpha(\lambda) = \frac{\left[A_1^* B_2 - A_2^* B_1\right]\left(\dfrac{\lambda_1}{\lambda_2^2} - \dfrac{\lambda_2}{\lambda_1^2} + \dfrac{\lambda_2 - \lambda_1}{\lambda^2}\right)}{\lambda\left[A_1^* B_2 - A_2^* B_1\right]\left(\dfrac{1}{\lambda_2^2} - \dfrac{1}{\lambda_1^2}\right)}
\tag{III.55}
$$

Ordering somewhat this last equation gives finally

$$
\alpha(\lambda) = \frac{\lambda_1^3\lambda^2 - \lambda_2^3\lambda^2 + (\lambda_2 - \lambda_1)\lambda_2^2\lambda_1^2}{\lambda^3(\lambda_1^2 - \lambda_2^2)}
\tag{III.56}
$$

which depends only on the wavelength.

III.5 Extended scalar theory: shading in blazed grating

III.5.1 Light coming from teeth side

a) Common approximated value

In the extended scalar theory (EST), the diffraction efficiency is given by the product of the ideal efficiency provided by the scalar theory (ST) times the active period to period ratio

$$\eta_{EST}=\eta_{ST}\frac{\Lambda'}{\Lambda} \tag{III.57}$$

The dead zone W_0 ($W_0=\Lambda-\Lambda'$) is determined using ray-tracing optics. Using geometric presented in Fig. III.3, i.e. an grating of refractive index n_g immerse in the air, with a thickness h and a blaze angle α.

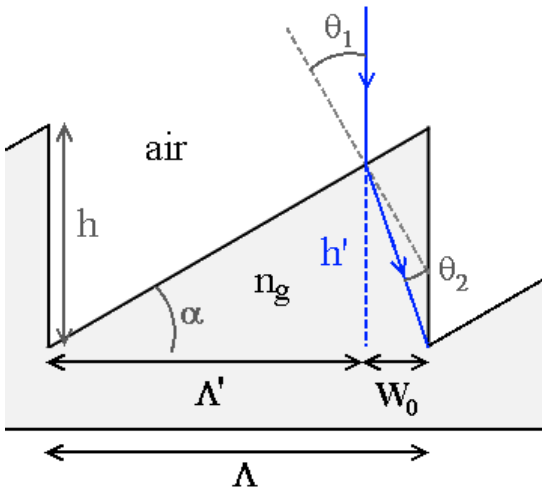

Fig. III.3 Geometry of a single teeth of a blaze grating

For small blaze angle

$$\tan(\theta_1-\theta_2)\simeq\theta_1-\theta_2\simeq\frac{W_0}{h} \tag{III.58}$$

with h

$$h=\frac{\lambda}{n_g-1} \tag{III.59}$$

and θ_1 and θ_2 follow Snell's law

$$\theta_1 \simeq n_g \theta_2 \tag{III.60}$$

Thus

$$W_0 \simeq \frac{\lambda}{n_g - 1}\left(\theta_1 - \frac{\theta_1}{n_g}\right) = \frac{\lambda \theta_1}{n_g} \tag{III.61}$$

The incoming angle corresponds to the blaze angle, so

$$\tan\alpha = \tan\theta_1 = \frac{h}{\Lambda} \simeq \theta_1 \tag{III.62}$$

Substituting (III.61) in (III.62) gives

$$W_0 \simeq \frac{\lambda}{n_g(n_g - 1)}\frac{\lambda}{\Lambda} \tag{III.63}$$

Finally,

$$\frac{\Lambda'}{\Lambda} = 1 - \frac{W_0}{\Lambda} \simeq 1 - \left[\frac{1}{n_g(n_g - 1)}\frac{\lambda^2}{\Lambda^2}\right] \tag{III.64}$$

Which is the ratio used in literature [Lal99].

b) Exact value of the shading

Using the diffraction equation to the first order,

$$\frac{\lambda}{\Lambda} = n_g \sin\theta_1 \tag{III.65}$$

and observing that

$$\tan\theta_1 = \frac{W_0}{h'} = \frac{\Lambda W_0}{\Lambda' h} \tag{III.66}$$

and transforming the tangent in sine using trigonometric identities

$$\tan x = \frac{\sin x}{\sqrt{1 - \sin^2 x}} \tag{III.67}$$

in order to insert Eq. (III.65) in Eq. (III.66):

$$W_0=\frac{\lambda h\Lambda'}{n_g\Lambda^2}\frac{1}{\sqrt{1-\left(\frac{\lambda}{n_g\Lambda}\right)^2}} \tag{III.68}$$

since W_0=Λ-Λ', Λ'=Λ-W_0 and Eq. (III.68) becomes

$$W_0\left[1+\frac{\lambda h}{n_g\Lambda^2\sqrt{1-\left(\frac{\lambda}{n_g\Lambda}\right)^2}}\right]=\frac{\lambda h}{n_g\Lambda\sqrt{1-\left(\frac{\lambda}{n_g\Lambda}\right)^2}}, \tag{III.69}$$

thus,

$$W_0=\frac{\lambda h}{n_g\Lambda\sqrt{1-\left(\frac{\lambda}{n_g\Lambda}\right)^2}}\left[\frac{n_g\Lambda^2\sqrt{1-\left(\frac{\lambda}{n_g\Lambda}\right)^2}}{n_g\Lambda^2\sqrt{1-\left(\frac{\lambda}{n_g\Lambda}\right)^2}+\lambda h}\right] \tag{III.70}$$

which simplifies into

$$W_0=\frac{\lambda h\Lambda}{n_g\Lambda^2\sqrt{1-\left(\frac{\lambda}{n_g\Lambda}\right)^2}+\lambda h}. \tag{III.71}$$

Finally,

$$\frac{W_0}{\Lambda}=\frac{\lambda h}{n_g\Lambda^2\sqrt{1-\left(\frac{\lambda}{n_g\Lambda}\right)^2}+\lambda h}. \tag{III.72}$$

If λ is the design wavelength λ_0, then

$$\frac{W_0}{\Lambda}(\lambda_0)=\frac{\lambda_0^2}{(n_g-1)}\frac{1}{n_g\Lambda^2\sqrt{1-\left(\frac{\lambda_0}{n_g\Lambda}\right)^2}+\lambda_0^2/(n_g-1)} \tag{III.73}$$

Finally,

$$\frac{W_0}{\Lambda}(\lambda_0)=\frac{\lambda_0^2}{\Lambda^2}\frac{1}{n_g(n_g-1)}\frac{1}{\sqrt{1-\left(\frac{\lambda_0}{n_g\Lambda}\right)^2}+\left(\frac{\lambda_0^2}{\Lambda^2}\frac{1}{n_g(n_g-1)}\right)} \qquad \text{(III.74)}$$

III.5.2 Light coming from flat side

The exact value of the shading when light comes from the flat is straightforward. Strictly speaking, there is no shading, but "voids" (see Fig. III.4) between each teeth. This void awakens the diffraction effect and thus the diffraction efficiency.

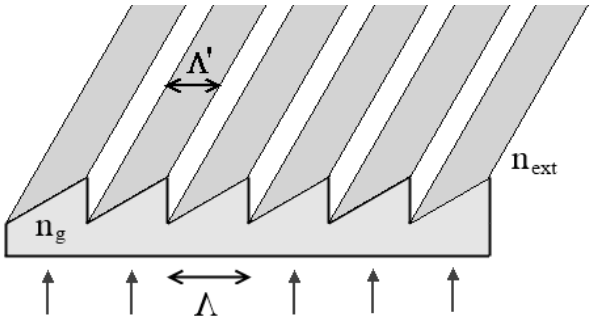

Fig. III.4: "shading" effect due to a void between adjacent teeth

Still using the same notation as in the above demonstrations except for the diffraction angle represented with θ_d, obeying the diffraction equation

$$\sin\theta_d=\frac{m\lambda}{\Lambda} \qquad \text{(III.75)}$$

The void, W_0, is in direct relation with the diffraction angle and the thickness of the teeth

$$\tan\theta_d=\frac{W_0}{h} \qquad \text{(III.76)}$$

Using trigonometric identities, we have

$$\tan\theta_d=\frac{W_0}{h}=\frac{\sin\theta_d}{\sqrt{1-\sin^2\theta_d}}=\frac{m\lambda}{\Lambda}\frac{1}{\sqrt{1-\left(\frac{m\lambda}{\Lambda}\right)^2}} \qquad \text{(III.77)}$$

Thus, without approximation, the shading ratio is

$$\frac{W_0}{\Lambda}=\frac{m\lambda}{\Lambda^2}\frac{h}{\sqrt{1-\left(\frac{m\lambda}{\Lambda}\right)^2}} \tag{III.78}$$

If the wavelength corresponds to the design wavelength for the m^{th} order,

$$\frac{W_0}{\Lambda}=\frac{(m\lambda_0)^2}{(n_g-1)\Lambda^2}\frac{1}{\sqrt{1-\left(\frac{m\lambda_0}{\Lambda}\right)^2}} \tag{III.79}$$

III.5.3 Ideal thickness grating

In the scalar theory, the grating depth introducing a 2π phase-shift with the neighbouring teeth is simply given by

$$h_{SC}=\frac{\lambda_0}{n(\lambda_0)-1} \tag{III.80}$$

The scalar theory assume that this phase modulation occurs in an infinitely thin layer (only after what the thickness of the profile is deduced). This unrealistic assumption no longer applies in extended scalar theory. We will used the method proposed by Swanson [Swa91] to determine the ideal thickness of a grating taking into account that the phase delay arises in a finite thickness. The system to be solved is presented in Fig. III.5.

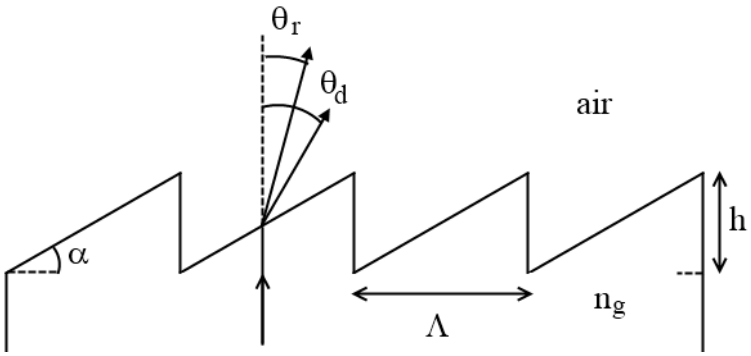

Fig. III.5: Geometrical value of blazed diffraction grating

The refraction angle θ_r and the diffraction angle θ_d must correspond for the design wavelength. For the refraction angle we use Snell's law

$$n_g\sin\alpha=\sin(\alpha+\theta_r). \tag{III.81}$$

For the diffraction angle we use the diffraction grating equation

$$\sin\theta_d=\frac{\lambda}{\Lambda}. \tag{III.82}$$

Setting $\theta_d = \theta_r = \theta$, gives

$$n_g\sin\alpha=\sin\alpha\cos\theta+\sin\theta\cos\alpha \tag{III.83}$$

$$\sin\alpha(n_g-\cos\theta)=\frac{\lambda}{\Lambda}\cos\alpha \tag{III.84}$$

Using trigonometric identities

$$\frac{\tan\alpha}{\sqrt{1+\tan^2\alpha}}(n_g-\sqrt{1-\sin^2\theta})=\frac{\lambda}{\Lambda}\frac{1}{\sqrt{1+\tan^2\alpha}} \tag{III.85}$$

$$\frac{h}{\Lambda}(n_g-\sqrt{1-\sin^2\theta})=\frac{\lambda}{\Lambda} \tag{III.86}$$

$$h\left[n_g-\sqrt{1-\left(\frac{\lambda}{\Lambda}\right)^2}\right]=\lambda \tag{III.87}$$

Finally,

$$h_{EST}=\frac{\lambda}{n_g-\sqrt{1-\left(\frac{\lambda}{\Lambda}\right)^2}}. \tag{III.88}$$

III.5.4 Ideal thickness under incidence angle

For a given angle of incidence, the method to be used to find the ideal thickness, is the same as before: the refraction angle must be the same as the diffraction angle.

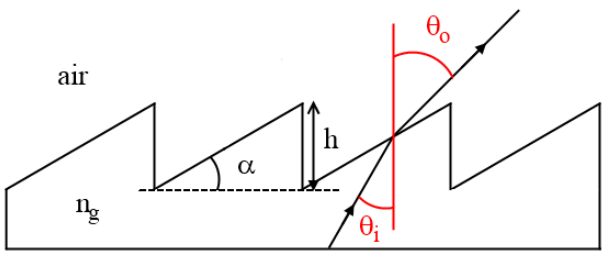

Fig. III.6: Blazed grating geometry for an incidence angle θ_i

So, the conditions are

$$\begin{cases} -n_g \sin\theta_i + \sin\theta_o = \dfrac{\lambda}{\Lambda} \\ n_g \sin(\theta_i + \alpha) = \sin(\alpha + \theta_o) \end{cases} \tag{III.89}$$

which is equivalent to

$$\begin{cases} \sin\theta_o = \dfrac{\lambda}{\Lambda} + n_g \sin\theta_i \\ n_g \sin\theta_i \cos\alpha + n_g \cos\theta_i \sin\alpha = \sin\alpha\cos\theta_o + \cos\alpha\sin\theta_o \end{cases} \tag{III.90}$$

We will now express every terms α in terms of tangent,

$$\begin{cases} \sin\theta_o = \dfrac{\lambda}{\Lambda} + n_g \sin\theta_i \\ \dfrac{n_g \sin\theta_i}{\sqrt{1+\left(\dfrac{\lambda}{\Lambda}\right)^2}} + n_g \cos\theta_i \dfrac{h/\Lambda}{\sqrt{1+\left(\dfrac{\lambda}{\Lambda}\right)^2}} = \dfrac{h/\Lambda}{\sqrt{1+\left(\dfrac{\lambda}{\Lambda}\right)^2}} \cos\theta_o + \dfrac{\sin\theta_o}{\sqrt{1+\left(\dfrac{\lambda}{\Lambda}\right)^2}} \end{cases} \tag{III.91}$$

and we change every expressions in θ_i and θ_o in $\sin(\theta_i)$ and $\sin(\theta_o)$ respectively.

$$\begin{cases} \sin\theta_o = \dfrac{\lambda}{\Lambda} + n_g \sin\theta_i \\ n_g \sin\theta_i + n_g \sqrt{1-\sin^2\theta_i}\, \dfrac{h}{\Lambda} = \dfrac{h}{\Lambda}\sqrt{1-\sin^2\theta_o} + \sin\theta_o \end{cases} \tag{III.92}$$

We may now inject the diffraction condition into the refraction condition:

$$n_g \sin\theta_i + n_g \sqrt{1-\sin^2\theta_i}\, \frac{h}{\Lambda} = \frac{h}{\Lambda}\sqrt{1-\left(\frac{\lambda}{\Lambda} + n_g \sin\theta_i\right)^2} + \frac{\lambda}{\Lambda} + n_g \sin\theta_i \tag{III.93}$$

Finally, the optimum thickness is

$$h = \frac{\lambda}{n_g \sqrt{1-\sin^2\theta_i} - \sqrt{1-\left(\frac{\lambda}{\Lambda} + n_g \sin\theta_i\right)^2}} \tag{III.94}$$

III.6 Relation between dn/dT and α_L

Thermal expansion of polymers are answered by modification of the density that causing, to its turn, a change of refractive index. This yielded to the establishment of Lorentz-Lorenz equation, also known as Clausius–Mossotti relation for the molecule density:

$$\rho=\frac{N_{tot}}{r^3}=\frac{3}{4\pi\alpha}\frac{n^2-1}{n^2+2} \tag{III.95}$$

where N_{tot} is the number of molecules in a volume r^3 and α is the polarizability. Since the change of refractive index is mainly due to the variation of density, the effect of temperature on the polarizability is negligible. Indeed, Cariou *et al.* shown that $n(T) \propto (n^2\text{-}1)/(n^2\text{+}2)$ [Car86]. Therefore, the differentiation of Eq. (III.95) yields to

$$\begin{aligned} -3\frac{N_{tot}}{r^4}\frac{dr}{dT} &= -3\frac{\rho}{r}\frac{dr}{dT} = -3\rho\alpha_L \\ &= \frac{3}{4\pi\alpha}\left(\frac{2n}{n^2+2}\frac{dn}{dT}-2n\frac{n^2-1}{(n^2+2)^2}\frac{dn}{dT}\right). \end{aligned} \tag{III.96}$$

Then,

$$-3\frac{3}{4\pi\alpha}\frac{n^2-1}{n^2+2}\alpha_L=\frac{3}{4\pi\alpha}\left(\frac{2n}{n^2+2}\frac{dn}{dT}-2n\frac{n^2-1}{(n^2+2)^2}\frac{dn}{dT}\right) \tag{III.97}$$

$$-3(n^2-1)\alpha_L=2n\left(1-\frac{n^2-1}{n^2+2}\right)\frac{dn}{dT} \tag{III.98}$$

So that,

$$\frac{dn}{dT}=\frac{-3\alpha_L}{2n}\frac{(n^1-1)(n^2+2)}{(n^2+2)-(n^2-1)} \tag{III.99}$$

Finally,

$$\frac{dn}{dT}=-\alpha_L\frac{(n^2+2)(n^2-1)}{2n}. \tag{III.100}$$

IV List of publications

IV.1 Peer-reviewed journals

- F. Languy, K. Fleury, C. Lenaerts, J. Loicq, D. Regaert, T. Thibert and S. Habraken, "Flat Fresnel doublets made of PMMA and PC: combining low-cost production and very high concentration ratio for CPV", Optics Express **19**, A280-A294 (2011) [Impact factor in 2010, 3.587]
- F. Languy and S. Habraken, "Performance comparison of four kinds of flat nonimaging Fresnel lenses made of polycarbonates and polymethyl methacrylate for concentrated photovoltaics", Optics Letters **36**, 2743-2745 (2011) [Impact factor in 2011, 3.399].
- F. Languy, C. Lenaerts, J. Loicq, T. Thibert and S. Habraken, "Performance of solar concentrator made of an achromatic Fresnel doublet measured with a continuous solar simulator and comparison with a singlet", accepted for publication in Solar Energy Materials and Solar Cells [Impact factor in 2011, 4.542].

IV.2 Contribution to international conferences

- F. Languy, C. Lenaerts and S. Habraken, "High Solar Concentration Using Diffractive Optics", in: Proceedings of the 23rd European Photovoltaic Solar Energy Conference and Exhibition, Valencia, Spain, September 1-5, 2008.
- F. Languy, C. Lenaerts, J. Loicq and S. Habraken, "Achromatization of solar concentrator thanks to diffractive optics," presented at the 2nd Int'l Workshop on Concentrating Photovoltaic Power Plants, Darmstadt, Germany, March 9-10, 2009, http://www.concentrating-pv.org/darmstadt2009/index.html.
- F. Languy, C. Lenaerts, J. Loicq and S. Habraken, "Achromatization of solar concentrator using diffractive optics", in: Proceedings of the 24th European Photovoltaic Solar Energy Conference and Exhibition, Hamburg, Germany, September 24-28, 2009.
- T. Thibert, M.-L. Hellin, J. Loicq, E. Mazy, J.-M. Gillis, F. Languy, S. Habraken, J.-H. Lecat, J.-M. Defise, "Continuous Solar Simulator for Concentrator Photovoltaic Systems", in: Proceedings of the 25th European Photovoltaic Solar Energy Conference and Exhibition, Valencia, Spain, September 6-10, 2010.
- F. Languy, C. Lenaerts, J. Loicq, T. Thibert and S. Habraken, "Achromatization of solar concentrators with diffractive optics", in: Proceedings of the 25th European Photovoltaic Solar Energy Conference and Exhibition, Valencia, Spain, September 6-10, 2010.
- T. Thibert, M.-L. Hellin, J. Loicq, E. Mazy, A. Mazzoli, L. Jacques, D. Verstraeten, J.-M. Gillis, F. Languy, C. Emmerechts, E. Beeckman and, J.-H. Lecat, "Performance of Solmacs, a High PV Solar Concentrator With Efficient Optics", in: Proceedings of 8th International Conference on Concentrating Photovoltaic Systems, Toledo, Spain, April 16-18, 2012.
- F. Languy, C. Lenaerts, J. Loicq, T. Thibert and S. Habraken, "Experimental Results of Flat Fresnel Doublets made of PMMA and PC", in: Proceedings of 8th International Conference on Concentrating Photovoltaic Systems, Toledo, Spain, April 16-18, 2012.
- C. Michel, J. Loicq, A. Mazzoli, F. Languy and S. Habraken, "Study of a space solar concentrator for space applications based on a diffractive/refractive combination", in: Proceedings of Optics for Solar Energy (SOLAR), Eindhoven, The Netherlands, November 11-14, 2012.

- F. Languy, C. Lenaerts, J. Loicq, T. Thibert and S. Habraken, "Experimental Results of Hybrid and Refractive Achromatic Doublets Made of PC and PMMA", in: Proceedings of Optics for Solar Energy (SOLAR), Eindhoven, The Netherlands, November 11-14, 2012.
- F. Languy and S. Habraken, "Hybrid Lens for Solar Concentration: Optimization of the Multilayer Diffractive Lens", in: Proceedings of Optics for Solar Energy (SOLAR), Eindhoven, The Netherlands, November 11-14, 2012.

V Full text peer-reviewed publications

Flat Fresnel doublets made of PMMA and PC: combining low cost production and very high concentration ratio for CPV

Fabian Languy,[1,*] Karl Fleury,[2] Cédric Lenaerts,[2] Jérôme Loicq,[2] Donat Regaert,[3] Tanguy Thibert,[2] and Serge Habraken[1]

[1]*Hololab, Physics Department, Bat. B5a, Université de Liège, 17 allée du 6 Août, B-4000 Liège, Belgium*
[2]*Centre Spatial de Liège, Avenue du Pré-Aily, B-4031 Angleur, Belgium*
[3]*Laboratoire de Physique du Solide, Facultés Universitaires Notre-Dame de la Paix, 61 rue de Bruxelles, B-5000 Namur, Belgium*
**flanguy@ulg.ac.be*

Abstract: The linear chromatic aberration (LCA) of several combinations of polycarbonates (PCs) and poly (methyl methacrylates) (PMMAs) as singlet, hybrid (refractive/diffractive) lenses and doublets operating with wavelengths between 380 and 1600 nm – corresponding to a typical zone of interest of concentrated photovoltaics (CPV) – are compared. Those comparisons show that the maximum theoretical concentration factor for singlets is limited to about 1000 × at normal incidence and that hybrid lenses and refractive doublets present a smaller LCA increasing the concentration factor up to 5000 × and 2 × 10^6 respectively. A new achromatization equation more useful than the Abbé equation is also presented. Finally we determined the ideal position of the focal point as a function of the LCA and the geometric concentration which maximizes the flux on the solar cell.

OCIS codes: (080.4298) Nonimaging optics; (220.1770) Concentrators; (050.1965) Diffractive lenses; (220.1000) Aberration compensation; (160.4760) Optical properties.

References and links

1. C. Algora, "Very high concentration challenges of III–V multijunction solar cells," in *Concentrator Photovoltaics,* A. Luque, and V. Andreev, ed. (Springer, 2007), Chap. 5.
2. Spectrolab datasheet: *www.spectrolab.com/DataSheets/PV/CPV/CDO-100-C3MJ.pdf*, accessed on 02/06/2011.
3. Website for NREL's AM1, 5 Standard Data set: http://rredc.nrel.gov/solar/spectra/am1.5/ASTMG173/ASTMG173.html, accessed on 02/06/2011.
4. R. Winston, "Light Collection within the Framework of Geometrical Optics," J. Opt. Soc. Am. **60**(2), 245–247 (1970).
5. S. Puliaev, J. L. Penna, E. G. Jilinski, and A. H. Andrei, "Solar diameter observations at Observatório Nacional in 1998-1999," Astron. Astrophys. Suppl. Ser. **143**(2), 265–267 (2000).
6. J. Chaves, *Introduction to nonimaging optics* (CRC Press, 2008), Chap. 1.
7. E. Hecht, *Optics* 4th Ed. (Addison-Wesley, 2002), Chap. 5.
8. D. A. Buralli, G. M. Morris, and J. R. Rogers, "Optical performance of holographic kinoforms," Appl. Opt. **28**(5), 976–983 (1989).
9. Fresnel lens brochure of the Fresnel Technologies Inc.: *www.fresneltech.com/materials.html*, accessed on 02/06/2011.
10. S. N. Kasarova, N. G. Sultanova, C. D. Ivanov, and I. D. Nikolov, "Analysis of the dispersion of optical plastic materials," Opt. Mater. **29**(11), 1481–1490 (2007).
11. J. D. Lytle, "Polymeric Optics," in *Handbook of Optics*, 3rd Edition, Vol. IV, M. Bass, ed. (McGraw-Hill, 2009), Chap. 3.
12. ASAP™ optical design software of Breault Research Organization, *http://www.breault.com*.
13. Y. B. Lee, and T. H. Kwon, "Modeling and numerical simulation of residual stresses and birefringence in injection molded center-gated disks," J. Mater. Process. Technol. **111**(1-3), 214–218 (2001).
14. V. Moreno, J. F. Román, and J. R. Salgueiro, "High efficiency diffractive lenses: Deduction of kinoform profile," Am. J. Phys. **65**(6), 556–562 (1997).

#143631 - $15.00 USD Received 4 Mar 2011; revised 28 Mar 2011; accepted 29 Mar 2011; published 8 Apr 2011

15. D. C. O'Shea, T. J. Suleski, A. D. Kathman, and D. W. Prather, *Diffractive Optics: Design, Fabrication, and Test* (Spie Press, 2004), Chap. 4.
16. B. H. Kleemann, M. Seeßelberg, and J. Ruoff, "Design concepts for broadband high–efficiency DOEs," J. Eur. Opt. Soc. Rapid Publ. **3**, 08015 (2008).
17. F. Languy, C. Lenaerts, J. Loicq, and S. Habraken, "Achromatization of solar concentrator thanks to diffractive optics," presented at the 2nd Int'l Workshop on Concentrating Photovoltaic Power Plants, Darmstadt, Germany, 9–10 March 2009, *http://www.concentrating-pv.org/darmstadt2009/index.html*.
18. M. Born, and E. Wolf, *Principles of Optics*, 7th Ed. (Cambridge University Press, 2003), p. 188.
19. G. K. Skinner, "Design and imaging performance of achromatic diffractive-refractive x-ray and gamma-ray Fresnel lenses," Appl. Opt. **43**(25), 4845–4853 (2004).

1. Introduction

Nowadays, lots of optical systems like cameras, telescopes, microscopes etc. use an achromatic doublet of glasses, which delivers good image quality but is quite expensive, bulky and heavy. Even for a single glass lens the cost, bulk and weight might be a problem. This is why Fresnel lenses are often used, especially when built in optical plastic, e. g. headlights, solar concentrators, projectors, traffic lights, etc. So, in order to combine small chromatic aberrations with low-cost production, we suggest using achromatic Fresnel doublets for concentrated photovoltaics (CPV). The reduction of the chromatic aberration allows for a higher concentration ratio and a higher efficiency of multijunction photovoltaic cells [1]. Even if most optical systems work in the visible range, we extended our study to a typical zone of interest of wavelengths for solar concentration: from 380 to 1600 nm. Typically, out of this range the external quantum efficiency of a triple junction cell drops to about 40% [2] and the direct solar flux is also low [3].

2. Influence of the LCA on the optical concentration ratio

Considering a concentrator with a collector surface A' and a receiver surface A. The ratio A'/A corresponds to the geometrical concentration factor C_{geo}. If Φ' is the flux collected and Φ the flux absorbed, then Φ'/Φ refers to the optical efficiency η_{opt}. Finally, the optical concentration factor C_{opt} is given by Eq. (1).

$$C_{opt} = \eta_{opt} C_{geo} = \frac{\Phi'}{\Phi}\frac{A'}{A}. \tag{1}$$

For a collector of rotational symmetry, the upper limit of concentration is achieved with an optical efficiency of 100% and for a concentrator where both collector and absorber are immersed in the air is given by Eq. (2) where θ represents the acceptance half angle of the incoming light [4].

$$C_{opt}^{\max} = \sin^{-2}\theta. \tag{2}$$

On Earth, for two degrees of concentration, the upper limit of solar concentration is about 46,000 due to a semi-acceptance angle of the sun of ~960" (i.e. 0.267°) [5]. For a polychromatic source, this concentration may be achieved with reflective surfaces (like the compound parabolic concentrator [6]). But systems suffering from chromatic aberration will not be able to achieve such high concentration ratio. This is the case for lenses since their focal distances depend on the wavelength: $f = f(\lambda)$.

Considering two wavelengths λ_A and λ_B, the linear chromatic aberration (LCA) corresponds to the difference of the focal distances:

$$LCA = f(\lambda_B) - f(\lambda_A). \tag{3}$$

The way the focal distance of an ideal (with only chromatic aberration) thin refractive lens having a front and back radii of curvature R_1 and R_2 changes is given by Eq. (4) [7] while for a diffractive lens it is given by Eq. (5) [8].

#143631 - $15.00 USD Received 4 Mar 2011; revised 28 Mar 2011; accepted 29 Mar 2011; published 8 Apr 2011

$$\frac{1}{f_{ref}(\lambda)} \simeq \left(\frac{1}{R_1} - \frac{1}{R_2}\right)\left(n(\lambda) - 1\right), \tag{4}$$

$$f_{dif}(\lambda) = \frac{\lambda_A}{\lambda} f(\lambda_A). \tag{5}$$

Hereafter, we arbitrarily chose to take λ_0 as a reference: λ_0 is such that the minimum LCA and the maximum LCA – achieved with λ_m and λ_M respectively – are equal in absolute value. The system is thus optimised to decrease the maximum longitudinal chromatic aberration in absolute value $|\mathrm{LCA}_{\max}|$ (see Fig. 1a).

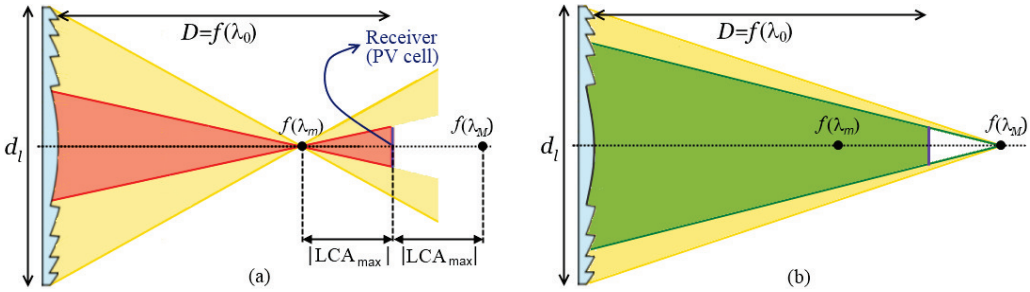

Fig. 1. Representation of the optical efficiency of two wavelengths having the same LCA in absolute value but having different optical efficiency (yellow part corresponds to losses).

For easier comparison, the notation with an asterisk as exponent is introduced, corresponding to a normalisation with λ_0. The LCA for the refractive and diffractive cases may be thus rewritten respectively as Eq. (6) and Eq. (7). It appears that both depend only on the wavelength. And it can be easily shown, that if the detector is placed in $f(\lambda_0)$, the geometrical concentration allowing for the collection of the whole flux is given by Eq. (8).

$$LCA^*_{ref}(\lambda) = \frac{f(\lambda) - f(\lambda_0)}{f(\lambda_0)} = \frac{n(\lambda_0) - n(\lambda)}{n(\lambda) - 1}, \tag{6}$$

$$LCA^*_{dif}(\lambda) = \frac{f(\lambda) - f(\lambda_0)}{f(\lambda_0)} = \left(\frac{\lambda_0}{\lambda} - 1\right), \tag{7}$$

$$C^{\max}_{geo} = \left(\frac{1 - LCA^*}{LCA^*}\right)^2. \tag{8}$$

Imaging optics tends to decrease the $|LCA_{\max}|$ but in non-imaging optics, to maximize the amount of collected rays on the collector, minimising the LCA is not sufficient. Figure 1 shows two wavelengths with the same LCA in absolute value but the amount of light collected with λ_m (red part) in Fig. 1a is more important than the amount of light collected with λ_M (green part) in Fig. 1b. It is easy to show that the ideal position of the detector z_{det} as a function of the LCA^* corresponds to a parabola of Eq. (30) (see Appendix A). This position allows for higher concentration as represented in Fig. 2a while Fig. 2b shows the gain of geometric concentration factor achieved by moving the detector from $f(\lambda_0)$ to z_{det}. In CPV, the maximum concentration is given by the angular size of the sun, but if the LCA^* is greater than 0.466% then the upper limit is driven by the LCA and becomes lower than 46,000.

#143631 - $15.00 USD Received 4 Mar 2011; revised 28 Mar 2011; accepted 29 Mar 2011; published 8 Apr 2011

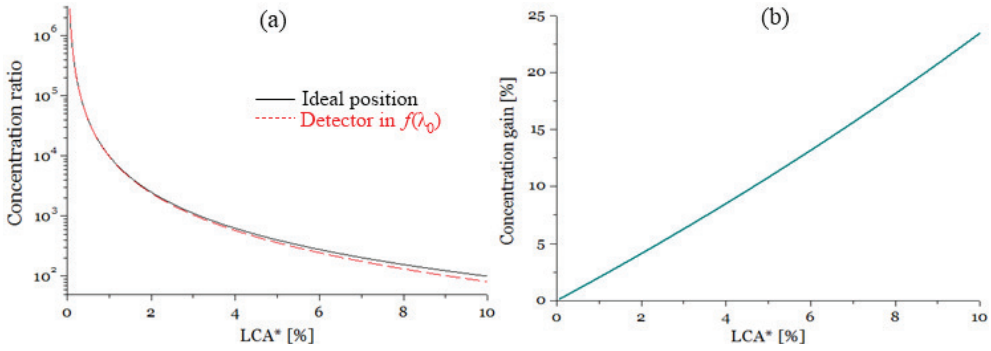

Fig. 2. Concentration ratio at normal incidence as a function of the *LCA** (a) and gain if the detector is moved from the position of the minimum $|LCA_{max}|$ to the ideal position (b).

However lens designers do not always have the choice of detector size and position. For a given $|LCA_{max}|$ and geometrical concentration factor, where should λ_0 be focused: before collector position or after? Focusing after the detector increases the LCA but the view angle of fast converging wavelengths decreases, which is favourable for systems with fast converging wavelengths with $\eta_{opt} < 1$. Focusing before the detector position decreases the LCA but a higher amount of fast converging wavelengths will miss the detector. The ideal position and the optical efficiency as a function of the *LCA** and the geometrical concentration factor are given in Fig. 3.

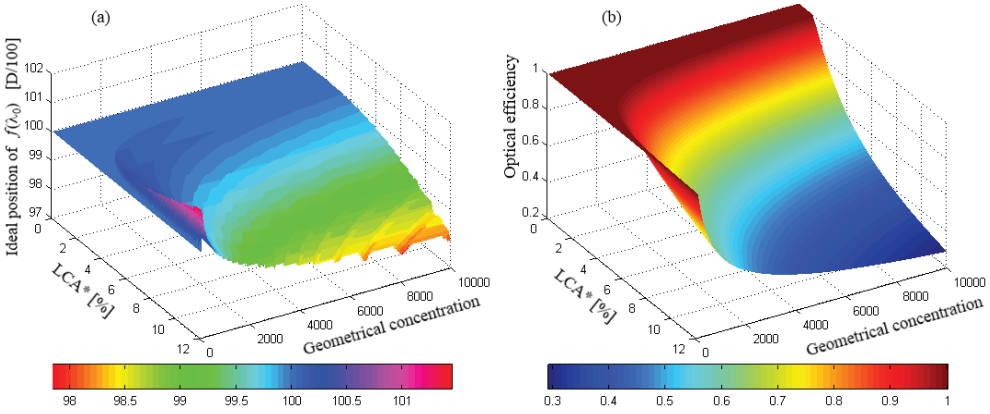

Fig. 3. Ideal position of $f(\lambda_0)$ (a) and optical efficiency (b) as functions of the *LCA** and the geometrical concentration.

A very important point of this section is that the optical concentration factor could be even more limited by the LCA rather than by the acceptance angle.

3. Dispersion curves

PMMA is probably the most common optical plastic (OP) used in solar concentration thanks to its high transmittance and low dispersion curve. Another common OP used for Fresnel lenses is PC, with similar spectral transmission and high impact resistance [9]. Thanks to their high difference of refractive index (about 0.1 at 550 nm), PC and PMMA are good candidates for refractive doublets. Some data about OPs may be found in Kasarova *et al.* article [10], Handbook of optical materials [11] and some ray tracing software like ASAP™ [12]. But depending on the supplier and the injection parameters, OPs properties change. This is why we made our own ellipsometric measurements on several samples. Eight OPs were taken,

#143631 - $15.00 USD Received 4 Mar 2011; revised 28 Mar 2011; accepted 29 Mar 2011; published 8 Apr 2011

three from the literature and we determined the dispersion curve of five OPs coming from our suppliers. In total five PCs and five PMMAs listed in Table 1 were studied.

Table 1. Information about the PMMAs and PCs

PMMA	Data	Provider (P) or Trade Mark (TM)	PC	Data	Provider (P) or Trade Mark (TM)
PMMA #1	[11]	Unknown	PC #1	[10][1]	Unknown
PMMA #2	CSL[2]	Altuglas (TM)	PC #2	[11]	Unknown
PMMA #3	CSL[2]	Diakon (TM)	PC #3	CSL[2]	Calibre 1080 DVD (TM)
PMMA #4	CSL[2]	Evonik (P)	PC #4	CSL[2]	Makrolon (TM)

[1] Referenced as PC in [10].
[2] CSL: Ellipsometric measurements from Centre Spatial of Liege

The refractive index n depends on the wavelength λ. The way the refractive index changes with the wavelength might be approximated with several functions. Two popular functions of dispersion are used in this publication. Equation (9) corresponds to Sellmeier's equation and Eq. (10) to Laurent's (also called Schott's) equation. In this article, Sellmeier's equation is limited to $m = 3$ and Laurent's equation is limited to the term in λ^{-8} ensuring typically a difference lower than ± 0.001 between interpolated and experimental data [10].

$$n(\lambda) = \sqrt{1 + \sum_{i=1}^{m} \frac{B_i \lambda^2}{\lambda^2 - C_i}}, \tag{9}$$

$$n(\lambda) = \sqrt{A_1 + A_2\lambda^2 + \frac{A_3}{\lambda^2} + \frac{A_4}{\lambda^4} + \frac{A_5}{\lambda^6} + \ldots} \quad . \tag{10}$$

The dispersion coefficients are presented in Table 2. Note that those coefficients must be used with the wavelength expressed in microns, both Laurent's and Sellmeier's equations were used for each sample, but only the one giving the smallest is presented. The curves of the refractive indexes are presented in Fig. 4 (a) and (b) for PMMAs and PCs respectively. The variation of refractive index from a sample to another might be explained by the fact that industrial process is not constant and injection parameters might be different for every injection leading to variation in the refractive index [13]. Nevertheless, the curve "PC #1 (old)" has an abnormal behaviour: above 1200 nm the refractive index drops too rapidly compared to any other PCs. This might be simply explained by the fact that the dispersion coefficients were retrieved by Kasarova *et al.* from measurements going from 435.8 to 1052 nm and the extrapolation outside of this range gives wrong results. We performed another interpolation (PC #1) giving more probable results in the near infrared region. Thus, PC #1 (old) will no longer be considered hereafter.

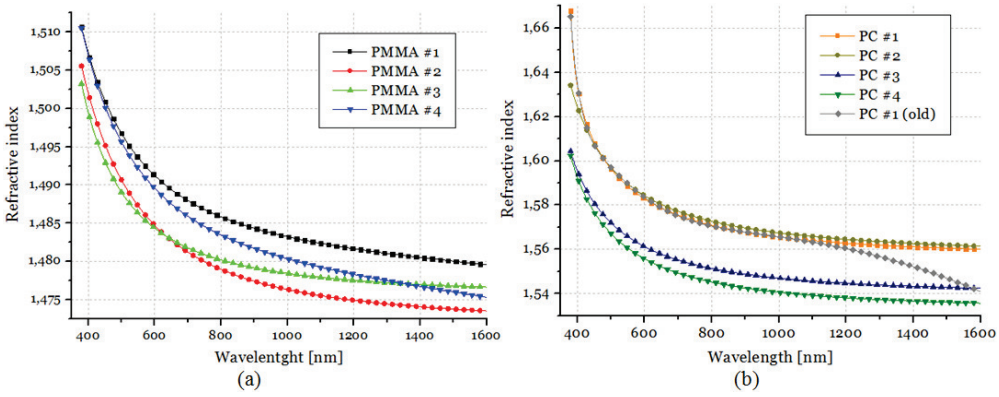

Fig. 4. Dispersion curves of PMMAs (a) and PCs (b).

#143631 - $15.00 USD Received 4 Mar 2011; revised 28 Mar 2011; accepted 29 Mar 2011; published 8 Apr 2011

Table 2. Dispersion Coefficients Some PCs and PMMAs

Material (L/S)[1]	Dispersion coefficients					
	A_1 or B_1	A_2 or C_1	A_3 or B_2	A_4 or C_2	A_5 or B_3	A_6 or C_3
PMMA #1 (L)	2.190664	-2.330317e-3	1.122194e-2	4.765210e-4	-5.040529e-5	3.423433e-6
PMMA #2 (S)	4.841120e-1	3.353637e-4	6.815579e-1	1.096254e-2	1.028035e-2	1.184708e-2
PMMA #3 (S)	6.997099e-1	2.731275e-1	2.043425e-1	-5.777416e-4	-5.784644e-4	4.291190e-2
PMMA #4 (S)	1.838458e-1	2.827502e+1	0. 998312e-1	1.127337e-2	6.664339e+3	1.127703e-2
PC #1 (S)[2]	1.341659e-2	2.410966e-1	1.168465	1.329927e-1	1.811373e-2	1.812526e-2
PC #2 (L)	2.430734	-1.343233e-3	2.714995e-2	3.244405e-4	7.013408e-5	5.615956e-6
PC #3 (S)	2.583939e-2	3.675250e-1	9.769463e-1	9.453662e-2	1.483129e-2	1.488111e-2
PC #4 (S)	2.205583e-2	2.532511e-1	1.073656	1.004816e-1	1.630428e-2	1.623521e-2

[1] Dispersion mode: Laurent (L) or Sellmeier (S)
[2] Recalculated dispersion coefficients to get more probable results in the near infrared region

4. Chromatic aberration of single lenses

4.1 Refractive lens

For an ideal (with only chromatic aberration) thin refractive lens in paraxial condition, the focal distance f may be approximated by Eq. (4) which has been rewritten in Eq. (11):

$$f(\lambda) \simeq \frac{RoC_{eq}}{n(\lambda)-1}, \tag{11}$$

with RoC_{eq} the equivalent radius of curvature of the lens [7]. Following the definition of the asterisk as an exponent

$$RoC^{*}_{eq} = \frac{RoC_{eq}}{f(\lambda_0)} = \left(\frac{R_1 R_2}{R_2 - R_1}\right)\frac{1}{f(\lambda_0)} = \left(n(\lambda)-1\right)\times 100\%. \tag{12}$$

As explain in the previous section, the system is optimised to decrease the maximum longitudinal chromatic aberration in absolute value $|LCA_{max}|$ giving the focal distances of Fig. 5.

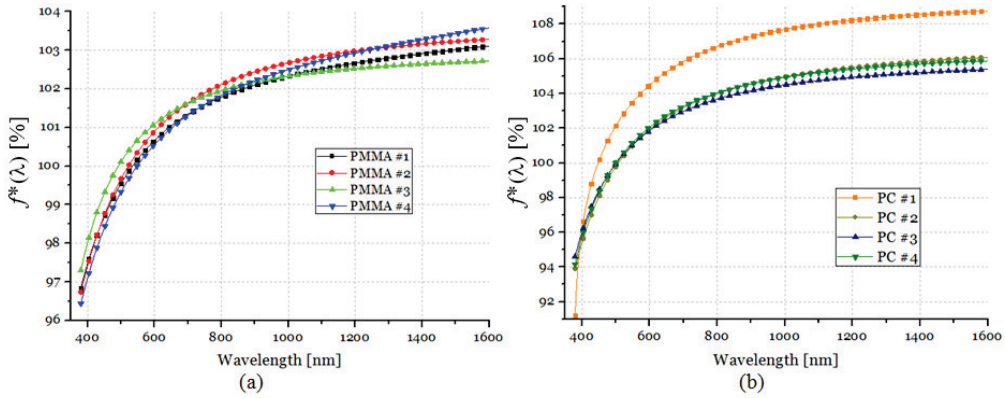

Fig. 5. Relative focal distances for PMMAs (a) and PCs (b).

Table 3 hereunder gives the central wavelength (λ_0) and compares the $|LCA^{*}_{max}|$ of each material as well as the equivalent radius of curvature. In the case of a singlet, $|LCA_{max}|$ is achieved for the two extreme wavelengths: λ_m = 380 nm and λ_M = 1600 nm. As shown on Fig. 4 and 5, the LCA is more important for PCs than PMMAs. This is due to the high dispersion of the refractive indexes of PCs compared to the refractive indexes of PMMAs. It is common to use the Abbé number v_d to measure the dispersion in the visible region.

#143631 - $15.00 USD Received 4 Mar 2011; revised 28 Mar 2011; accepted 29 Mar 2011; published 8 Apr 2011

$$v_d = (n_d - 1)/(n_F - n_C), \tag{13}$$

d, *F* and *C* being three Fraunhofer lines in the visible region corresponding respectively to 587.562, 486.134 and 656.281 nm. In order to take into account the wide spectrum band studied, we use the solar Abbé number $v_\odot$:

$$v_\odot = (n_{990nm} - 1)/(n_{380nm} - n_{1600nm}). \tag{14}$$

Table 3. Data for Singlets

Material	Information for singlets					
	λ_0 [nm]	RoC^*_{eq} [%]	LCA^* [%]	$C^{\max}_{opt}$	v_d	$v_\odot$
PMMA #1	534	48.995	3.159	1002	57.231	15.561
PMMA #2	522	48.906	3.282	928	52.270	14.868
PMMA #3	492	48.959	2.720	1351	66.522	17.990
PMMA #4	548	49.231	3.579	781	51.710	13.642
PC #1	448	60.911	8.794	129	27.928	5.249
PC #2	508	59.556	6.086	270	29.894	7.806
PC #3	502	57.166	5.393	344	33.746	8.854
PC #4	500	56.717	5.877	290	33.271	8.106

4.2 Diffractive lens

Diffractive lenses may be designed in different ways. For a single wavelength, only the kinoform (Fig. 6) may have one focus and a theoretical diffraction efficiency of 100% [14]. The ideal kinoform looks like a Fresnel lens, composed of a multitude of zones with a constant thickness *h* of few microns. Each zone of the diffractive lens is designed by keeping the optical path length constant all over the zone. Between two adjacent zones, a 2π-phase shift is introduced. In other words, there is no discontinuity in the wavefront and the diffraction efficiency is maximum at the designed wavelength λ_0. This continuity is ensured by a constant thickness of the teeth: $h = \lambda_0 / (n(\lambda_0) - 1)$ [8].

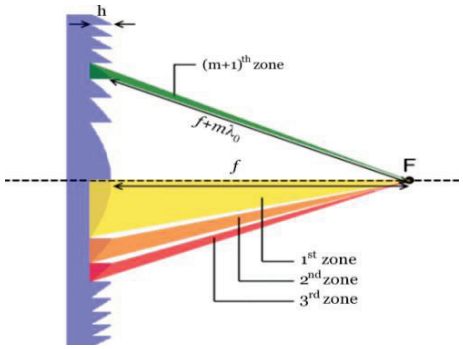

Fig. 6. Schematic representation of a kinoform diffractive lens.

While illuminating the lens with another wavelength, the focal distance will be modified following Eq. (5), independently of the refractive index . The Abbé number corresponding to this dispersion is thus also independent of the refractive index [15] and is given by Eq. (15).

$$v_{d,diff} = \frac{d}{F - C} = -3.4518. \tag{15}$$

Similarly, $v_\odot = -0.8115$. The Abbé number is negative and has lower absolute value than any refractive material, meaning that for a converging lens, long wavelengths will converge shorter than short wavelengths and that diffractive lenses are more dispersive which is

#143631 - $15.00 USD Received 4 Mar 2011; revised 28 Mar 2011; accepted 29 Mar 2011; published 8 Apr 2011

unfavourable for small *LCA* designs. Moreover, the farther they are used from the design wavelength, the more diffractive lenses suffer from a lack of diffraction efficiency. The diffraction efficiency at the first order η_1 is given by Eq. (16). E. g., for PMMA #2, with λ_0 = 550nm, the diffraction efficiency at the first order remains above 90% only between 472 and 663 nm.

$$\eta_1(\lambda) = \mathrm{sinc}^2\left\{1 - \frac{\lambda_0}{\lambda}\frac{n(\lambda)-1}{n(\lambda_0)-1}\right\}. \tag{16}$$

Those problems of high dispersion and low diffraction efficiency explain why diffractive lenses are never used alone in systems needing low LCA. Nevertheless the lack of diffraction efficiency may be drastically diminished using multilayers [16,17] without affecting the focal distance.

5. Achromatization

In order to decrease the LCA, the combination of two lenses might prove to be very powerful ($LCA^*_{\max} < 1\%$) since the lens designer may choose two wavelengths (λ_1 and λ_2) that will focus at the same point. In general, to create a doublet one uses the well-known Abbé condition given by Eq. (17) [18] in combination with the formula of the effective focal length (Eq. (18)).

$$f_1 v_1 + f_2 v_2 = 0, \tag{17}$$

$$f_{eff}^{-1} = f_1^{-1} + f_2^{-1}. \tag{18}$$

We have thus two possibilities: combining a diverging and a converging refractive lens or a converging refractive lens with a converging diffractive lens. Which of those combinations gives the best results? Before answering this question, we point out that the Eq. (17) is not fully useful for someone wishing to achromatize its system at a given focal distance. Indeed, if the formula $f_{1,d}v_{1,d} + f_{2,d}v_{2,d} = 0$ is used, $f(\lambda_C)$ and $f(\lambda_F)$ will be the same but only the focal distance of λ_d is known directly. Moreover nothing proves that having the same focal distance for λ_F and λ_C gives the smallest LCA^*_{max}. Therefore, we suggest using a more straightforward formula giving directly the focal distance of two chosen wavelengths λ_1 and λ_2.

5.1 Refractive doublet

It can be shown (Appendix B) that for a given back focal length (*bfl*) – i.e. the distance from the back of the second lens to the focal point (see Fig. 7) – the focal distance of the second lens is given by Eq. (19) and (20).

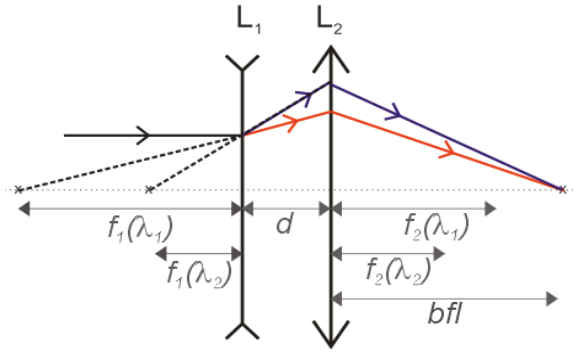

Fig. 7. Schematic representation of a doublet.

#143631 - $15.00 USD Received 4 Mar 2011; revised 28 Mar 2011; accepted 29 Mar 2011; published 8 Apr 2011

$$f_2(\lambda_1) = \frac{-B \pm \sqrt{B^2 - 4AC}}{2A}, \tag{19}$$

with

$$\begin{aligned} A &= \left(bfl + d\right)\left(\frac{n_2(\lambda_1)-1}{n_2(\lambda_2)-1}\right)\left(1 - \frac{n_1(\lambda_2)-1}{n_1(\lambda_1)-1}\right), \\ B &= bfl\left\{d\left(\frac{n_2(\lambda_1)-1}{n_2(\lambda_2)-1} - \frac{n_1(\lambda_2)-1}{n_1(\lambda_1)-1}\right) + \left(bfl + d\right)\left(\frac{n_1(\lambda_2)-1}{n_1(\lambda_1)-1}\frac{n_2(\lambda_1)-1}{n_2(\lambda_2)-1} - 1\right)\right\}, \\ C &= d\,bfl^2\left(1 - \frac{n_1(\lambda_2)-1}{n_1(\lambda_1)-1}\right). \end{aligned} \tag{20}$$

In this equation, if $0 < d \ll bfl$, A and C are always positive while B depends on the order of the materials. The first lens will have another expression of the focal distance

$$f_1(\lambda_1) = \frac{d(bfl) - (bfl + d) f_2(\lambda_1)}{(bfl) - f_2(\lambda_1)}. \tag{21}$$

Those two equations ensure that $bfl(\lambda_1) = bfl(\lambda_2) = bfl$ where bfl, λ_1 and λ_2 are three parameters. For the other wavelengths in the refractive regime,

$$bfl_{ref}(\lambda) = \frac{f_2(\lambda)\left(d - f_1(\lambda)\right)}{d - f_1(\lambda) - f_2(\lambda)}. \tag{22}$$

If the first material – of refractive index $n_1(\lambda)$ – has a dispersion higher than $n_2(\lambda)$, B will be negative and thus $f_2(\lambda)$ will be positive if the plus sign is chosen, which is in accordance with the Abbé condition (Eq. (17)). In Eq. (19), if the minus sign was chosen, then $f_2(\lambda)$ would have been negative and $f_1(\lambda)$ positive, which is not in accordance with the Abbé condition. This kind of doublets has a higher LCA than doublets obeying to Abbé conditions and may have LCA more pronounced compared with singlets. Equation (19) to (22) allow for a quicker optimisation of the LCA, when bfl is fixed we have just to find λ_1 and λ_2 optimizing the LCA. Note that the choice of bfl does not affect the LCA^* as may be understood from Eq. (6).

5.2 Hybrid lens

A hybrid lens results in the combination of a refractive and a diffractive lens. In this case, there is no need for a combination of two different optical materials since the focal length of a diffractive lens is independent of the refractive index. A hybrid lens could thus be manufactured in only one piece. Moreover the whole profile could be engraved on one surface (corresponding thus to $d = 0$), simply by summing the refractive and the diffractive profiles [19]. The focal distance of the refractive lens corresponds to one mathematical solution of a quadratic equation

$$f_{ref}(\lambda_1) = \frac{-B - \sqrt{B^2 - 4AC}}{2A} \tag{23}$$

with

#143631 - $15.00 USD Received 4 Mar 2011; revised 28 Mar 2011; accepted 29 Mar 2011; published 8 Apr 2011

$$A = (bfl + d)\left(\frac{n(\lambda_1)-1}{n(\lambda_2)-1}\right)\left(1-\frac{\lambda_2}{\lambda_1}\right),$$
$$B = bfl\left\{d\left(\frac{\lambda_2}{\lambda_1}-\frac{n(\lambda_1)-1}{n(\lambda_2)-1}\right)+(bfl+d)\left(\frac{\lambda_2}{\lambda_1}\frac{n(\lambda_1)-1}{n(\lambda_2)-1}-1\right)\right\}, \quad (24)$$
$$C = d\,bfl^2\left(1-\frac{\lambda_2}{\lambda_1}\right).$$

The expression of the focal distance of the diffractive lens f_{dif} given by Eq. (25) corresponds exactly to Eq. (21).

$$f_{dif}(\lambda_1) = \frac{d(bfl)-(bfl+d)f_{ref}(\lambda_1)}{(bfl)-f_{ref}(\lambda_1)}. \quad (25)$$

In the case of the hybrid lens, both f_{ref} and f_{dif} are positive for a converging lens.

6. Performance

6.1 Refractive doublet

In Table 4 the two wavelengths (λ_0 and λ_0') minimizing the $|LCA_{\max}|$ have been determined with a precision of 1nm for each. For every combination of materials, under the two wavelengths of better achromatization, $|LCA_{\max}|$ is presented followed by radii of curvature of the PC and the PMMA respectively. All those combinations are graphically represented in Fig. 8: each of the four PCs in combination with all PMMAs is presented. Combining a weakly crown OP (PMMA) with a flint OP (PC) may lead to very different performances. But low LCA may also be achieved with two PMMAs or two PCs. However – as it might be understood from the Abbé condition – this leads to very small radii of curvature. And since $|LCA^*_{\max}|$ is greater than 1% we no longer have to consider this possibility hereafter.

Table 4. Combination of PCs and PMMAs for Achromatic Doublets

OPs in PMMA	OPs in PC				Best $C_{\max}$ (line)
	PC #1	PC #2	PC #3	PC #4	
PMMA #1	1.221 (386 – 711) -114.798, 32.496	0.421 (406 – 1033) -56.380, 24.081	0.570 (402 – 1087) -41.403, 20.810	0.544 (400 – 1063) -49.691, 23.139	56,420
PMMA #2	1.260 (386 – 641) -106.638, 31.301	0.344 (400 – 693) -51.363, 22.659	0.501 (396 – 745) -37.449, 19.378	0.483 (396 – 739) -45.221, 21.723	84,505
PMMA #3	0.788 (386 – 551) -137.950, 34.087	0.124 (432 – 1107) -74.049, 27.091	0.084 (456 – 943) -55.978, 24.196	0.068 (468 – 961) -64.669, 26.059	2,137,410
PMMA #4	1.571 (387 – 806) -94.770, 30.176	0.792 (408 – 1157) -42.459, 20.537	1.081 (404 – 1175) -29.644, 16.860	0.978 (402 – 1159) -37.011, 19.498	15,942
Best $C_{\max}$ (column)	16,105	650,360	1,417,233	2,137,410	

$|LCA^*_{\max}|$ [%] (λ_0 [nm] – λ'_0 [nm]), RoC^*_{eq}(PC), RoC^*_{eq} (PMMA)

Best result of achromatization is achieved with a combination of PMMA #3 and PC #4, leading to a LCA^*_{max} of 0.068 corresponding to a maximal concentration of 2.1×10^6 with incoming flux at normal incidence.

#143631 - $15.00 USD Received 4 Mar 2011; revised 28 Mar 2011; accepted 29 Mar 2011; published 8 Apr 2011

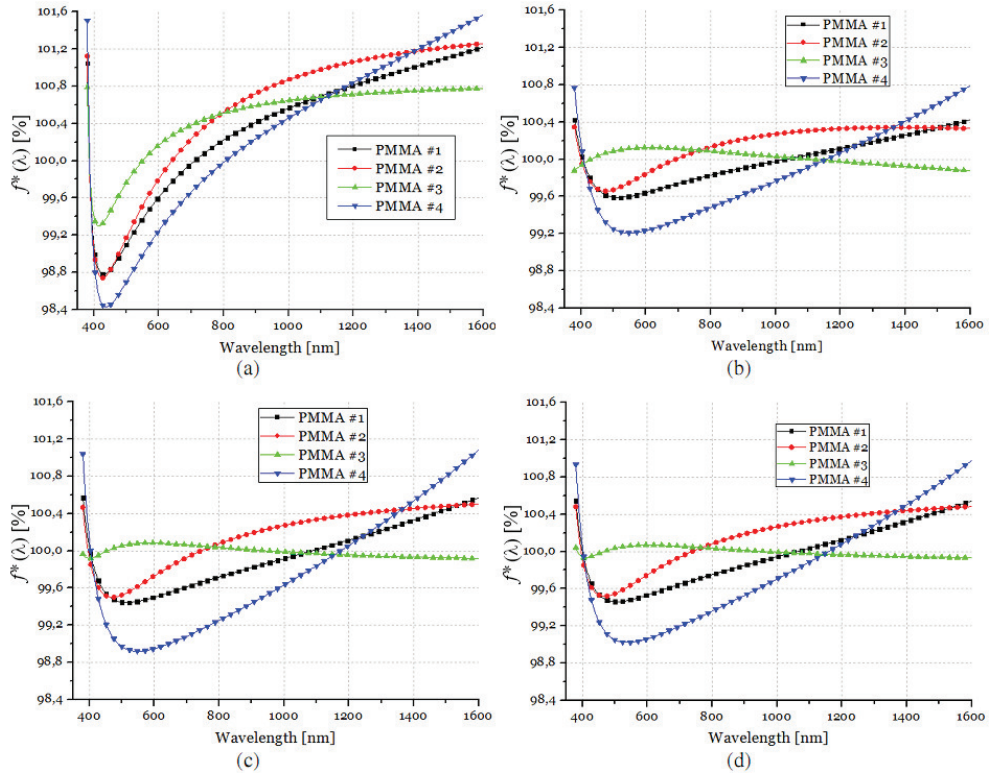

Fig. 8. Doublets with PC #1 (a), PC #2 (b), PC #3 (c) and PC #4 (d).

6.2 Hybrid lens

Since the focal distance of the hybrid lens depends only on the dispersion curve of the refractive part and on the two wavelengths of achromatization, all OPs have been considered in a single plot (Fig. 9).

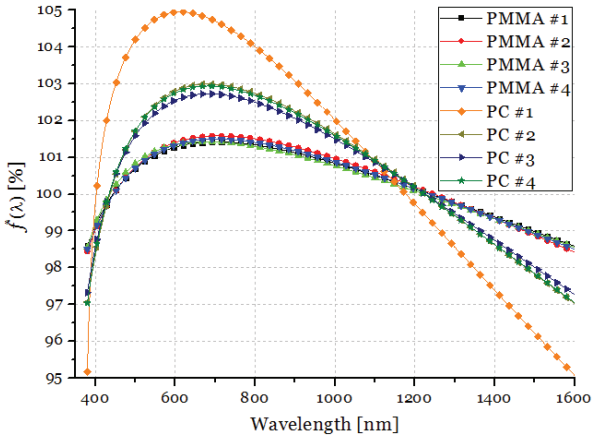

Fig. 9. Evolution of the focal distance for hybrid lenses in OP considering the curve minimizing the LCA.

Table 5 presents the two wavelengths of achromatization (λ_0 and λ'_0) giving the smallest and the equivalent radius of curvature.

#143631 - $15.00 USD Received 4 Mar 2011; revised 28 Mar 2011; accepted 29 Mar 2011; published 8 Apr 2011

Table 5. Data for Achromatized Hybrid Lenses

OP	λ_0 and λ'_0 [nm]	RoC^*_{eq} [%]	LCA^* [%]	$C^{\max}_{opt}$
PMMA #1	444 – 1239	51.302	1.423	4938
PMMA #2	446 – 1247	50.756	1.581	4000
PMMA #3	436 – 1223	50.409	1.450	4756
PMMA #4	446 – 1236	51.365	1.502	4432
PC #1	402 – 1177	66.775	4.954	407
PC #2	436 – 1225	63.752	2.992	1117
PC #3	434 – 1225	60.689	2.731	1341
PC #4	434 – 1223	60.466	2.965	1138

7. Discussion

This section shows the performance of achromatization for both hybrid and doublet lenses. Table 6 collects most important data to be compared.

Table 6. Major Data about Singlets, Doublets, and Hybrid Lenses

OPs	v_d	$v_\odot$	$C^{\max}_{opt}$ for singlets [%]	$C^{\max}_{opt}$ for hybrid [%]	Highest $C^{\max}_{opt}$ with a doublet [%]
PMMA #1	57.231	15.561	1002	4938	56,420
PMMA #2	52.270	14.868	928	4000	84,505
PMMA #3	66.522	17.990	1351	4756	2,137,410
PMMA #4	51.710	13.642	781	4432	15,942
PC #1	27.928	5.249	129	407	16,105
PC #2	29.894	7.806	270	1117	650,360
PC #3	33.746	8.854	344	1341	1,417,233
PC #4	33.271	8.106	290	1138	2,137,410

Though $v_\odot$ is in direct relation with $|LCA^*_{\max}|$ of the singlet and materials with high $v_\odot$ are more suitable to be used in a hybrid lens, there is absolutely no direct relation between Abbé numbers and good achromatization with a refractive doublet. But it clearly appears that even if hybrid lenses have a smaller LCA than singlets, a refractive doublet is even more powerful decreasing the $|LCA^*_{\max}|$ of the singlet up to a factor 2×10^6 while this factor is limited to 5000 × in the case of hybrid lenses. Hybrid lenses have some advantages: they could be manufactured in only one material and have a higher radius of curvature. Moreover studies are still under way to improve hybrid lenses for high concentration systems [17] but at this time, lens designers would probably prefer refractive doublets to avoid the lack of diffraction efficiency and to get a higher achromatization performance.

Note that the maximum concentration is limited by the diffraction limit. For a circular lens with a radius of 10 cm and a focal of 20 cm, the concentration is limited to about 1.5×10^{16}.

8. Conclusions

Abbé formula is useful to achromatize at two wavelengths and to see that is preferable to choose two materials with Abbé numbers strongly different from each other in order to get high radii of curvature. But firstly the Abbé does not give any information about the quality of the achromatization. Secondly it does not allow choosing the focal distances of the two achromatized wavelengths. And thirdly this formula does not take into account the distance between the two lenses. Equations (19) to (22) are thus more useful for lens designers.

Not only is the Abbé number not sufficient but also the dispersion curves in the literature are limited to a spectral bandwidth and are dependent on the type of plastic, production conditions etc.

Hybrid lenses allow for fast converging systems since both lenses are converging. Unfortunately they suffer from a lack of diffraction efficiency at the focus due to spurious orders but they reduce the $|LCA^*_{\max}|$ by about a factor 4.2 compared to the singlets. The

#143631 - $15.00 USD Received 4 Mar 2011; revised 28 Mar 2011; accepted 29 Mar 2011; published 8 Apr 2011

maximum geometrical concentration achieved with a hybrid lens corresponds to about 5000 under normal incidence, which lies well under the maximum theoretical concentration of 46,000 under solar angular incidence.

As for refractive doublets, they allow – at normal incidence – a theoretical concentration ratio up to 50 times higher than 46,000. The linear chromatic aberration of such doublets can thus be regarded as not limiting the concentration ration. Doublets are thus good candidates to achieved very high concentration at low cost.

Appendix A

Considering a lens of diameter *2r* and a given *LCA** around $f(\lambda_0)$.

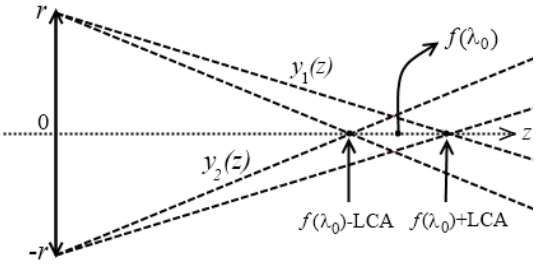

Fig. 10. Schematic representation of a converging lens with LCA.

Referring to Fig. 10, the best position of the detector is given by the intersection of the lines given by Eq. (26) and (27).

$$y_1(z) = \frac{-r}{f(\lambda_0)(1+LCA^*)}z + r, \tag{26}$$

$$y_2(z) = \frac{r}{f(\lambda_0)(1-LCA^*)}z - r. \tag{27}$$

Thus

$$\frac{1}{f(\lambda_0)(1-LCA^*)}z - 1 = \frac{-1}{f(\lambda_0)(1+LCA^*)}z + 1, \tag{28}$$

$$z\left(\frac{1+LCA^*+1-LCA^*}{1-\left(LCA^*\right)^2}\right) = 2f(\lambda_0), \tag{29}$$

$$z = f(\lambda_0)\left(1-LCA^{*2}\right). \tag{30}$$

Quod erat demonstrandum.

Appendix B

The notation of this appendix follows Hecht's books [7] with the thin lens formula given by

$$\frac{1}{f} = \frac{1}{s_o} + \frac{1}{s_i}, \tag{31}$$

where *f* is the focal distance, s_o the lens-object distance and s_i the lens image distance. In order to calculate the *bfl*, let's define $\hat{f}$.

#143631 - $15.00 USD Received 4 Mar 2011; revised 28 Mar 2011; accepted 29 Mar 2011; published 8 Apr 2011

$$\hat{f} = bfl + d. \tag{32}$$

For a doublet, it doesn't matter if the first lens is the converging one or the diverging one as will be proved in the following subsections.

a) Diverging lens first

If the light coming from infinity strikes the diverging lens first, the image of the first lens – having a focal distance $f_1(\lambda)$ and a refractive index $n_1(\lambda)$ – is virtual

$$\frac{1}{f_1} = \frac{1}{s_{i1}} \qquad with\ f_1 < 0. \tag{33}$$

The image of the first lens becomes the object of the second lens (the converging one) having a focal distance $f_2(\lambda)$ and a refractive index $n_2(\lambda)$:

$$s_{o2} = |f_1| + d. \tag{34}$$

The final image is thus situated at a distance s_{i2} from the second lens

$$\frac{1}{s_{i2}} = \frac{1}{f_2} - \frac{1}{s_{o2}} = \frac{1}{f_2} - \frac{1}{d - f_1} = \frac{d - f_1 - f_2}{f_2(d - f_1)}. \tag{35}$$

Thus, from the first lens, the final image is situated at

$$\hat{f} = s_{i2} + d = \frac{f_2(d - f_1)}{d - f_1 - f_2} + d. \tag{36}$$

b) Converging lens first

Equation (33) to (36) become now

$$\frac{1}{f_1} = \frac{1}{s_{i1}} \qquad with\ f_1 > 0, \tag{37}$$

$$s_{o2} = f_1 - d, \tag{38}$$

$$\frac{1}{s_{i2}} = \frac{1}{f_2} - \frac{1}{s_{o2}} = \frac{1}{f_2} + \frac{1}{f_1 - d}, \tag{39}$$

$$\hat{f} = s_{i2} + d = \frac{f_2(d - f_1)}{d - f_1 - f_2} + d, \tag{40}$$

which is exactly the same expression as Eq. (36).

c) Expression of the focal distances

Since focal distances f_1 and f_2 depend on the wavelength, *bfl* depends on the wavelength and thus f^* also. But we would like to have the same back focal distance for two chosen wavelengths λ_1 and λ_2: $bfl(\lambda_1) = bfl(\lambda_2) = bfl$ which is equivalent to

$$\hat{f}(\lambda_1) = \hat{f}(\lambda_2) = \hat{f}. \tag{41}$$

To ensure Eq. (41), let's determine the focal distances $f_1(\lambda)$ and $f_2(\lambda)$. Considering both lenses as thin lenses the focal distance is given by Eq. (11). Thus

$$f_1(\lambda_1) = f_1(\lambda_2)\left(\frac{n_1(\lambda_2) - 1}{n_1(\lambda_1) - 1}\right) = \alpha\ f_1(\lambda_2), \tag{42}$$

#143631 - $15.00 USD Received 4 Mar 2011; revised 28 Mar 2011; accepted 29 Mar 2011; published 8 Apr 2011

$$f_2(\lambda_2) = f_2(\lambda_1)\left(\frac{n_2(\lambda_1)-1}{n_2(\lambda_2)-1}\right) = \beta\ f_2(\lambda_1). \tag{43}$$

In order to facilitate the reading, we define

$$f_{ij} \triangleq f_i(\lambda_j) \tag{44}$$

from Eq. (36)

$$f_{11} = \frac{\hat{f}\ f_{21} - bfl\ d}{f_{21} - bfl} = \alpha \frac{\hat{f}\,\beta f_{21} - bfl\ d}{\beta f_{21} - bfl}, \tag{45}$$

effectuating the cross product

$$\left(\hat{f}\ f_{21} - bfl\, d\right)\left(\beta f_{21} - bfl\right) = \left(f_{21} - bfl\right)\alpha\left(\hat{f}\,\beta f_{21} - bfl\, d\right), \tag{46}$$

and separating the terms in ${f_{21}}^2, f_{21}, {f_{21}}^0$

$$f_{21}^2\left\{\hat{f}\beta - \hat{f}\alpha\beta\right\} + f_{21}\left\{bfl\left(\alpha d + \hat{f}\alpha\beta - \hat{f} - \beta d\right)\right\} + \left\{d\ bfl^2 - \alpha bfl^2 d\right\} = 0. \tag{47}$$

Thus

$$f_{21}\frac{-B \pm \sqrt{B^2 - 4AC}}{2A}, \tag{48}$$

with

$$\begin{cases} A = (bfl + d)\beta(1-\alpha), \\ B = bfl\left(d(\alpha-\beta) + (bfl + d)(\alpha\beta - 1)\right), \\ C = d\, bfl^2(1-\alpha). \end{cases} \tag{49}$$

Finally, replacing α and β with Eq. (42) and (43), Eq. (49) turns into Eq. (24).
Quod erat demonstrandum.

Acknowledgements

The authors are grateful to the Ministry of the Walloon Region (DGTRE) for the financial support accorded in the framework of the Solwatt program (Convention Solwatt 850552). Thank you too to Amos and Optim Test Centre, societies from Liege for the diamond turning and injection molding of plastic Fresnel doublets. A finally, thank you to all interns of Hololab for their indirect collaboration.

#143631 - $15.00 USD Received 4 Mar 2011; revised 28 Mar 2011; accepted 29 Mar 2011; published 8 Apr 2011

Performance comparison of four kinds of flat nonimaging Fresnel lenses made of polycarbonates and polymethyl methacrylate for concentrated photovoltaics

Fabian Languy* and Serge Habraken

Hololab, Physics Department, Bat. B5a, University of Liege, 17 allée du 6 Août, B-4000 Liege, Belgium
**Corresponding author: flanguy@ulg.ac.be*

Received April 28, 2011; revised June 8, 2011; accepted June 10, 2011;
posted June 10, 2011 (Doc. ID 146630); published July 14, 2011

Solar concentrators made of a single refractive primary optics are limited to a concentration ratio of about 1000× [Opt. Express **19**, A280 (2011)], due only to longitudinal chromatic aberration, while mirrors are limited to ~46, 000× by the angular size of the Sun. To reduce the chromatic aberration while keeping cost-effective systems for concentrated photovoltaics, a study of four different kinds of flat Fresnel doublets made of polycarbonates and polymethyl methacrylate is presented. It reveals that Fresnel doublets may have fewer optical losses than non-Fresnel doublets, with a lower lateral chromatic split allowing for even higher concentration ratio. © 2011 Optical Society of America

OCIS codes: 220.4298, 220.1770, 220.1000, 350.6050, 080.2740.

Since lenses exhibit chromatic aberration, unlike mirrors, their applicability in solar concentration is limited [1]. Considering a spectrum of 380 to 1600 nm—a typical range for concentrated photovoltaics (CPVs) since out of this range solar flux is low and the external quantum efficiency of a triple junction cell is about 40% [2–5]—the longitudinal chromatic aberration (LCA) of a single Fresnel lens limits the concentration to ~1000× under normal incidence [6], while the theoretical limit on earth due to the acceptance angle of the solar semidiameter (959″ [7]) is about 46, 000× [8]. To achieve a high concentrating ratio at low cost, four different flat Fresnel doublets made of polycarbonates (PCs) and polymethyl methacrylate (PMMA) have been designed and compared at normal incidence. Ellipsometric measurements have been performed to determine the dispersion curves of the PCs and PMMA. Those curves have been fitted using Sellmeier's equation [9] [given in Eq. (1) with the wavelength λ in micrometers], with a Δn error between data and the fitted curve inferior to 5e-5 over the full spectrum:

$$n(\lambda) = \sqrt{A_1 + A_2\lambda^2 + \frac{A_3}{\lambda^2} + \frac{A_4}{\lambda^4} + \frac{A_5}{\lambda^6} + \frac{A_6}{\lambda^8}}. \quad (1)$$

For the PC, $A_1 = 2.205583\text{e-}2$, $A_2 = 0.2532511$, $A_3 = 1.073656$, $A_4 = 0.1004816$, $A_5 = 1.630428\text{e-}2$, and $A_6 = 1.62352\text{e-}2$. For the PMMA, $A_1 = 0.6997099$, $A_2 = 0.2731275$, $A_3 = 0.2043425$, $A_4 = -5.777416\text{e-}4$, $A_5 = -5.784644\text{e-}4$, and $A_6 = 4.291190\text{e-}2$.

Considering a doublet of radius R, all four designs respond to the following specifications: (a) single lens thickness (excluding teeth), $e = R/10$; (b) teeth height, $h = R/40$; (c) detector position from the bottom lens, $4R$, i.e., f-number $\simeq 2$; (d) $\mathrm{bfl}(\lambda_1 = 468\,\mathrm{nm}) = \mathrm{bfl}(\lambda_2 = 961\,\mathrm{nm}) = 4R$ exactly, to minimize the greatest LCA in absolute value Fig. 1, with bfl being the back focal length. These specifications are in accordance with low-cost production by injection molding [10]. The advantages and disadvantages of each flat Fresnel doublet are presented and have been compared with their equivalent non-Fresnel (nF) doublets in Fig. 2.

The easiest way to manufacture a Fresnel doublet consists of two faceted lenses with a flat interface [see designs (1a′) and (1b′) of Fig. 2], called TFT for teeth–flat–teeth doublets. But should we put the diverging lens above or under the converging lens? The answer lies mainly in the shadowing of the teeth. Following the achromatic doublet condition $f_1 v_1 + f_2 v_2 = 0$ [11], the diverging lens has to be made of PC and the converging lens of PMMA since PMMA has a higher Abbe number. If the converging lens is Sun facing [Fig. 3(a)], lots of rays will be lost because of the high deviation angle at the first interface [Fig. 3(a)(i)]. At the last interface, it is easy to avoid any geometric loss: the outgoing rays diverge from their normal at the interface so that they will never strike the draft facet [circled in Fig. 3(a)] of the tooth. Except the very first tooth of the top lens, every tooth from 2 to $i_{\max}$ causes an optical loss. The dead zone (dz) at one dimension (1D) is given by

$$\mathrm{dz}_{1\mathrm{D}}(1\mathrm{a}') = \sum_{i=2}^{i_{\max}} h \frac{\sin(\alpha_i)\cos(\theta_i)}{\cos(\alpha_i - \theta_i)}, \quad (2)$$

where α_i and θ_i are angles that refer to the closest ray from the draft facet that is not lost. Those two angles

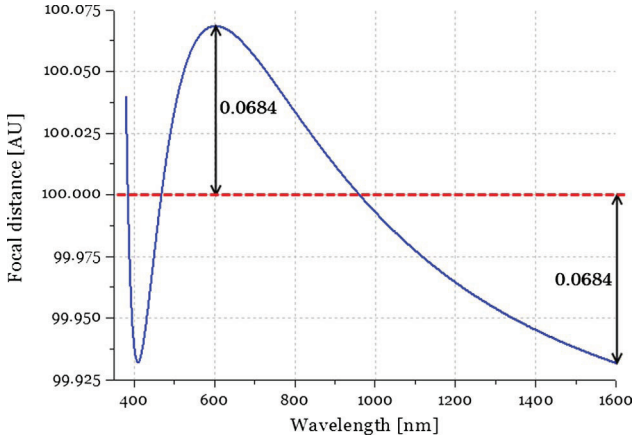

Fig. 1. (Color online) Evolution of the focal distance minimizing the maximum LCA to 0.0684% of the design focal distance (represented by the dotted line).

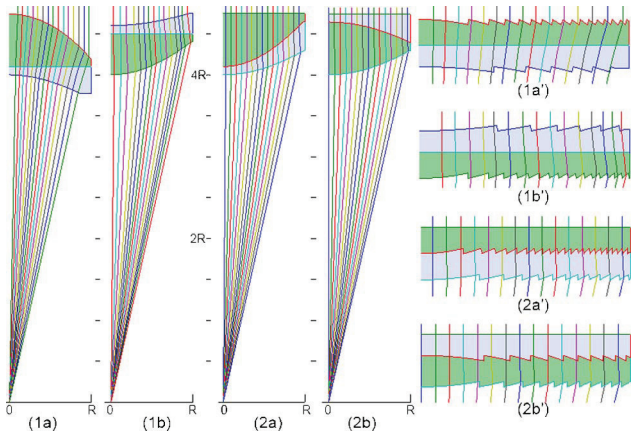

Fig. 2. (Color online) Four kinds of nF doublets [(1a) to (2b)] and their Fresnel equivalent [(1a′) to (2b′)]. Green coloration corresponds to PMMA and blue to PC (PC appears lighter in gray scale).

correspond, respectively, to the deviation angle after the first interface [see Fig. 3(a)] and to the angle of incidence with the normal to the teeth. Lens designers may open the draft angle of the two lenses represented in Fig. 3(a) (ii) for the top lens, making the lens easier to manufacture, with the total loss remaining the same. Since all draft angles may be greater than 2 deg, it ensures an easier ejection from the mold without affecting the global loss. Moreover, by choosing the value of the draft angle, the location of the stray may be somewhat controlled.

If the light reaches the diverging lens first [Fig. 3(b)] fewer rays than in the previous design will be lost since the curvature is smaller. Nevertheless, beyond a certain radius, the incoming rays will be deviated farther than the radial edge of the lens, causing a nonnegligible loss. However, there are no optical losses at the latest interface: the rays left the lens in the opposite direction of the draft side of the next tooth. For this design, too, the lens designer may open the draft angle [Fig. 3(b)(ii)] without affecting the dz, which lies in a range given by Eq. (3), where γ is the deviation angle in the second lens [Fig. 3(b)]:

$$\sum_{i=1}^{i_{\max}-1} h\frac{\sin(\alpha_i)\cos(\theta_i)}{\cos(\alpha_i-\theta_i)} + e(\tan\alpha_{\max}+\tan\gamma_{\max}) \le \mathrm{dz}_{1\mathrm{D}}(1\mathrm{b}') \le \sum_{i=1}^{i_{\max}-1} h\frac{\sin(\alpha_i)\cos(\theta_i)}{\cos(\alpha_i-\theta_i)} + (e+h)(\tan\alpha_{\max}+\tan\gamma_{\max}). \quad (3)$$

The performance of the doublet is linked to the discretization of the Fresnel ring (i.e., the segment size) of each lens of the doublet. The top lens may have a discretization as high as desired. The discretization of the bottom lens is limited by the maximum difference of impact between the rays at the extreme wavelengths coming from the same incoming ray. For a given segment of lens having an angle β with the detector, two wavelengths strike this segment with their own angle of incidence (θ_r and θ_b) that remains the same along the whole segment $|P_1P_2|$ in the first approximation. If the detector is centered on the output beams, the detector size must be larger than the lateral chromatic split s given by Eq. (4) with parameters in accordance with Fig. 4(a):

$$s = \left(\frac{\sin(\theta_r-\beta)}{\sin(\theta_r)} + \frac{\sin(\theta_b-\beta)}{\sin(\theta_b)}\right)|P_1P_2|. \quad (4)$$

Since, in the first design, two rays of different wavelengths coming from the same point will diverge in both lenses, the thicker the lenses, the higher the lateral chromatic split [Fig. 4(b)]. For the second design, two rays of different wavelength will diverge in the first lens, but they will cross each other at a certain distance from the PC–PMMA interface [Fig. 4(c)]. It is thus possible to decrease the lateral chromatic split to increase the concentration ratio.

To optimize the active zone and the discretization of the lens while keeping a flat design, we suggest using flat–teeth–teeth (FTT) lenses, which present some optical performance advantages but also cause fewer soiling problems—easier to clean and no accumulation of dust in the hollow of the teeth. If the first lens is made of PMMA and the second of PC [Fig. 5(a)], then a dz appears—some rays strike the draft face of the interface teeth. Since the rays diverge from the interface, the thicker the second lens, the bigger the dz. The expression of the dz [Eq. (5)] is thus almost the same as design (1b′):

$$\mathrm{dz}_{1\mathrm{D}}(2a') = \sum_{i=1}^{i_{\max}-1} h\frac{\sin(\gamma_i)\cos(\theta_i)}{\cos(\gamma_i-\theta_i)} + e\gamma_{\max}. \quad (5)$$

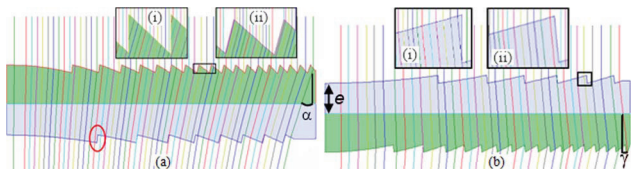

Fig. 3. (Color online) Both cases of TFT doublets with zoom on top teeth: with (a) top-converging lens and (b) back-converging lens. Zoom (ii) refers to open draft angle and (i) to closed draft angle.

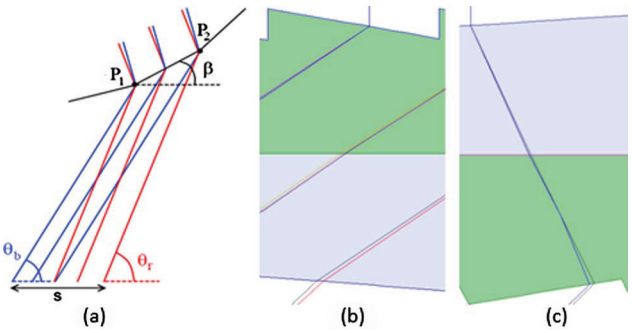

Fig. 4. (Color online) (a) Schematic representation of the chromatic splitting on a single segment. Figures (b) and (c) are laterally stretched representations of both cases of TFT lenses.

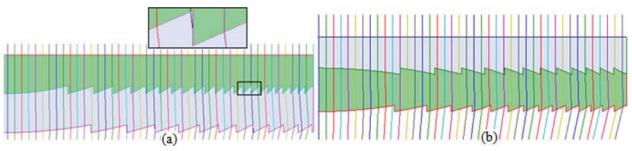

Fig. 5. (Color online) FTT doublets: (a) PMMA top plus zoom on the intermediate teeth and (b) PC top.

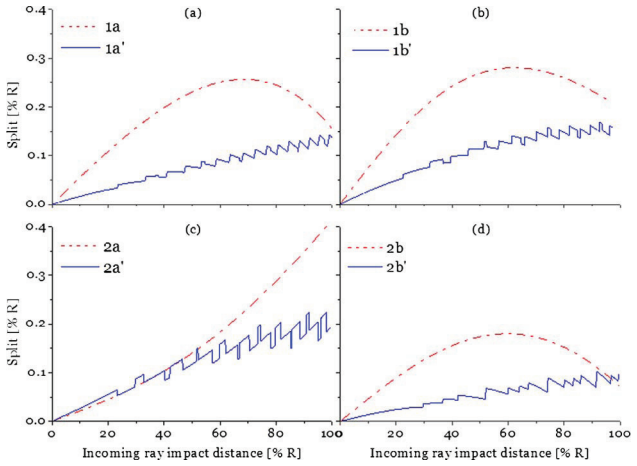

Fig. 6. (Color online) Chromatic split for the Fresnel doublets and their equivalent nF doublets. The notation of the designs is in accordance with Fig. 2. (All figures have the same scale).

The last design—consisting of a lens of PC on top of a lens of PMMA, as illustrated in Fig. 5(b)—avoids the problem of shadowing at the PC–PMMA interface since the rays diverge from the draft part of the teeth. Only the shadowing due to the diverging rays on the radial edge occurs. The dz at 1D is thus given by

$$\mathrm{dz}_{1D}(2b') = e\beta_{\max}. \tag{6}$$

Figure 6 compares the chromatic split of the Fresnel doublets with their equivalent nF doublets. Wavelengths $\lambda_1 = 468\,\mathrm{nm}$ and $\lambda_2 = 961\,\mathrm{nm}$ were chosen instead of extreme wavelengths in order to study the chromatic split without being affected by the variation of focal distance. In Table 1, the performance of the eight kinds of Fresnel doublets is presented in terms of dz (as a percentage of the incoming surface, dz^*), lateral chromatic split (s^*) and global thickness (t^*), both as a percentage of the lens radius. The optical concentration (C_{opt}) at two dimensions (2D) is calculated as follows:

$$C_{\mathrm{opt,\,2D}} = \left(\frac{2R}{s}\right)^2\left(1 - \frac{\mathrm{dz}_{2D}}{\pi R^2}\right) = \left(\frac{2}{s^*}\right)^2(1 - \mathrm{dz}^*_{2D}). \tag{7}$$

For ideal thin doublets made of PC–PMMA, the maximum concentration under normal incidence is about 2e6 [6], but for real designs, the lateral chromatic split becomes even more limiting than the LCA, reducing the upper value to 3.80e6. Obviously, in practice, misalignment and manufacture reduce even more the performance.

Table 1. Doublets Performance Comparison

Design	dz^*_{1D} [%][a]	dz^*_{2D} [%][a]	s^* [%]	t^* [%]	$C_{\mathrm{opt,2D}}$
(1a)	0.00 + 0.00	0.00 + 0.00	0.322	64.3	0.39e6
(1b)	0.00 + 3.25	0.00 + 6.39	0.280	75.2	0.48e6
(2a)	0.00 + 2.25	0.00 + 4.45	0.406	63.0	0.23e6
(2b)	0.00 + 0.53	0.00 + 1.06	0.232	62.0	0.74e6
(1a′)	7.88 + 0.00	11.7 + 0.00	0.143	25	1.73e6
(1b′)	1.26 + 2.40	1.86 + 4.74	0.168	25	1.32e6
(2a′)	1.04 + 0.50	1.54 + 1.00	0.224	25	0.78e6
(2b′)	0.00 + 0.53	0.00 + 1.06	0.102	25	3.80e6

[a]Expressed as $A + B$ where A corresponds to the dz due to the teeth and B to the finite radius.

The main problem of TFT doublets is an important loss at the first interface because of the high deviation of the rays toward the draft angle of the teeth, especially if the top lens is convergent [design (1a′)]. If the first lens is the diverging lens, then the losses due to the Fresnelization of the lens are highly reduced, but a loss due to the finite dimension of the lens occurs: some rays diverge outside of the lens and do not reach the bottom interface.

Regarding the FTT with PMMA on top [design (2a′)], a high curvature at the interface is needed, which causes a more important chromatic split than in the TFT cases, but the angles of divergence remain smaller and the thickness between the two faceted surfaces is shorter. Globally this doublet has fewer lost rays than in the previous cases. Finally, the FTT system with PC on top has no loss due to Fresnelization and has a small loss due to the diverging angle that appears at the PC–PMMA interface.

The lowest optical concentration of the Fresnel doublets (0.78e6) is higher than the highest optical concentration of the nF doublets (0.74e6) (see Table 1). Those concentrations—under normal incidence—remain well above 46,000×, showing that, under solar incidence, the concentration factor will be affected by the angular size of the Sun much more than by the chromatic effects. We note that Fresnel doublet (2b′) has the highest optical concentration and a small dz, making it the best candidate in terms of optical properties to replace mirrors.

In conclusion, doublets could have really small LCA allowing for high concentration ratios and, among the Fresnel designs, design (2b′) minimizes both the lateral chromatic split and the shadowing (about 1% at 2D).

Thanks to C. Lenaerts and K. Fleury from Center Spatial of Liege for ellipsometric measurements. This work is supported by the Wal ID Sol project from the Solwatt program (Convention 850552) of the Walloon Region.

References

1. R. Leutz and A. Suzuki, *Nonimaging Fresnel Lenses* (Springer, 2001), Chap. 1.
2. A. W. Bett, F. Dimroth, and G. Siefer, in *Concentrator Photovoltaics* (Springer, 2007), Chap. 4.
3. Spectrolab data sheets, www.spectrolab.com/DataSheets/PV/CPV/CDO-100-C3MJ.pdf.
4. National Renewable Energy Laboratory AM 1.5 Standard Dataset, http://rredc.nrel.gov/solar/spectra/am1.5/, accessed on February 6, 2011.
5. C. A. Gueymard, Sol. Energy **71**, 325 (2001).
6. F. Languy, K. Fleury, C. Lenaerts, J. Loicq, D. Regaert, T. Thibert, and S. Habraken, Opt. Express **19**, A280 (2011).
7. S. Puliaev, J. L. Penna, E. G. Jilinski, and A. H. Andrei, Astron. Astrophys. Suppl. Ser. **143**, 265 (2000).
8. R. Winston, J. Opt. Soc. Am. **60**, 245 (1970).
9. S. N. Kasarova, N. G. Sultanova, C. D. Ivanov, and I. D. Nikolov, Opt. Mater. **29**, 1481 (2007).
10. J.-T. Mäkinen and R. de Schipper, "Injection molding for solar concentrators," presented at the Workshop on CPV Power Plants, Germany, 2007, http://www.concentrating-pv.org/marburg2007/papers.html.
11. M. Born and E. Wolf, *Principles of Optics*, 7th ed. (Cambridge U. Press, 2003), p. 188.

Solar Energy Materials & Solar Cells 109 (2013) 70–76

Contents lists available at SciVerse ScienceDirect

Solar Energy Materials & Solar Cells

journal homepage: www.elsevier.com/locate/solmat

Performance of solar concentrator made of an achromatic Fresnel doublet measured with a continuous solar simulator and comparison with a singlet

Fabian Languy [a,*], Cédric Lenaerts [b], Jérôme Loicq [b], Tanguy Thibert [b], Serge Habraken [a]

[a] Hololab, Physics Department, University of Liege, Allée du 6 Août, 17 B-4000 Liège, Belgium
[b] Centre Spatial de Liège, Avenue du Pré-Aily, B-4031 Angleur, Belgium

ARTICLE INFO

Article history:
Received 25 April 2012
Received in revised form
3 October 2012
Accepted 8 October 2012

Keywords:
Fresnel doublet
Solar concentrator
Achromatization
Solar simulator

ABSTRACT

A primary optics for solar concentrator made of an achromatic Fresnel doublet has been designed and manufactured. The achromatic Fresnel doublet combines the advantages of plastic lenses without being affected by chromatic aberrations. The performance has been determined experimentally using a homemade continuous solar simulator and compared to paraxial theory and ray-tracing simulations. Experimental results are in good agreement with theory and show that the achromatic Fresnel doublet is tolerant to manufacturing errors and uncertainty on the dispersion of the refractive index: the concentration factor remains above 1600× with an *f*-number of 2.

1. Introduction

Mainly two kinds of technologies are being used in solar concentration as primary optics nowadays: mirrors and refractive lenses. To a lesser extent, hybrid transmission systems exist like holographic/refractive lens [1] and diffractive/refractive lens [2] but they are still at research level. Each system has its advantages and disadvantages. Mirrors are said to be more prone to manufacturing errors and are less tolerant than lenses to a slope error [3]. On the other hand, refractive optics suffers from chromatic aberrations but lenses are more tolerant to manufacturing errors than mirrors. To overcome the chromatic problem, lots of optical systems like cameras, telescopes, microscopes etc. use an achromatic doublet of glasses which is too heavy, bulky and expensive to be used in concentrated photovoltaics (CPV). To our knowledge, to the notable exception of dome-shaped Fresnel lens designed by Ralf Leutz [3] in the end of the 1990s, no major progress on Fresnel lens as primary optics for CPV has been conducted in recent years. Recently, we proposed a theoretical design of achromatic Fresnel lens which combines the advantage of mirrors (achromatism) and plastic lenses (good tolerance to manufacturing errors) [4]. These advantages allow for very high concentration and offer design flexibility making possible to avoid, for example, hot spot problems. In the continuation of the theoretical investigations a first achromatic flat Fresnel lens made of poly(methyl methacrylate) (PMMA) and polycarbonate (PC) has been manufactured and subjected to an experimental setup.

2. Maximum concentration with flat refractive lens

Under normal incidence, the maximum concentration ratio achievable with mirrors is limited by diffraction. The half angular aperture of the source θ_s limits the maximum concentration $C_{\max}$ due to the étendue conservation [5]. This leads to the sine law of concentration, which is given by Eq. (1) for a concentrator of rotational symmetry immersed into a material of refractive index n [6].

$$C_{\max} = \left(\frac{n}{\sin\theta_s}\right)^2 \tag{1}$$

For Sun's half angular aperture (0.265°) the maximum concentration is around 42,000×. Such a concentration is theoretically achievable with compound parabolic concentrator (CPC) but in practice CPC are note used as primary optics in CPV due to their very high aspect-ratio (height $\approx 25\times10^3$ the diameter of the receiver).

Fresnel lenses however are generally thin, from 2.5 to 5.5 mm according to Miller and Kurtz [7], but cannot achieve such high concentration due to two independent factors. The first is intrinsic to the optical plastic used to the manufacturing of the lens, typically PMMA. The dispersion curve, i.e., the variation of refractive index with wavelength, makes shorter wavelengths converge faster than longer wavelengths. The longitudinal chromatic

* Corresponding author.
E-mail address: flanguy@ulg.ac.be (F. Languy).

0927-0248/$ - see front matter © 2012 Elsevier B.V. All rights reserved.
http://dx.doi.org/10.1016/j.solmat.2012.10.008

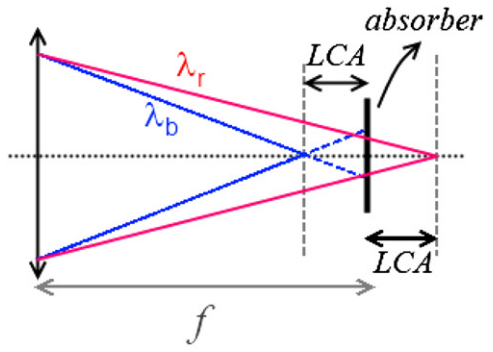

Fig. 1. Sketch depicting of the longitudinal chromatic aberration (*LCA*).

aberration (*LCA*), which is the distance between the absorber and the focal distance, see Fig. 1, changes with the wavelength.

The limiting factor is the wavelength that focuses the further from the absorber, in other words the wavelength with the maximum *LCA*. In Appendix A, we show that the maximum 2D concentration achievable with a given maximum *LCA* is

$$C_{\max} = \left(\frac{1}{LCA^*}\right)^2 \tag{2}$$

where LCA^* is the normalised maximum *LCA* for a spectral range between 380 and 1600 nm and is defined in Eq. (3).

$$LCA^* = \left(\frac{LCA_{\max}}{f}\right) \tag{3}$$

where f is the focal distance measured from the lens to the plane of the absorber. Languy et al. [8] showed that a typical value of the LCA^* for PMMA is 3.1% which limits the concentration factor to approximately $1000\times$.

The second limiting is the *f*-number of the design. Since the chief ray passes through the centre of the lens without being deviated, the higher the *f*-number, the lower the concentration ratio as illustrated in Fig. 2 where r_l is the radius of the lens and r_a the radius of the absorber.

The relation between the angular aperture, the *f*-number and the maximum concentration is

$$C_{\max} = \left(\frac{r_l}{r_a}\right)^2 = \left(\frac{1}{2F/\#\tan\theta_s}\right)^2 \tag{4}$$

3. Fresnel doublet design

In a previous work, we have investigated four kinds of flat Fresnel lenses [4]. For manufacturing reasons, we designed and developed a refractive Fresnel doublet with a flat interface, even if the outwards textured surface is subject to soiling problems. The configuration with the diverging lens facing the Sun has been selected since it has a lower dead zone than the configuration with the converging lens facing the Sun.

Design parameters were chosen in accordance to the recommendations of Mäkinen and Schipper [9], and Duerr et al. [10]. We designed lenses with a radius of 2 cm, a focal length of 8 cm and a thickness of 2 mm (teeth excluded). A sketch of the Fresnel doublet is depicted in Fig. 3.

The *f*-number of the Fresnel lens is thus fixed to two. In this case, according to Eq. (4), the maximum concentration ratio that can be achieved with Sun's angular aperture is $2920\times$.

Once these design parameters set, the lens designer may profit from two other parameters: the curvature of the first and last interfaces. To determine the shape of both lenses, we used

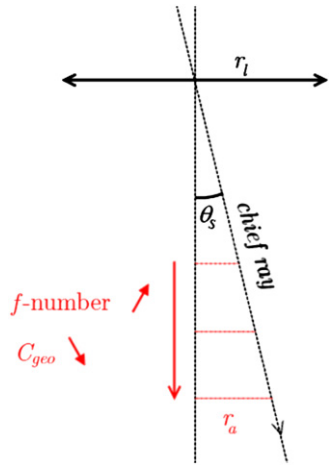

Fig. 2. Relation between *f*-number, angular size of the source and maximum concentration.

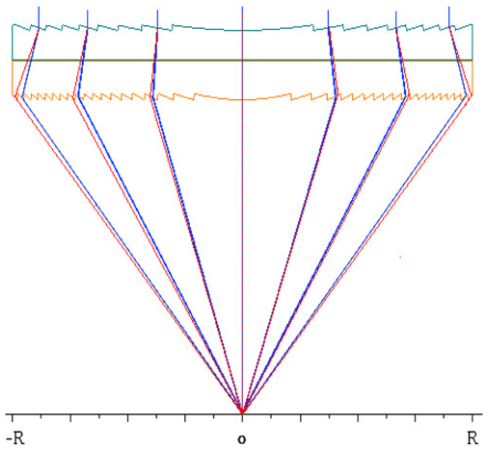

Fig. 3. Schematic achromatic Fresnel doublet (not to scale).

Newton's method [11] for two selected wavelengths (λ_1 and λ_2) in order to obtain $f(\lambda_1)=f(\lambda_2)$. Wavelengths λ_1 and λ_2 were chosen to minimize the LCA^* (see Fig. 4) achieved with $\lambda_3 \in$ [380–1680 nm] which depends on the dispersion curves of the materials used for each of the lenses. PMMA and PC are perfectly suitable for the minimization of the LCA^* since it may be decreased down to 0.1% along the visible (VIS) and near-infrared (NIR) regions [8].

The method used to design nonimaging Fresnel doublets is slightly different from the algorithm developed by Ralf Leutz for dome-shaped Fresnel lenses [3] and is better suited for flat lens designs. The break condition in Newton's method loop is based on the symmetry between edge-rays (see Fig. 5). Therefore, there is no need to specify the size of the detector but more importantly this ensures a maximal concentration ratio one the back length (*bfl*) is set.

The achromatic Fresnel doublet was designed for a given PMMA (that we identified as PMMA-1) and PC, but another PMMA (PMMA-2) was used during the injection moulding process. The refractive indices of these three optical plastics were obtained by ellipsometric measurements and were interpolated with Eq. (5) – wavelength λ being expressed in μm – corresponding to Sellmeier's formula [12] with parameters presented in Table 1. The three dispersion curves are shown in Fig. 6. These dispersion curves drove the design of the lens to 9 teeth ~350 μm-thick for the diverging lens in PC and 19 teeth

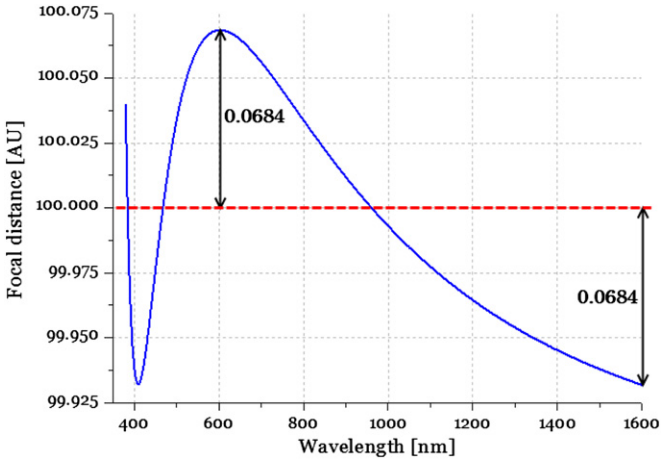

Fig. 4. Evolution of the focal distance with wavelength. *LCA** corresponds to 0.0684% achieved at 600 and 1600 nm. Design wavelengths λ_1 and λ_2 are 468 and 961 nm.

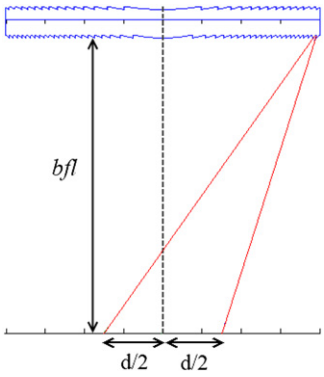

Fig. 5. Nonimaging Fresnel doublet designed to obtain edge-rays impacting symmetrically the plane of the absorber.

Table 1
Dispersion coefficients for PMMA-1, PC and PMMA-2.

	PMMA-1	PC	PMMA-2
A_1	+6.99710e−1	2.20558e−2	4.87933e−1
A_2	+2.73128e−1	2.53251e−1	2.96708e−6
A_3	+2.04343e−1	1.07366e+0	6.99678e−1
B_1	−5.77742e−4	1.00482e−1	1.06442e−2
B_2	−5.78464e−4	1.63043e−2	1.32562e−1
B_3	+4.29119e−2	1.62352e−2	1.05887e−2

∼415 μm-thick for the converging lens in PMMA.

$$n(\lambda)=\sqrt{1+\frac{A_1\lambda^2}{\lambda^2-B_1}+\frac{A_2\lambda^2}{\lambda^2-B_2}+\frac{A_3\lambda^2}{\lambda^2-B_3}}. \quad (5)$$

4. Performance analysis tools

The Fresnel doublet has been investigated in three different ways: by paraxial calculations, experimentally using a solar simulator and by ray-tracing simulations. The Fresnel doublet has been compared with the singlet in terms of focal distance and focal spot.

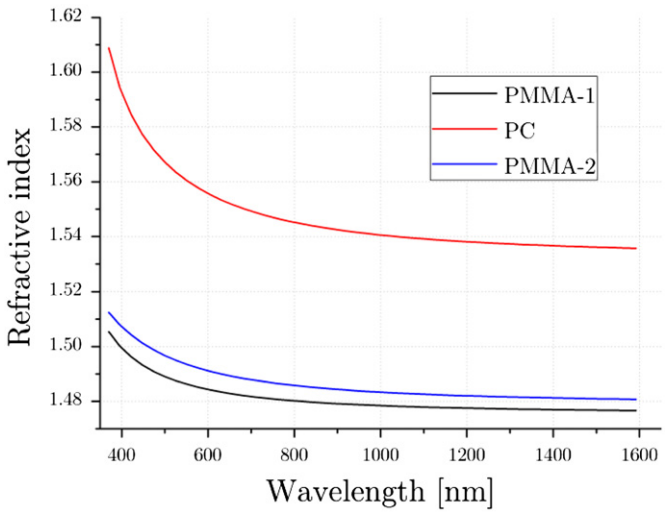

Fig. 6. Refractive indices of PMMA-1, PC and PMMA-2 according to coefficients depicted in Table 1.

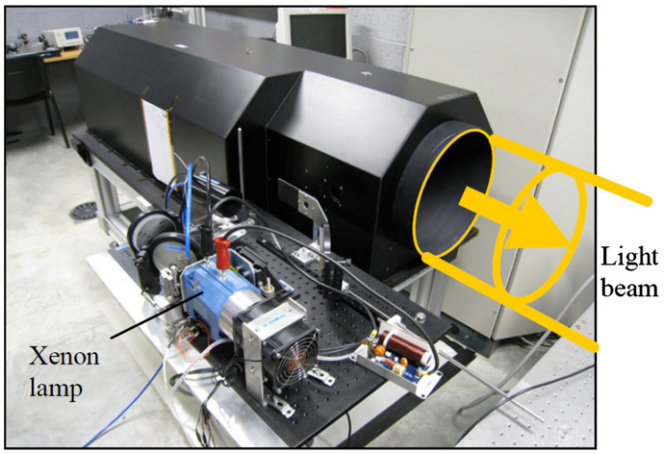

Fig. 7. Home-made continuous solar simulator at Centre Spatial of Liege [17].

4.1. Paraxial calculation

To determine the evolution of the paraxial *bfl* of the doublet with the wavelength we used Eq. (6) where d is the distance that separates the lenses (4 mm in our case) of focal distances f_1 and f_2.

$$bfl(\lambda)=\frac{f_2(d-f_1)}{d-(f_1+f_2)} \quad (6)$$

In first approximation, the focal length of a thin lens is given by

$$f(\lambda)=\left(\frac{1}{R_1}-\frac{1}{R_2}\right)^{-1}\frac{1}{n(\lambda)-1}=\frac{RoC_{eq}}{n(\lambda)-1} \quad (7)$$

with R_1 and R_2, respectively the front and back radii of the lens and RoC_{eq} is defined as the equivalent radius of curvature [13]. This formula shows the dependence between the focal distance and the refractive index itself depending on the wavelength. For a given lens shape designed for a refractive index n, the use of another refractive index n' turns the focal distance f into f' given by

$$f'(\lambda)=\frac{n(\lambda)-1}{n'(\lambda)-1}f(\lambda). \quad (8)$$

This kind of situation arises if another material is used in place of the design one or if the material suffers from a variation of temperature [14,15]. On the other hand, a manufacturing error or an expansion of the lens material could lead to an error in the

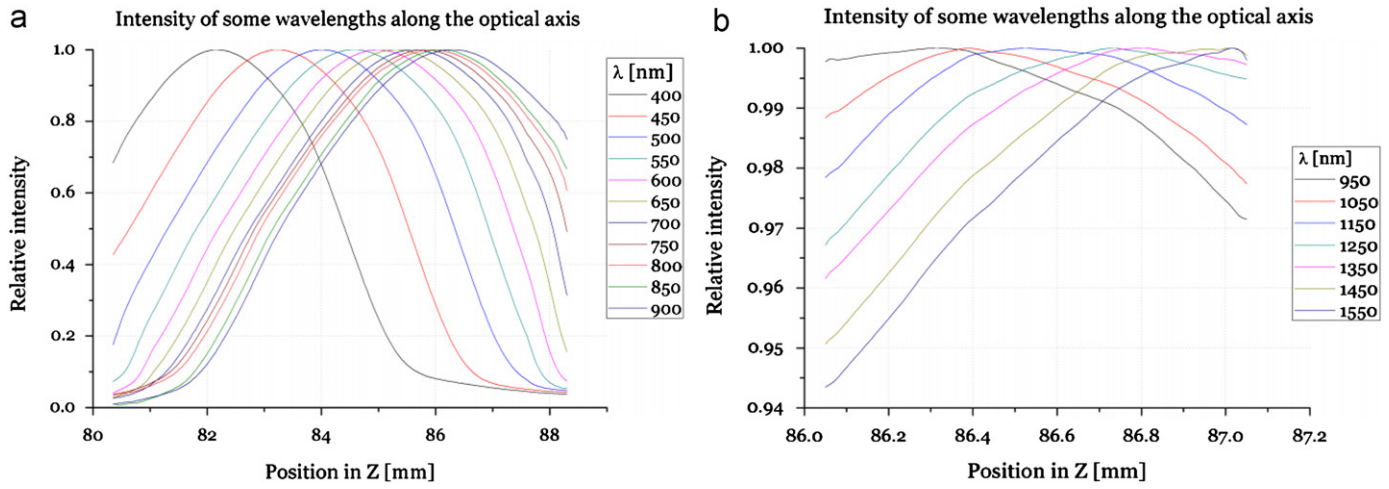

Fig. 8. Relative intensity along the optical axis in the VIS region (a) and in the NIR region (b) for singlet lens.

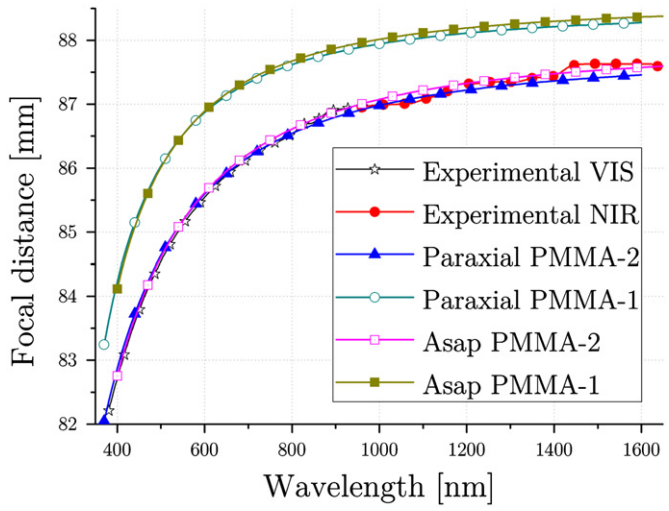

Fig. 9. Comparison between focal distances of different kind of singlets: experimental and theoretical results.

radius of curvature, turning the RoC_{eq} into RoC''_{eq} conferring a focal distance f' to the lens, given by

$$f''(\lambda) = \frac{RoC''_{eq}}{RoC_{eq}} f(\lambda) \tag{9}$$

The paraxial equations here above allow for a fast determination of the *bfl* of the doublet in case of manufacturing error.

4.2. Solar simulator

To avoid cloudy skies, tracking errors and luminosity variations, a continuous solar simulator has been designed and developed (see Fig. 7) with the following characteristics: a continuous xenon arc-lamp power of 700 W, an output diameter of 30 cm, a radiant exitance of 130 ± 20 W/m^2 and a divergence: $0.24 \pm 0.01^\circ$. Note that with a divergence of 0.24° with an *F*/2 concentrator, Eq. (4) gives a maximum concentration factor of 3560 ×.

The focal length dispersion has been investigated with an optical fibre that has a core diameter of 50 μm translated with a 3-axis motorized system. The focal distance has been considered as the distance where the maximum energy is collected within the core of 50 μm. Two spectrometers had to be used to cover a spectral range from 380 to 1600 nm: a VIS spectrometer (AvaSpec-2048 from Avantes) and a NIR spectrometer (NIRQuest 512 from Ocean Optics).

To determine the spot size, several intensity maps have been measured perpendicularly to the optical axis. For each map, the acquisition was stopped when the intensity dropped under 1% of the maximum intensity (located on the optical axis). Since the spectrometer used was not calibrated and the lamp spectrum does not exactly correspond to the Sun's spectrum, a relative intensity map was measured for several wavelengths (from 380 to 1600 nm with a step of 20 nm). A weight (g_λ) was then attributed for each wavelength according to a blackbody of 5780 K. Finally the total intensity I_{tot} was considered as being given by the following equation:

$$I_{tot} = \sum_{\lambda=380}^{1600\ nm} g_\lambda I_\lambda \tag{10}$$

4.3. Ray-tracing

We used a non-sequential ray-tracing tool developed by Breault Research Organization: ASAP® [16]. For each optical system studied, 48,000 beams were launched for all wavelengths from 380 to 1600 nm with a step of 20 nm and with a weight corresponding to a blackbody of 5780 K. In order to compare in an appropriate way the experimental results to the ray-tracing simulations, the simulated light source in ASAP fits the angular aperture of the solar simulator i.e., 0.24°.

5. Results

We first investigated the converging singlet made of PMMA-2. The relative intensity acquired by the spectrometer for the VIS and NIR-regions is represented in Fig. 8. The maximum intensity for each wavelength has been considered as the focal distance. It has been plotted and compared with paraxial approximation calculations and ray-tracing results in Fig. 9. Since PMMA-2 has a higher refractive index than PMMA-1, the focal distance of the lens is shorter as can be deduced from Eq. (8). The error between experimental results, ray-tracing simulations and theoretical results obtained with paraxial theory lies under 0.2%.

The focal properties of the achromatic Fresnel doublet were measured in the same way. The original lens was conceived to have a focal distance of 80 mm. Due to the use of another PMMA, the measured focal distance should have been around 78.5 mm

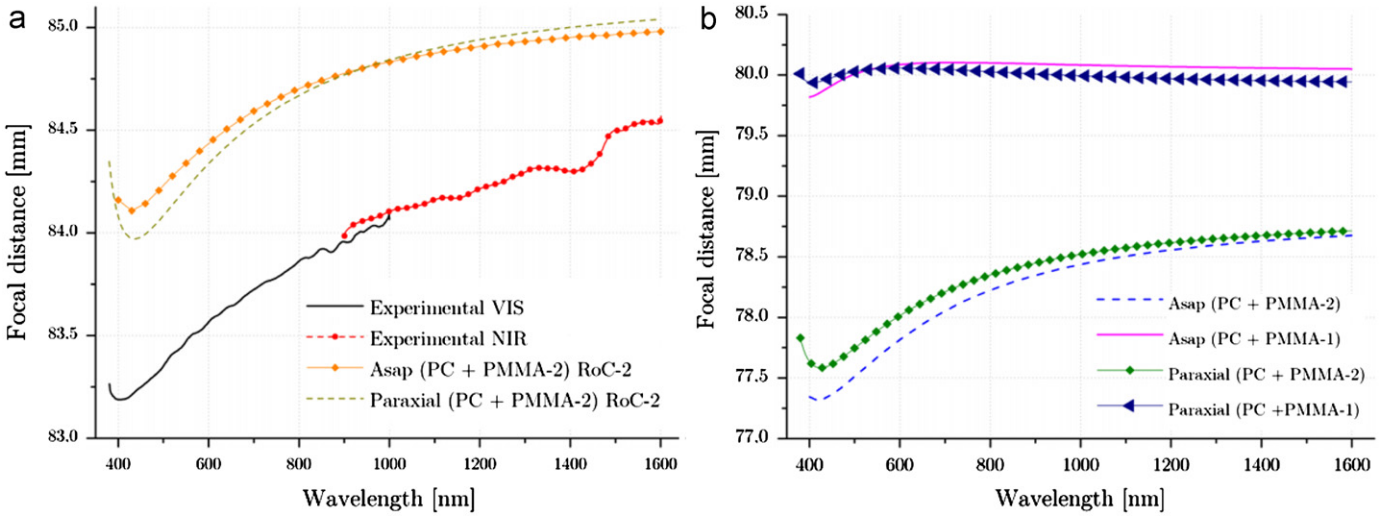

Fig. 10. Focal distances of the achromatic Fresnel doublet: experimental and theoretical results.

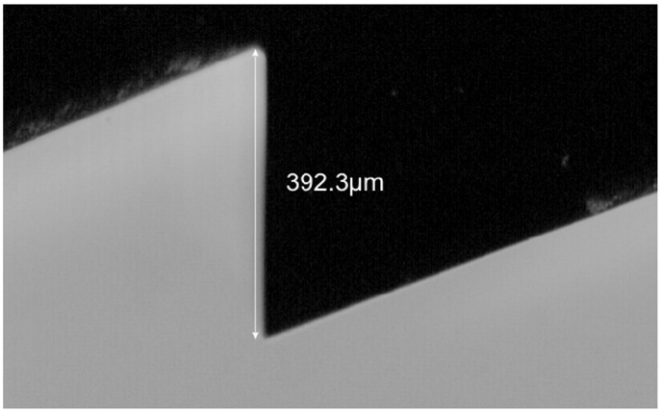

Fig. 11. Silicone negative replica of the converging lens. Measured thickness of the lens is 392.3 μm in place of 414 μm.

for a wavelength of 1000 nm. However, experimental measurements indicate a focal length of about 84 mm (see Fig. 10). This might be explained by the shrinkage of the PMMA and PC that were erroneously estimated. In order to confirm the supposition, the lenses were analysed by means of silicone negative replica. Measurements by optical microscope show a maximal error of the radius of curvature of −5.5% for the PMMA-2 (see Fig. 11) and −1.2% for the PC. The focal dispersion curve for this case is annotated with "*RoC*-2". Using this maximal error we obtain an overestimated focal length which effectively lies above the measured focal length. This error has low influence on the *LCA**: 0.63% for PMMA-2 in paraxial condition, 0.72% for the *RoC*-2 design and 0.82% for the experimental measurements.

To evaluate the performance of the Fresnel doublet we performed the summation of intensity maps (see Fig. 12) of the focal plane and we calculated the encircled energy and compared it to the ray-tracing simulations using the same angular aperture as the solar simulator.

Experimental results of the encircled energy are presented in Fig. 13. They are in good agreement with the encircled energy obtained with ray-tracing simulations using an illumination source which fits the solar simulator characteristics. The concentration factor of the doublet is almost four times higher than the one achieved with a singlet. As predicted by ray-tracing simulations, if the lens had been injected with the design PMMA, the concentration ratio would have been even higher: 3200× for 90% of the encircled energy. Nevertheless, despite the use of another PMMA than initially planned, we obtain a very high concentration factor, about 2400× for 90% of the encircled energy.

6. Conclusions

Refractive Fresnel doublets allow for a very high concentration thanks to highly reduced chromatic aberration. In case of manufacturing error – leading to an alteration of the curvature of the lens – a modification of the focal distance occurs without significant deterioration of the achromatic behaviour of the Fresnel doublet. The same conclusion may be drawn with the refractive index: an error on the refractive index induces a modification of the focal distance without significant alteration of the chromatic aberration thus retaining a high concentration factor. Refractive Fresnel doublets are therefore very tolerant and are suitable in real conditions where the temperature induces a modification of the refractive indices and the shape of the lenses.

Acknowledgment

This work is supported by the Wal ID Sol project from the Solwatt program (Convention 850552) of the Walloon Region. The authors thank Optim Test Center for the injection moulding and Amos S.A. for the diamond turning. The authors are also grateful to Gopal Thalluri for its careful reading.

Appendix A

Using the geometry and parameters presented in Fig. A1, we are able to determine the ideal position of the receiver to maximize the concentration ratio. In this figure, λ_m is the wavelength with the shortest focal distance and λ_M the wavelength with the longest focal distance. They have both the same *LCA* in absolute value compared to λ_0. So,

$$f(\lambda_0) = \frac{f(\lambda_m)+f(\lambda_M)}{2} \tag{11}$$

To collect all the refracted beams on the smallest receiver, we may deduced from the above figure that it should be placed closer to $f(\lambda_m)$ than $f(\lambda_M)$. The ideal position is determined by the intersection of the end rays of wavelengths λ_m and λ_M, that can be

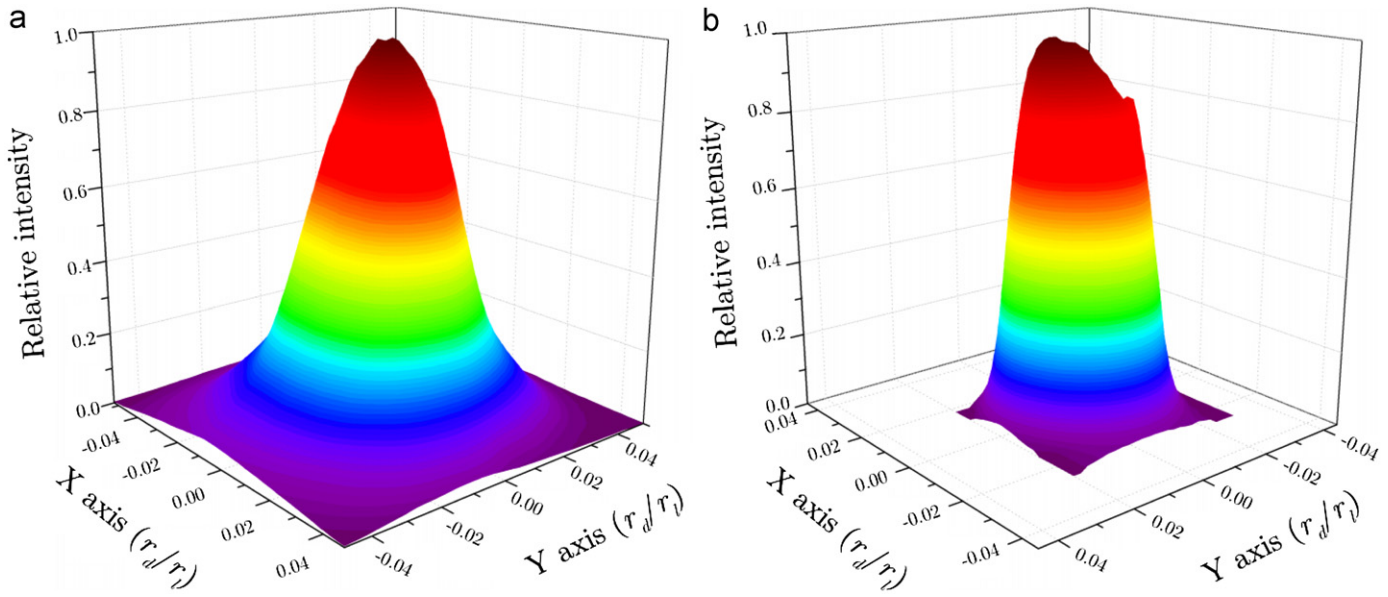

Fig. 12. Experimental relative intensity for (a) the Fresnel singlet and (b) the Fresnel doublet.

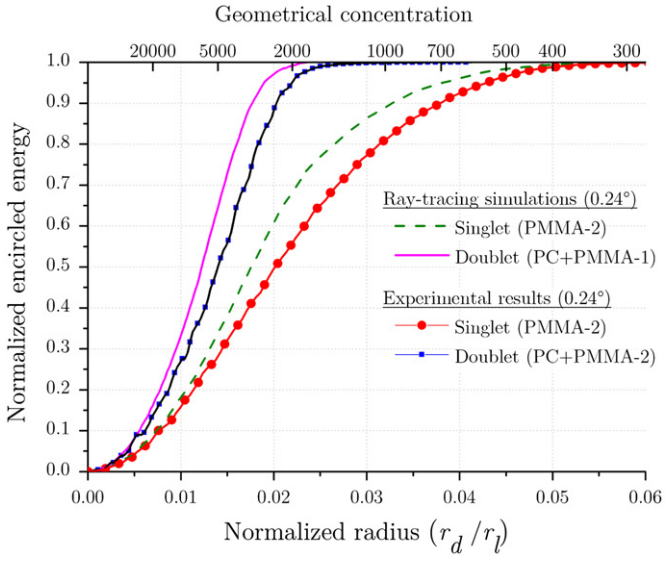

Fig. 13. Experimental and ray-tracing simulations results for the enclosed energy and geometrical concentration: comparison between doublet and singlet Fresnel lenses.

described with functions $y_1(z)$ and $y_2(z)$

$$\begin{cases} y_1(z) = \frac{-r_l}{f(\lambda_0)(1+|LCA^*|)}z + r_l \\ y_2(z) = \frac{-r_l}{f(\lambda_0)(1-|LCA^*|)}z - r_l \end{cases} \quad (12)$$

The intersection occurs at a value z_{int} given by

$$z_{\text{int}}\left(\frac{1+|LCA^*|+1-|LCA^*|}{1-LCA^{*2}}\right) = 2f(\lambda_0) \quad (13)$$

thus the intersection occurs at

$$z_{\text{int}} = f(\lambda_0)\left(1-LCA^{*2}\right) \quad (14)$$

To calculate the minimum size of the receiver, introduce Eq. (14)

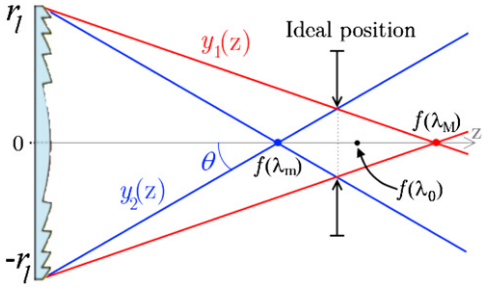

Fig. A1. Ideal position of the receiver.

in (12)

$$y(z_{\text{int}}) = \frac{f(\lambda_0)\left(1-LCA^{*2}\right)(-r_l)}{f(\lambda_0)(1-LCA^*)} + r_l \quad (15)$$

since $A^2-B^2=(A+B)(A-B)$,

$$y(z_{\text{int}}) = r_l \times LCA^* \quad (16)$$

Finally, the maximum concentration achievable is

$$C_{\max}(LCA^*) = \left(\frac{r_l}{y(z_{\text{int}})}\right)^2 = \left(\frac{1}{LCA^*}\right)^2 \quad (17)$$

References

[1] J. Loicq, E. Mazy, M.-L. Hellin, T. Thibert, J.-H. Lecat, D. Verstraeten, P. Lemaire, Design of high concentration photovoltaic hybrid lens composed of refractive and holographic lenses to reduce chromatic aberration, in: Proceedings of the Workshop on Concentrating Photovoltaic Power Plants: Optical Design and Grid Connection, Darmstadt, Germany, March 9–10, 2009.
[2] F. Languy, C. Lenaerts, J. Loicq, S. Habraken, Achromatization of solar concentrator thanks to diffractive optics, in: Proceedings of the Workshop on Concentrating Photovoltaic Power Plants: Optical Design and Grid Connection, Darmstadt, Germany, March 9–10, 2009.
[3] R. Leutz, A. Suzuki, Nonimaging Fresnel Lenses, Design and Performance of Solar Concentrators, Springer-Verlag, New York, 2001.
[4] F. Languy, S. Habraken, Performance comparison of four kinds of flat nonimaging Fresnel lenses made of polycarbonates and polymethyl methacrylate for concentrated photovoltaics, Optics Letters 36 (2011) 2743–2745.
[5] J. Chaves, Introduction to Nonimaging Optics, CRC Press, Taylor & Francis Group, Florida, 2008.

[6] R. Winston, J.C. Minano, P. Benitez (Eds.), Elsevier Academic Press, New York, 2005.
[7] D.C. Miller, S.R. Kurtz, Durability of Fresnel lenses: a review specific to the concentrating photovoltaic application, Solar Energy Materials and Solar Cells 95 (2011) 2037–2068.
[8] F. Languy, K. Fleury, C. Lenaerts, J. Loicq, D. Regaert, T. Thibert, S. Habraken, Flat Fresnel doublets made of PMMA and PC: combining low cost production and very high concentration ratio for CPV, Optics Express 19 (2011) A280–A294.
[9] J.-T. Mäkinen, R. de Schipper, Injection molding for solar concentrators, in: Proceedings of the Workshop on Concentrating Photovoltaic Power Plants: Optical Design and Grid Connection, Darmstadt, Germany, March 9–10, 2009.
[10] F. Duerr, Y. Meuret, H. Thienpont, Miniaturization of Fresnel lenses for solar concentration: a quantitative investigation, Applied Optics 49 (2010) 2339–2346.
[11] E.W. Weisstein, Newton's Method, in Math World, A Wolfram Web Resource. 〈http://mathworld.wolfram.com/NewtonsMethod.html〉, (last accessed on 09/09/2012).
[12] S.N. Kasarova, N.G. Sultanova, C.D. Ivanov, I.D. Nikolov, Analysis of the dispersion of optical plastic materials, Optical Materials 29 (11) (2007) 1481–1490.
[13] E. Hecht, Optics, fourth ed., Addison-Wesley, 2002, Chapter 5.
[14] J.M. Cariou, J. Dugas, L. Martin, P. Michel, Refractive-index variations with temperature of PMMA and polycarbonate, Applied Optics 25 (1986) 334–336.
[15] T. Hornung, M. Steiner, P. Nitz, Estimation of the influence of Fresnel lens temperature on energy generation of a concentrator photovoltaic system, Solar Energy Materials and Solar Cells 99 (2012) 333–338.
[16] Breault Research Organization, 〈http://www.breault.com/software/asap.php〉, (last accessed on 09/09/2012).
[17] T. Thibert, M.-L. Hellin, J. Loicq, E. Mazy, J.-M. Gillis, F. Languy, S. Habraken, J.-H. Lecat, J.-M. Defise, Continuous solar simulator for concentrator photovoltaic systems, in: Proceedings of the 25th European Photovoltaic Solar Energy Conference and Exhibition, Valencia, Spain, September 6–10, 2010.

Abstract

In the field of concentrated photovoltaics, the main disadvantage of lenses compared to mirrors lies in their chromaticity: Snell's law is related to the refractive index which is wavelength dependent. Consequently, even for purely collimated beams under normal incidence, the maximum concentration achievable with typical lenses made of PMMA is limited to ~1000×. This maximum value becomes even lower when considering Sun's angular aperture. Since the law of reflection is not wavelength dependent, mirrors can theoretically achieve the thermodynamic limit of concentration which is about 46'000×.

This thesis aims at the design and the manufacturing of an achromatic Fresnel lens suitable for photovoltaic solar concentration, i.e. combining high concentration, low production cost and tolerance to manufacturing errors.

Firstly, we investigated a hybrid lens made of a refractive lens and a diffractive lens. The investigations showed that the concentration ratio could be multiplied by 4. A full chapter is dedicated to the optimisation of blazed diffraction gratings to finally achieve the design of the diffractive lens. Nevertheless, a bilayer diffractive lens is needed to obtain a high diffraction efficiency which makes the diffractive lens highly sensitive to manufacturing errors and consequently not suitable for photovoltaic solar concentration.

Purely refractive achromatic Fresnel doublets were then investigated and several designs were compared. They allow for very high concentration ratios in the case of collimated beams under normal incidence, higher than 100'000×. Therefore, contrary to singlets, Fresnel doublets are much more affected by the angular size of the source than by the chromatic aberration. Moreover, it was shown that they are tolerant to manufacturing error, change of temperature and uncertainty on the refractive index.

It emerges from this thesis that the concept of achromatic doublets is a tolerant and low-cost production solution to achieve a highly concentrated white flux. Although bilayer diffractive lenses are not suitable for concentrated photovoltaics, the combination of refractive with diffractive structures seems to be promised to a bright future for spectrum splitting applications, including spectrum splitting for concentrated photovoltaics.